

THE INFLUENCE OF THE INVAR EFFECT ON THE ELASTIC PROPERTIES AND
THE MARTENSITIC TRANSFORMATION OF Fe_3Pt

by

HUNG CHI LING

B.Sc. (Physics), Massachusetts Institute of Technology
1972

M.A. (Physics), State University of New York at Stony Brook
1974

Submitted in partial fulfillment of the requirements
for the degree of

DOCTOR OF SCIENCE

at the

MASSACHUSETTS INSTITUTE OF TECHNOLOGY

June, 1978

© Massachusetts Institute of Technology 1978

Signature of Author

Department of Materials Science and Engineering
May 5, 1978

Certified by

Thesis Supervisor

Accepted by

Chairman, Departmental Committee on Graduate
Students

ARCHIVES

MASSACHUSETTS INSTITUTE
OF TECHNOLOGY

FEB 16 1979

LIBRARIES

ABSTRACT

THE INFLUENCE OF THE INVAR EFFECT ON THE ELASTIC PROPERTIES AND
THE MARTENSITIC TRANSFORMATION OF Fe_3Pt

by

HUNG CHI LING

Submitted to the Department of Materials Science and Engineering on May 5, 1978, in partial fulfillment of the requirement for the degree of Doctor of Science.

The alloy Fe_3Pt was chosen to study (1) the effects of ordering on the Invar effect, and (2) how changes in the elastic properties of the austenite on ordering affect the elastic accommodation of plates of martensite.

The ordering kinetics of Fe_3Pt was studied by "short-time" annealing at 650°C and by equilibrium annealing at various temperatures below the critical ordering temperature. From X-ray diffraction and elastic constant measurements, it is concluded that ordering in Fe_3Pt is by a nucleation and growth mechanism.

The temperature dependence of the single crystal elastic constants C_L , C and C' was measured as a function of the degree of order. The C_L elastic constant softens above the Curie temperature, passes through a minimum and increases again at lower temperatures. The minimum becomes broader and shallower with increasing degree of order. For the two shear constants C and C' , the magnetic contribution is negative and begins near the Curie temperature. They decrease monotonically with decreasing temperature below T_C . Softening of the C and C' elastic constants decreases when the austenite C is highly ordered. This decrease in the magnitude of the Invar effect as ordering increases is interpreted in terms of the spatial dependence of the nearest-neighbor exchange integral. On the Bethe curve Fe_3Pt , in its various ordered states, lies in the range where the first derivative of the exchange integral is positive. In this range of interatomic separation, the exchange interaction between γ -Fe atoms is antiferromagnetic and that between Fe and Pt atoms, ferromagnetic.

On ordering the austenite, the M_S temperature is depressed such that the temperature interval between the Curie temperature and M_S increases, resulting in decreasing values of elastic moduli at M_S with ordering. Eshelby's model of the strain fields produced by an inclusion embedded in a continuous medium was utilized to calculate the stress fields surrounding a plate of martensite in an isotropic matrix of austenite. For a plate of fixed aspect ratio, the plastic zone decreases drastically with ordering due to the decrease of the elastic moduli and the increase of the flow stress at M_S . Using the criterion of no plastic deformation along the broad γ/α interface an upper limit of 100 cal/mole was derived for the chemical driving force

per unit volume, Δg_c , for the thermoelastic growth of an isolated single plate. An anisotropic calculation does not alter this estimate significantly.

Self-accommodation of neighboring plates with opposite shape strain limits the plastic zone to the edges of the plates, thus enabling thicker plates to exist in thermoelastic equilibrium for a fixed Δg_c . From the analysis of stress fields surrounding ellipsoidal and square plates, it is suggested that the optimum configuration is for plates with tapered edges to be in contact over a large area.

Theoretical calculation of the chemical free energy difference per mole, ΔG^{chem} , between the austenite and the martensite phases was carried out based on the Olson-Cohen nucleation model. Taking into account the tetragonality of the martensite phase, the estimate of the minimum value of ΔG^{chem} at M_s is $-106 \text{ cal/mole} (-437 \text{ J/mole})$. It is suggested that a lower minimum value may be obtained by considering a different dislocation structure of the nucleus in a $\text{fcc} \rightarrow \text{bct}$ transformation than that proposed by Olson and Cohen for a $\text{fcc} \rightarrow \text{bcc}$ transformation.

Thesis Supervisor: Walter S. Owen

Title: Professor of Materials Science and Engineering

TABLE OF CONTENTS

<u>Chapter Number</u>		<u>Page Number</u>
	TITLE PAGE -----	1
	ABSTRACT -----	2
	TABLE OF CONTENTS -----	4
	LIST OF FIGURES -----	8
	LIST OF TABLES -----	13
	ACKNOWLEDGEMENTS -----	15
1	PURPOSE OF RESEARCH -----	16
2	THE INVAR EFFECT -----	18
	2.1 Introduction -----	18
	2.2 Theoretical Models -----	28
	2.3 Ferromagnetism: Localized Models Versus Itinerant Models -----	36
	2.4 The Localized Exchange Integral -----	44
	2.5 Magnetic Contributions to the Elastic Constants -----	46
	2.5.1 General Considerations -----	46
	2.5.2 Formulation in Terms of Localized Model -----	48
	2.5.3 Correction Terms -----	50
	2.5.4 Dependence of an Isotropic Exchange Integral on the Degree of Order in Cu_3Au ($L1_2$) Type Ordering -----	51
3	EXPERIMENTAL PROCEDURE -----	56
	3.1 Materials -----	56
	3.2 Specific Heat Measurement -----	58
	3.3 X-ray Measurement -----	58
	3.4 Elastic Constant Measurement -----	59

Table of Contents (cont'd)

5

<u>Chapter Number</u>		<u>Page Number</u>
	3.5 Calculation of Average Elastic Moduli From Single Crystal Elastic Constants -----	64
	3.6 Heat Treatment -----	66
4	EXPERIMENTAL RESULTS AND DISCUSSION -----	70
	4.1 Ordering -----	70
	4.2 Specific Heat -----	76
	4.3 Elastic Moduli of Polycrystalline Specimens -----	82
	4.3.1 Fe-30Ni Austenite -----	82
	4.3.2 Fe-30Ni Martensite -----	85
	4.3.3 Fe-22Pt Martensite -----	87
	4.4 Single Crystal Elastic Constants of Fe-25Pt -----	87
	4.4.1 General Considerations -----	87
	4.4.2 Effect of an Applied Ex- ternal Field -----	85
	4.4.3 Elastic Constants as a Func- tion of Degree of Order -----	95
	4.4.4 Average Elastic Moduli as a Func- tion of Degree of Order -----	112
	4.5 Variation of Exchange Integral with Interatomic Distance -----	113
5	THERMOELASTIC MARTENSITE -----	130
	5.1 Introduction -----	130
	5.2 Theoretical Considerations -----	136
	5.3 A Model of Growth -----	141
	5.4 The Model of Inclusion -----	147
	5.5 Results and Discussion -----	149

Table of Contents (cont'd)

<u>Chapter Number</u>		<u>Page Number</u>
	5.5.1 A Single Plate -----	149
	5.5.2 An Assembly of Plates -----	158
	5.5.3 Anisotropic Calculation of the Elastic Strain Energy and the Stress Field -----	163
6	THEORETICAL CALCULATION OF ΔG^{chem} AT M_s -----	172
	6.1 A Nucleation Model -----	172
	6.2 An Infinite Screw Dislocation Wall -----	176
	6.3 An Infinite Edge Dislocation Wall -----	179
	6.4 Coherent Strain Energy -----	182
	6.5 ΔG^{chem} at M_s and the Effect of Tetragonality -----	183
7	CONCLUSIONS -----	189
8	SUGGESTIONS FOR FURTHER WORK -----	191
APPENDIX A	THE STRAIN FIELDS OF AN ELLIPSOIDAL INCLUSION IN AN ISOTROPIC MATRIX -----	193
APPENDIX B	THE STRAIN FIELDS OF A SQUARE PLATE IN AN ISOTROPIC MATRIX -----	205
APPENDIX C	ANISOTROPIC CALCULATION OF THE ELASTIC STRAIN ENERGY OF AN ELLIPSOIDAL INCLUSION IN AN INFINITE MATRIX -----	207
APPENDIX D	ANISOTROPIC CALCULATION OF THE STRESS FIELD DUE TO AN ELLIPSOIDAL INCLUSION IN AN INFINITE MATRIX -----	225
APPENDIX E	THE STRESS FIELDS OF A $(111)[110]$ SCREW DISLOCATION WALL -----	237

<u>Chapter</u> <u>Number</u>		<u>Page</u> <u>Number</u>
APPENDIX F	THE STRESS FIELDS OF A $(\bar{1}\bar{1}1)[110]$ EDGE DISLOCATION WITH BURGERS' VECTOR $\frac{a_{fcc}}{6} [\bar{1}\bar{1}2]$ -----	239
APPENDIX G	BAIN DEFORMATION IN THE fcc \rightarrow bct TRANSFORMATION OF ORDERED Fe ₃ Pt -----	243
APPENDIX H	INTENSITY TRACES OF SINGLE CRYSTAL (110) AND (220) DIFFRACTION PEAKS IN Fe ₃ Pt -----	244
REFERENCES	-----	248
BIOGRAPHICAL NOTE	-----	255

LIST OF FIGURES

<u>Figure Number</u>		<u>Page Number</u>
1.	Linear Expansion Coefficient as a Function of Concentration in Fe-Ni and Fe-Pt Alloys -----	19
2.	Room Temperature Lattice Parameter Versus Concentration in Fe-Pt Alloys -----	20
3(a)	Spontaneous Volume Magnetostriction Versus Concentration in Fe-Ni Alloys -----	23
3(b)	Spontaneous Volume Magnetostriction Versus Magnetization Squared in Ordered and Disordered Fe-28Pt. -----	23
4.	Temperature Dependence of Elastic Constants in Fe-35Ni and Disordered Fe-28Pt -----	26
5.	Reduced Magnetization Versus Reduced Temperature in Fe-32Ni, ordered and disordered Fe-28Pt Compared with Theoretical Curves -----	35
6.	Neutron Scattering Result Showing Individual Atomic Moments in $\text{Ni}_{1-x}\text{Fe}_x$ -----	41
7.	X- α Cluster Calculation Compared with Band Theory Results -----	42
8.	Different Lattice Sites in $L1_2$ Ordering -----	53
9.	Temperature Cycle of Single Crystal Growth -----	57
10.	Block Diagram of Electronics for Pulse Superposition Technique -----	61
11.	Long Range Order Parameter S Versus Ordering Temperature in Fe_3Pt -----	71
12.	Room Temperature Lattice Parameter a_0 versus Degree of Order S in Fe_3Pt -----	72
13(a)	Heat Capacity Calculated for Various Quantum States According to Weiss Theory -----	77

List of Figures (cont'd)

<u>Figure Number</u>		<u>Page Number</u>
13(b)	Determination of the Curie Temperature From the Square of Magnetization Versus Temperature Curve (Schematic) -----	77
14.	Temperature Dependence of Specific Heat As a Function of S -----	79
15.	Variation of the Curie Temperature T_c and the M_s Temperature With Degree of Order in Fe_3Pt -----	80
16.	Traces of Specific Heat Measurement for S = 0.2 -----	81
17.	Polycrystalline Elastic Moduli of Fe-30 Ni Austenite Versus Temperature -----	84
18.	Polycrystalline Elastic Moduli of Fe-30Ni Martensite Versus Temperature -----	86
19.	Polycrystalline Elastic Moduli of Fe-22Pt Martensite Versus Temperature -----	88
20.	Temperature Dependence of Single Crystal Elastic Constants in Fe_3Pt S = 0.2 and 0 -----	90
21.	Temperature Dependence of the Linear Expan- sion Coefficient in Disordered and Ordered Fe-28Pt -----	94
22(a)	Temperature Dependence of the C_L Elastic Con- stant S = 0.85. H = 8 and 0 kG -----	96
22(b)	Temperature Dependence of the C Elastic Con- stant S = 0.85. H = 8 and 0 kG -----	97
22(c)	Temperature Dependence of the C' Elastic Constant. S = 0.85. H = 8 and 0 kG -----	98
23.	Temperature Dependence of the Three Elastic Constants as a Function of the Degree of Order S. H = 8 kG -----	99
24.	Temperature Dependence of the C Elastic Con- stant as a Function of $(T - T_c)$ and order S. H=8 kG -----	102

<u>Figure Number</u>		<u>Page Number</u>
25.	Temperature Dependence of the C' Elastic Constant as a Function of $(T-T_c)$ and degree of Order S. H=8 kG -----	103
26.	Functional Dependence of the Reduced Magnetization, I/I_0 , on the Reduced Temperature, T/T_c , in Ordered and Disordered Fe ₃ Pt -----	108
27.	Magnetic Contribution to the Shear Elastic Constants Versus Reduced Magnetization Squared for S = 0.85, 0.60, 0.55 and 0.40 -----	109
28.	Temperature Dependence of the Anisotropy Ratio as a Function of the Degree of Order S -----	110
29.	Temperature Dependence of the Average Shear Modulus as a Function of the Degree of Order S -----	114
30.	Temperature Dependence of the Young's Modulus as a Function of the Degree of Order S -----	115
31.	Temperature Dependence of the Bulk Modulus as a Function of the Degree of Order S -----	116
32.	Temperature Dependence of the Poisson's Ratio As a Function of the Degree of Order S -----	117
33.	The Bethe-Slater Curve -----	126
34.	Spatial Dependence of the Nearest-Neighbor Exchange Integral in Fe ₃ Pt (Schematic) -----	127
35.	Temperature Dependence of the 0.2% Flow Stress in Fe ₃ Pt. S ≈ 0.5 -----	146
36(a)	The σ_{13} Shear Stress Along x Axis Due to an Ellipsoidal Plate Lying in xy Plane with Shear in x Direction. S = 0.6 -----	152
36(b)	The σ_{13} Shear Stress Along the z Axis. S = 0.6 -----	153

List of Figures (cont'd)

<u>Figure Number</u>		<u>Page Number</u>
37(a)	Matrix Yield Stress Contours in the xz Plane as a Function of Aspect Ratio and the Degree of Order S -----	154
37(b)	Matrix Yield Stress Contours in the yz Plane as a Function of the Degree of Order S. Aspect Ratio 0.08 -----	155
38.	The Radius of the Yield Stress Envelope Along the z Axis as a Function of Aspect Ratio for S = 0.6, 0.4 and 0.2 -----	156
39.	The Radius of the Yield Stress Envelope at Various Points x in the [100] Direction. S = 0.6 -----	157
40.	Matrix Yield Stress Contours of an Assembly of Two Plates with Opposite Shear Strain. Aspect Ratio 0.08 -----	160
41.	Matrix Yield Stress Contours for Square Plates Lying in x y Plane with Shear in x Direction. S = 0.6. Aspect Ratio 0.042 -----	161
42.	An Assembly of Two Self-Accommodating Plates ---	162
43.	Elastic Strain Energy of an Ellipsoidal Plate of Martensite in a Matrix of Austenite at M_s as a Function of Aspect Ratio. S = 0.6 -----	167
44.	Anisotropic Elastic Strain Energy as a Function of Aspect Ratio. S = 0.6, 0.4, 0.2 and 0 -----	168
45(a)	Interfacial Dislocation Structure of the Olson-Cohen Nucleation Model -----	174
45(b)	An Infinite Screw Dislocation Wall -----	174
45(c)	An Infinite Edge Dislocation Wall -----	174
46.	The σ_{yz} Stress of an Infinite $(\bar{1}\bar{1}1)[110]$ Screw Dislocation Wall -----	178
47.	The σ_{xx} and σ_{xy} Stresses of an Infinite $(\bar{1}\bar{1}1)[110]$ Edge Dislocation Wall -----	180

List of Figures (cont'd)

<u>Figure Number</u>		<u>Page Number</u>
C.1	Elastic Strain Energy of an Ellipsoidal Inclusion Undergoing Uniform Dilatation in an Isotropic Matrix -----	212
C.2	Elastic Strain Energy of an Ellipsoidal Inclusion Undergoing Uniform Shear in an Isotropic Matrix -----	213
D.1	Anisotropic Stress Field Calculation Compared with Exact Isotropic Calculation -----	229

LIST OF TABLES

<u>Table Number</u>		<u>Page Number</u>
1	Bonding Materials for Elastic Constant Measurement -----	63
2	Heat Treatments of Powder Specimens -----	68
3	Heat Treatments of Single Crystal Specimen -----	69
4	Parameters Associated with the Invar Effect in Fe ₃ Pt as a Function of the Degree of Order S -----	107
5	Elastic Moduli as a Function of Temperature. S = 0.85 -----	118
6	Elastic Moduli as a Function of Temperature. S = 0.60 -----	119
7	Elastic Moduli as a Function of Temperature. S = 0.55 -----	120
8	Elastic Moduli as a Function of Temperature. S = 0.40 -----	121
9	Elastic Moduli as a Function of Temperature. S = 0.20 -----	122
10	Elastic Moduli as a Function of Temperature. S = 0. -----	123
11	Elastic Properties of Austenite and Marten- site at the M _s Temperature -----	124
12	Input Parameters for the Anisotropic Calcula- tion of Elastic Strain Energy and Stress Fields in Ordered Fe ₃ Pt -----	166
13	The Stresses Along the z Axis Due to an Ellipsoidal Plate of Martensite in an Aniso- tropic Matrix. S = 0.4 -----	171

List of Tables (Cont'd)

<u>Table Number</u>		<u>Page Number</u>
14	Theoretical Calculation of ΔG^{chem} at M_s (fcc \rightarrow bcc transformation) -----	184
15	Theoretical Calculation of ΔG^{chem} at M_s (fcc \rightarrow bct Transformation) -----	188
C1	Accuracy of Numerical Calculation of Anisotropic Elastic Strain Energy -----	211

ACKNOWLEDGMENTS

15

A doctoral thesis would be a difficult undertaking without the guidance and encouragement of an advisor like Professor Walter S. Owen, who also allows the author great freedom in pursuing his research interest and to whom he is greatly indebted.

Discussions with Dr. G.B. Olson throughout the duration of this thesis was very interesting and helpful. His sincere interest in this work is appreciated.

Discussions with the thesis review committee consisting of Professors P. Clapp, M. Cohen, R. Kaplow and B. Wuench were very helpful. Their valuable comments helped this thesis into its final form.

The growth of a single crystal of Fe_3Pt by Robert Marshall at the Air Force Geophysics Laboratory in Bedford, Massachusetts is greatly appreciated. The author is also grateful to Miss Mim Rich for her many technical helps; to her and to Miss Marge Meyer for many comforting words as well.

The essentials of life, food and shelter, and the overall research program was supported by the National Science Foundation. (DNR 7422719) The platinum used in this program was supplied by Engelhard Industries, Inc.

Lastly, the author is greatly indebted to his parents for their constant encouragement and support throughout this lengthy quest for knowledge, and to his many friends who help to make life enjoyable besides working.

CHAPTER 1PURPOSE OF RESEARCH

In the Fe-Pt system, the composition Fe-25 at/o Pt was chosen for study. There are two reasons. The stoichiometric composition shows a strong Invar effect which is a magnetic phenomenon. By proper heat treatment, varying degrees of long range order can be attained. Through the measurement of single-crystal elastic constants, the first and second derivatives of the exchange interaction can be obtained using a localized electron model. This allows a systematic study of the effect of ordering on the exchange interaction through the change in interatomic spacing and the number of near-neighbor atom pairs. The second reason is that at this composition, the martensitic transformation shows a gradual change in the growth behavior depending on the degree of order of the austenite. In the disordered state, growth is of the burst type similar to the Fe-Ni alloys. As the austenite is ordered, the hysteresis on thermal cycling decreases drastically. In the highly ordered state, the plates of martensite grow and shrink so slowly that changes in size can be observed optically and that the shape and volume changes involved in the growth of a plate are accommodated by the austenite without deformation slip of a magnitude that can be detected on a prepolished surface. Since accommodation of shape and volume changes involves the elastic and plastic properties of the austenite, a study of the elastic moduli and flow stress as a function of ordering should shed light on this transition in the growth behavior. As martensitic transformation follows definite crystallographic relationships, the elastic anisotropy of the austenite may

affect elastic accommodation in a significant way. Hence it is essential to determine the single-crystal elastic constants of Fe_3Pt . The first part of this thesis deals with the Invar Effect in Fe_3Pt as the degree of order changes. Consideration of the thermoelastic growth behavior of martensite begins in Chapter 5.

CHAPTER 2

THE INVARI EFFECT

2.1 Introduction

In certain metals, deviations occur in the thermal expansion behavior which cannot be explained by the contribution of lattice vibration and/or conduction electrons alone. Such deviations are well known for pure Ni and Fe,^[1] but the term Invar is generally reserved to describe the Fe-35%Ni alloy which exhibits an unusually large anomaly, leading to very small thermal expansion near room temperature. Actually, there is a range of composition in fcc Fe-Ni alloys from 30% to 45%Ni within which the alloys show large deviation from normal behavior.^[2] In Fe-Pt alloys between 24 a/oPt and 30 a/oPt, this effect is even more pronounced.* The thermal expansion coefficients become negative below the Curie temperature^[3] (Figure 1). As a result, the room temperature lattice parameter as a function of Pt concentrations shows a small deviation from Vegard's law in the Invar range (Figure 2). The magnitude of the anomalous expansion in Fe-Ni and Fe-Ni-Cr was investigated by Chevenard^[4,5] who found that the variation of this quantity with temperature was similar to the temperature dependence of the square of the spontaneous magnetization. Thus, these early observations established a correlation between magnetism and the anomalous thermal expansion. Henceforth, we shall use the term Invar alloys to include all materials which exhibit an anomalous

* page 21 listed the phase transformations in Fe-25 a/o Pt

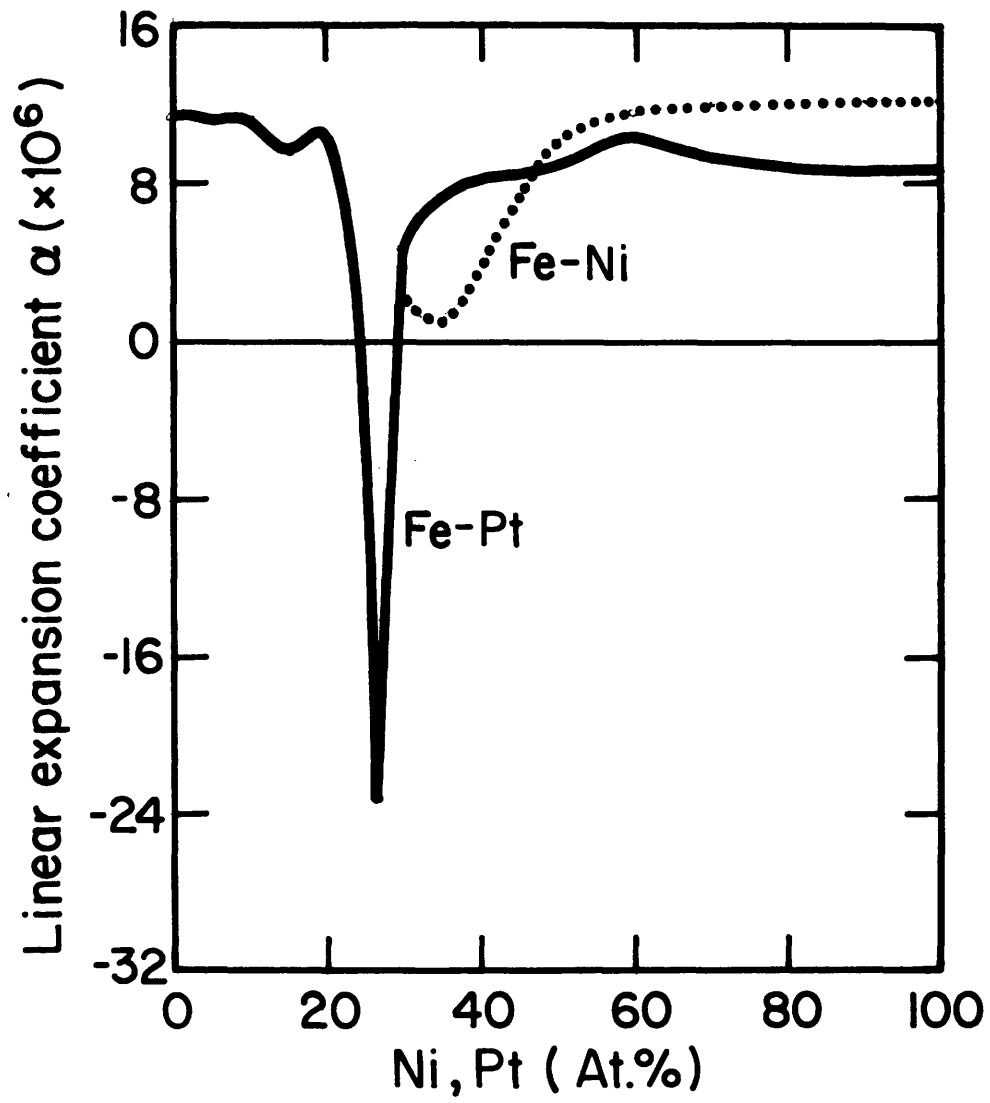


Figure 1. Linear expansion coefficient as a function of concentration in Fe-Ni and Fe-Pt alloys (ref. 2 and 3) at room temperature.

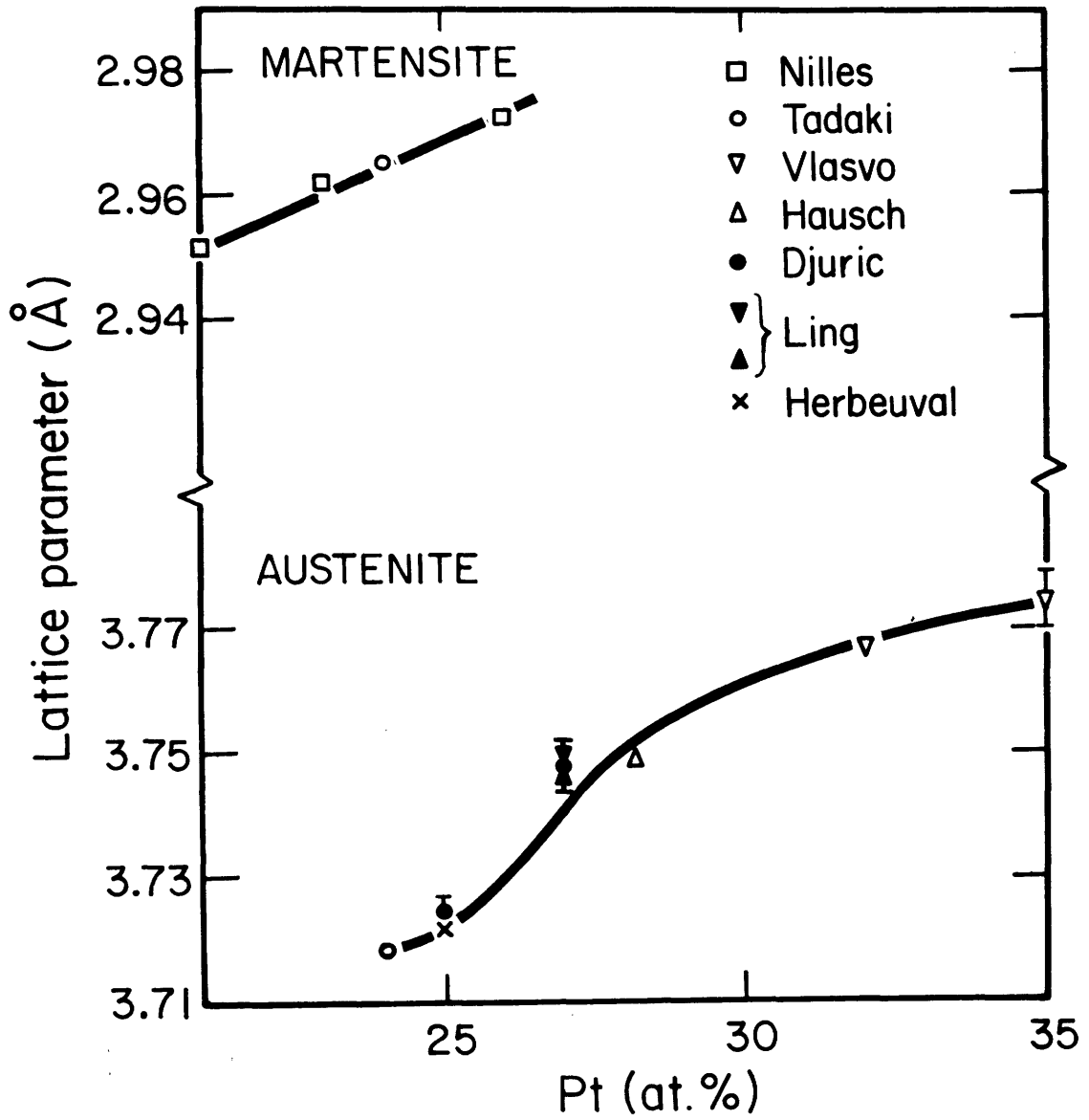


Figure 2. Room temperature lattice parameter versus concentration in disordered Fe-Pt alloys.

Phase Transformation in Fe-25 at/o Pt

characteristic temperature	phase transformation
$\theta_c = 735^\circ\text{C}$	order-disorder
$T_c = 0^\circ\text{C}$ (disordered) 160°C (ordered)	ferromagnetic (Invar effect)
$M_s = 0^\circ\text{C}$ (disordered) -196°C (ordered)	martensitic

behavior in thermal expansion as a result of a magnetic transition.

In the paramagnetic state, contributions to the thermal expansion coefficient are from lattice vibration and the conduction electrons. If these two contributions are subtracted from the values measured in the ferromagnetic state, one obtains the spontaneous volume magnetostriction, w_m , by integration over temperature. The values of w_m as a function of composition for Fe-Ni alloys^[2] are shown in Figure 3a. w_m is -5.0×10^{-4} at pure Ni, 0 around 75% Ni and as the Ni concentration further decreases into the Invar range, w_m sharply increases to as much as 142.3×10^{-4} at 35.7% Ni. The temperature dependences of the spontaneous volume magnetostriction of Fe-Ni^[24] are similar to the variation of magnetization with temperature as measured by Hausch and Warlimont.^[6] For Fe-Pt alloys, the volume magnetostriction and magnetization of Fe-28 at% Pt have been studied.^[7] It was found that in Fe-Pt alloys also w_m can be described as linearly proportional to the square of the spontaneous magnetization. The results are reproduced in Figure 3b.

In addition to a small thermal expansion coefficient, Invar alloys possess other anomalous properties, such as a large pressure dependence of the Curie temperature and a positive temperature dependence of the elastic constants below the Curie temperature. The variation of Curie temperature as a function of pressure has been determined by many investigators. In alloys such as Fe-Ni,^[8-11] Fe₃Pt^[12,13] and Fe-Mn,^[14,15] dT_c/dP ranges from -3 to -10 K/kbar while dT_c/dP is -0.1 k/kbar in Permalloy and ≈ 0 in Fe and Co.^[8] Positive values have been

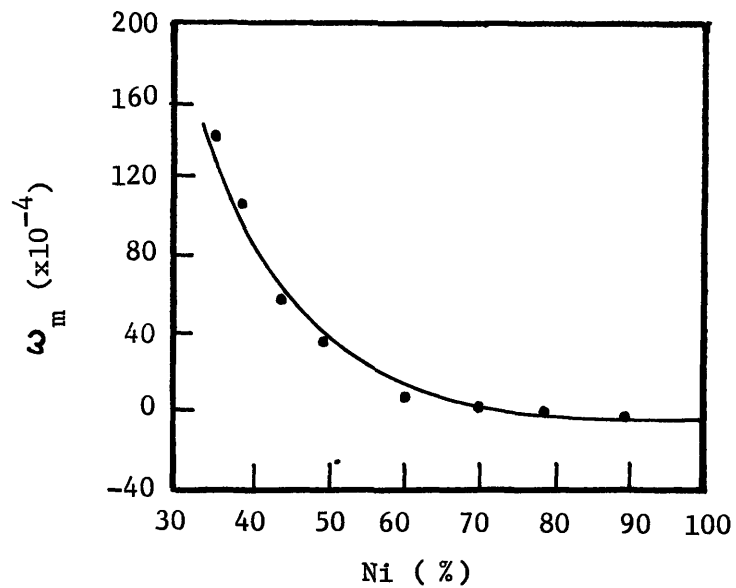


Figure 3a. Spontaneous volume magnetostriction ω_m at $T=0$ K in Fe-Ni alloys (ref. 2).

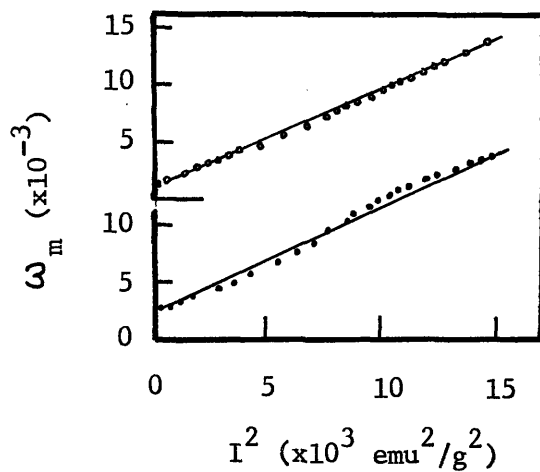


Figure 3b. Spontaneous volume magnetostriction versus the square of magnetic moment for ordered (○) and disordered (●) Fe-28 Pt (ref. 7).

found in Ni^[8] (0.32 K/kbar) and Ni-Co alloys.^[10]

The elastic moduli of polycrystalline alloys of Fe-Ni^[16-18] and Fe-Pt^[3,19,20] have been measured over limited ranges of composition and temperature. The Invar effect profoundly affects the moduli of Fe-Ni alloys in the Invar range, causing the temperature dependence of the Young's modulus E and the shear modulus G to change from weakly negative to strongly positive, so that at low temperature, both moduli are much smaller than expected. The temperature coefficients of E and G of α phase alloys containing between 0 and 25%Ni are negative and they decrease with increasing Ni content. They are positive on entering the α phase at 31%Ni, pass through a maximum at 35%Ni and become negative again for more concentrated alloys outside the Invar range. In the Fe-Pt system, the effect is strongest in the 25 a/o Pt alloy. In the ordered state, the modulus at liquid nitrogen temperature is only one-third of the value at room temperature.

The single-crystal elastic constants of γ -phase Fe-Ni Invar alloys show the same trends as E and G for polycrystalline specimens. The extensive data published by Hausch and Warlimont^[6] show that alloys with compositions (45 and 51.4%Ni) outside the Invar range behave normally at temperatures below the Curie temperature. That is, all the elastic constants increase linearly with decreasing temperature, except at temperatures close to 0°K. The slope dC/dT approaches zero at absolute zero. The alloys in the Invar range exhibit an anomalous behavior. The shear constants C_{44} and $(C_{11}-C_{12})/2$ behave normally over the temperature range in which the alloys are paramagnetic but they de-

crease linearly with decreasing temperature over the range in which the alloys are ferromagnetic. The change from a negative slope to a positive slope occurs over a narrow temperature range in the vicinity of the Curie temperature. The variation of the elastic constant $(C_{11} + C_{12} + 2C_{44})/2$ with temperature is also anomalous but the change in slope occurs 150-200°C above the Curie temperature and the transition is broader. It passes through a minimum and then rises again with decreasing temperature. This phenomenon had been observed earlier in an Fe-30Ni alloy. [21,22] Hausch and Warlimont attributed this anomaly to finely dispersed, coherent precipitates of an ordered phase based on Fe_3Ni , but the experimental evidence supporting this conclusion is not convincing.

In the Fe-Pt system, measurement of single crystal elastic constants have been reported in disordered Fe-28 Pt only. [23] The three independent elastic constants behave similarly to the corresponding constants in the Fe-Ni Invar alloys. Because of the much larger Invar effect associated with the Fe-Pt alloys, the elastic constants show larger deviations from normal behavior (Figure 4). Both the shear constants decrease in the ferromagnetic region. The decrease in $(C_{11}-C_{12})/2$ is remarkable. It is so large that the anisotropy ratio, A , which is 5 at room temperature, is 19 at liquid nitrogen temperature. The C_L elastic constant passes through a deep minimum before it rises again at lower temperatures. This quantity was also reported for an ordered Fe-28%Pt alloy. In the ordered state, C_L has a shallower minimum which is shifted to a higher temperature, probably because the

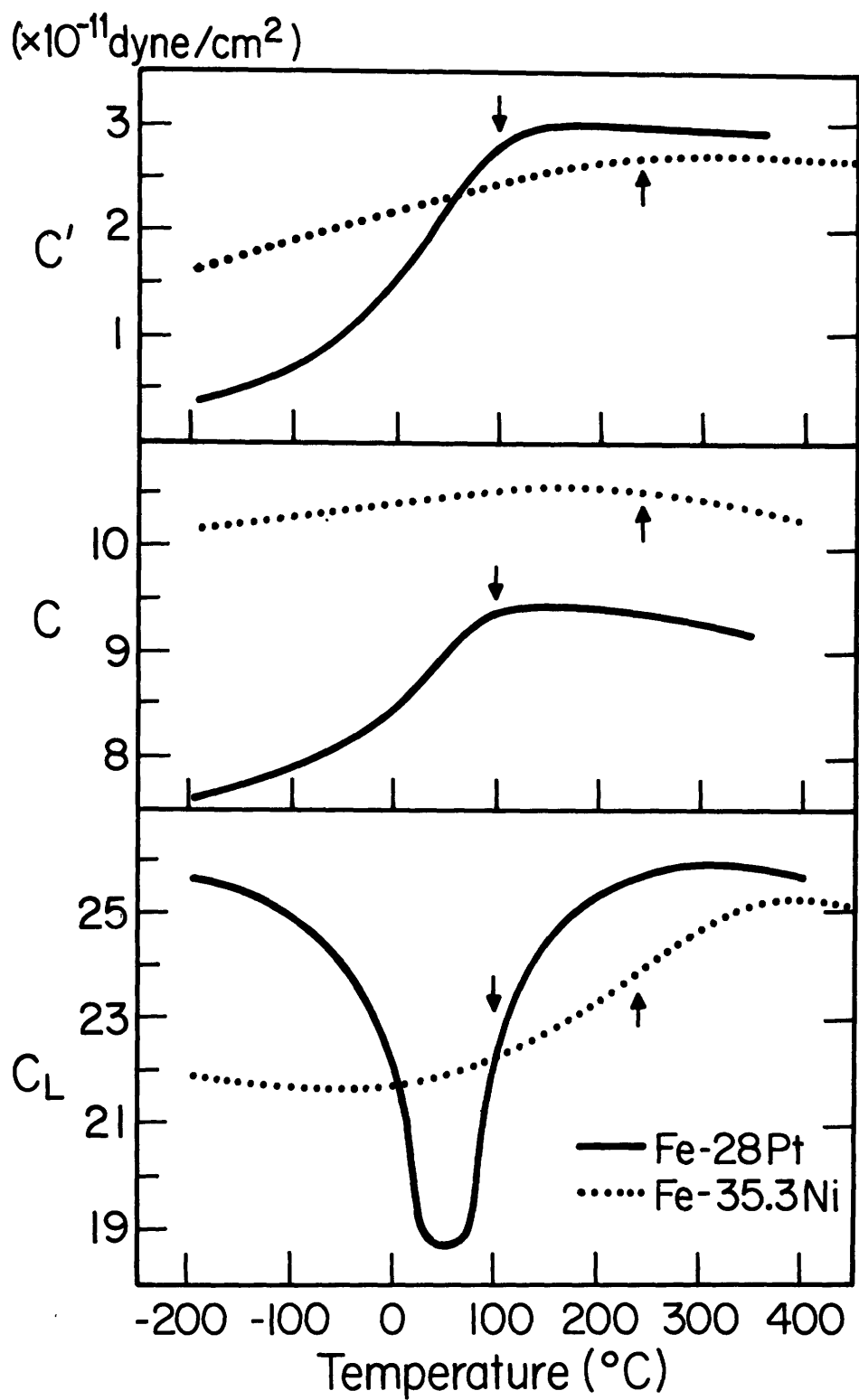


Figure 4. Single crystal elastic constants versus temperature in Fe-35Ni and disordered Fe-28Pt. (ref. 6 and 23)

Curie temperature is raised. The broad transition region above T_c still persists. These results show clearly that this phenomenon cannot be due to ordered regions in a disordered matrix, as proposed by Hausch and Warlimont to explain their results on Fe-Ni alloys.

Since the magnetic properties of metals and alloys depend on the arrangement and separation of atoms in the lattice, studies on alloys that undergo atomic ordering can yield important information on the variation of exchange interaction with interatomic distance and the number of nearest neighbors. There is no clear experimental evidence that Fe-Ni alloys undergo ordering in the Invar range. In Fe_3Pt , the evidence that long-range ordering can be developed to any desired degree in the γ -phase is unambiguous.^[25-27] The ordering is of the Cu_3Au type ($L1_2$) with Fe atoms occupying the face-center positions and the Pt atoms at the corners of a FCC array in the fully ordered state. The critical temperature for ordering is $735^\circ C$ for the stoichiometric composition. Herbeval^[27] has studied the variation of the long range order S with annealing temperature for a Fe-25 Pt alloy. The specimens were annealed for a sufficiently long period of time at each temperature so that the equilibrium state was attained. He found that the value of S varies smoothly with the annealing temperature below the critical ordering temperature. S does not exhibit an abrupt jump at the critical ordering temperature, which is typical of other $L1_2$ ordering. The room temperature lattice parameter remains constant at 3.723\AA between $S = 0$ and $S = 0.6$ and then increases rapidly to 3.733\AA at $S = 1$.

It is known that ordering raises the Curie temperature of Fe-Pt alloys near Fe_3Pt .^[12,28] It has also been found that ordering leads to a decrease in the pressure dependence of the Curie temperature and linear magnetostriction.^[7,12] However, there is only a limited amount of information on the effect of ordering on the temperature dependence of the elastic constants. In polycrystalline Fe-25 Pt^[20] at temperatures above the M_s temperature,^[6] the disordered alloy show a larger decrease in the Young's modulus with decrease in temperature than the ordered alloy. The single-crystal C_L elastic constant, the only one reported for the ordered state, passes through a shallower minimum before it rises again in the low temperature region. So far most investigations of the effect of ordering in Fe_3Pt on the behavior of the elastic constants or the martensitic transformation have used the length of time at a certain annealing temperature as the parameter characterizing the degree of atomic ordering. Comparisons have generally been made between a highly ordered and the disordered states. This is unsatisfactory. Not knowing the atomic order in the lattice, one cannot analyze the data even in terms of phenomenological models of localized exchange interaction. Any discussion along these lines is then necessarily qualitative.

2.2 Theoretical Models

A number of theories have been proposed to explain the Invar behavior. These can be divided into two groups. The first group is based on ideas of magnetic or structural inhomogeneity. These assume that anti-ferromagnetic iron has a different atomic structure, with lower magnetic moment and smaller volume than ferromagnetic iron. The second group contains models which are more fundamental. They explain

the Invar Effect in terms of the spatial dependence of the exchange integral in the localized Heisenberg model or to the strain dependence of the molecular field coefficient and band structure in the itinerant electron model.

Kondorsky and Sedov^[29] postulated that FCC iron is antiferromagnetic at low temperature due to a negative exchange interaction between neighboring iron atoms in the lattice. They suggested that in alloys with composition between the antiferromagnetic and the "fully" ferromagnetic, there should be grouping of spins at high temperature. The large electrical resistivity of the Invar alloys, for example, is attributed to the scattering of conduction electrons by the magnetic moment heterogeneities. Shiga and Nakamura^[30] proposed that ferromagnetic iron has a permanent moment and antiferromagnetic iron has an induced moment which vanishes in the absence of an exchange field. They interpret atomic moment as the polarization of the 3d band in iron alloys. As the polarization increases on cooling below T_c , the up-spin band becomes filled and the contribution of the down-spin band to the cohesive energy is decreased, causing the lattice constant to increase.

Weiss^[31] extended the idea that there are two electronic configurations of the iron atom in an FCC lattice to Fe-Ni Invar alloys. He proposed that the energy difference between the two electron levels depends upon the surrounding of the iron atom, with the difference going through zero at 29%Ni. In pure γ iron, the antiferromagnetic γ_1 state is the ground state (smaller lattice constant). On alloying, the ferromagnetic γ_2 state becomes the ground state above 29%Ni.

Thermal excitation of the γ_1 level decreases the atomic volume in opposition to the normal anharmonic source of expansion and, depending on the energy difference between the two levels, can yield an extremely small expansion coefficient. One apparent difficulty, as pointed out by Colling and Carr,^[32] is that, based on this model, the temperature dependence of the anomalous strain is not necessarily connected with the Curie temperature of the alloy.

After their Mössbauer result on fine-grained Fe-Ni alloys indicated the coexistence of ferromagnetic and antiferromagnetic phases at liquid helium temperature, Asano and coworkers^[33,34] proposed a concentration fluctuation model to explain the Invar expansion anomaly. The paramagnetic lattice constant is assumed to be smaller than the ferromagnetic lattice constant and they postulated a distribution of regions with different compositions and hence different Curie temperatures. The low thermal expansion coefficient is a result of the lattice contraction when the ferromagnetic domains of various composition successively pass through their own Curie temperature and change into the paramagnetic state.

Since Invar behavior is found in alloys systems which are ferromagnetic such as Fe-Ni, antiferromagnetic such as Fe-Mn,^[35] and much smaller magnetovolume effects are observed in the pure elements Fe, Ni, Mn,^[11] it follows that a more general treatment of magnetovolume effects must be independent of the specific assumptions invoked in the above models. One has to look for the development of models compatible with the fundamental theories of magnetism. So far three approaches have been advanced,

namely, Zener's theory of ferromagnetism extended by Colling and Carr, itinerant electron model by Wohlfarth and coworkers, and the localized electron model by Alers, et al and Hausch and Warlimont.

Carr and Colling^[32,36] adopted Zener's idea^[60] that in metals, there are two competing exchange interactions. One is the ferromagnetic coupling of localized atomic spins via itinerant electrons in the metal (the s-d coupling). The other is a direct antiferromagnetic coupling of localized spins due to the overlap of neighboring wavefunctions. Parallel spins on neighboring sites are unfavorable with respect to the direct coupling. Thus, the ferromagnetic coupling expands the lattice at low temperature and up to the Curie temperature, a contraction is produced with increasing temperature. They postulated that in the Invar alloys, these two exchange energies are comparable in magnitude. Hence, the direct exchange contribution to the spontaneous magnetostriction becomes large, resulting in a small expansion coefficient. So far this approach has been developed rather qualitatively and has not been extended to cover the other anomalous effects associated with the Invar behavior.

From the itinerant electron approach, Terao and Katsuki^[37,38] considered magneto-volume effects at 0°K in the rigid band limit by allowing both the molecular field coefficient and the bandwidth to be strain dependent. As such it cannot predict the temperature dependence. Attempts to develop the finite temperature behavior are complicated by the appearance of the Fermi distribution function and no simple expressions can be obtained. In the strong

correlation limit, Lang and Ehrenreich^[39] calculated the pressure dependence of the Curie points for Ni and Ni-Cu alloys using a model hamiltonian introduced by Hubbard,^[40] Kanamori^[41] and Gutzwiller.^[42] In this formulation, correlation effects are regarded to be important only among the 3d electrons and because of screening by the conduction electrons, are assumed to be confined to the carriers at the same atomic site. In the simple approximation the intra-atomic Coulomb forces in the same orbitals are taken to be infinite; the inter-orbital interactions and effects of the conduction band on the d carriers are neglected; and the d band is assumed to widen uniformly with pressure. The entire theory involves a single energy parameter, the band width, and is independent of the band structure. In this form, it was applied successfully to Ni and Ni-Cu alloys using a rectangular band structure. Generalization of the hamiltonian to include other interactions induces a dependence on the band structure and fails to give an accurate description of Ni-Cu alloys in the rigid band model. The use of a non-rigid band model yields better agreement with experiment.

A more complete attempt to explain the various Invar phenomena on the basis of itinerant electron theory was made by Wohlfarth and co-workers.^[43-45] From the original Stoner-Wohlfarth model of ferromagnetism,^[46,47] they developed a theory for very weak itinerant ferromagnets^[48,49] defined by $I(0,0) < n N_A \mu_B$ where $I(0,0)$ is the saturation magnetization, n is the number of electrons per atom, N_A is the number of atoms per unit volume and μ_B , the Bohr magneton. This is a much

simpler hamiltonian than that of Lang and Ehrenreich.^[39] In addition to the single particle energy levels which give rise to the band structure, there is an exchange interaction between the carriers of the form

$$E_{\text{exch}} = -\frac{1}{2} N_e k \theta' \xi^2 \quad (1)$$

where N_e is the number of electrons or holes of both spins, ξ is the relative magnetization, θ' is the exchange interaction parameter and k , the Boltzmann constant. They proposed that Invar alloys belong to the class of weak itinerant ferromagnets. Their result indicates that the strain dependence enters through the exchange interaction parameter θ' and the density of state $N(\epsilon)$ at Fermi energy ϵ_F . For example, the spontaneous magnetostriction is found to be

$$\omega_m(T) = -\kappa C I^2(0,0) \left[1 - \frac{I^2(0,T)}{I^2(0,0)} \right] \quad (2)$$

where κ is the compressibility and

$$C = \frac{1}{2nN_e \mu_B} \left\{ k \frac{\partial \theta'}{\partial \omega} + k \theta' \frac{\partial \ln N(\epsilon_F)}{\partial \omega} + \frac{n}{N(\epsilon_F)} \left(\frac{T_C}{T_F} \right)^2 \frac{\partial \ln T_F}{\partial \omega} \right\} \quad (3)$$

N_e is the number of atoms per unit volume, k the Boltzmann constant, μ_B the Bohr magneton, n the number of carriers per atom and T_F is a degeneracy temperature which is defined in terms of the fine

structure in the density-of-states curve. For $T_C/T_F < 1$, which in general holds over a temperature range including the Curie temperature, T_C ,

$$\left[\frac{I(0,T)}{I(0,0)}\right]^2 = 1 - \left(\frac{T}{T_C}\right)^2 \quad (4)$$

Figure 5 shows the magnetization measurement of Fe-28Pt in the ordered and disordered state.^[7] The function $[1-(T/T_C)^2]$ gives a good fit to the data of ordered Fe-28Pt while a Brillouin function of $j = 1/2$ seems to represent better the data of disordered Fe-28Pt. The data of Fe-32Ni, also an Invar type alloy, shows large deviation from the two theoretical curves.

In the Stoner model, θ' is a parameter adjusted to obtain agreement between theory and experiment. Other than representing a mean field approximation to the exchange interaction between the electrons, its functional dependence is not clear. Furthermore, extending the Stoner theory to describe magnetic alloys using the rigid band model results in prediction of properties which do not agree with experiment. Hence, Wohlfarth and coworkers made no attempt to calculate the strain dependence of these quantities theoretically. This formulation has not been extended to cover the magnetic contribution to the elastic constants which are of main interest in this thesis.

The localized model of ferromagnetism assumes that exchange interaction is short-range, extending only over the near neighbors. This energy term, the intrinsic magnetic contribution to the elastic constants, was first discussed by Sato.^[50] In a later paper with Alers and

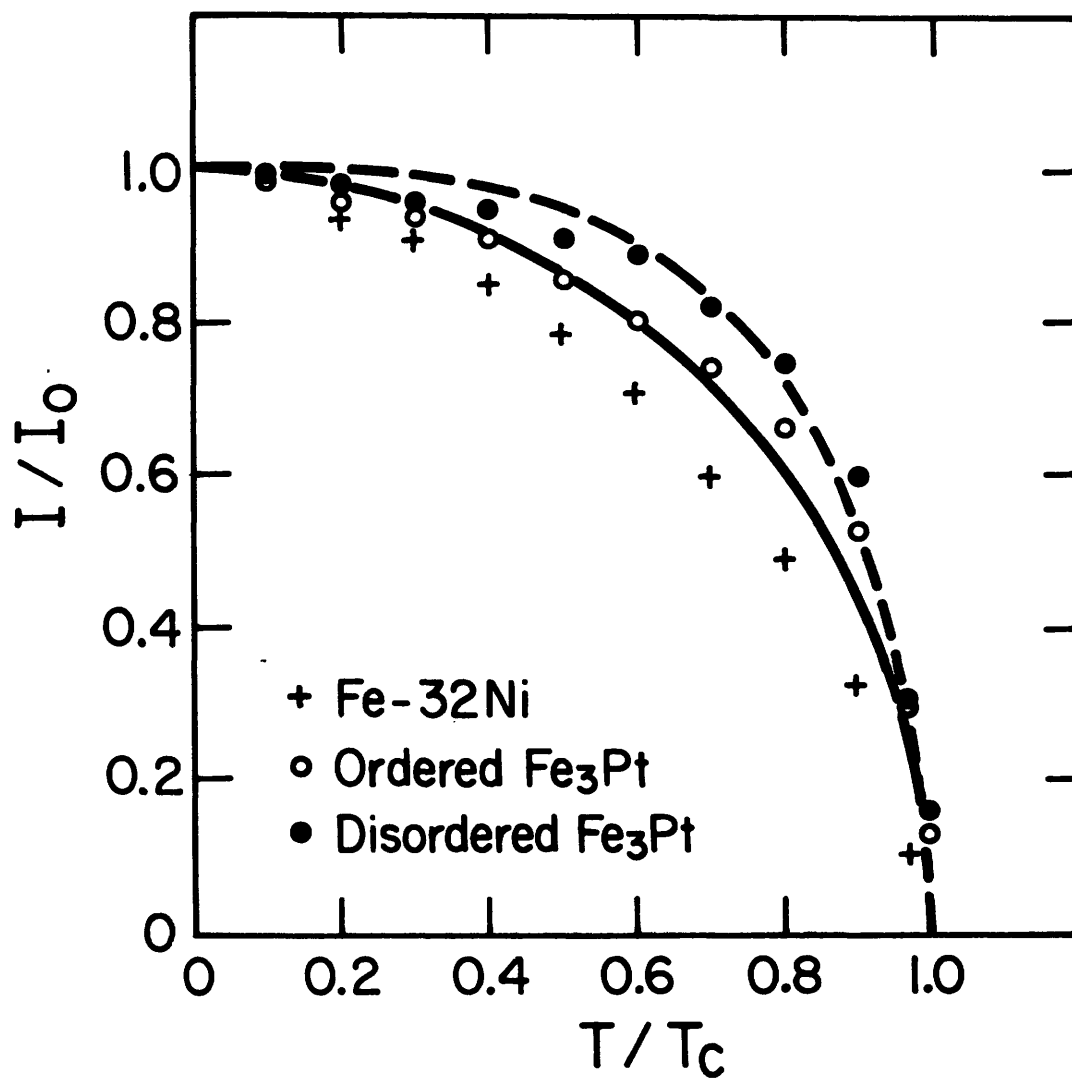


Figure 5. The reduced magnetization, I/I_0 , versus the reduced temperature, T/T_c , in Fe-32Ni, ordered and disordered Fe-28Pt compared with theoretical curves $[1-(T/T_c)^2]^{1/2}$ (—) and Brillouin function $j=1/2$ (---).

Neighbors,^[51] a formal expression for the magnetic contribution to the elastic constants were developed and applied to calculate the derivatives of the exchange integrals for Ni and Fe-30Ni using the elastic constant data for these materials. Following this approach, Hausch^[52-54] gave a systematic treatment of the various anomalies associated with the Invar Effect, namely the pressure dependence of the Curie temperature, spontaneous and forced magnetostriction and elastic constants using the Heisenberg hamiltonian and mean field theory. They applied this formulation to calculate the first and second derivatives of an isotropic exchange integral for Fe-28Pt and several Fe-Ni alloys.^[6,23] From two different sets of data: the spontaneous volume magnetostriction and the elastic constant measurements, agreement within a factor of two was obtained. This is a reasonably good result considering the simplicity of the model. Since this is the only formulation that has been developed to cover the magnetic contribution to the elastic constants, we shall use it to analyze the measured elastic constant data for a Fe-25 a/oPt alloy. Before a full account of this theory is developed in Section 2.5, we shall first discuss the appropriateness of a localized model in describing the magnetic behavior of metallic alloys.

2.3 Ferromagnetism: the Localized Model versus the Itinerant Model

Magnetism in real metals have been discussed in the literature from two different points of view: the localized spin model, based on Heisenberg's work,^[55] and the itinerant model, built on that of Bloch.^[56] Many arguments have been advanced in favor of one picture or the other, particularly for metals of the iron group. The itinerant

electron model is supported by some experimental evidence including d-band specific heat, non-integral magneton numbers of the moments, and evidence for participation of d electrons in conduction. Arguments favoring the localized picture have been based on experimental observations of the critical scattering of neutrons, entropies of ferromagnetic transitions, spin waves and the behavior of ferromagnetic moments on alloying. In the light of modern refinements of the theories many of these arguments have lost the significance originally claimed for them. The itinerant picture has outgrown its original formulation in terms of determinantal wavefunctions and the incorporation of correlation into the theory now provides explanations for spin waves, critical fluctuations and other phenomena once considered explicable only by the localized model. The latter model, in turn, has been generalized by allowing conduction electrons to mediate the exchange coupling (indirect exchange) in certain situations, and also by allowing magnetic electrons to participate in conduction. Thus, each model has acquired some of the principal features of the other. This does not mean that one model might not be more suitable in describing a certain class of metals than the other. In his lengthy review of exchange interaction among itinerant electrons, Herring^[57] argued in favor of an itinerant model for iron-group metals and a localized model for rare earths. This is the prevailing view today.

A truly fundamental understanding requires a detail knowledge of the energy distribution of all the electronic states in the system. This type of information is difficult to develop. In the case of pure transition group metals, the presence of the conduction bands and the overlap

of the broad energy bands with narrower, unfilled d or f bands introduce formidable complications into any basic calculation. Various approximation methods have been resorted to, but these have generally disagreed in their detail predictions about electronic band structure and its manifestation. The even more complex problem posed by their alloys is almost intractable at this fundamental level.

At a less fundamental level, but still based on the band theory of metals, the collective electron model developed by Stoner^[47] established useful relationships between many of the intrinsic magnetic properties of the transition group metals and certain specific features of the electronic band-structure. Assuming a simple band structure with various adjustable parameters, Stoner, Wohlfarth and others^[47] derived a plausible explanation for the measured properties of all the pure metals of the iron group. In its application to ferromagnetic alloys, the collective model, in its simplest form, is known as the rigid band model in which it is assumed that the band structure (the density of states) is rigidly fixed and that a change in the number of electrons per atom on alloying simply causes an adjustment of the Fermi energy level. However, this model fails to predict the magnetic properties of alloys of nickel and cobalt.^[59] The theoretical calculations of Lang and Ehrenreich^[39] show the model to be inappropriate in these cases. Furthermore, the rigid band model is inherently unable to distinguish between the ordered and disordered states of an alloy. In view of the inadequacy of the rigid band model when applied to magnetic alloys and in the absence of a more rigorous band theory, we seek an alternate approach on a more phenomenological level.

The use of Heisenberg hamiltonian $-2J_{ij} \sum_i S_i \cdot S_j$ to describe the exchange interaction is known to be valid for direct exchange between atoms with well separated, unfilled inner orbitals in ionic solids and insulators and for superexchange between magnetic ions which are separated by non-magnetic ions in Heusler alloys. Even the indirect exchange proposed by Zener, [59,60] due to the coupling of localized spins of unfilled innershells of atoms in metals by means of the interaction of these shells with the conduction electrons, can be expressed in the form $-2J_{ij} \sum_i s_i \cdot s_j$. In iron-group transition metals and alloys, the predominant exchange interactions occur between the 3d electrons. They are mobile to a certain extent and may not remain long enough on a lattice site to allow an atomic spin operator to be defined. Nevertheless, we shall discuss two pieces of evidence which indicate that the use of a short range, localized exchange interaction in this case might not be totally unfounded. In addition to the often quoted diffuse neutron scattering experiments on ferromagnetic solid solutions which showed that different magnetic moments are associated with the constituent atomic species of an alloy, we shall discuss some recent calculations which indicate that fairly short range interaction in a cluster of atoms can reproduce the essential features of the band structure in a solid.

Kouvel [58] has summarized the neutron diffraction experiment by Shull and Wilkinson [61] on various ferromagnetic solid solution alloys. From the saturation moment which represents the compositional average of the magnetic moments μ_A and μ_B of elements A and B, $\bar{\mu}$, in a disordered alloy $A_{1-x}B_x$,

$$\bar{\mu} = (1-x)\mu_A + x\mu_B \quad (5)$$

and the cross-section for the magnetic diffuse scattering

$$d\sigma_M \propto x(1-x)(\mu_A - \mu_B)^2 \quad (6)$$

both μ_A and μ_B can be determined individually. The results on Ni-Fe are reproduced in Figure 6. Both μ_{Fe} and μ_{Ni} are nearly composition independent and this provides a quantitative explanation of the almost linear variation of saturation moment $\bar{\mu}$ with composition. The difference in magnetic moment is clearly revealed. It does not follow, however, that all atoms of a given kind in an alloy of specific composition have the same magnetic moment, regardless of any differences in their local environment. Low angle neutron scattering experiments by Low and Collins^[62-64] on Ni based alloys show that the disturbance around a Cr solute atom extends out to the Ni nearest neighbors, but an Fe solute atom produces a disturbance essentially limited to itself. Similar conclusions have been drawn about other dilute alloys from nuclear magnetic resonance and Mössbauer studies. This variability of magnetic moment at lattice sites of different atoms suggests the possible use of an atomistic model with localized spins.

On another front, there are some recent calculations of the electronic structures of small metallic clusters (copper, nickel, palladium and platinum) using the self-consistent field X- α scattering

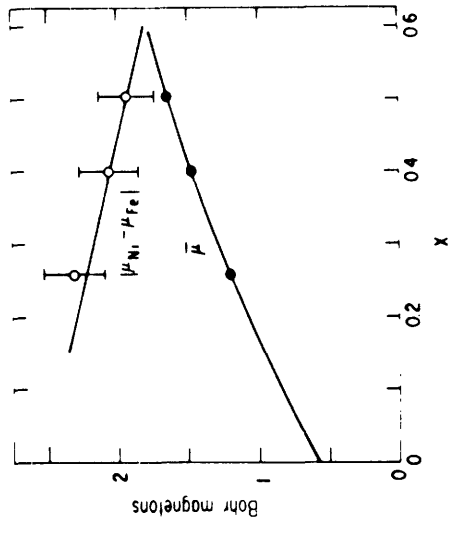
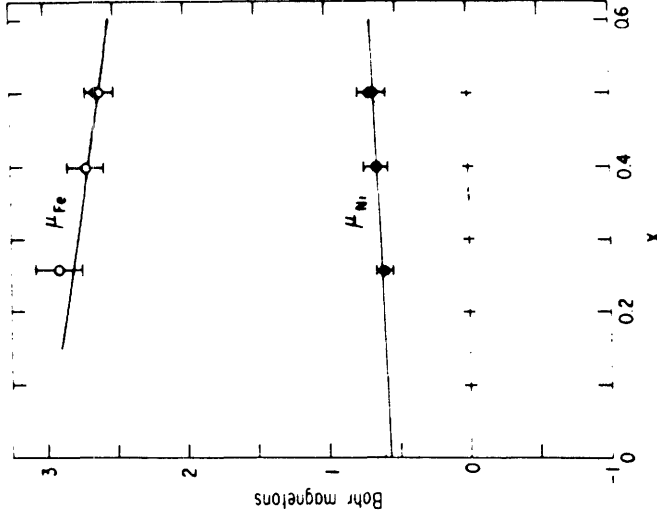
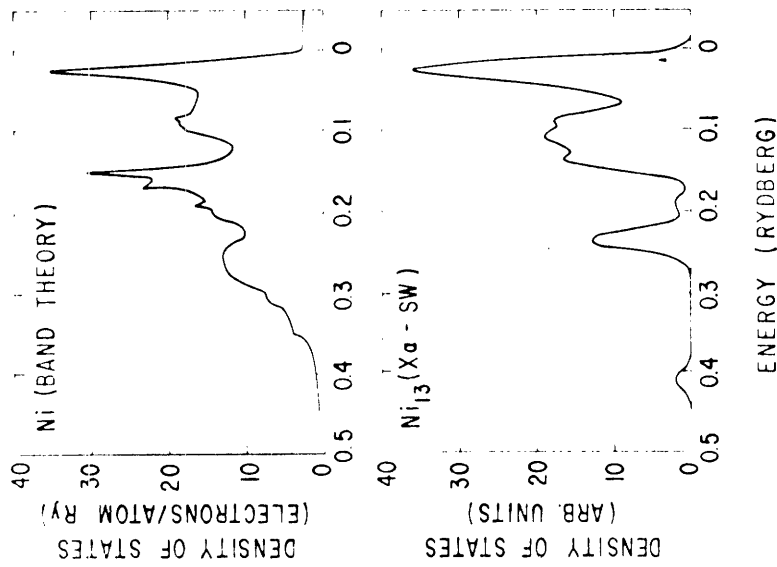
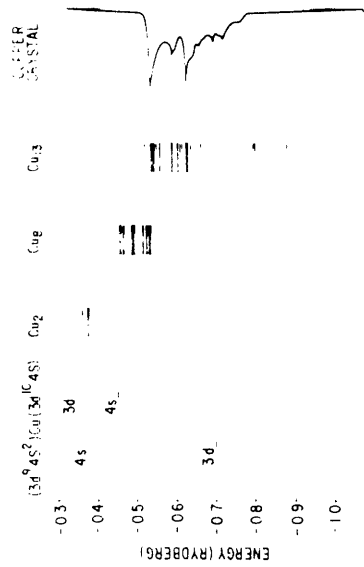


Figure 6. Neutron scattering result showing individual atomic moments in $Ni_{1-x}Fe_x$ (ref. 61)



Comparison of the majority-spin electronic density of states for bulk crystalline nickel, calculated by the SCF-X α -LCAO method (Ref. 32) with the "density of states" for a cubo-octahedral Ni₁₃ cluster based on the Gaussian-broadened SCF-X α -SW energy levels shown in Fig. 8.



Comparison of the occupied SCF-X α -SW electronic energy levels for Cu₂, Cu₈, and Cu₁₃ with the electronic density of states for bulk crystalline copper calculated by SCF-X α -KKR band-structure theory (Ref. 34). For the sake of comparison, the latter has been adjusted so that the Fermi levels of the crystal and Cu₁₃ cluster approximately coincide. Also shown for comparison are the SCF-X α energy levels of the isolated Cu atom for two different electronic configurations.

Figure 7. X- α cluster calculation compared with band theory results.

wave approach to molecular orbital (MO) theory.^[5] As the cluster size and coordination numbers are increased, the MO results show increasing similarity to the electronic structures of the corresponding crystalline metals, with the result for 13-atom cubo-octahedral clusters exhibiting all the main features of the bulk band structures, e.g. a sharp peak in the density of states around the Fermi level in the case of Ni, Pd and Pt and increasing d band width through the series Cu, Ni, Pd and Pt. The clustering of the energy levels and the total band width of d orbitals in a Cu_{13} cluster closely match the main features of the d-band density of states for bulk copper (Figure 7). These results suggest that short range order, as represented by the 13-atom cubo-octahedral cluster, could determine the principal features of the band structure for crystalline metals. Since a large density of states near the Fermi level, which is essential for ferromagnetism to occur, is generated by short range interaction among the atoms in a cluster, it can be argued that the exchange interaction, which is responsible for the magnetic energy, should also be short-ranged.

In summary, we share the view of Kouvel^[58] that even though it should be possible to trace the variability of magnetic moments in an alloy to certain fairly localized exchange interaction effects on the band structure, it is simpler and more useful to incorporate this variability phenomenologically into an atomistic model. The use of an exchange integral J to describe the exchange coupling between neighboring atoms allows the extension to concentrated ferromagnetic alloys and through statistics, takes into account the effect of local environment.

2.4 The Localized Exchange Integral

The theoretical calculation of the exchange integral J for metallic alloys must include bandwidth effects. The simple form applicable to molecules is not appropriate. Slater^[66] discussed the use of the X- α cluster method to set up the calculation for the energy difference between a ferromagnetic material in its ground state and in a state in which the magnetic moment of one atom is reversed in direction. This same energy difference can be expressed in the Heisenberg exchange integral J in the following way. On reversing the magnetic moment of one atom, the exchange term changes from $2JzS^2$ to $-2JzS^2$, where z is the number of nearest neighbors and S the atomic spin. The energy difference is $4JzS^2$. In this process of orientation, there are $2S$ electrons, each with spin $1/2$, the magnetic moments of which are reversed. Thus, the average energy difference per electron is

$$\Delta\epsilon = 2JzS \quad (7)$$

This is the energy obtainable directly from a transition state calculation by the X- α cluster method. The transition state consists of half the total number of electrons with the initial spin and the rest with reversed spin. Hence, at the location of the atom which is to have its moment reversed, the potential is non-spin polarized in the transition state. At every other atomic site, the potential is the original spin polarized potential. The wavefunctions that are localized around the reversed atom have their tails spread out to the

neighboring atoms, where there is a difference between the spin-up and spin-down charge densities and hence between their exchange correlated potentials. These localized wavefunctions show no energy difference between the spin-up and spin-down levels if they are completely localized on the reversed atom. It is the small energy difference from the overlap contribution between the localized orbitals in the transition state and the neighboring atoms that should agree with $\Delta\epsilon$ in Eq'n (7).

To account for the effect of the bandwidth, which is essential to explain the disappearance of ferromagnetism, Slater discussed the necessity of using a more elaborate expression which leads to a positive value of J for ferromagnetic material and a negative value in other cases. The rationale is that one can remove an electron of wavevector \vec{k}_p from the spin-up band and insert it in the spin-down band with the same wavevector \vec{k}_p or a different wavevector $\vec{k}_q = \vec{k}_p + \vec{k}$. As \vec{k} departs more and more from zero, the excited states broaden the energy band. In particular, there may exist a set of values of \vec{k}_p and \vec{k} such that $\epsilon_1(\vec{k}_p)$ corresponds to the highest energy in the spin-up band while $\epsilon_2(\vec{k}_p + \vec{k})$ corresponds to the lowest energy in the spin-down band, and the lowest levels of the spin-down bands lie below the highest levels of the spin-up band. Then, electrons will fall from the top of the spin-up band to the bottom of the spin-down band, thereby decreasing the magnetization and bringing the bands closer together. Eventually this will lead to a completely nonmagnetic ground state. If the energy bands are not broad enough to overlap, however, this situation will not occur. In this description, it is the interaction between the broadened energy bands of the spin-up and spin-down states that is responsible for the appear-

ance of a negative exchange integral.

No attempt has yet been made to calculate the Heisenberg exchange integral as outlined by Slater. He believed that the exchange energies of the 3d transition elements, indicated by their Curie temperatures to be of the order of hundredth of a Rydberg, are within the range of accuracy of the X- α cluster method. It should be mentioned, however, that Herring^[57] argued that when itinerancy is important, contributions to the exchange energy from the 3d electrons, and other mechanisms such as indirect exchange, if they are present, cannot be compounded additively. One has to start out with the correct wavefunctions and hamiltonian that take all the mechanisms into account. According to this view, the Slater treatment of the Heisenberg exchange integral would not be appropriate to the iron-group transition elements.

2.5 Magnetic Contribution to the Elastic Constants

2.5.1 General Consideration

In the ferro-or antiferromagnetic state the elastic constants

$$C(T) = C_{\ell}(T) + \Delta C(T) \quad (8)$$

where $C_{\ell}(T)$ and $\Delta C(T)$ are the lattice and magnetic contributions, respectively. The lattice term, $C_{\ell}(T)$, increases linearly with decreasing temperature except at very low temperature, where the slope dC_{ℓ}/dT approaches zero at absolute zero.^[67] In the ferromagnetic region, $C_{\ell}(T)$ can be determined by extrapolation from the high temperature paramagnetic region. The magnetic contribution, $\Delta C(T)$, is given by

$$\Delta C(T) = \Delta C_{\text{ex}}(T) + \Delta C_{\text{CF}}(T) + \Delta E_{\omega}(T) + \Delta E_{\lambda}(T) \quad (9)$$

where ΔC_{ex} is the exchange term, ΔC_{CF} the crystal field, ΔE_{ω} the Döring term and ΔE_{λ} the domain wall rotation contribution.

When tension is applied to an unmagnetized ferromagnetic material, its length increases as a result of (1) a purely elastic expansion and (2) an expansion resulting from the orientation of the domain under stress. The increase in length of the second kind results from the magnetostriction associated with the domain orientation, and it is responsible for the fact in ferromagnetic materials Young's modulus, E , depends on the amplitude of strain and the intensity of magnetization. The change of Young's modulus with magnetization due to domain reorientation is called the ΔE_{λ} effect. [16] In a saturating magnetic field, the magnetic domains are aligned in the direction of the applied magnetic field and domain orientation is not affected by small stresses. Hence, the ΔE_{λ} effect is eliminated if the elastic constants are measured in a saturating magnetic field. The Döring term, ΔE_{ω} , arises indirectly through the stress induced change of the spontaneous magnetization. [68,69] It gives rise to a stress induced spontaneous volume magnetostriction, always lowering the elastic constants. This term occurs only in the C_L elastic constant because the shear elastic constants are not affected by a forced volume magnetostrictive contribution. The crystal field contribution, ΔC_{CF} , results from the strain dependence of the anisotropic portion of the magnetic free energy. Following Hausch, [52] we shall assume that the magnitude of the crystal field effect in the Invar alloys

is similar to that in Fe and Ni. In Fe and Ni, $|\Delta C_{CF}/C| \sim 0.1\%$. This is very ⁴⁸ small indeed compared with a total change of more than 10% in C in Invar alloys and hence it can be neglected. We are, therefore, left with the exchange term, ΔC_{ex} , as the intrinsic, isotropic magnetic contribution which shall be discussed in some detail.

2.5.2 Formulation in Terms of a Localized Exchange Integral

Keeping in mind the discussion in Section 2.3 on the various models of ferromagnetism, we shall describe the Invar alloys in terms of a localized Heisenberg exchange interaction. The treatment follows closely that of Alers, ^[51] et al and Hausch. ^[52] Using a molecular field approximation, the isotropic magnetic energy term can be expressed as ^[70]

$$U_{ex} = -\frac{1}{2} N_v V \left(\frac{I}{I_0}\right)^2 \sum_i z_i J_i \quad (10)$$

where N_v is the number of atoms/cm³, z_i the number of i-th nearest neighbors, r_i the interatomic separation from and J_i the exchange interaction with the i-th nearest neighbors. We have neglected higher order terms in $(I/I_0)^2$ and spin fluctuation near T_c . The latter has been treated by Levanyuk ^[71] and by Young and Bienenstock. ^[72] As a first approximation, we consider only first nearest neighbor interactions.

In this approximation, U_{ex} is a function only of r . One can use Fuchs' Equation ^[73] in which the elastic constants are derived from a lattice potential $\phi(r)$. Then the elastic constants are the second derivatives of energy with respect to strain and the exchange contribution can be written for the single crystal elastic constants $C = C_{44}$,

$C' = \frac{1}{2} (C_{11} - C_{12})$ and $C_L = \frac{1}{2} (C_{11} + C_{12} + 2C_{44})$ and for the bulk modulus $B = \frac{1}{3} (C_{11} + 2C_{12})$ of a face-centered cubic material as follows:

$$C_m = -\frac{z_1}{8} (2r_1^2 J_1'' + 6r_1 J_1') N_V \left(\frac{I}{I_0}\right)^2 = -K_2 \left(\frac{I}{I_0}\right)^2 \quad (11a)$$

$$C_m' = -\frac{z_1}{8} (r_1^2 J_1'' + 7r_1 J_1') N_V \left(\frac{I}{I_0}\right)^2 = -K_1 \left(\frac{I}{I_0}\right)^2 \quad (11b)$$

$$C_{L,m} = -\frac{z_1}{8} (5r_1^2 J_1'' + 3r_1 J_1') N_V \left(\frac{I}{I_0}\right)^2 \quad (11c)$$

$$B_m = -\frac{z_1}{3} (r_1^2 J_1'' - 2r_1 J_1') N_V \left(\frac{I}{I_0}\right)^2 \quad (11d)$$

where $z_1 = 12$. Here J_1 is the exchange integral between the nearest neighbor atoms and J_1' , J_1'' denote its first and second derivatives with respect to interatomic distance. In Eq'n (10), the volume dependence of $(I/I_0)^2$ leads to additional terms contributing to ΔC where the most important one is ΔE_ω . Combining Eq'ns (11a) and (11b), one can obtain J_1' and J_1'' through the experimental values of the two shear elastic constants C and C' , namely,

$$J_1' = (2K_1 - K_2) / N_V z_1 r_1 \quad (12a)$$

$$J_1'' = (7K_2 - 6K_1) / N_V z_1 r_1^2 \quad (12b)$$

From the coupling coefficients K_1 and K_2 , one can also calculate the

pressure dependence of the Curie temperature and the coupling coefficient of the magnetovolume relation. These have been formulated by Hausch^[54,55] based on the same assumption of a localized exchange interaction.

2.5.3 Correction Terms

There are two correction terms to the magnetic contribution to the elastic constants that should be considered: additional changes due to the spontaneous volume magnetostriction and the ΔE_{ω} effect. Each will be discussed.

The appearance of spontaneous magnetization produces nonlinear volume changes below the Curie point which give rise to additional changes in the elastic constants. A thermodynamic treatment was given by Alers, et al.^[52] This effect can be viewed simply as follows. The magnetic contributions to the elastic constants, ΔC_{ex} , is given by

$$\Delta C_{ex} = C_{T,I,V_0} - C_{T,0,V_0} \quad (13)$$

whereas experimentally one determines

$$\Delta C^* = C_{T,I,V'} - C_{T,0,V_0} \quad (14)$$

i.e., $\Delta C^* - \Delta C_{ex}$ should be subtracted from the experimentally determined values.

$$\begin{aligned} \frac{\Delta C^* - \Delta C_{\text{ex}}}{C} &= \frac{C(V')_{T,I} - C(V_0)_{T,I}}{C} \\ &= - \frac{B}{C} \frac{\partial C}{\partial P} \omega_m(T) \end{aligned} \quad (15)$$

where B , $\frac{\partial C}{\partial P}$ and ω_m are the bulk modulus, the pressure dependence of the elastic constants and the spontaneous volume magnetostriction, respectively. With $\omega_m \sim 10^{-3}$ for Invar materials, $\frac{\partial C}{\partial P} \sim 1$ [67] and $B/C \sim 1$, the correction amounts to $\sim 0.1\%$ which is negligible.

The ΔE_ω effect accounts for the change in the elastic constants due to a stress induced change in the spontaneous magnetization. This gives rise to a change in the volume magnetostriction. Based on thermodynamic arguments, Döring [69] obtained the following relation:

$$\Delta E_\omega = - \frac{1}{9} C^2 \left(\frac{\partial \omega}{\partial H} \right)^2 \left(\frac{\partial I}{\partial H} \right)^{-1} \quad (16)$$

This term occurs only in the C_L elastic constant because the two shear elastic constants are not affected by a forced volume magnetostrictive contribution. Using $\partial \omega / \partial H = 1.43 \times 10^{-8} \text{ Oe}^{-1}$, $\frac{\partial I}{\partial H} = 1.7 \times 10^{-3} \text{ G/Oe}$, and $E = 17.9 \times 10^{11} \text{ dyn/cm}^2$, one obtains the correction to the Young's modulus of Fe-35%Ni at room temperature of $-0.44 \times 10^{11} \text{ dyn/cm}^2$. This represents a change of 2-3%, and should not be neglected.

2.5.4 Dependence of the Exchange Integral J on the Degree of Order in $\text{Cu}_3\text{Au}(\text{Ll}_2)$ Type Ordering

An isotropic, short range exchange integral J in an alloy $A_x B_{1-x}$

with long range order parameter S is a statistical average of the exchange interactions between the various atom-pairs: J_{AA} , J_{AB} and J_{BB} . In the disordered state, all the lattice sites in a fcc unit cell are likely to be populated by either A or B atoms, the probability being proportional to their concentrations in the alloy. Suppose the alloy undergoes Ll_2 type ordering below a critical ordering temperature and forms the ordered alloy A_3B . The A atoms occupy the face-center positions while the B atoms take up the corner positions in the original unit cell (Figure 8). In the intermediate degree of order, some of the atoms will be occupying the wrong sites. Following X-ray diffraction theory,^[74] let α denote the correct sites for A atoms and β for B atoms in the fully ordered state. r_i and ω_i are the fraction of 'right' and 'wrong' atoms occupying the i sites respectively. The long-range order parameter S is defined by

$$S = \frac{r_\alpha - x}{1-x} \quad (17)$$

$S = 1$ when an alloy with the stoichiometric composition is fully ordered.

Then the following relationships hold:

$$\begin{aligned} r_\alpha &= S(1-x) + x \\ \omega_\alpha &= 1-r_\alpha = (1-x)(1-S) \\ r_\beta &= Sx + (1-x) \\ \omega_\beta &= 1-r_\beta = x(1-S) \end{aligned} \quad (18)$$

We shall derive the expression for the first nearest-neighbor exchange integral J_1 in terms of J_{AA} , J_{AB} , J_{BB} , S and x .

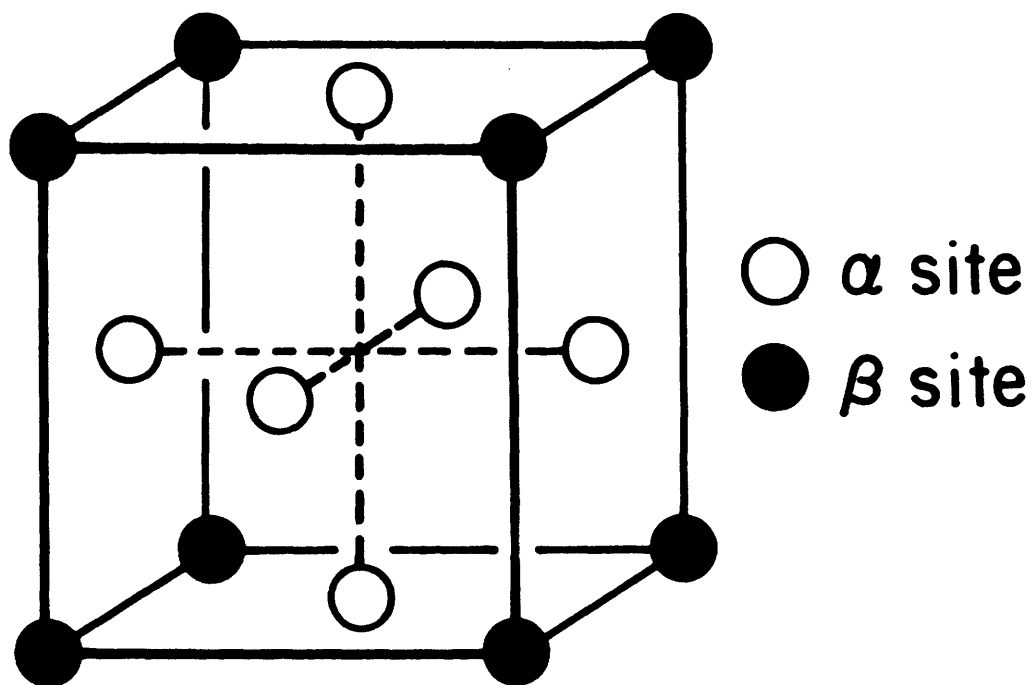


Figure 8. Different atom sites in L1₂ type ordering.

An α site has four first nearest-neighbor β sites and eight first neighbor α sites, while a β site has twelve nearest-neighbor α sites. An A atom in a α site has $(4\omega_\beta + 8r_\alpha)$ number of A atoms and $(4r_\beta + 8\omega_\alpha)$ number of B atoms as its nearest neighbors. It experiences an average interaction energy

$$J_\alpha(A) = \left(\frac{4}{12}\omega_\beta + \frac{8}{12}r_\alpha\right) J_{AA} + \left(\frac{4}{12}r_\beta + \frac{8}{12}\omega_\alpha\right) J_{AB} \quad (19a)$$

For an A atom in a β site, it has $12r_\alpha$ number of A atoms and $12\omega_\alpha$ number of B atoms as nearest neighbors. The average interaction energy is

$$J_\beta(A) = r_\alpha J_{AA} + \omega_\alpha J_{AB} \quad (19b)$$

Similar analysis for the B atoms shows that for a B atom in a α site,

$$J_\alpha(B) = \left(\frac{8}{12}\omega_\alpha + \frac{4}{12}r_\beta\right) J_{BB} + \left(\frac{8}{12}r_\alpha + \frac{4}{12}\omega_\beta\right) J_{AB} \quad (19c)$$

and for a B atom in a β site,

$$J_\beta(B) = \omega_\alpha J_{BB} + r_\alpha J_{AB} \quad (19d)$$

Averaging over A and B atoms in the α site, one obtains

$$J_\alpha = r_\alpha J_\alpha(A) + \omega_\alpha J_\alpha(B) \quad (20a)$$

A similar expression can be written for the β site,

$$J_{\beta} = \omega_{\beta} J_{\beta}(A) + r_{\beta} J_{\beta}(B) \quad (20b)$$

The final averaging is over the α and β sites. Of all the lattice sites, three-fourths are α sites and one-fourth β sites. Hence

$$J_1 = \frac{3}{4} J_{\alpha} + \frac{1}{4} J_{\beta} \quad (21)$$

In terms of r_{α} , ω_{α} , r_{β} and ω_{β}

$$\begin{aligned} J_1 = & \frac{1}{2} [r_{\alpha}^2 + r_{\alpha}\omega_{\beta}] J_{AA} + \frac{1}{2} [r_{\alpha}r_{\beta} + 2r_{\alpha}\omega_{\alpha} + \omega_{\alpha}\omega_{\beta}] J_{AB} \\ & + \frac{1}{2} [\omega_{\alpha}^2 + r_{\beta}\omega_{\alpha}] J_{BB} \end{aligned} \quad (22)$$

For the special cases of disordered ($S = 0$) and fully ordered ($S = 1$) states, Eq'n (22) reduces to the familiar result:

$$S = 0 \quad J_1(r_1) = x^2 J_{AA}(r_1) + 2x(1-x) J_{AB}(r_1) + (1-x)^2 J_{BB}(r_1) \quad (23a)$$

$$S = 1 \quad J_1(r_1) = \frac{1}{2} J_{AA}(r_1) + \frac{1}{2} J_{AB}(r_1) \quad (23b)$$

CHAPTER 3EXPERIMENTAL PROCEDURES3.1 Materials

A large single crystal is required for the measurement of elastic constants using the ultrasonic pulse echo technique.* A number of attempts were made to grow a single crystal of Fe_3Pt by the Bridgman technique and one attempt using the electron beam heating technique. All failed to produce a sufficiently large single crystal.** The successful attempt was made on November 10, 1976 at the Air Force Geophysics Laboratory in Bedford, Massachusetts. Pure Pt (99.99%) and Ferrovac E Fe in the composition of Fe-25a/oPt were arc-melted several times in an argon atmosphere. The charge was then cut up into pieces to improve homogeneity and put into an alumina crucible with a 30° cone tip. This was enclosed by a recrystallized alumina inner crucible and a graphite outer crucible. The furnace is made of resistance-heated graphite and the sensor for temperature control is a tungsten 5% rhenium/tungsten 26% rhenium thermocouple. The furnace plus the crucible assembly was outgassed under vacuum for one day at room temperature and one day at temperatures up to 915°C, and afterwards backfilled with high purity argon gas to one atmosphere. The temperature cycle (Fig. 9) was programmed into a computer after which the growth process proceeded automatically. At the stoichiometric composition and in the disordered state, M_S is around room temperature. To prevent martensite transformation from taking place as the crystal cools down, an ordering heat treatment was included in the

* approximate size required $1 \times 1 \times 1 \text{ cm}^3$

**failure due to polycrystalline growth or martensite formation

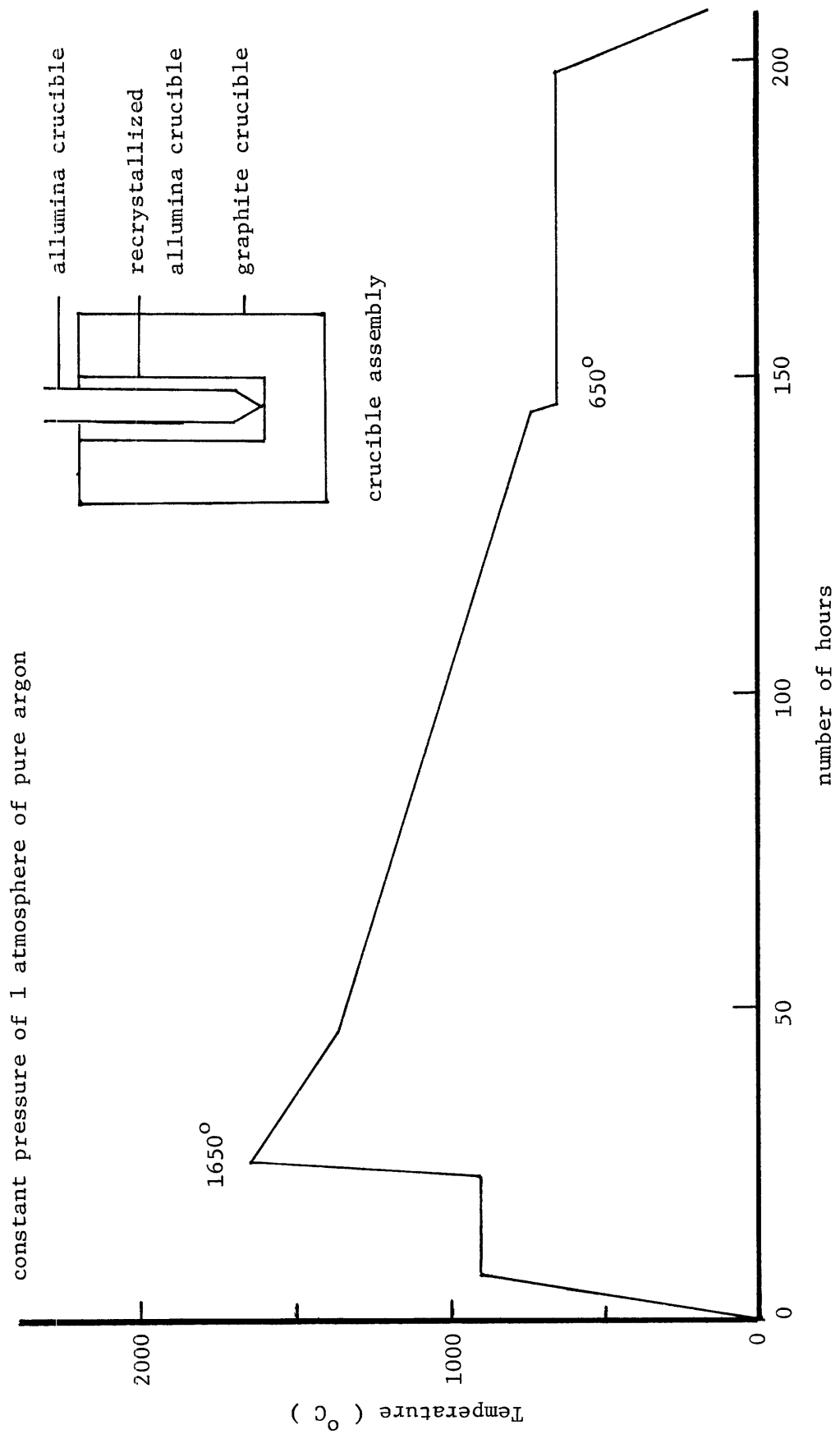


Figure 9. Temperature schedule of crystal growth.

last stage of the temperature cycle to depress M_S below room temperature. A single crystal of about $1 \times 1 \times 1 \text{ cm}^3$ was cut from the ingot. It was encapsulated in a quartz tube under vacuum and homogenized at 1250°C for 1 week. Two parallel (110) surfaces were planed and the orientation located to within $\pm 1^\circ$ by back-reflection Laue technique. From the remainder of the ingot, small disks of approximately 0.5cm diameter were cut for specific heat measurement and powder samples were filed for X-ray experiments. The powders passed through a 200 mesh screen. The composition was determined to be Fe-25.2a/o Pt from the room temperature lattice parameter of a disordered sample (Figure 2).

3.2 Specific Heat Measurements

Specific heat as a function of temperature was measured continuously using a Perkin-Elmer differential scanning calorimeter in two temperature ranges: 150 K-400 K and 310 K-600 K. Accuracy in a continuous run is about 1%. Reproducibility on separate runs is within 3%.

3.3 X-ray Measurements

Powder samples are pasted on glass slides with a mixture of Amyl Acetate and collodion and X-ray reflections taken on a General Electric diffractometer using Cu K radiation. With a 0.2° per minute slow scan, lattice parameter determined from doublet-resolved (420) reflections is within $\pm 0.0004\text{\AA}$. Peak area measurement of intensity using a planimeter is accurate within 2% which, combined with the uncertainties in calculating the polarization factor, etc., yields an overall accuracy of about 3% for the determination of long range order parameter S. A slightly

larger error is expected for small S.

Single-crystal diffraction patterns were recorded using a goniometer stage attached to the same G.E. diffractometer. The single crystal was rocked into a position of maximum intensity on the (220) reflection and rechecked at the (110) superlattice reflection before 2 θ scans were made of the two peaks at a rate of 0.4° per minute.

3.4 Elastic Constants Measurement

The elastic constants were measured using the ultrasonic pulse superposition technique. [75,77] This method of measuring ultrasonic wave velocity in solids involves a high frequency quartz transducer, usually 5-10 MHz, cemented to one end of a specimen having two parallel end faces. The transducer serves both as the generator and detector of radio frequency pulse propagating in the specimen. It is assumed that identical pulses are produced at regular intervals, t , approximately equal to some multiple p of the round trip travelling time, δ , of the ultrasonic wave. Periodically a few pulses are omitted so that the superposed echoes in the time slot immediately following the last applied pulse can be observed. When t is critically adjusted, the amplitude of the summed echoes can be made a maximum. For this in-phase condition

$$\delta = t/p = \frac{1}{f} \left[\frac{n}{p} - \gamma/360 \right] \quad (24)$$

where δ is the round trip travelling time in the specimen, γ is a phase angle associated with waves reflected at the transducer, f is the frequency of the wave in the pulse and n is an integer which may

take on both positive and negative values. n takes into account that it is not certain that identical crest in each pulse are superimposed. The γ term is small and remains fairly constant over a temperature interval of several hundred degrees. It can be omitted from Eq'n (24) with an error of a few parts in 10^4 . By measuring the transit time at the resonant frequency f_R and at a different frequency f_L (e.g. 10% lower), the difference

$$\Delta t = n \left(\frac{1}{f_L} - \frac{1}{f_R} \right) \quad (25)$$

$\Delta t = 0$ determines the transit time corresponding to $n = 0$. Then

$$\delta = t/p \quad (26)$$

A block diagram of the electronic circuitry and the specimen holder are shown in Figure 10. A small magnet provides a saturating magnetic field of 8 kilogauss to suppress the ΔE_λ effect. The narrow pole gap of this magnet restricted the sizes of the heating and cooling unit. The heating element consists of a brass jacket wrapped around by Nichrome wires to provide resistance heating. The unit is placed inside the pole gap insulated from the environment by slices of fire brick. The cooling was achieved by liquid nitrogen vapor blown into the brass jacket in the pole gap which is insulated from the environment by foam rubber and glass wool. The temperature was controlled in the ranges from room temperature to 200°C and from room temperature down to the lowest temperature

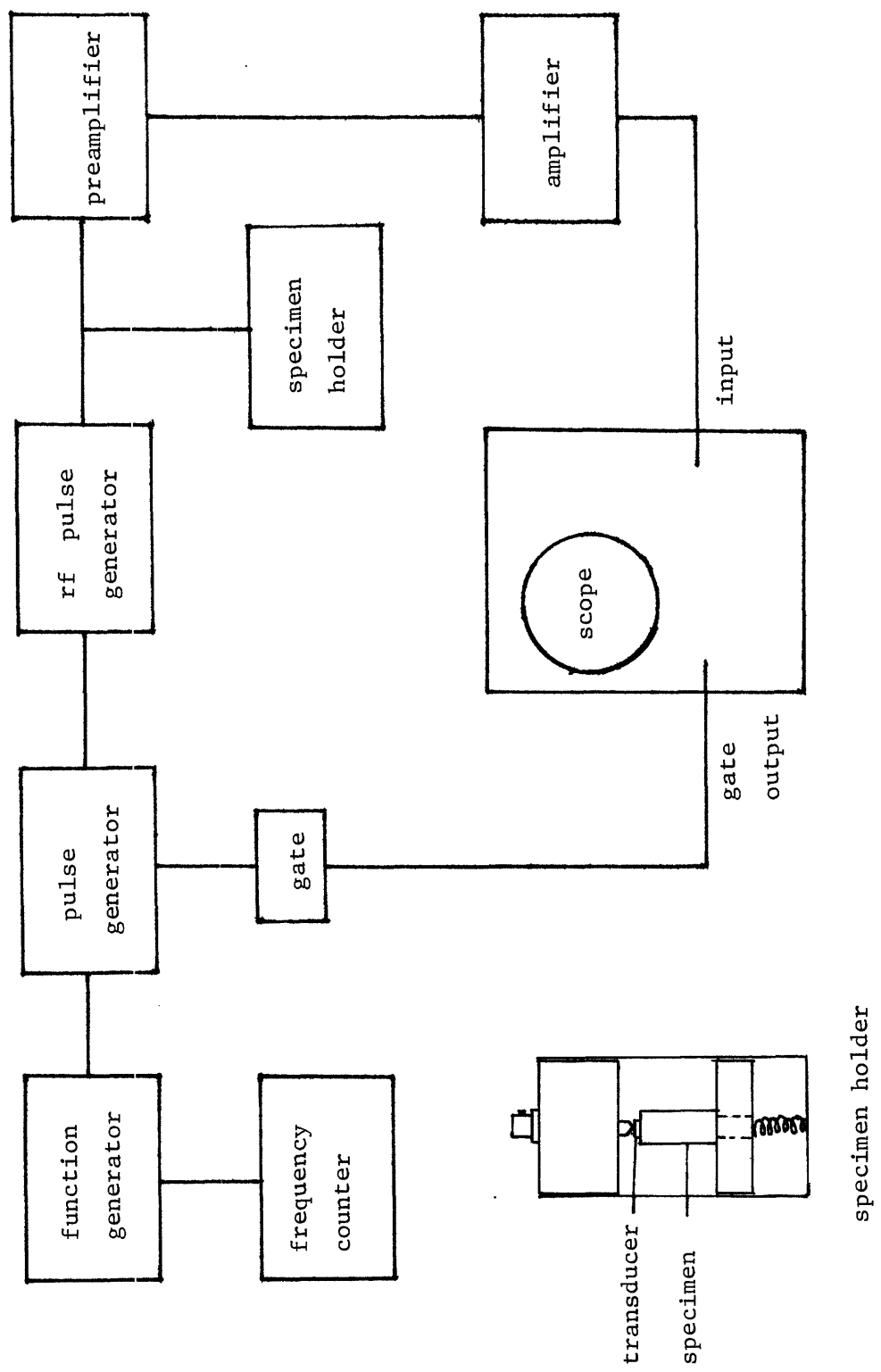


Figure 10. Block diagram of electronics for pulse superposition technique.

at which the bonding agent fixing the transducer to the specimen could hold. Measurements were made after the temperature, read by a copper-constantan thermocouple placed close to the sample and indicated through a digital voltmeter, has been stabilized. The temperature control is maintained to within 1°.

The bonding agents are listed in Table 1 together with the temperature range in which they are used. For the shear waves, EPY500 gives a better bonding above 200°C than saureisen. Between room temperature and 200°C, however, it gives broader echoes and is more difficult to remove after use. Hence the bulk of the shear wave velocity measurements in the high temperature range used saureisen as the bonding agent. In the low temperature region, none of the agents is able to provide good bonding down to liquid nitrogen temperature. Glycerin and nonaqueous stop-cock grease no longer transmit echoes below -125°C and -85°C, respectively. The range of temperature covered in the measurements, however, is sufficiently large that the data obtained are adequate for subsequent analysis.

Along the [110] propagating direction, three independent sound wave velocities were measured: one longitudinal and two transverse. By rotating the transducer in the (110) plane so that the shear direction is along either [110] or [001], only one of the transverse wave was excited. The elastic constants are given by

$$C_L = \rho V_l^2; \quad C = \rho V_{t1}^2; \quad C' = \rho V_{t2}^2 \quad (27)$$

where ρ is the density of the specimen. For polycrystalline materials,

Table 1. Bonding materials for elastic constant measurement

Material	Temperature range	type of wave
glycerin	-125°C - 200°C	longitudinal
Dow Resin	-40°C - 40°C	transverse
Sauereisen	-20°C - 200°C	transverse
Nonaqueous stopcock grease	-80°C - 20°C	transverse

only one longitudinal and one transverse wave velocity were measured.⁶⁴

By averaging over these two velocities both the Young's modulus E and the shear modulus G can be calculated: [78]

$$G = \rho v_t^2 \quad (28)$$

$$E = \frac{\rho v_t^2 (3v_\ell^2 - 4v_t^2)}{v_\ell^2 - v_t^2} \quad (29)$$

The combined error in the elastic constant measurement, including transit time, path length and density is less than 1%.

3.5 Calculation of the Average Elastic Moduli E, B and G from the Single Crystal Elastic Constants

The bulk modulus B is independent of any specific averaging procedures:

$$B = C_L - C - C'/3 \quad (30)$$

C_L , C and C' are the single crystal elastic constants usually determined in sound velocity measurements.

For the calculation of the shear modulus, G, several methods have been proposed in the literature: [79] the average after W.Voigt, [80]

$$G_V = \frac{1}{5} (2C' + 3C) \quad (31a)$$

and the average after A. Reuss, [81]

$$G_R = \frac{1}{5} \left(\frac{2}{C'} + \frac{3}{C} \right) \quad (31b)$$

Further averaging procedures have been proposed by R. Hill, [82]

$$\begin{aligned} G_H &= \frac{1}{2} (G_V + G_R) \\ &= \frac{1}{10} \frac{38CC' + 6C'^2 + 6C^2}{2C + 3C'} \end{aligned} \quad (32)$$

W. Voigt assumed constant stress while A. Reuss assumed constant strain within the individual grains. R Hill has shown that these methods lead to upper and lower limits of the true value of G. He proposed the arithmetic mean of G_V and G_R as a better approximation. For our work, we used the Voigt-Reuss-Hill (VRH) method proposed by Hill.

Since a polycrystalline material has only two independent elastic moduli, Young's modulus E can be calculated from B and G as follows:

$$E = \frac{9BG}{3B + G} \quad (33)$$

and the Poisson's ratio

$$\nu = \frac{E}{2G} - 1. \quad (34)$$

3.6 Heat Treatment

In all heat treatments, specimens were encapsulated in a quartz tube with a vacuum better than 2×10^{-6} torr. For powder samples, spongy pieces of titanium were also placed in the tube separated from the powder by glass wool. Prior to ordering treatment, the titanium was heated by a blow torch to form titanium oxide, thus removing any trace of oxygen left in the encapsulated tube.

There is only limited information on the kinetics of ordering in Fe_3Pt . Most investigations on the effect of ordering in Fe_3Pt used the length of annealing time at an ordering temperature to characterize the atomic state. At short annealing times, it is doubtful that the specimen is in thermodynamic equilibrium. Hence we establish a curve of the variation of the equilibrium long-range order S with annealing temperature for the present alloy as a guide for subsequent heat treatments. Following Herbeuval,^[27] powder samples were annealed at temperatures below the critical ordering temperature for long periods of time to establish thermodynamic equilibrium. The samples were quenched into water without breaking the capsule. X-ray diffraction patterns were taken to determine S and the room temperature lattice parameter. (Figure 11 and 12). Detail discussion on the X-ray results will be made in the next chapter. Below 710°C , the value of S rises rapidly. Hence it is difficult to obtain partially ordered states of small S which are in thermodynamic equilibrium. Observations by B. Djuric^[83] showed that rapid quenching of Fe_3Pt specimens produced stress concentration near the grain boundaries which etched preferentially. To avoid such stress con-

centration in the single crystal specimen, it was always furnace cooled after the ordering treatments except for the disordered state which was produced by quenching from 900°C into water without breaking the capsule. The furnace cooling rate is approximately 400 degrees per hour. It is sufficiently fast to prevent significant changes in the value of S as the crystal cooled through the ordering range. After a complete set of data was taken on the single crystal with degree of order S , it was annealed at 900°C for 1 hour to disorder the lattice before the next ordering treatment was carried out.

Ordering of the single crystal and the disk specimens at 625°C for 3 days and at 690°C for 12 hours resulted in $S = 0.85$ and 0.55 respectively. Later heat treatments followed those of Kajiwara and Owen^[91] in order to reproduce the elastic conditions of the ausentite under which changes in the growth behavior of the martensite were observed. These were 5 hours, 1 hour and 10 minutes at 650°C, with $S = 0.6$, 0.4 and 0.2 respectively. For the last heat treatment, 10 minutes at 650°C, the capsule was air-cooled. All the heat treatments are tabulated in Tables 2 and 3.

Table 2. Heat treatment of powder specimens

T (°C)	duration	order parameter S	a_0 (Å)
750	18 hrs.	0	3.7240
700	36 hrs.	0.33	3.7250
675	40 hrs.	0.93	3.7345
650	36 hrs.	0.88	3.7338
625	168 hrs.	0.92	3.7345
600	168 hrs.	0.91	3.7340

Quenching: water quench without breaking capsule

Table 3. Heat treatment of single crystal specimen

T (°C)	duration	order parameter S
1. 625	72 hrs.	0.85
2. 690	18 hrs.	0.55
3. 650	5 hrs.	0.60
4. 650	1 hr.	0.40
5. 650	10 min.	0.20
6. 900	1 hr.	0

Quenching: 1.-4. furnace cool

5. air cool

6. water quench without breaking capsule

CHAPTER 4EXPERIMENTAL RESULTS AND DISCUSSION4.1 Ordering

A series of powder specimens were prepared and heat treated in the manner described in Section 3.6. With Herbeuval's result^[27] as a guide, we had lengthened the annealing time at each temperature. To determine the long range order parameter S , the peak areas of two fundamental reflections and one superlattice reflection were measured using a planimeter. The two fundamentals are the (200) and (220) reflections and the superlattice reflection corresponds to (300) and (221) combined. These three reflections occurred within a 2θ range of 30 degrees. This ensures that the X-ray beam was incident on the same area of the powder specimen where the density of powder was uniform. The values of S calculated from the intensity ratio of the superlattice reflection to either (200) or (220) reflection were in agreement to within 5%. The arithmetic mean of the two values was taken to be the equilibrium S for that ordering temperature. The variation of S with ordering temperature is shown in Figure 11. Room temperature lattice parameters were determined in two ways. The (420) fundamental had well-resolved doublets and being at a high enough 2θ angle ($\sim 140^\circ$), the lattice parameter calculated from this reflection was a good approximation to the actual a_0 value. The second method plotted a_0 determined from all the fundamentals versus the appropriate diffractometer function and extrapolated to $2\theta = 180^\circ$ to obtain the lattice parameter. The results are shown in Figure 12. In both Figures 11 and 12, we have also reproduced Herbeuval's result (dash-line) for the purpose of comparison.

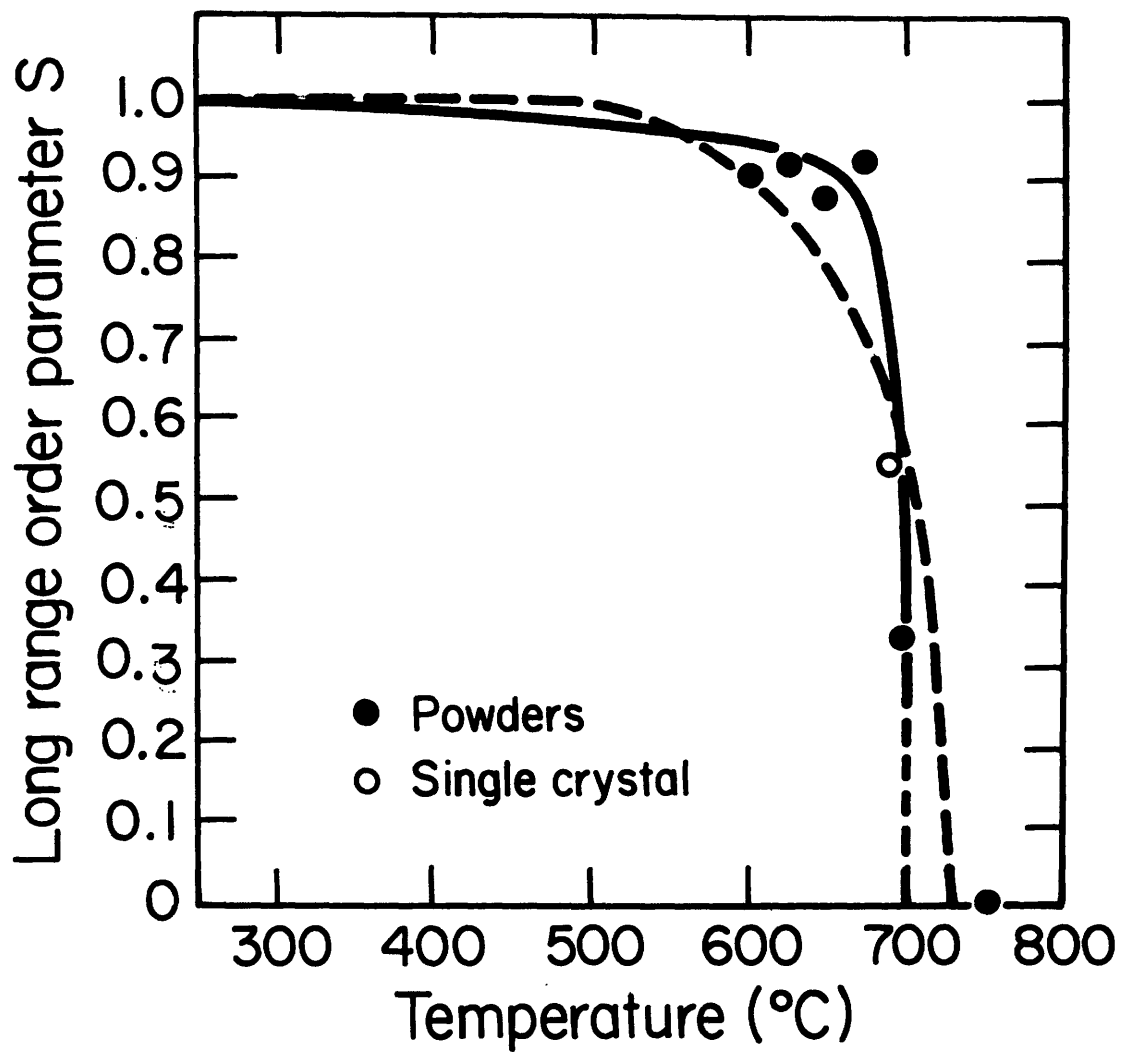


Figure 11. Long range order parameter S versus ordering temperature in Fe_3Pt . (Dash line from reference 27).

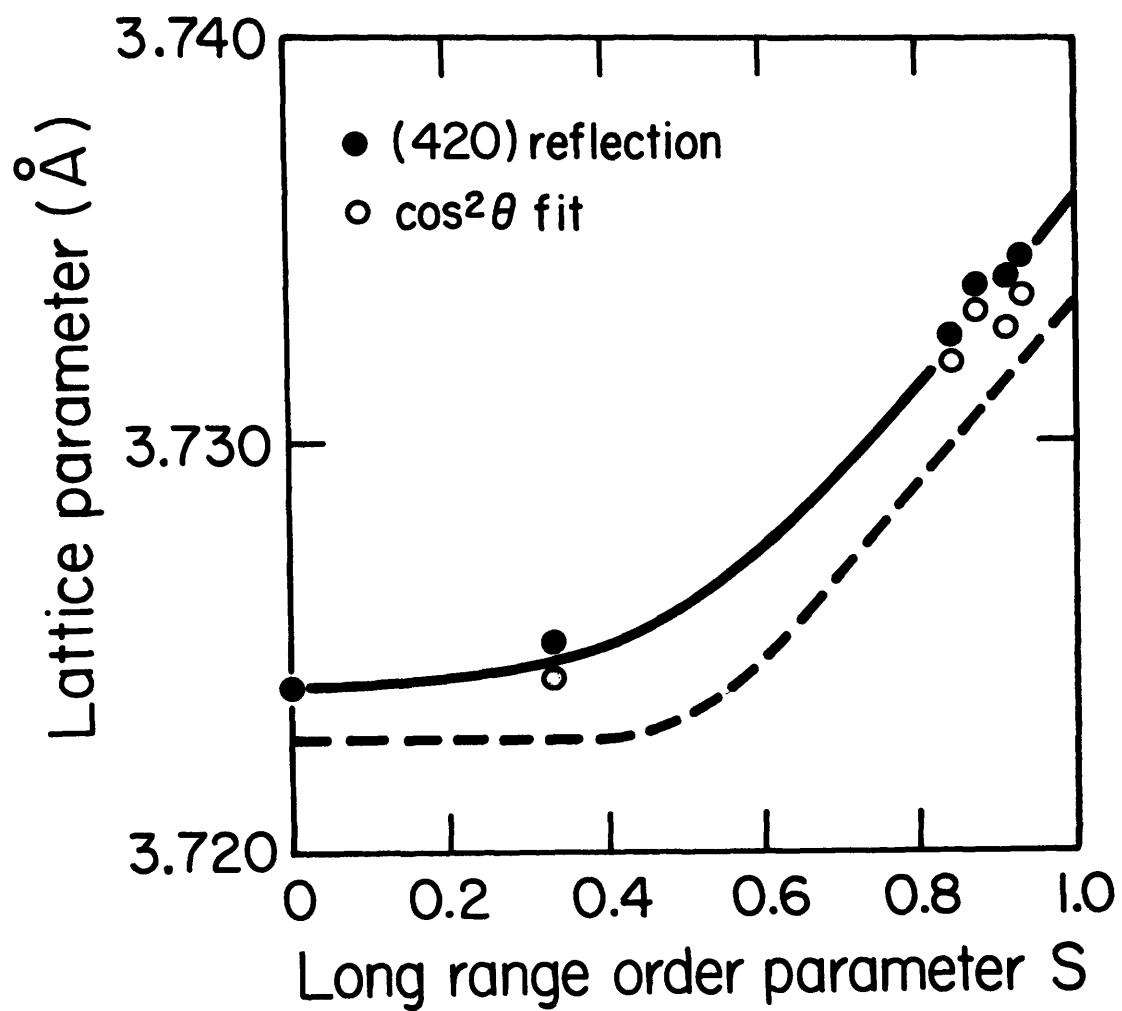


Figure 12. Room temperature lattice parameter a_0 versus the degree of order S in Fe_3Pt . (Dash line from reference 27).

The room temperature lattice parameter a_0 remains essentially constant at 3.724\AA between $S = 0$ and 0.4 , then increases linearly with S to 3.736\AA at $S = 1.0$. This behavior is similar to that observed by Herbeuval. The rate at which a_0 increases with S beyond $S = 0.5$ is the same in both cases. The difference in the magnitude of the lattice parameter indicates a small difference in the composition between the two sets of specimens.

The variation in the degree of order, S , with ordering temperature (Figure 11) shows a rapid change in S near the critical temperature for ordering, θ_c , rising from $S = 0$ at 705°C to $S = 0.9$ at 675°C . Then S increases slowly to the maximum value of 1 attainable at this composition. Ordering is very sluggish at the lower temperatures. Three days at 625°C yielded a S of 0.85 while seven days at the same temperature resulted in a S of 0.92 . At 500°C , seven days' annealing gave an S of 0.4 . This value of S was confirmed by X-ray measurement on a powder specimen and on the single crystal heat treated in the same manner. The (420) fundamental reflection did not show a resolved doublet, as were obtained in the diffraction patterns of specimens ordered at high temperatures. Measurement of the C' elastic constant also showed that magnetic softening began around 140°C , meaning that the single crystal contained a phase which was in a more ordered state than indicated by $S = 0.4$. These evidences suggest that the nucleation and growth of ordered regions is very slow at low temperatures in Fe_3Pt , and the specimen contained a mixture of ordered and disordered regions. This is different from the result obtained by Herbeuval. After annealing for seven days at 460°C ,

the state $S = 1$ was attained in his specimen. Another difference is that he found a more gradual variation of S with temperature near the critical temperature for ordering. It is not clear whether a compositional difference of less than 1/2 atomic pct., determined from the difference in lattice parameter, could cause this change in the ordering kinetics.

Fe_3Pt undergoes Ll_2 type ordering. In the fully ordered state, the Pt atoms occupy the corner sites and the Fe atoms the face-center positions of the original disordered FCC unit cell. Hence, the superlattice is composed of four interpenetrating structures, with the Pt atoms occupying one structure and the Fe atoms occupying the other three structures. In a typical Ll_2 type alloy, such as Cu_3Au , S decreases slowly from 1 to 0.8 on heating from the fully ordered state. At θ_c , S decreases discontinuously from 0.8 to 0, and at all temperatures above θ_c , S is zero. Certain Ll_2 and DO_{19} type alloys pass through an equilibrium two-phase condition, ordered plus disordered regions, as the temperature is raised. For example, Davies and Stoloff^[91] concluded, from the broadening of the (0002) fundamental reflection, that in Mg_3Cd , there is a two-phase region below θ_c , and the degree of order only changes from 1 to ~ 0.8 as for Cu_3Au even though S , calculated from X-ray measurement, varies continuously from 0 to 1. It is not clear whether this explanation can be applied to the Fe_3Pt specimens heat treated under equilibrium conditions. The difference in lattice parameter of the disordered (3.7240\AA for $S = 0$) and the ordered (3.7316\AA FOR $S = 0.8$) states are such that a splitting of 0.56° should occur at the (420) fundamental

reflection. This was not observed in the specimen with $S = 0.33$. There was no noticeable broadening of the other fundamental reflections.

Isothermal ordering of the single-crystal specimen at 650°C for 5 hours, 1 hour and 10 minutes resulted in values of $S = 0.6, 0.4$ and 0.2 respectively. For a short annealing time, the specimen would not be in thermodynamic equilibrium. In the case of $S = 0.2$, elastic constant measurements indicated that the specimen likely consisted of ordered regions in a disordered matrix. (section 4.4.1) Electron microscopy studies on Fe_3Pt specimens [10], which had been isothermally ordered at 650°C for 0.5 hour, showed bright ordered domains among dark areas. It is not clear, however, whether the dark areas correspond to a disordered matrix or to the contrast created by antiphase boundaries. The value of $S = 0.2$ should be taken to represent a long-range order parameter possibly averaged over a matrix of ordered and disordered regions. In summary, evidence from X-ray diffraction study suggests that ordering is by a nucleation and growth mechanism.

Short-range order was not measured in the specimens used in this study. An initial annealing at 900°C for 1 hour results in a certain degree of short-range order which is retained on quenching. [83] Above the critical ordering temperature, θ_c , measurements at temperature [27] showed that the short-range order coefficient $\alpha_1 \approx -0.1$. It represents a 83% probability of finding an Fe atom as a nearest-neighbor to a Pt atom. This is higher than a probability of 75% in a random solid solution. Subsequent annealing below θ_c allow this short-range order to develop into a long-range order. For short annealing times (small S), however, the short-range order is a more appropriate parameter in characterizing the nearest-neighbor correlation. This would be the case for specimens with long-range order $S = 0$ and 0.2 in the present study. It should be noted, however, that these two sets of

data were not used in the analysis of the effect of ordering on the Invar phenomenon.

4.2 Specific Heat

When a ferromagnetic material is heated, the energy of magnetization affects the rate at which a given inflow of heat will raise the temperature of the material. The Weiss theory of ferromagnetism predicts that the magnetic contribution to specific heat rises continuously with increasing temperature up to the Curie point, whereupon it drops to zero. The magnitude of the discontinuity at the Curie point depends on the value of the quantum number j , which determines the coupling between electron moments. The theoretical curves are shown in Figure 13a. Experiments show that the decrease in specific heat takes place over a range of temperature instead of precipitously. According to different authors,^[68] the transition region varies from 7° to 50°C for Ni. The drop in specific heat in the transition range was generally in fair agreement with theoretical value for $j = 1/2$. Most recent measurements on a series of Fe-Ni alloys were reported by Tanji, et al.^[83] Alloys in the Invar range exhibited two features which are different from pure Ni or Ni-rich alloys. The transition region near T_c extended over a larger temperature range, approximately 100°C, and the drop in the specific heat is only one-half to one-third as large. The temperature at which the peak in the specific heat versus temperature curve occurs is designated the Curie temperature. The same criterion of determining the Curie temperature will be adopted here.

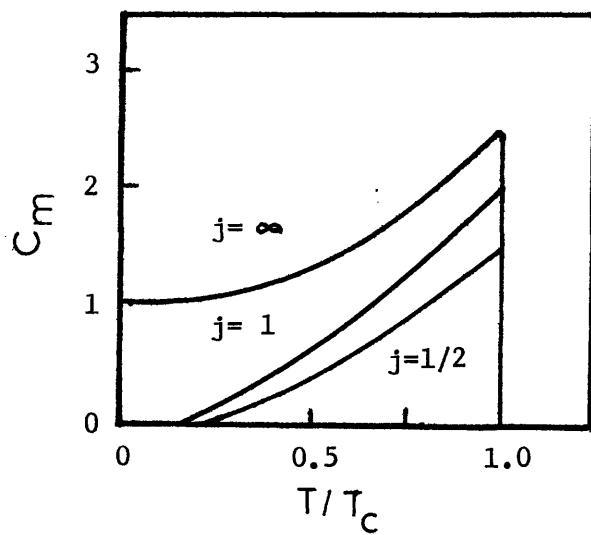


Figure 13a. Heat capacity calculated for various quantum states according to Weiss theory.

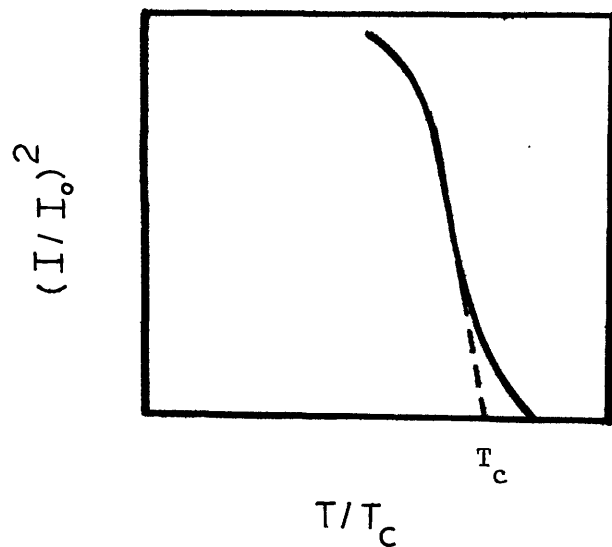


Figure 13b. Determination of the Curie temperature, T_c , from the square of magnetization versus temperature curve.

We have investigated the variation of specific heat with temperature under constant pressure in an Fe-25a/o Pt alloy with different degrees of long-range order (Figure 14). The essential features were similar to that of Fe-Ni Invar alloys.^[83] The transition region was found to decrease as the order of the specimen was decreased. This is in qualitative agreement with the magnetization measurement of a Fe-28a/oPt alloy reported by Sumiyama, et al.^[7] Near T_c , the magnetization of the ordered alloy changed more gradually with increasing temperature than that of the disordered alloy. The drop in specific heat near T_c is 0.003 cal/gm. This is of the same magnitude as observed in cobalt and is considerably below that given by theory for $j = 1/2$. The Curie temperatures as a function of order, determined by the criterion described above, are shown in Figure 15. The open circles in the same figure are for a disordered and a highly ordered state reported by Mizoguchi, et al.^[28]

In a specimen with $S = 0$, a rapid increase in the specific heat occurred at 0°C . This large release of energy corresponds to a burst in the martensitic transformation. Under optical microscope equipped with a cooling stage, the surface of such a specimen was observed to be covered entirely by martensite plates when 0°C was reached. The initial increase in the specific heat between room temperature and 0°C is due to the magnetic transition.

In specimens with $S = 0.2$, the martensitic transformation possesses some thermoelastic character. On the first cycle of cooling, small peaks on the specific heat curve preceded a narrow burst that was

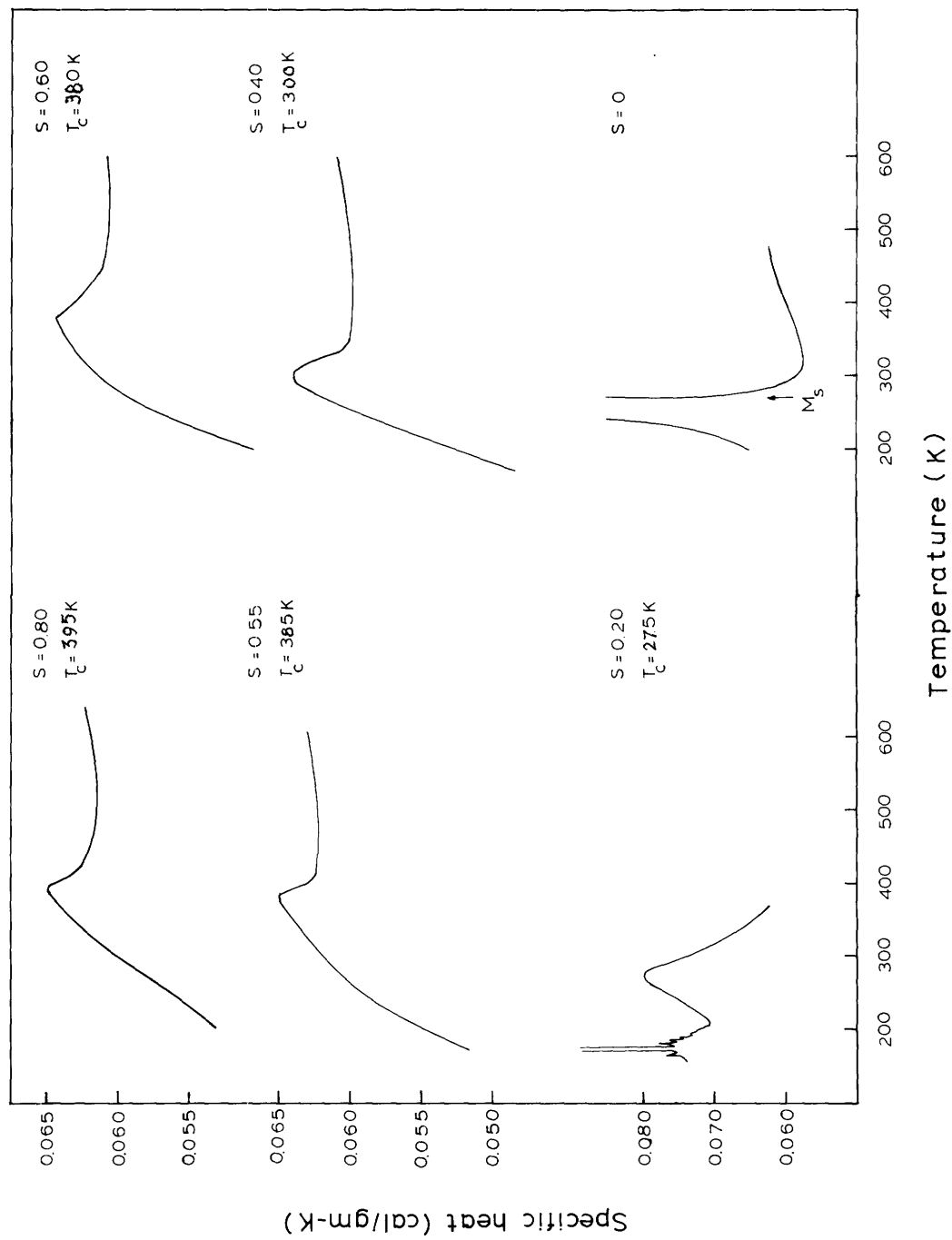


Figure 14. Specific heat versus temperature for different degree of order.

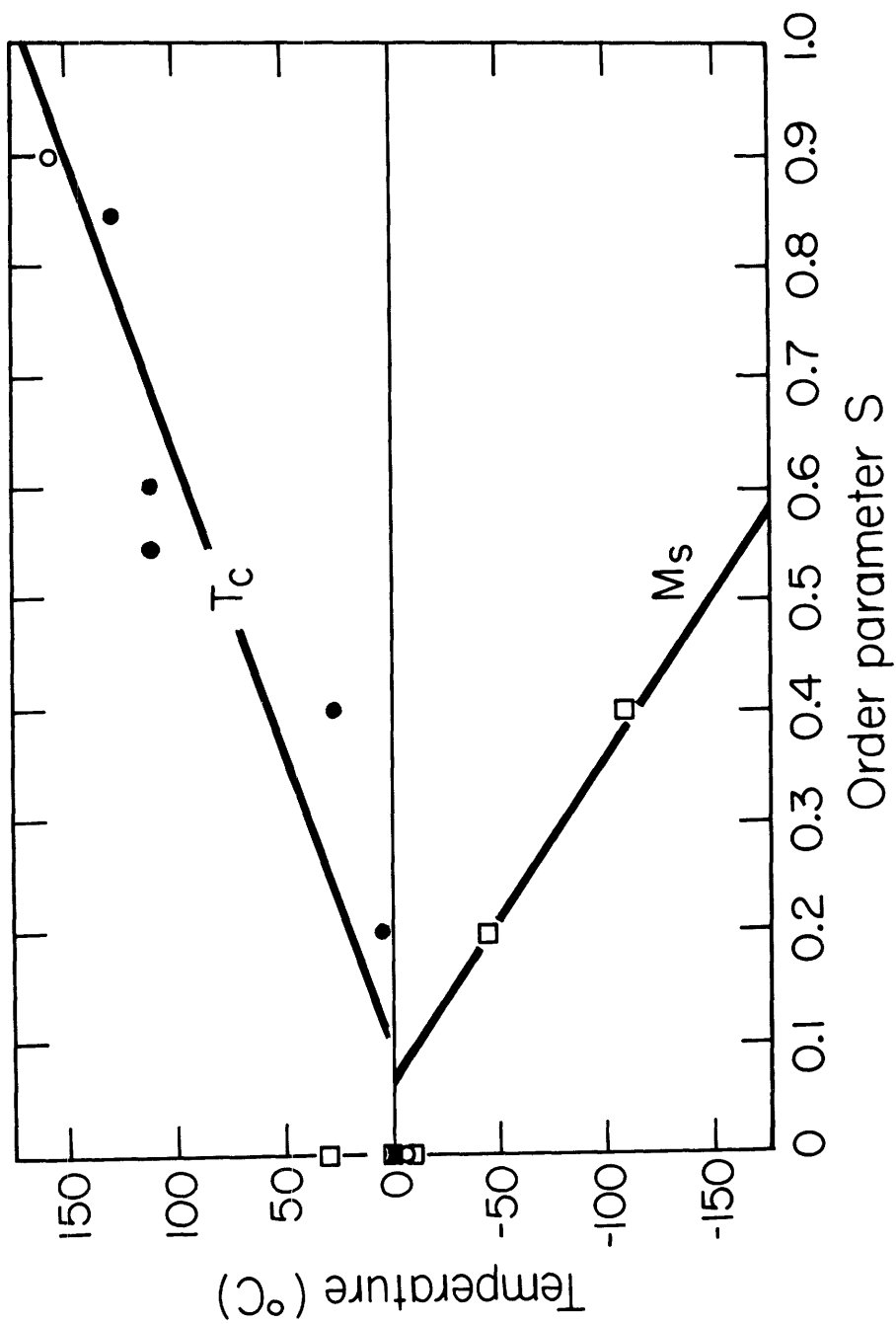


Figure 15. Variation of the Curie temperature, T_c , and the M_s temperature with the degree of order in Fe_3Pt . (\square reference 91; \bullet reference 28).

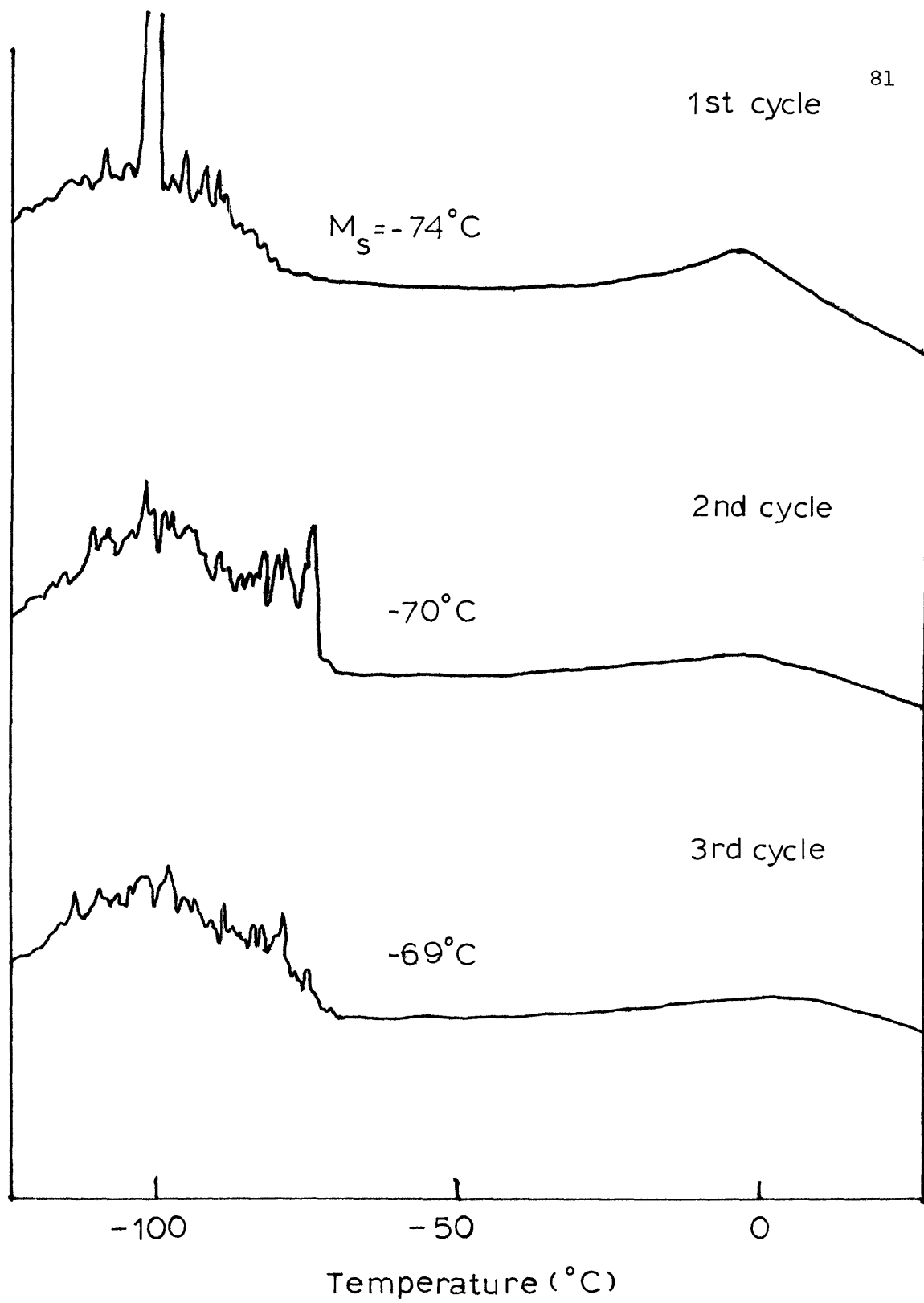


Figure 16. Traces of specific heat measurement. $S=0.2$.

small compared to that observed in the disordered specimen. More small peaks followed. On the second and third cycle of cooling, the burst behavior disappeared (Figure 16). The reverse transformation from $\alpha \rightarrow \gamma$ consisted of small peaks extending over a temperature range of 120 degrees. Presumably, the small peaks correspond to the transformation, either $\gamma \rightarrow \alpha$ or $\alpha \rightarrow \gamma$, of one or a few plates, while the burst was due to a large number of plates transforming simultaneously. Neither M_s nor A_s varied significantly over the first three thermal cycles. The M_s were -74°C (1st cycle), -70°C (2nd cycle) and -69°C (3rd cycle). This is in contrast to the result reported by Umemoto and Wayman^[84] for a partially ordered Fe-25a/oPt specimen (5 hours at 550°C) in which the M_s temperature showed significant increase with cycling and was found to be -54°C (1st cycle), 23°C (2nd cycle), 68°C (3rd cycle) and 95°C (8th cycle) after which cycling did not increase M_s .

4.3 Elastic Moduli of Polycrystalline Specimens

4.3.1 Fe-30 Ni Austenite

Single crystal elastic constants of Fe-30Ni had been measured from temperatures above the Curie temperature, T_c , down to the M_s temperature.^[21,22] The C' elastic constant showed a change from negative to positive temperature dependence around T_c and the decrease was 2.5% between T_c and M_s . The C elastic constant, however, did not exhibit any anomalous behavior near T_c . It increased with decreasing temperature. A slight positive temperature dependence was observed between 0°C and M_s . C_L behaved similarly to the corresponding elastic constant in Invar alloys.^[6,23] The change to positive temperature

dependence occurred approximately 150°C above T_c . These anomalous behaviors have been attributed to a magnetic contribution to the elastic constants.^[21] Average elastic moduli, calculated using the VRH method and suitable for describing polycrystalline specimens, are shown in Figure 17 (dash lines). The temperature dependence of the shear and the Young's moduli changed from negative to positive around T_c . However, no measurement had been reported on polycrystalline Fe-30Ni alloys over a temperature range that includes T_c . Goldman, et al^[80] made measurements from -30°C and 30°C and found that both the Young's modulus and the shear modulus showed positive slope of 0.03%/C and 0.08%/C respectively. It is not known from their work whether or not the positive temperature dependence of the moduli is a result of a magnetic transition. Hence, the longitudinal and shear wave velocities of a polycrystalline Fe-30Ni specimen were measured in a temperature range extending from above T_c and down to ~10 degrees above M_s . The grain size of the specimen was approximately 50 microns and the room temperature lattice parameter was determined to be 3.581Å. The path length was corrected using the thermal expansion measurements of Tanji, et al^[2]. The results are shown in Figure 17. They are in good agreement with the average moduli calculated from the single crystal elastic constant data of Alers.^[21] Both the Young's modulus and the shear modulus showed a change from negative to positive temperature dependence. The change occurred at a higher temperature in the Young's

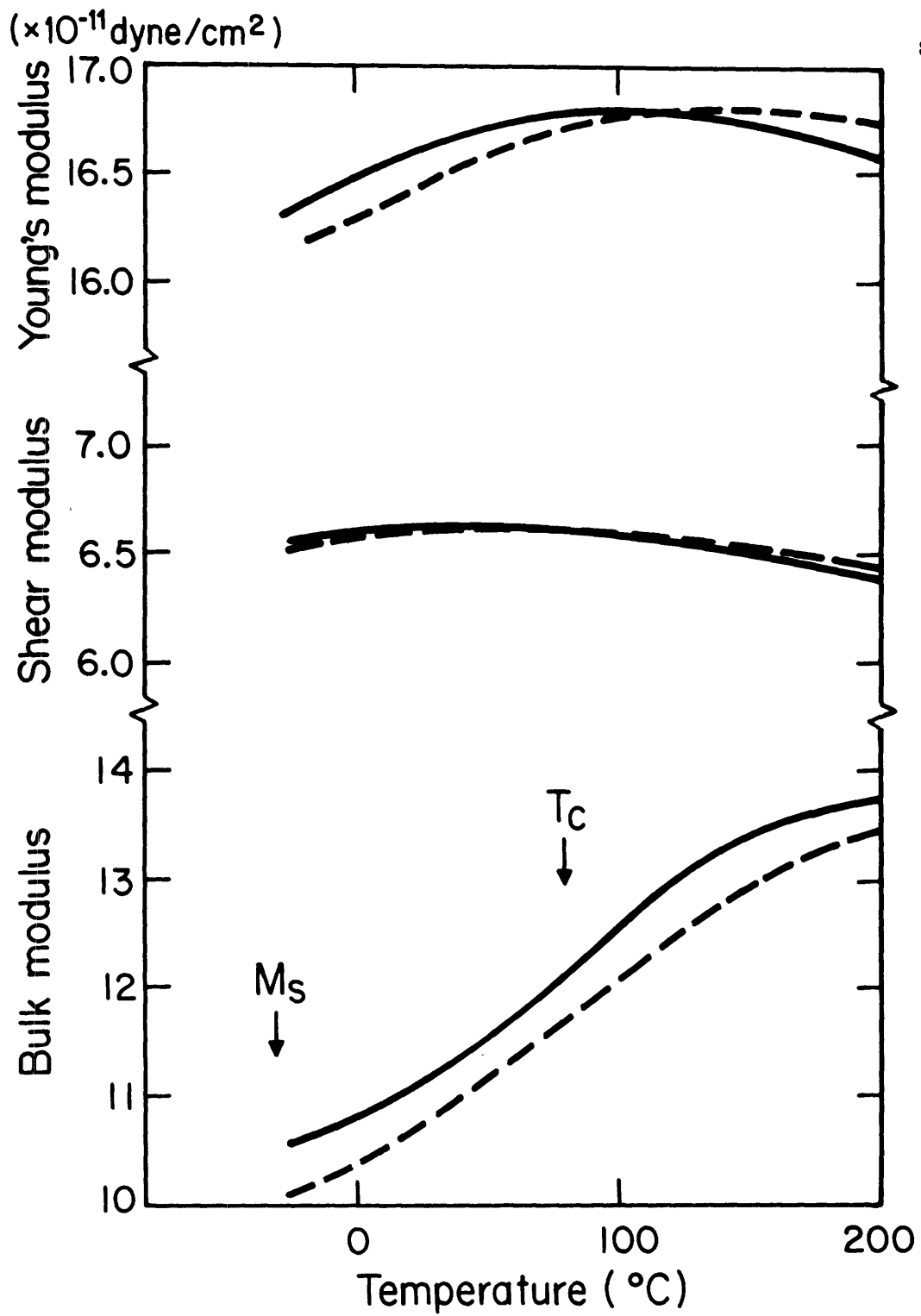


Figure 17. Polycrystalline elastic moduli of Fe-30Ni austenite versus temperature.

modulus because it is dependent on C_L which behaves anomalously above T_C . The bulk modulus, which is largely determined by the C_L elastic constant, decreased continuously from 200°C down to M_S . The discrepancy with Goldman's data is larger, especially in the Young's modulus. The difference of 3.5% is outside the experimental error. It could be due to a compositional difference between the two specimens. From the present set of measurements on a polycrystalline specimen, it can be said that the change in temperature dependence of the elastic moduli is associated with the Curie temperature, although the small change and broad transition region makes it difficult to establish this with certainty.

4.3.2 Fe-30Ni Martensite

Very little data had been reported on the temperature dependence of the elastic constants of Fe-30Ni martensite. Goldman, et al^[80] estimated the elastic moduli of martensite from measurements made on a two-phase specimen. The temperature dependence of the shear and Young's moduli were both found to be $-0.02\%/^{\circ}\text{C}$. In the present measurement, the martensitic state was produced by holding the specimen at -196°C for some time. After warming up to room temperature, X-ray diffraction indicated no peaks that corresponded to the austenitic phase. The lattice parameter of the martensite was determined to be 2.864\AA . This was in agreement with the result reported by Reed, et al^[81] that the lattice parameter of the martensite in Fe-Ni alloys decreases in the Invar range. Both the shear and Young's moduli showed a negative

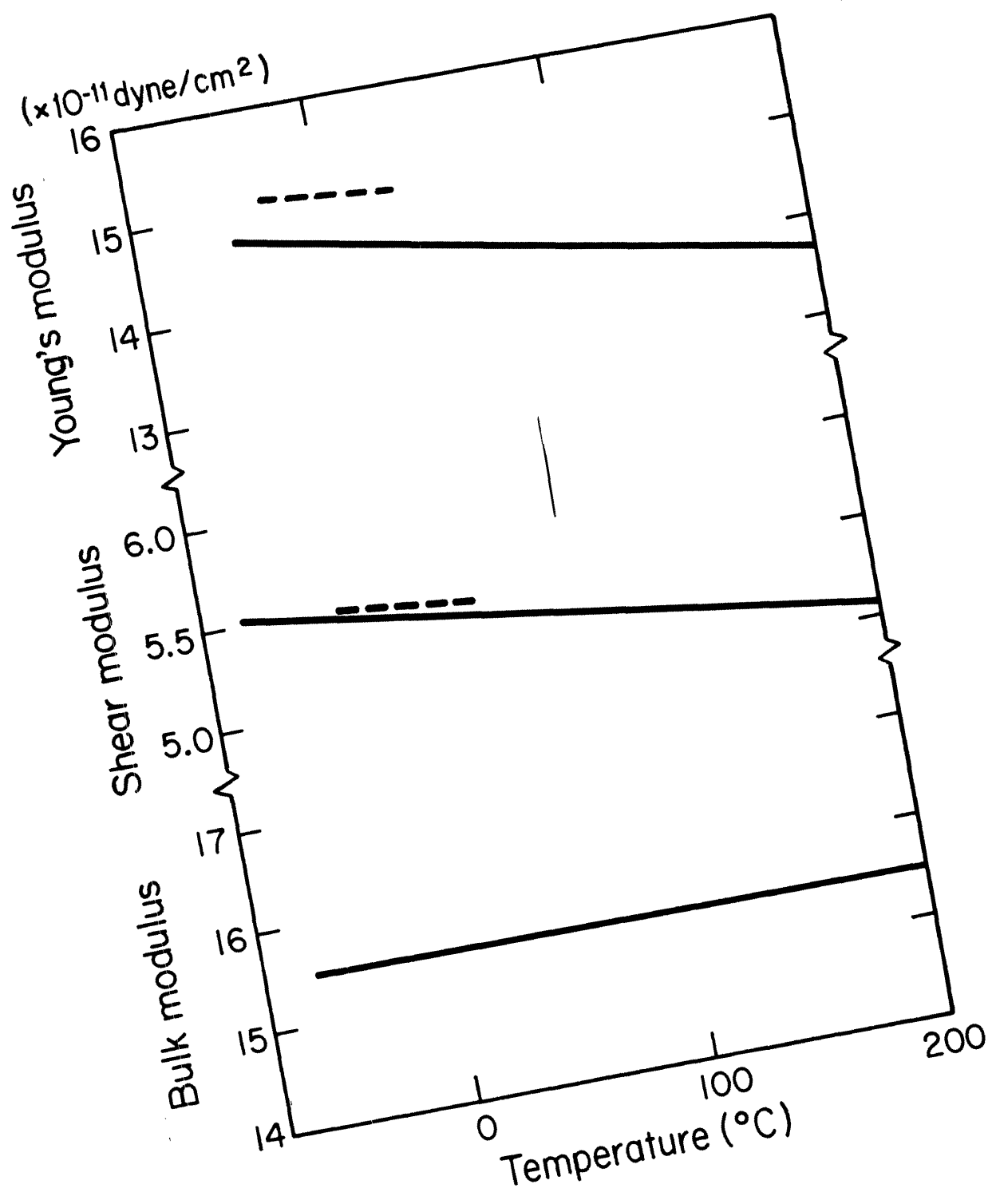


Figure 18. Polycrystalline elastic moduli of Fe-30 Ni martensite versus temperature.

temperature dependence, with a slope of $-0.03\%/^{\circ}\text{C}$ (Figure 18). There is a difference of 4% in the Young's modulus compared to the Goldman result. Their specimen probably had a lower Ni content, since they observed a two-phase structure at room temperature.

4.3.3 Fe-22Pt Martensite

We are not aware of any published data on the elastic moduli of martensite in Fe-Pt. The specimen for this measurement was obtained from the ingot of an unsuccessful attempt to grow a single crystal of Fe_3Pt . At room temperature, the specimen was all martensite. The composition was determined from the lattice parameter of 2.954\AA to be Fe-22a/oPt (Figure 2). The M_s is 100°C .^[82] In the temperature range of measurement (200°C to -100°C), the martensite is not expected to transform back to austenite. The results are shown in Figure 19. Similar to the elastic moduli of the Fe-30Ni martensite, a normal behavior of negative temperature dependence was observed. The slopes are $-0.023\%/^{\circ}\text{C}$ and $-0.03\%/^{\circ}\text{C}$ for the Young's modulus and the shear modulus respectively.

4.4 Single-Crystal Elastic Constants of Fe-25Pt

4.4.1 General Considerations

Measurements of sound velocities were carried out in zero field and with an applied field of 8 kilogauss to suppress domain reorientation. For the analysis of the magnetic contribution to the elastic constants, only the data measured in an external field can be used. These include the data sets for $S = 0.85, 0.60, 0.55$ and 0.40 . In the case of

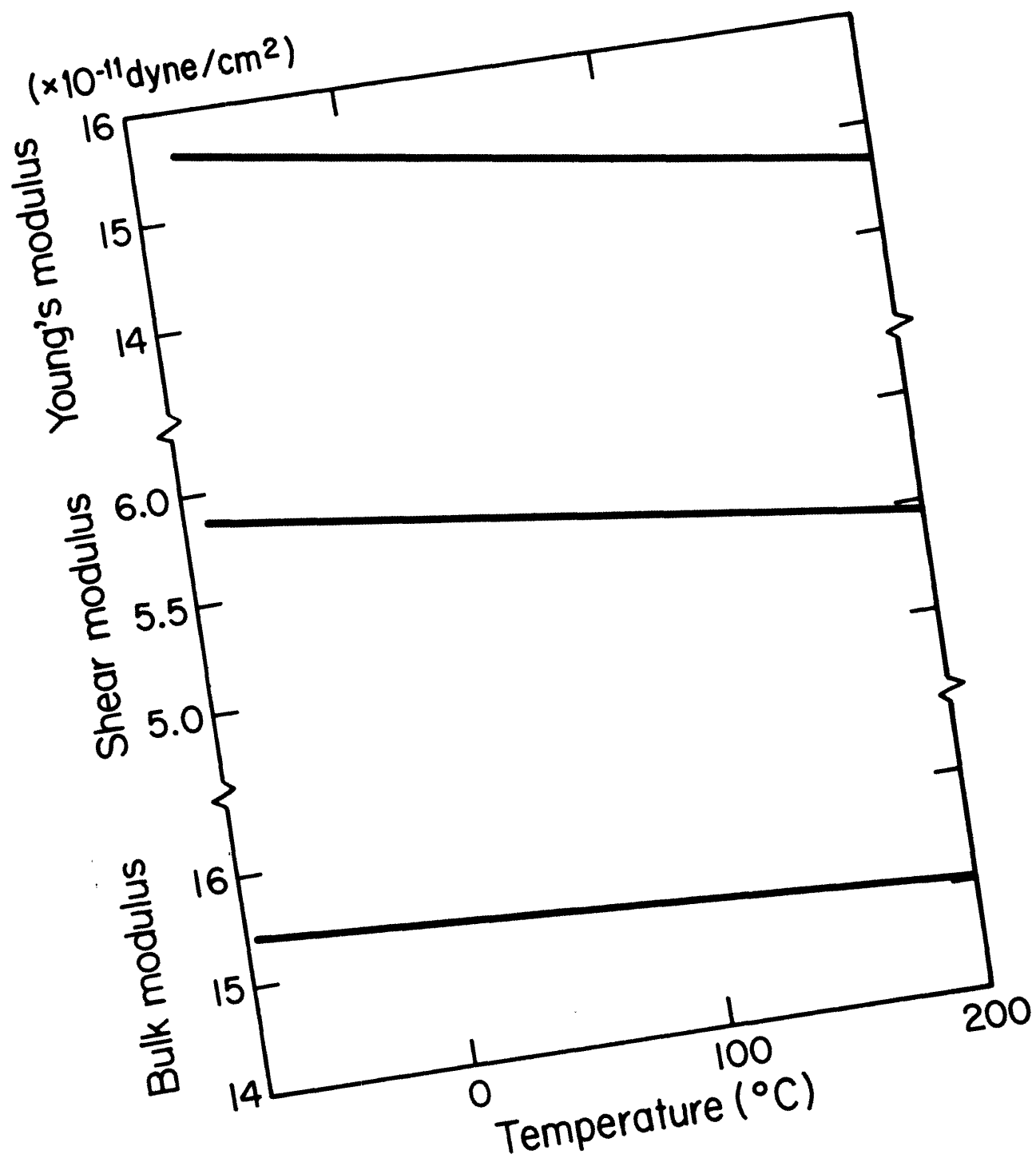


Figure 19. Polycrystalline elastic moduli of Fe-22Pt martensite versus temperature.

$S = 0.2$, all three modes of echoes, one longitudinal and two transverse, were slightly broader than that of the higher degree of order. An applied external field broadened the echoes even more and reduced the number of detectable echoes, especially in the C_L and C' modes. As the specimen was cooled further below the Curie temperature, ultrasonic attenuation increased rapidly. An explanation can be advanced as follows. A specimen with a low long-range order parameter S as determined by X-ray diffraction consists of partially ordered domains in a disordered matrix. In the absence of an applied field, these ordered regions serve as scattering centers if their size is of the order of the ultrasonic wavelength, resulting in broadened echoes and increased attenuation. If an external field is applied below the Curie temperature, the magnetic moments in the domains are aligned, further increasing the magnetic scattering. The magnetic scattering increases on cooling because the magnetization increases. Hence for the case of $S = 0.2$, no reasonable measurements can be obtained in an applied field. In the absence of a field, C and C' can be measured down to -40°C , but C_L can no longer be determined below -20°C . For $S=0$, the Curie temperature is only a few degrees above the M_S temperature. Measurements were made in a zero field and stopped at room temperature. The values of the elastic constants at the M_S temperature (0°C) were determined by extrapolation. The variation from the actual values are not expected to exceed 2%. These two sets of data, corresponding to $S = 0.2$ and $S = 0$, will be used in examining the growth behavior of martensites as a function of order in the austenite. (Figure 20).

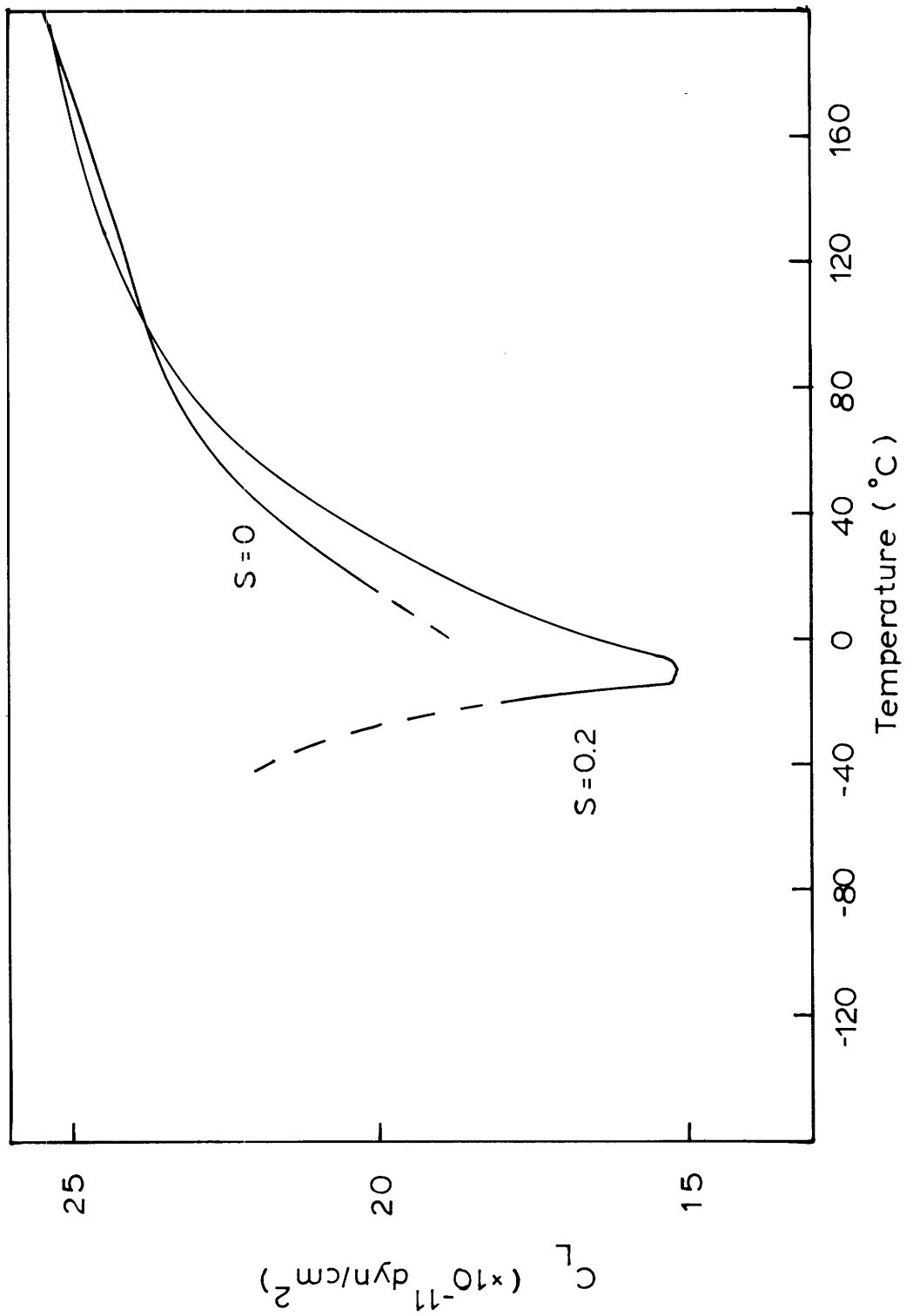


Figure 20a. The C_L elastic constant versus temperature. $H=0$.

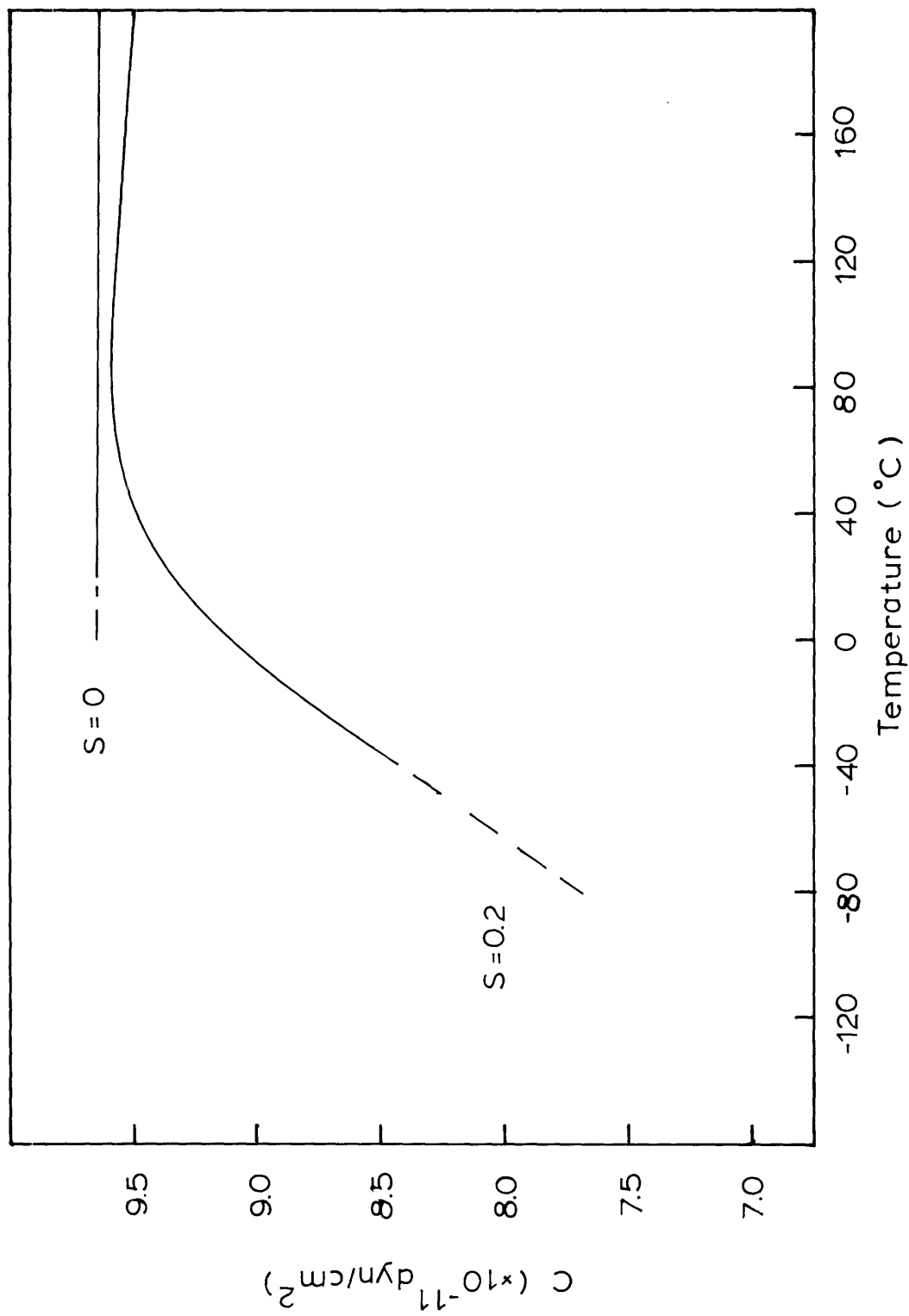


Figure 20b. The C elastic constant versus temperature. $H=0$.

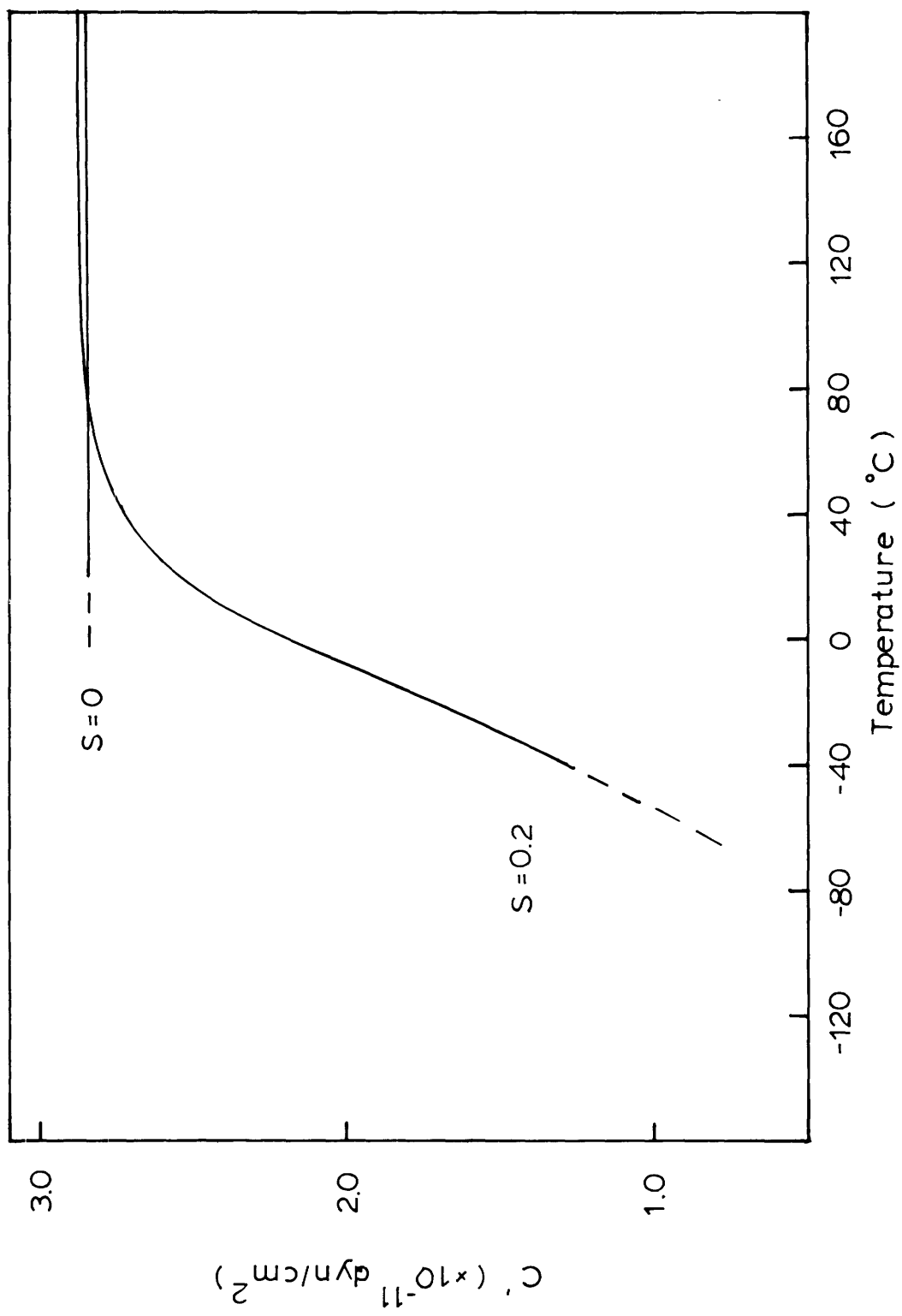


Figure 20c. The C' elastic constant versus temperature. H = 0.

The density for various degree of order was calculated from the molecular weight of 91.35 for the composition Fe-25.2a/oPt and the lattice parameters determined in Section 4.1. The correction for the change in length of the specimen due to thermal expansion was carried out as follows. Since the density ρ varies as $[\ell]^{-3}$ and the velocity $[\ell]$, ρV^2 varies as $[\ell]^{-1}$, we obtain

$$\rho V^2(T) = \frac{\rho_o (2\ell_o/\Delta t)^2}{1 + \int_{T_o}^T \alpha(T) dT} \quad (36)$$

In Equation (36), subscript o denotes quantities measured at room temperature, ℓ is the length of the specimen, Δt the round-trip traveling time of the sound wave and $\alpha(T)$ the thermal expansion coefficient. There is no published data on the thermal expansion coefficient as a function of order in Fe₃Pt. Measurement of the lattice parameter as a function of temperature for S = 1 by Herbeuval^[27] showed only less than 0.1% change over a range of 200° near room temperature. This small correction can be neglected considering that the error in the measurement could reach 1%. The thermal expansion measurement of Fe-28Pt by Sumiyama, et al showed a larger magnetic effect in the disordered state. The thermal expansion coefficient calculated from their data is shown in Figure 21 for both the ordered and the disordered states. The change in length still amounts to no more than 0.3% from the room temperature value in the temperature range we are interested in. Hence we shall neglect this correction.

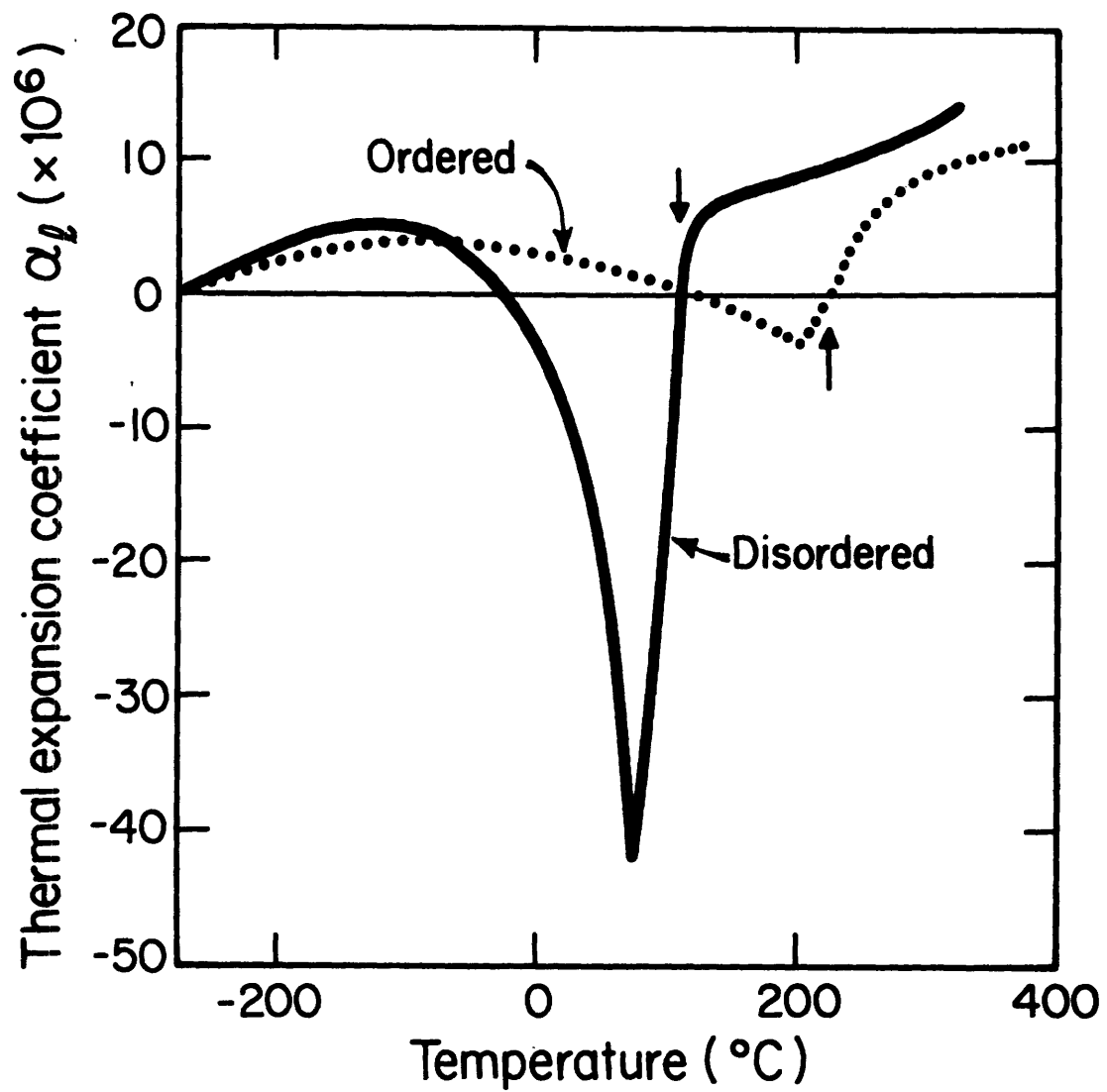


Figure 21. Temperature dependence of the thermal expansion coefficient in ordered and disordered Fe-28Pt.

4.4.2 Effect of an Applied External Field

The temperature dependence of the elastic constants C , C' and C_L for $S = 0.85$ are shown in Figure 22, where the dot-dashed and full curves correspond to the zero field and magnetically saturated states, respectively. The difference between these two curves is ascribed to the ΔE_λ effect due to domain wall motion and domain wall rotation (see Section 2.5.1). A ΔE_λ effect of the order of 3% is clearly noticeable in the C -mode. In the case of the C' -mode, a ΔE_λ effect could not be detected within the experimental accuracy. The C_L elastic constant shows the normal ΔE effect below T_c , i.e., the low field value is smaller than the high field value. However, a negative ΔE effect occurs in the transition region above T_c : the low field value is higher than the high field value. Such a behavior has been observed in Invar alloys [6,19,23] by various authors. All three modes of sound waves were measurable down to the lowest temperature at which the measurements could be made (see Section 3.4). This is in contrast to the observation of G.Hausch [23] that ultrasonic absorption in the C' mode increased rapidly below 0°C preventing further measurement below -40°C .

4.4.3 Elastic Constants as a Function of the Degree of Order

The temperature dependence of the elastic constants C , C' and C_L measured in an external field of 8 kilogauss are shown in Figures 23-25, for various states of atomic order. All three elastic constants display large magnetic contributions similar to the Fe-Ni alloys, [6] but are enhanced in magnitude. The change in the elastic constants are comparable to those reported for a disordered Fe-28a/oPt alloys. [23]

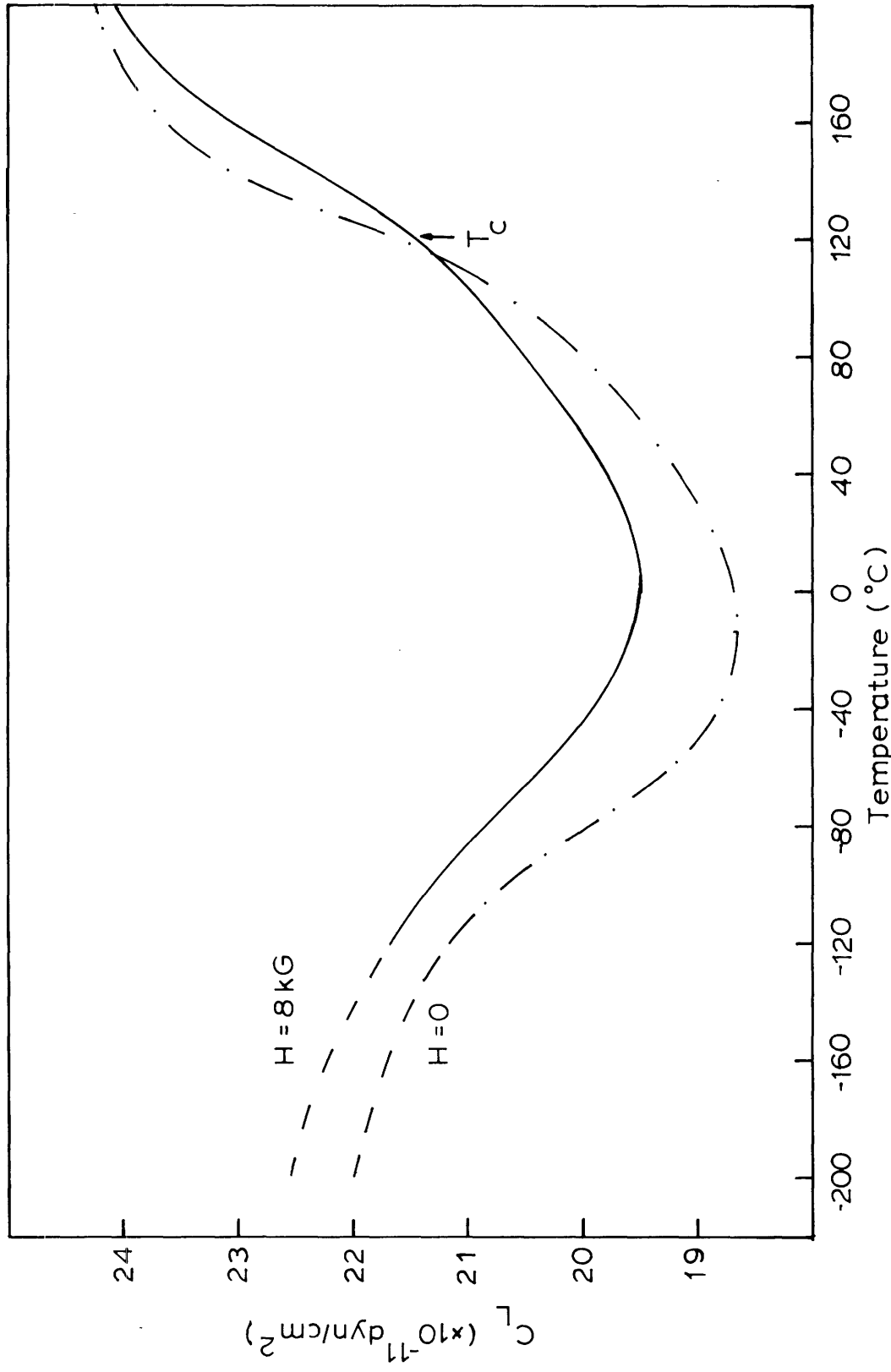


Figure 22a. The C_L elastic constant versus temperature. $S=0.85$.

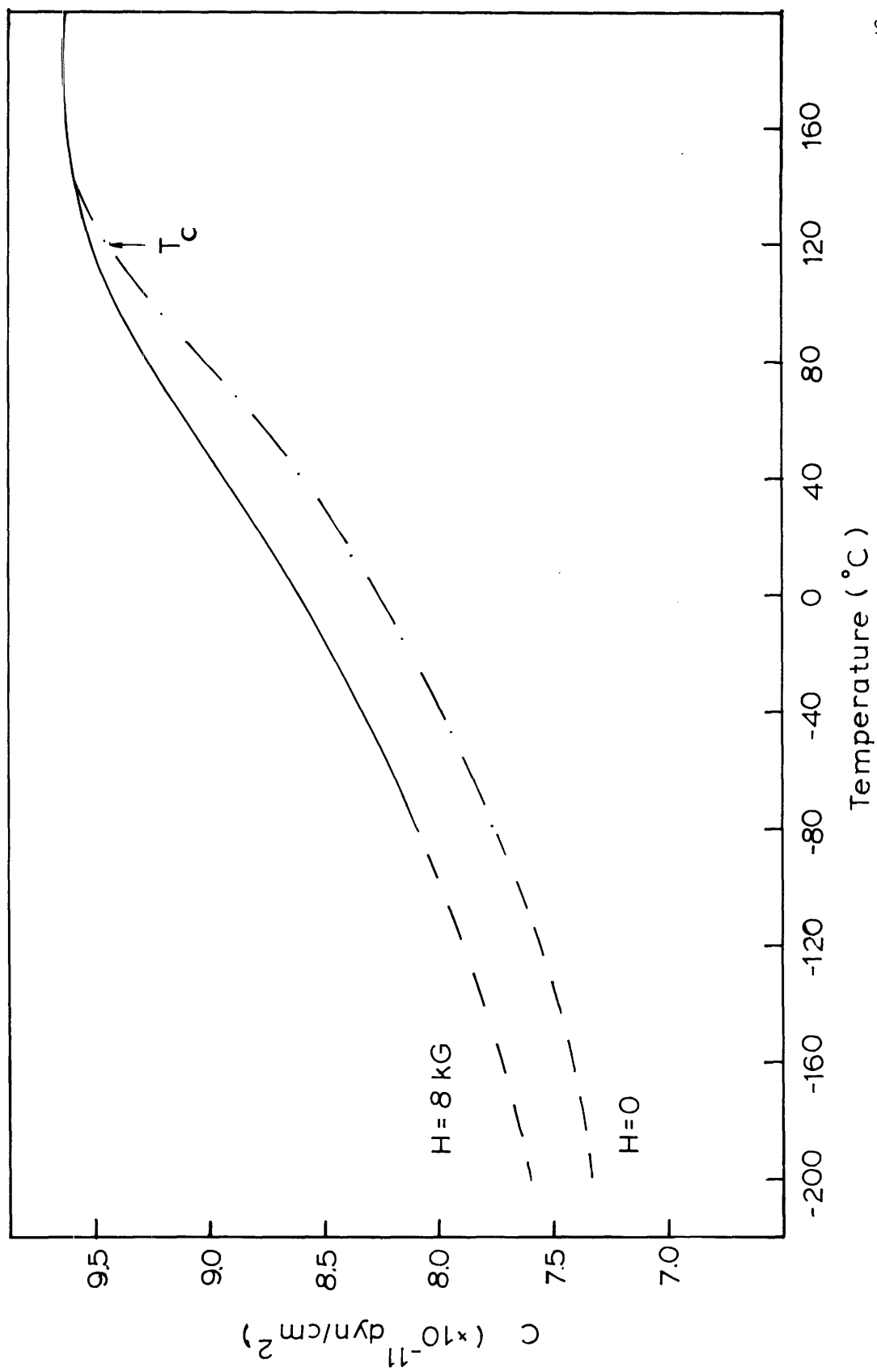


Figure 22b. The C elastic constant versus temperature. $S=0.85$.

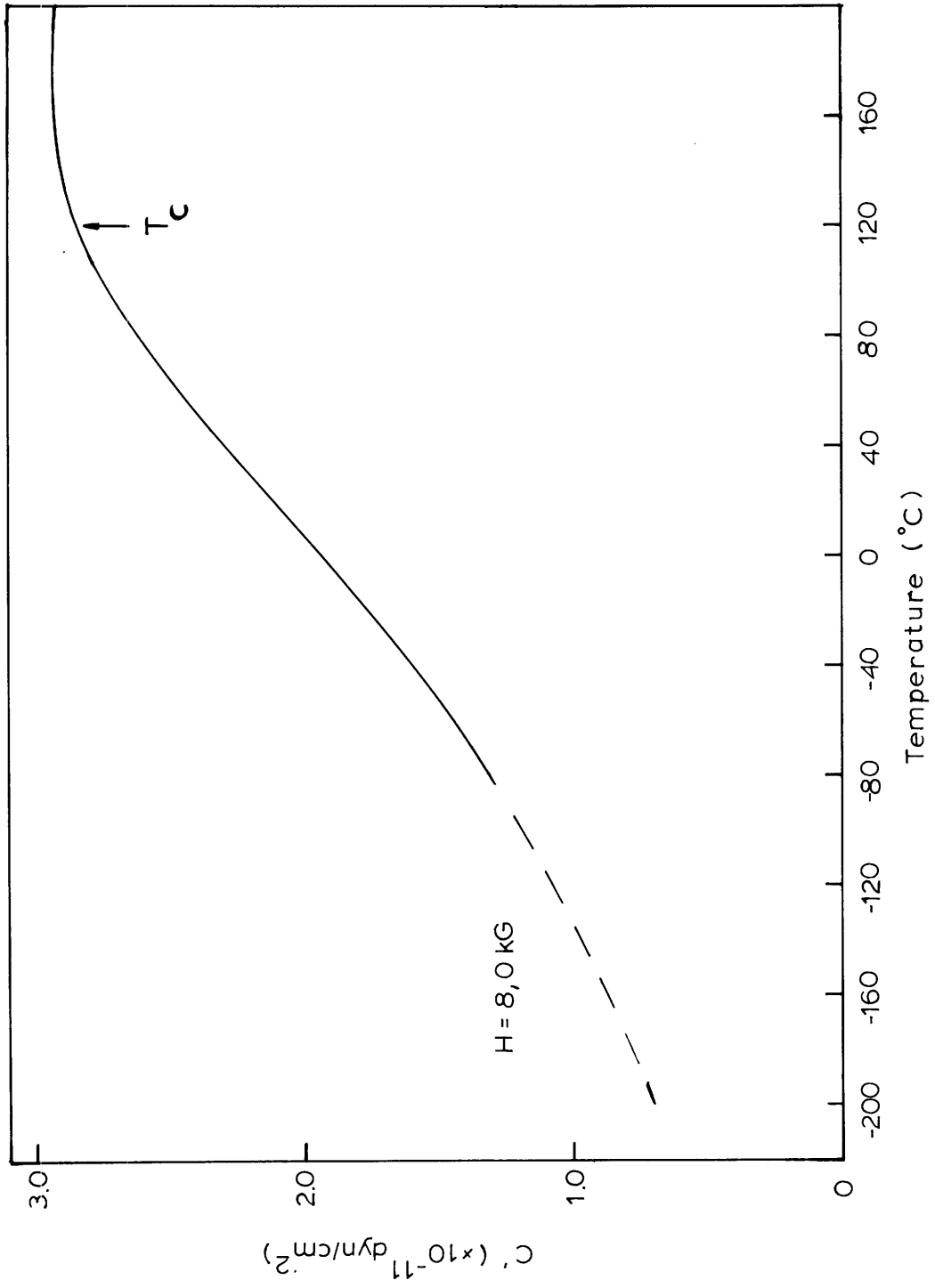


Figure 22c. The C' elastic constant versus temperature. $S=0.85$.

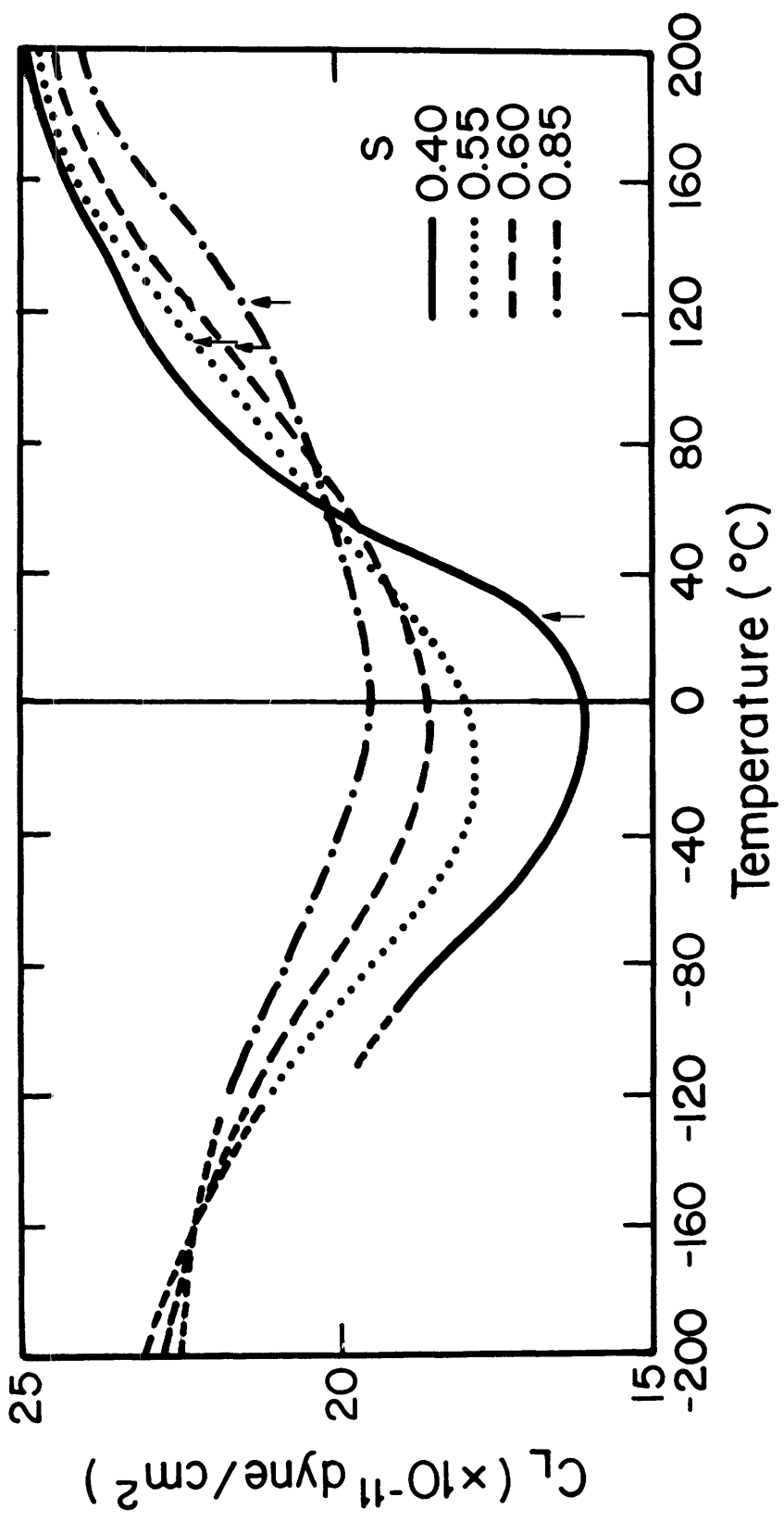


Figure 23a. Temperature dependence of the C_L elastic constant as a function of the degree of order S in Fe_3Pt . $H=8$ kG.

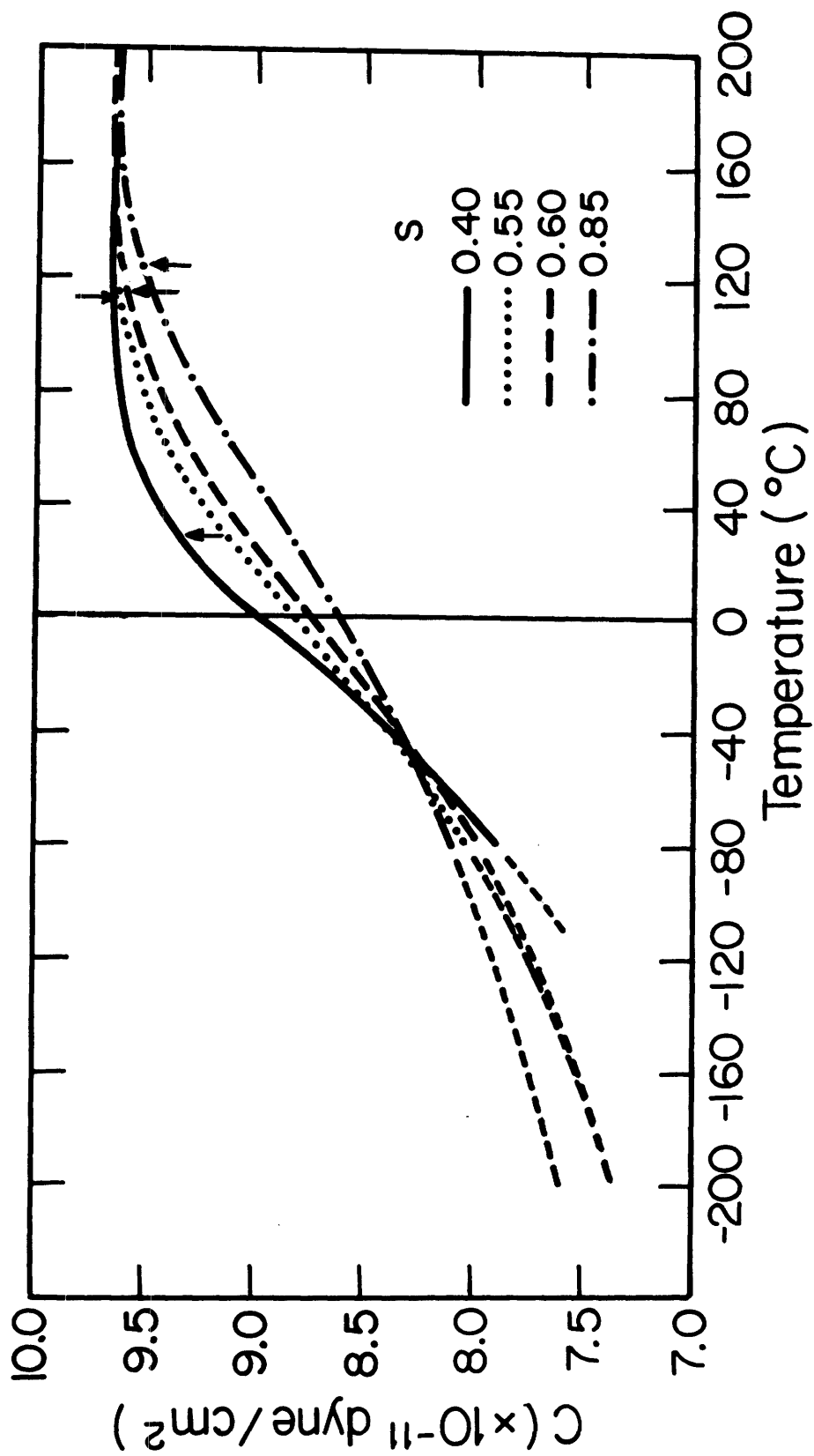


Figure 23b. Temperature dependence of the C elastic constant as a function of the degree of order S in Fe₃Pt. H=8 kG.

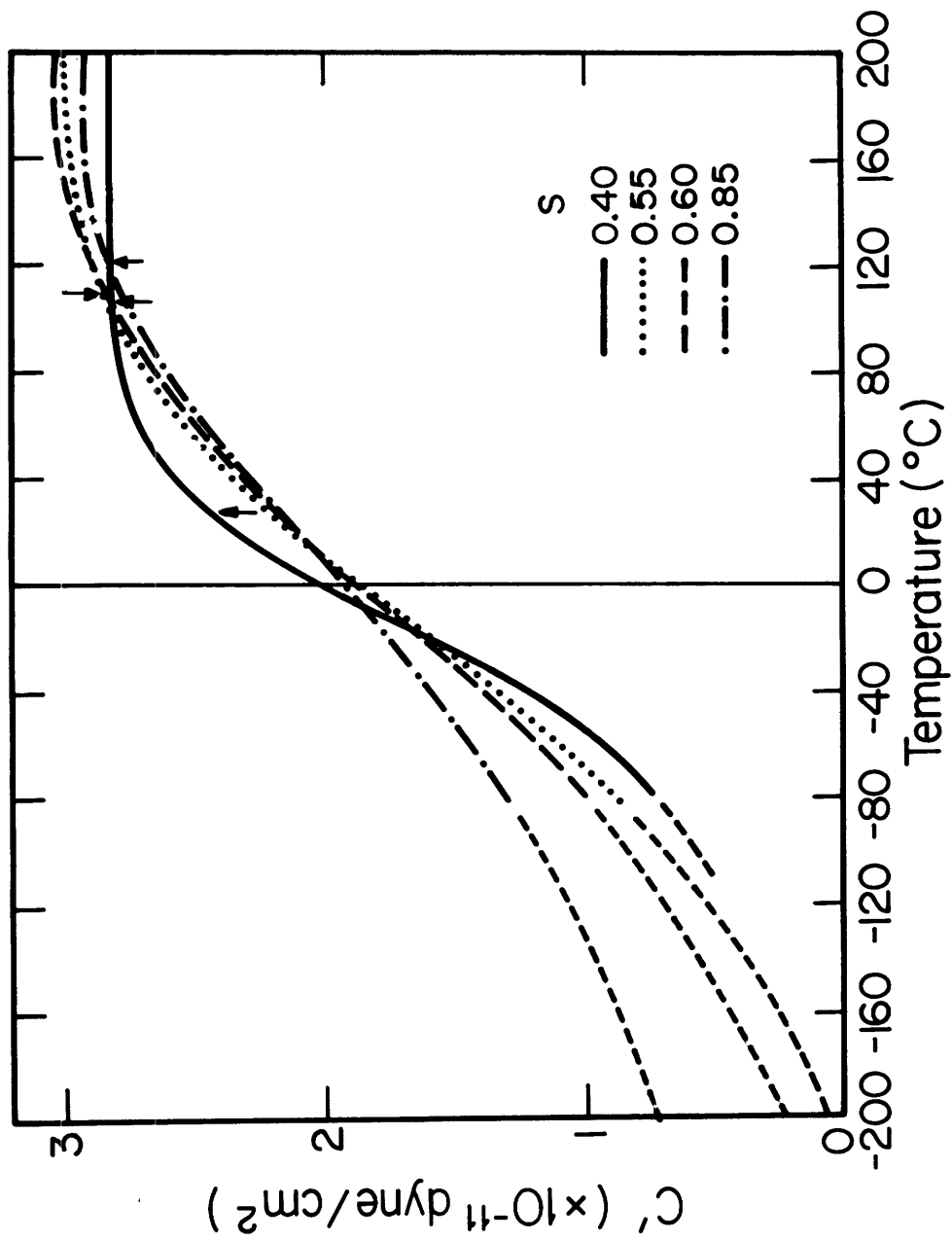


Figure 23c. Temperature dependence of the C' elastic constant as a function of the degree of order S in Fe_3Pt , $H=8$ kG.

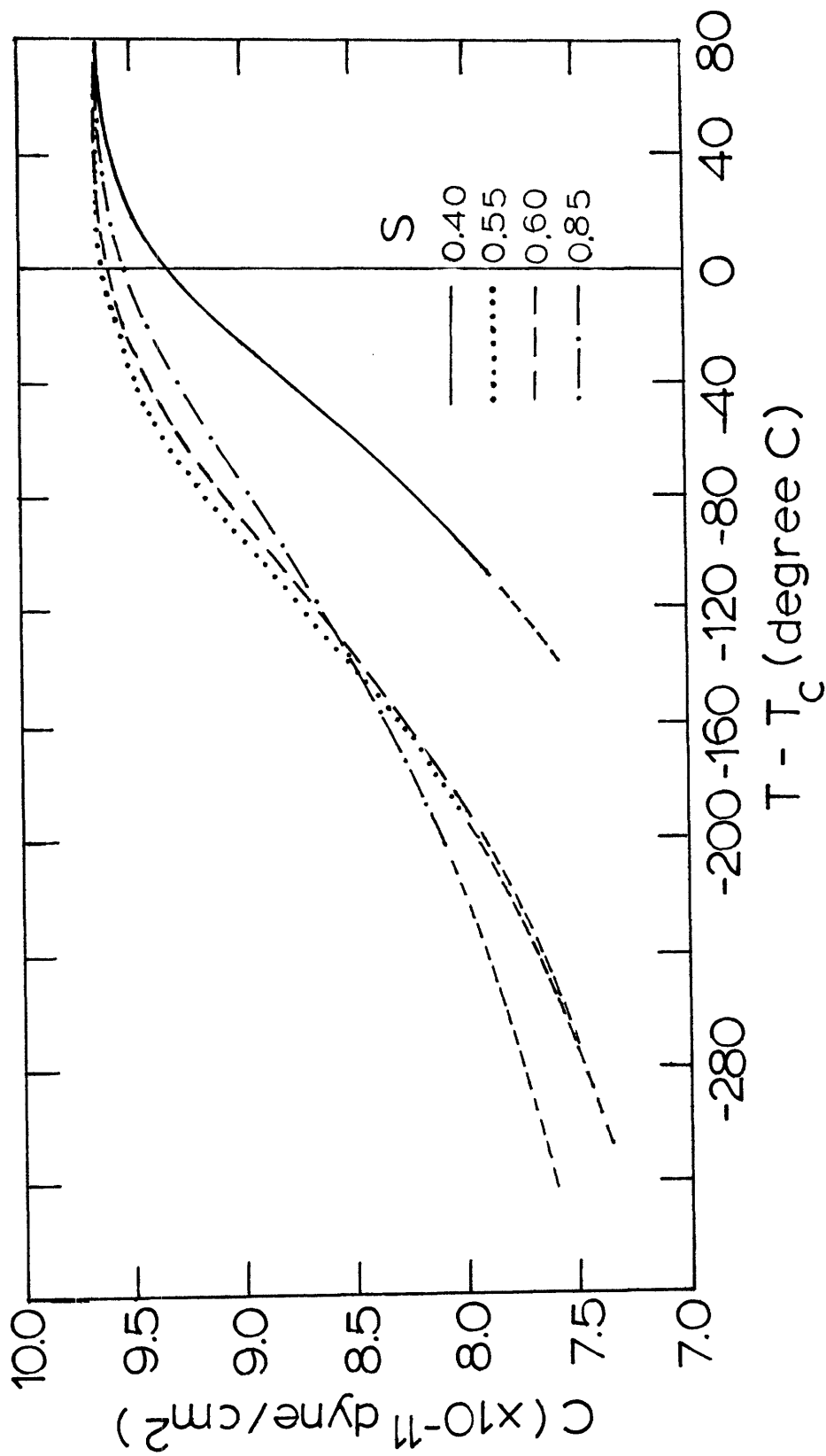


Figure 24. The C elastic constant versus $(T - T_c)$. $H = 8 \text{ kG}$.

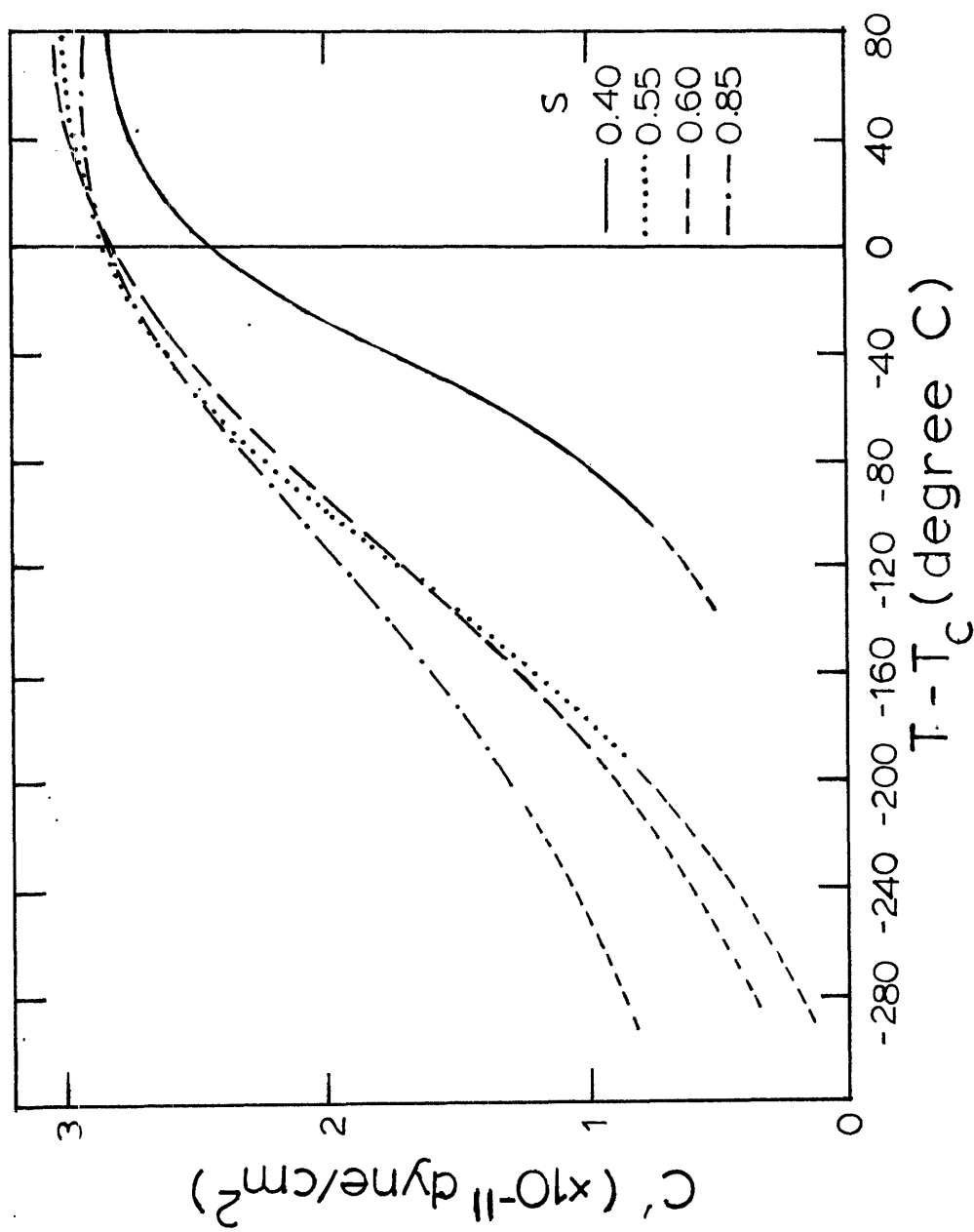


Figure 25. The C' elastic constant versus $(T - T_c)$. $H = 8$ kg.

A. The Shear Elastic Constants C and C'

At a fixed temperature in the paramagnetic region, there is no observable difference in the value of C between the various states of order. C', however, shows an increase from S = 0.85 to S = 0.60 after which it decreases as S is lowered. Below the Curie temperature, the shear constants decrease continuously with decreasing temperature. For small S, the rate at which C and C' decrease with temperature is more rapid than for large S. The curves cross near -50°C for C and near -15°C for C'. Above these points C and C' are larger for small S because Invar softening begins at a higher temperature in more highly ordered states. Below the crossover, C and C' are smaller for small S. This indicates a larger Invar effect in states of decreasing S. This observation is in agreement with the spontaneous magnetostriction measurements reported by Sumiyama, et al^[7] for a Fe-28a/oPt alloy. They found that the disordered state has a larger thermal expansion anomaly than the ordered state. Nakajima^[12] also reported that the linear magnetostriction decreased monotonically with increasing duration of ordering anneal.

According to the theory (Section 2.5.2), the magnetic contribution to C and C' are expected to obey the relations

$$-C'_m = K_1 (I/I_0)^2 \quad (11a)$$

$$-C_m = K_2 (I/I_0)^2 \quad (11b)$$

I/I_0 being the relative magnetization. Without available data on the temperature dependence of the magnetization in Fe_3Pt as a function of order, we used the magnetization measurements of an Fe-28Pt alloy in both ordered and disordered states by Sumiyama, et al^[7] and assumed that the dependence of the relative magnetization, I/I_0 , on the reduced temperatures, T/T_c in Fe_3Pt is the same as that in Fe-28a/oPt (Figure 26). We also made the assumption that states with $S \geq 0.5$ have the same dependence as the ordered Fe-28a/oPt alloy while those with $S < 0.5$ follow the dependence of the disordered Fe-28a/oPt alloy. Later analysis showed that changes in the quantities calculated are insensitive to the S value at which this division is assumed.

The exchange contribution to the elastic constants C and C' in the ferromagnetic region were calculated by subtracting the lattice contribution, determined by extrapolation from the paramagnetic regions, from the experimental values. Plots of $-C_m$ and $-C_m'$ versus $(I/I_0)^2$ are shown in Figure 27. Least square fits to the points in the range $(I/I_0)^2 = 0.4$ and 0.7 gave the slopes K_1 and K_2 in Equations (11a) and (11b). From K_1 and K_2 , one can calculate the first and second derivatives of the first nearest neighbor exchange integral, J_1' and J_1'' , from the equations.

$$J_1' = (2K_1 - K_2) / N_V z_1 r_1 \quad (12a)$$

$$J_1'' = (7K_2 - 6K_1) / N_V z_1 r_1^2 \quad (12b)$$

where $N_V z_1 = 9.11 \times 10^{23} \text{ cm}^{-3}$ and r_1 is the first nearest neighbor separation. The values of K_1 , K_2 , J_1' and J_1'' as a function of S are listed in Table 4. The error bounds are related to the inaccuracy associated with determining T_c from the specific heat measurements. The value of J_1' increases from $17.36 \times 10^{-6} \text{ dyn}$ in $S = 0.85$ to $21.09 \times 10^{-6} \text{ dyn}$ in $S = 0.6$, $23.04 \times 10^{-6} \text{ dyn}$ in $S = 0.55$ and $22.08 \times 10^{-6} \text{ dyn}$ in $S = 0.4$. Compared to a value of 16.65×10^{-6} in disordered Fe-28a/oPt^[23] and 7.1×10^{-6} in Fe-35%Ni,^[6] Fe₃Pt clearly exhibits the largest Invar effect. We shall discuss the physical meaning of the variation in J' in a later section.

Using K_1 and K_2 derived above, the values of C and C' below -80° were calculated using Eq'n (11). The reduction in the C' elastic constant is especially large in the partially ordered states. At liquid nitrogen temperature, C' is only $0.06 \times 10^{11} \text{ dyn/cm}^2$ for $S = 0.55$ compared to a value of $3 \times 10^{11} \text{ dyn/cm}^2$ in the paramagnetic region. The maximum reduction in the C elastic constant amounts to 30%.

An important factor which relates to the magnitude of C' is the anisotropy ratio, A , which is the ratio of the two shear elastic constants, C and C' . C' measures the resistance to shear deformation on $\{110\}\langle 110\rangle$, which is close to the direction of the lattice invariant deformation in the $\gamma \rightarrow \alpha$ transformation in Fe₃Pt. A high value of A indicates a small C' elastic constant, meaning that shear deformation along this direction can occur more readily due to reduced resistance. The temperature dependence of A as a function of S are shown in Figure 28. The magnetically induced reduction of the C' elastic constant is so

Table 4. Parameters associated with the Invar Effect in Fe₃Pt as a function of the degree of order S

S	T _c (°C)	a ₀ (Å)	ρ ₀ (g/cc)	K ₁ ⁻¹¹ (x10 ⁻¹¹)	K ₂ ⁻¹¹ (x10 ⁻¹¹)	J ₆ ¹ (x10 ⁶ dynes)	J ₁₂ ¹ (x10 ⁻² dyn/cm)
0.85	122	3.7325	11.67	3.75	3.33	17.36±1.5	1.24±0.70
0.60	107	3.7275	11.72	4.68	4.29	21.09±1.0	3.12±0.50
0.55	112	3.7267	11.72	4.88	4.22	23.04±1.0	0.43±0.10
0.40	27	3.7250	11.74	4.63	3.96	22.08±2.0	-0.09±0.06

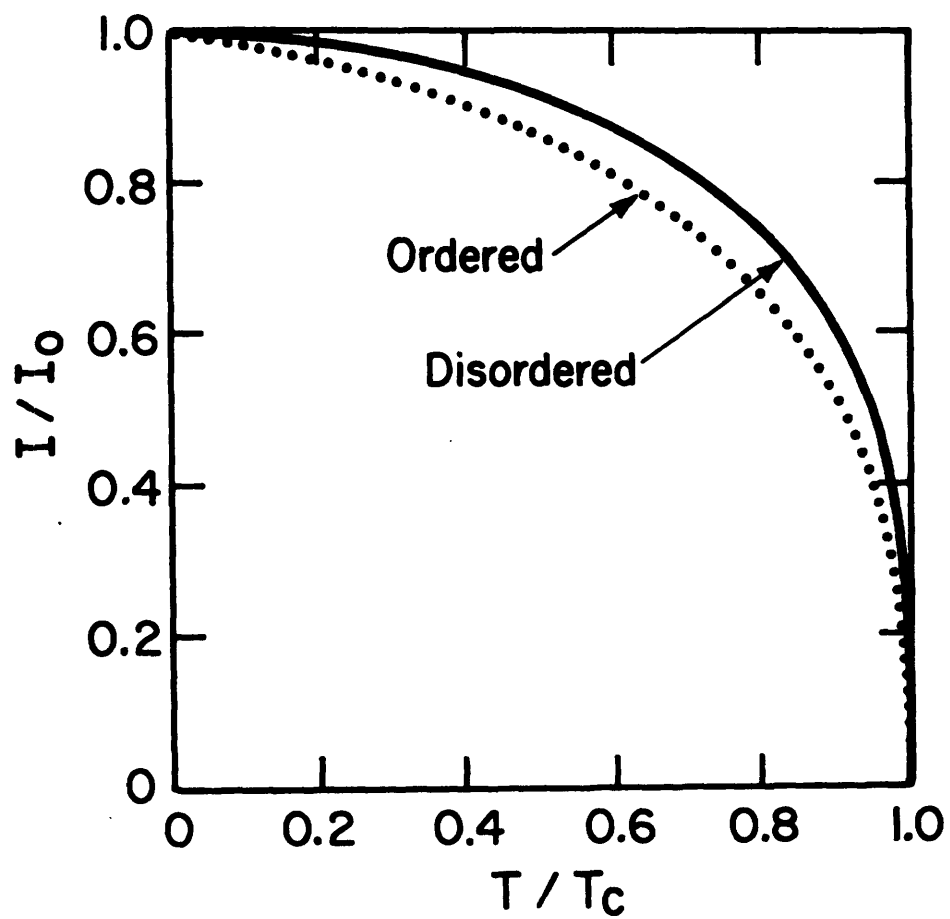


Figure 26. Functional dependence of the reduced magnetization, I/I_0 , on the reduced temperature, T/T_c , in ordered and disordered Fe_3Pt .

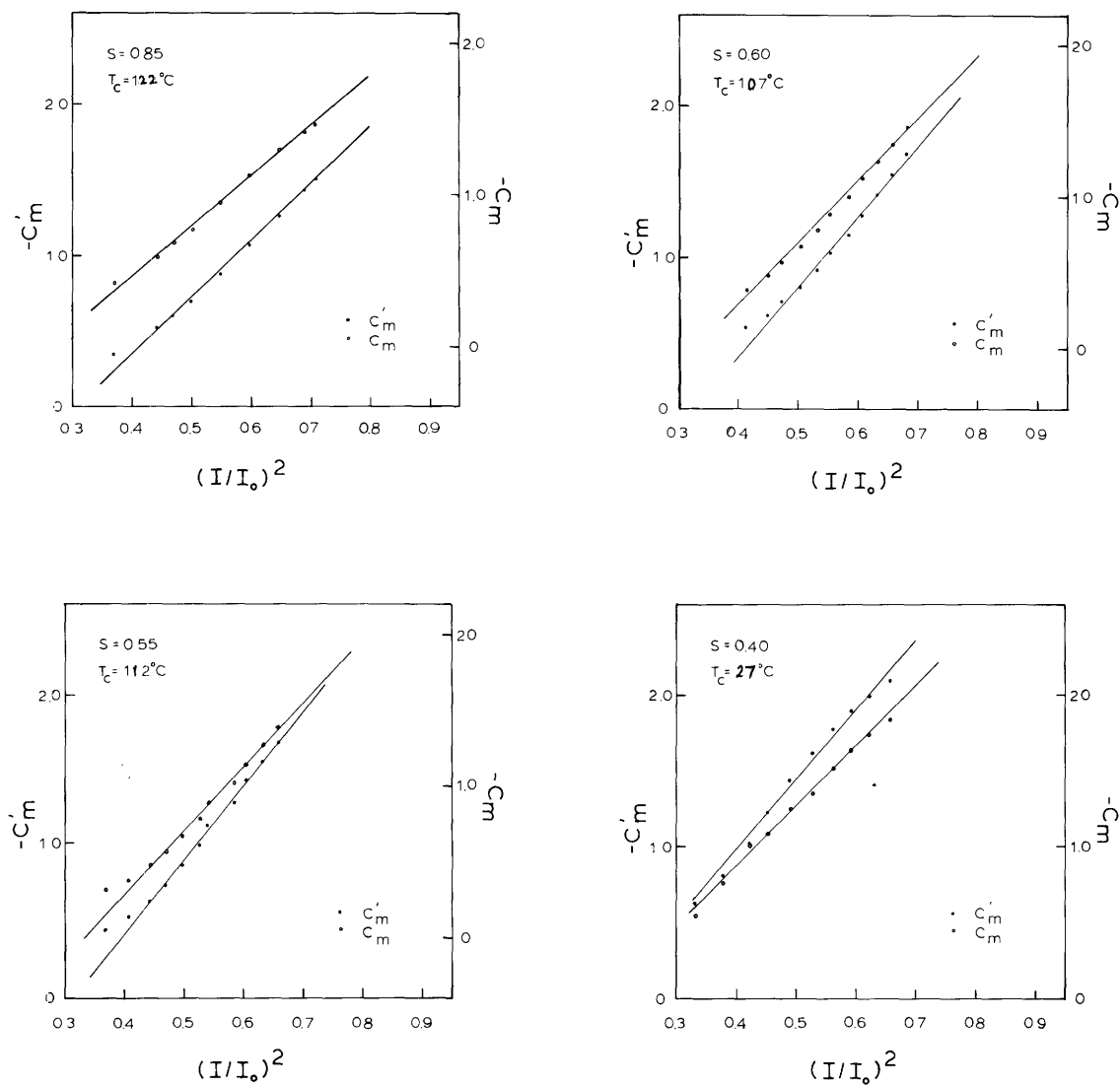


Figure 27. Magnetic contribution, C_m and C'_m , versus reduced magnetization squared. (C_m, C'_m in unit of 10^{11} dyn/cm²)

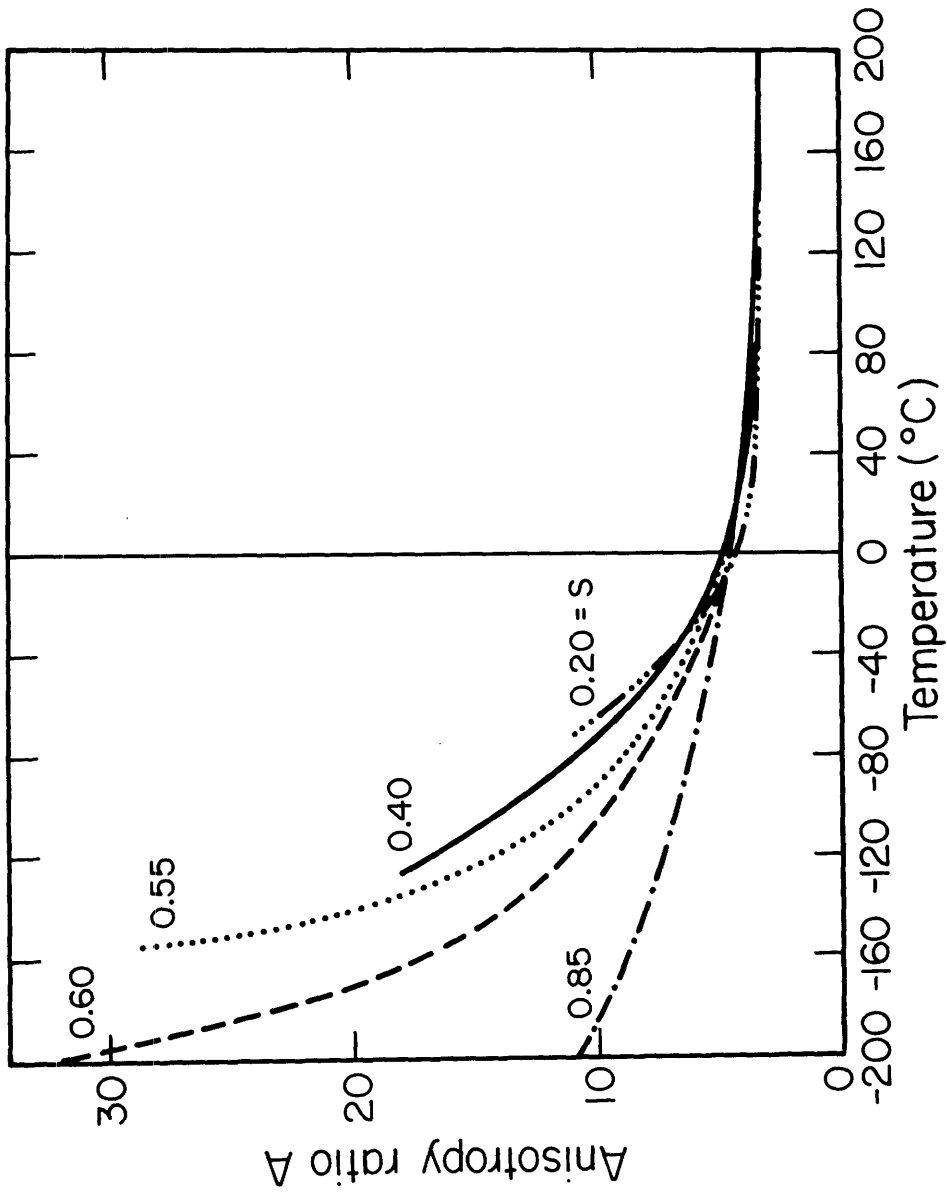


Figure 28. Temperature dependence of the anisotropy ratio, A, as a function of the degree of order S in Fe₃Pt.

large that A increases from a value of 4 at room temperature to 32 at -196°C for $S = 0.60$. This is larger than a value of 20 in disordered Fe-28a/oPt and 6 in Fe-35%Ni at -196°C .

B. The C_L Elastic Constant

For a given degree of order S , C_L shows a magnetically induced decrease starting at temperatures high above T_c , goes through a minimum below T_c and rises again at lower temperatures. In the paramagnetic region, C_L decreases with increasing degree of order at a fixed temperature. The size of the minimum below T_c also decreases with increasing S . The curves cross and below the cross-over point C_L is smaller for small S . At lower temperatures, extrapolations of the experimental curves indicate another cross-over around -160°C below which C_L for small S is again larger than that of the higher ordered states. The differences, however, are small. The minimum, occurring at approximately 0°C , does not shift significantly with ordering. This is different from the result of an Fe-28a/oPt alloy, [23] in which the minimum in C_L shifted from 175°C in the ordered state to 50°C in the disordered state, and remained approximately 50 degrees below T_c . The magnetic contribution to the elastic constant C_L is given by

$$-C_{L,m} = (-3K_1 + 4K_2) (I/I_0)^2 + \frac{C_L^2}{9} \left(\frac{\partial \omega}{\partial H} \right) \left(\frac{\partial I}{\partial H} \right)^{-1} \quad (37)$$

where the first term is the exchange contribution and the second is the Döring or ΔE_{ω} term. Using $\partial \omega / \partial H = 11 \times 10^{-9} \text{ Oe}^{-1}$ and $\partial I / \partial H = 2.5 \times 10^{-3} \text{ Gauss/Oe}$, [7] we calculated at room temperature that $C_{L,m} = -1.33 \times 10^{11}$,

-1.86×10^{-11} , -1.30×10^{11} and -0.94×10^{11} dynes/cm² for $S = 0.85$, 0.60 , 0.55 and 0.4 , respectively. These values are far too small to account for the observed minimum. The anomalous decrease above T_c and the magnitude of the minimum below T_c had been discussed in detail by Hausch and Warlimont [6,23] (see also Section 2.1). No satisfactory explanation has been advanced to this date.

4.4.4 Average Moduli as a Function of the Degree of Order

The average Young's modulus E , shear modulus G and bulk modulus B , suitable for describing polycrystalline specimens, were calculated from the single crystal elastic constants using the VRH method described in Section 3.5. The values of G , E , B and Poisson's ratio ν are tabulated in Tables 5-10 and plotted in Figures 29-32.

Both the shear and the Young's moduli behave similarly to the shear elastic constants C and C' . Below T_c , they decrease continuously with decreasing temperature. Their values are smaller for small S in the low temperature region. For $S = 0.55$, the shear modulus decreases from a value of 6×10^{11} dyn/cm² in the paramagnetic region to 2.25×10^{11} dyn/cm² at -196°C , a three-fold reduction. Decrease of similar magnitude is also observed in the Young's modulus. The bulk modulus and the Poisson's ratio are largely determined by the C_L elastic constant. Hence their behavior is similar to C_L , with the decrease beginning above T_c , going through a minimum below T_c and rising again at lower temperatures.

In order to reproduce the elastic conditions of the austenite under which changes in the growth behavior of the martensite were observed, we have followed the heat treatment of Kajiwara and Owen. [91]

They were 5 hours, 1 hour and 10 minutes at 650°C resulting in S of 0.6, 0.4 and 0.2, respectively. The disordered state was produced by quenching from 900°C into water without breaking the capsule. The M_S temperatures determined from disk specimens of the present alloy (grain size $\sim 4\mu\text{m}$) were lower than that of the polycrystalline specimens (grain size ~ 100 microns) of Kajiwara and Owen. For example, for the heat treatment of 10 minutes at 650°C, a M_S temperature of -74°C was obtained in the present alloy versus -45°C in Kajiwara's specimen. The effect of grain size on the M_S temperature has not been studied in Fe_3Pt . The cooling rates between the two sets of experiments are also probably different. Since most investigations on the transformation behavior in Fe_3Pt used polycrystalline specimens with grain size similar to Kajiwara's specimens, we shall use the M_S temperatures determined from his specimens as being representative of Fe_3Pt alloy with a certain degree of order S. The values of E, G, B and ν at M_S as a function of order are listed in Table 11 together with the single crystal elastic constants C, C and C_L . Were we to use the M_S temperature determined from the present alloy, conditions would be even more favorable for thermoelastic growth because of the greater softening in the C and C' elastic constants at a lower M_S temperature.

4.5 Variation of Exchange Integral with Interatomic Distance

In terms of the Heisenberg model, the ferromagnetic transition is due to quantum mechanical exchange forces acting between electrons in neighboring atoms. As two atoms are brought near to each other from a distance, this force causes electron spins in the two atoms to become

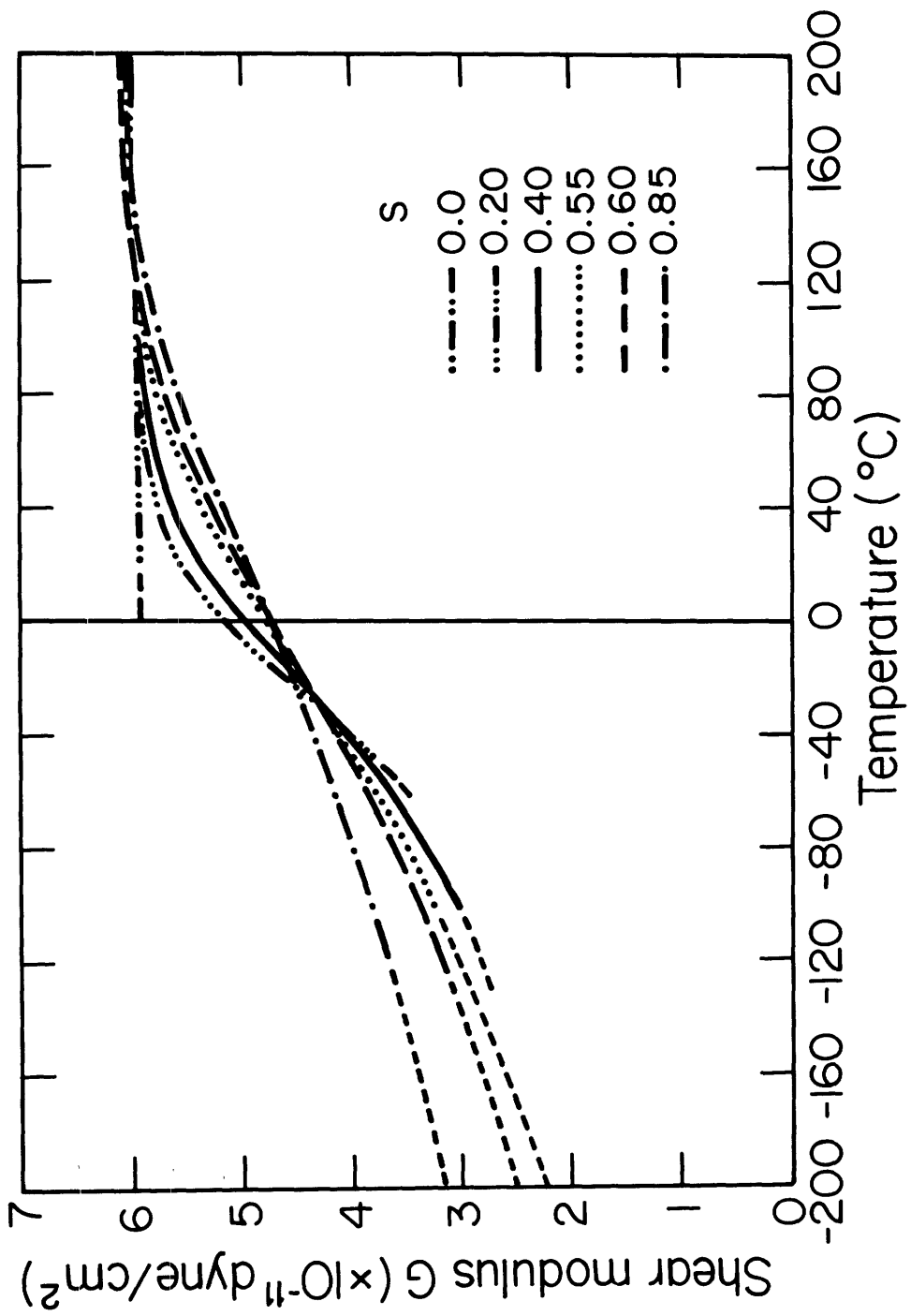


Figure 29. Temperature dependence of the average shear modulus, G , as a function of the degree of order S in Fe_3Pt .

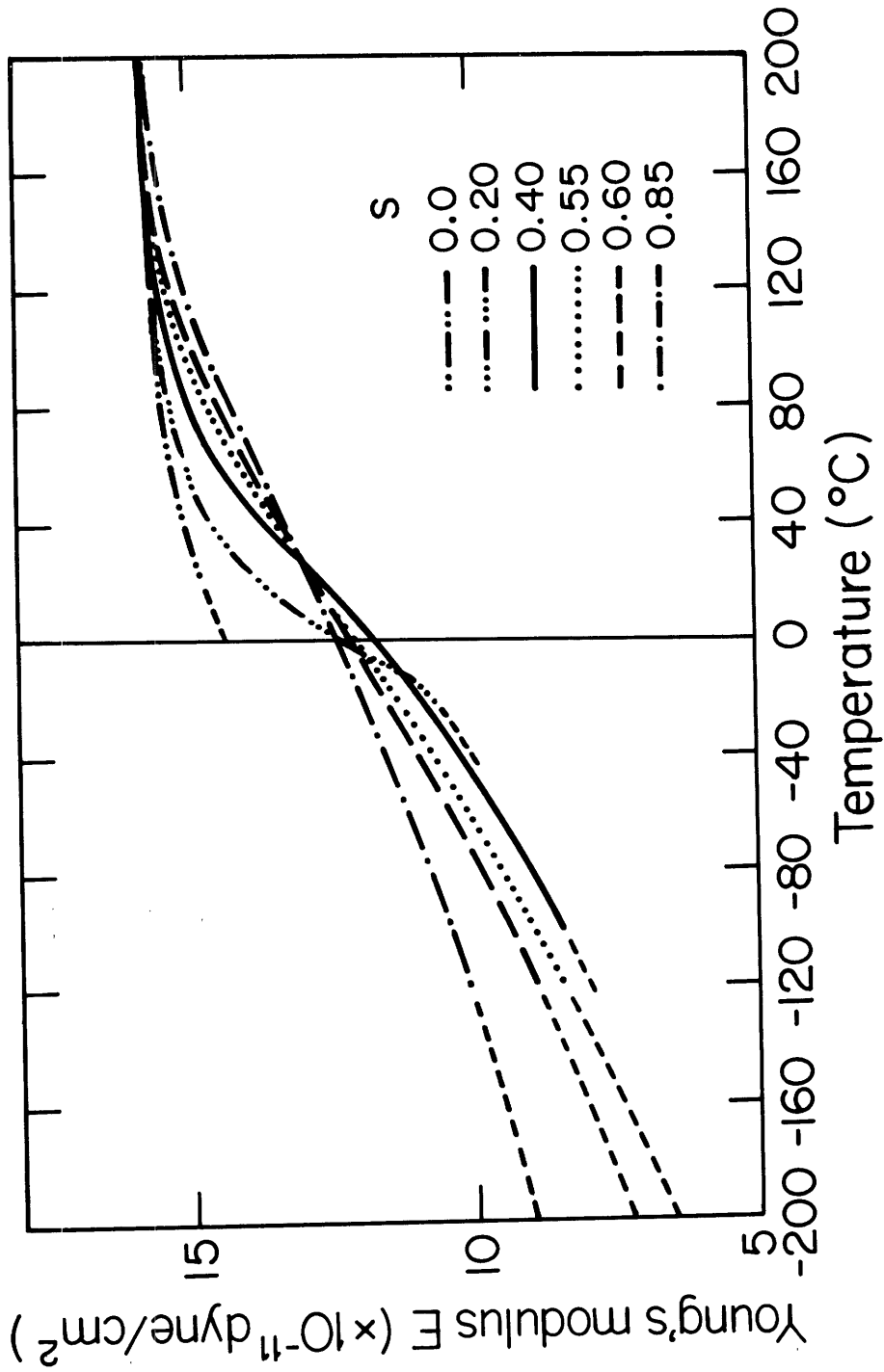


Figure 30. Temperature dependence of the Young's modulus, E , as a function of the degree of order S in Fe₃Pt.

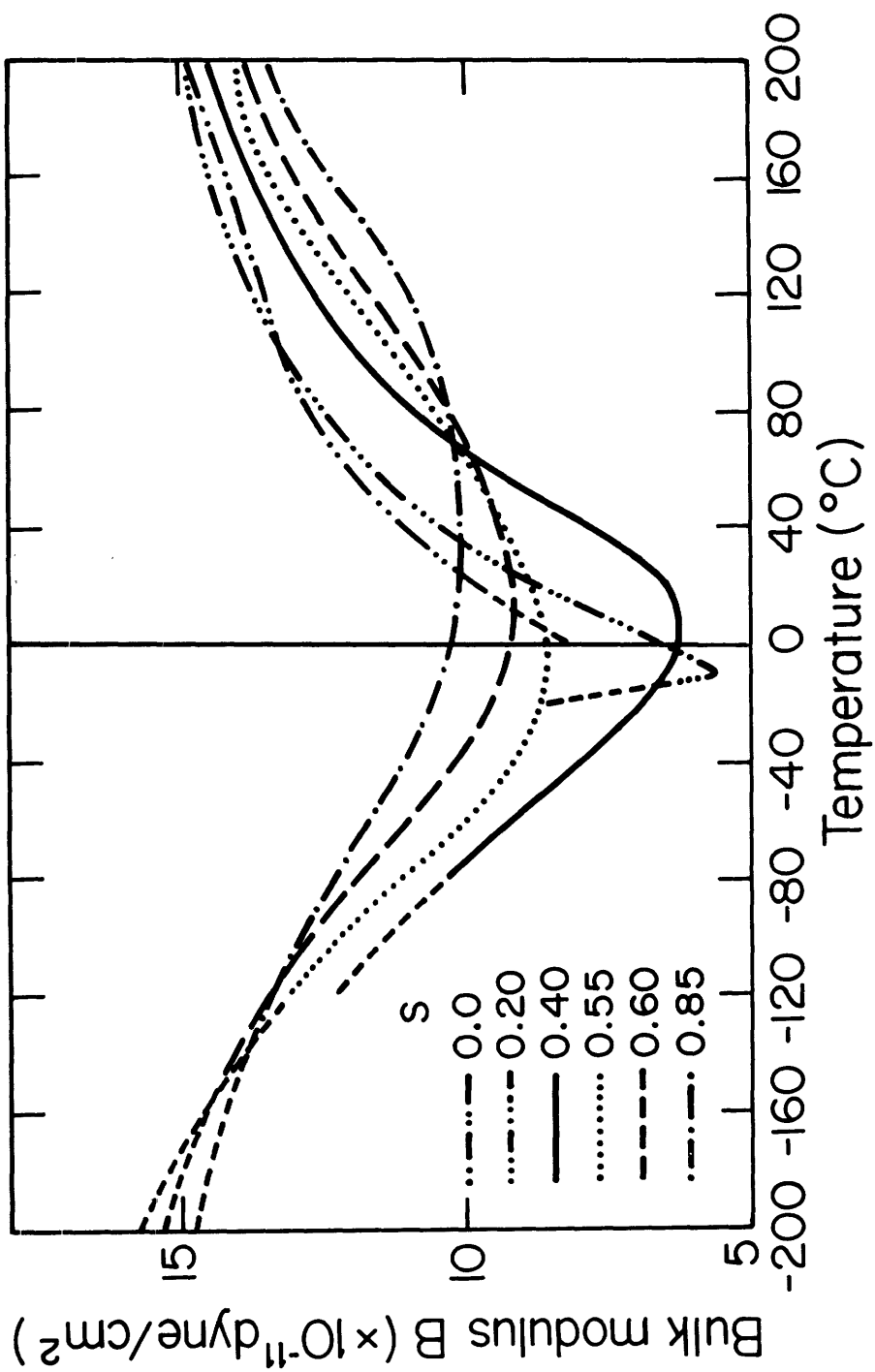


Figure 31. Temperature dependence of the bulk modulus, B , as a function of the degree of order S in Fe_3Pt .

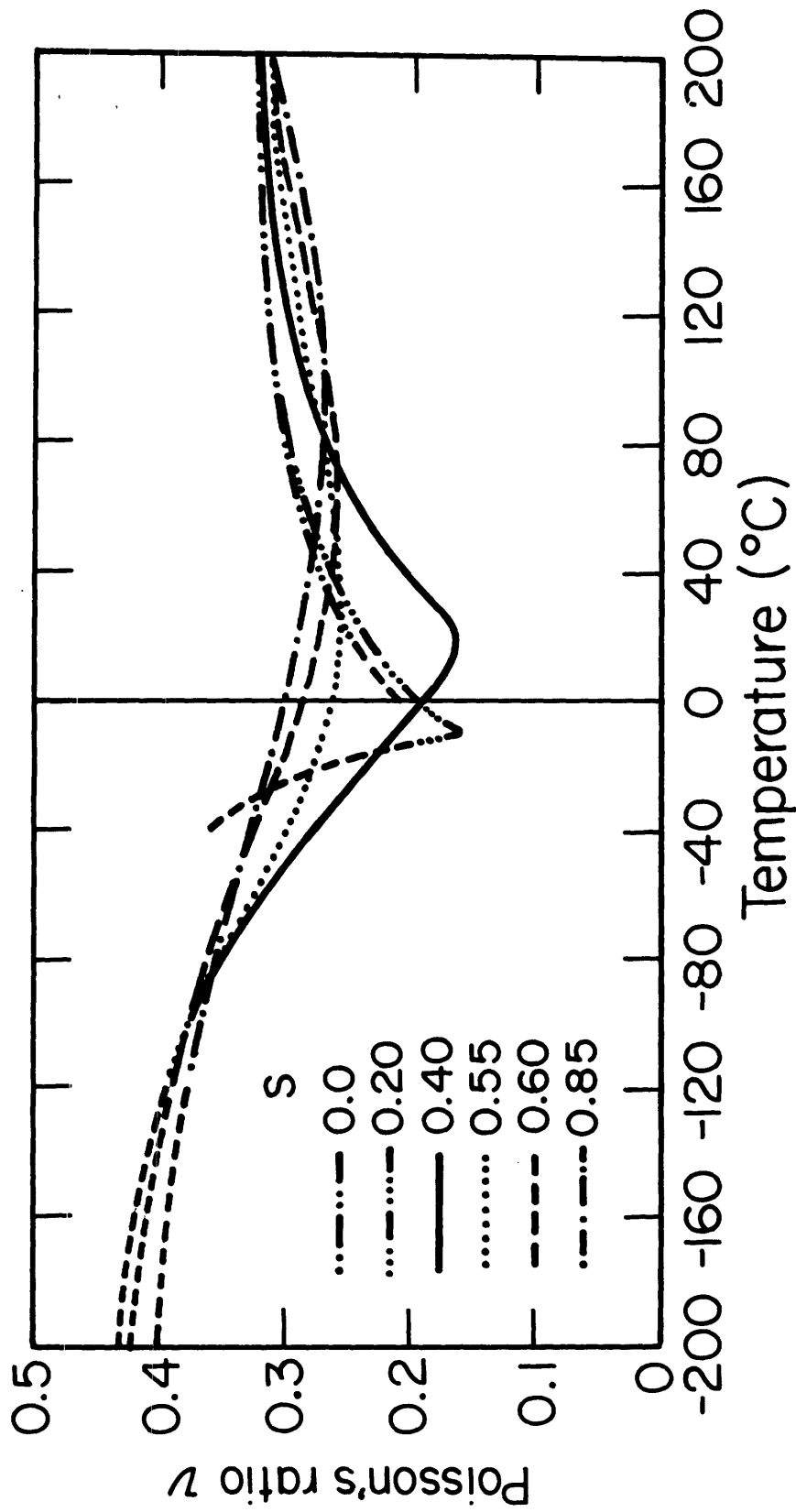


Figure 32. Temperature dependence of the Poisson's ratio, ν , as a function of the degree of order S in Fe_3Pt .

Table 5. Elastic moduli as a function of temperature. $S=0.85$.

		H=8 kG		$T_c=122^\circ\text{C}$		(modulus in units of 10^{11} dyn/cm ²)		
T ($^\circ\text{C}$)	C_L	C	C'	B	G	E	ν	A
200	24.05	9.61	2.92	13.47	5.97	15.62	0.31	3.29
180	23.67	9.63	2.93	13.06	5.99	15.59	0.30	3.29
160	23.00	9.64	2.94	12.38	6.00	15.50	0.29	3.28
150	22.55	9.61	2.94	11.96	6.03	15.48	0.28	3.30
140	22.10	9.61	2.91	11.52	5.97	15.26	0.28	3.30
120	21.37	9.50	2.85	10.92	5.88	14.95	0.27	3.33
100	20.87	9.38	2.76	10.57	5.76	14.62	0.27	3.40
80	20.47	9.26	2.62	10.34	5.60	14.23	0.27	3.53
60	20.10	9.10	2.46	10.18	5.41	13.79	0.27	3.70
40	19.80	8.94	2.23	10.12	5.16	13.22	0.28	4.01
20	19.55	8.77	2.11	10.08	4.99	12.85	0.29	4.16
0	19.50	8.60	1.93	10.26	4.77	12.39	0.30	4.46
-20	19.65	8.44	1.75	10.63	4.55	11.94	0.31	4.82
-40	19.92	8.34	1.58	11.05	4.36	11.55	0.32	5.28
-60	20.35	8.20	1.44	11.67	4.17	11.19	0.34	5.69
-80	20.85	8.09	1.30	12.33	4.00	10.82	0.35	6.22
-100	21.33	7.99*	1.18*	12.95	3.84	10.48	0.36	6.77
-120	21.72	7.89*	1.06*	13.48	3.68	10.12	0.38	7.44
-140	22.02*	7.81*	0.97*	13.89	3.56	9.83	0.38	8.05
-160	22.23*	7.76*	0.90*	14.17	3.47	9.61	0.39	8.62
-180	22.40*	7.67*	0.81*	14.46	3.34	9.30	0.39	9.47
-200	22.53*	7.59*	0.70*	14.71	3.19	8.91	0.40	10.84

* extrapolation

Table 6. Elastic moduli as a function of temperature. $S=0.60$. 119

T ($^{\circ}\text{C}$)	H=8 kG $T_c=107^{\circ}\text{C}$ (modulus in units of 10^{11} dyn/cm 2)							
	C_L	C	C'	B	G	E	ν	A
200	24.40	9.65	3.04	13.74	6.08	15.90	0.31	3.17
180	24.30	9.66	3.04	13.63	6.09	15.90	0.31	3.18
160	23.70	9.67	3.03	13.02	6.08	15.79	0.30	3.19
140	23.00	9.65	2.99	12.35	6.04	15.58	0.29	3.23
120	22.25	9.61	2.91	11.67	5.97	15.29	0.28	3.30
100	21.35	9.54	2.79	10.88	5.84	14.87	0.27	3.42
80	20.60	9.45	2.65	10.27	5.70	14.42	0.26	3.57
60	20.00	9.32	2.50	9.85	5.52	13.96	0.26	3.73
40	19.30	9.15	2.32	9.38	5.31	13.40	0.26	3.94
20	18.80	8.96	2.12	9.13	5.07	12.83	0.27	4.23
0	18.50	8.75	1.89	9.12	4.79	12.22	0.28	4.63
-10	18.50	8.63	1.76	9.28	4.63	11.90	0.29	4.90
-20	18.55	8.75	1.62	9.48	4.46	11.56	0.30	5.27
-40	18.98	8.33	1.36	10.20	4.14	10.93	0.32	6.13
-60	19.50	8.15	1.17	10.96	3.88	10.42	0.34	6.97
-80	20.15	7.98	1.00	11.84	3.65	9.92	0.36	7.98
-100	20.85	7.83*	0.84*	12.74	3.42	9.42	0.38	9.32
-120	21.37	7.70*	0.69*	13.44	3.21	8.92	0.39	11.16
-140	21.82*	7.60*	0.57*	14.03	3.03	8.49	0.40	13.33
-180	22.50*	7.43*	0.33*	14.96	2.68	7.59	0.42	22.52

Table 7. Elastic moduli as a function of temperature. S=0.55.

T (°C)	H=8 kG T _c =112°C (modulus in units of 10 ¹¹ dyn/cm ²)							
	C _L	C	C'	B	G	E	ν	A
200	24.70	9.61	3.00	14.09	6.04	15.85	0.31	3.20
180	24.48	9.63	2.98	13.85	6.04	15.83	0.31	3.23
160	24.10	9.64	2.98	13.47	6.03	15.74	0.31	3.23
140	23.50	9.65	2.94	12.87	6.01	15.59	0.30	3.28
130	23.15	9.64	2.92	12.54	5.99	15.49	0.29	3.30
120	22.70	9.63	2.89	12.11	5.96	15.35	0.29	3.33
100	21.80	9.58	2.81	11.28	5.88	15.02	0.28	3.41
80	21.00	9.51	2.70	10.59	5.76	14.63	0.27	3.52
60	20.28	9.39	2.55	10.04	5.59	14.15	0.27	3.68
40	19.53	9.24	2.36	9.50	5.38	13.57	0.26	3.92
20	18.70	9.05	2.12	8.94	5.10	12.86	0.26	4.27
0	17.95	8.84	1.86	8.49	4.79	12.10	0.26	4.75
-20	17.70	8.60	1.56	8.58	4.42	11.33	0.28	5.51
-40	17.95	8.36	1.31	9.15	4.10	10.69	0.30	6.38
-60	18.55	8.20	1.09	9.99	3.81	10.15	0.33	7.52
-80	19.42	8.05	0.91	11.07	3.57	9.67	0.35	8.85
-100	20.30	7.90*	0.71*	12.16	3.29	9.07	0.38	11.13
-120	21.05	7.76*	0.54*	13.11	3.05	8.48	0.39	14.37
-140	21.70*	7.64*	0.39*	13.93	2.82	7.93	0.41	19.59

* extrapolation

Table 8. Elastic moduli as a function of temperature. $S=0.40$.

H=8 kG $T_c=27^\circ\text{C}$ (modulus in units of 10^{11} dyn/cm²)

T ($^\circ\text{C}$)	C_L	C	C'	B	G	E	ν	A
180	24.80	9.62	2.82	14.24	5.90	15.55	0.32	3.41
140	23.58	9.64	2.82	13.00	5.91	15.39	0.30	3.42
100	22.56	9.66	2.82	11.96	5.91	15.23	0.29	3.43
80	21.60	9.63	2.79	11.04	5.88	14.98	0.27	3.45
70	20.85	9.62	2.76	10.32	5.85	14.75	0.26	3.48
60	20.05	9.58	2.72	9.56	5.80	14.48	0.25	3.52
50	19.20	9.54	2.66	8.77	5.74	14.14	0.23	3.59
40	18.25	9.48	2.58	7.91	5.65	13.69	0.21	3.67
20	16.35	9.48	2.58	7.91	5.40	12.58	0.16	3.94
10	16.05	9.15	2.20	6.17	5.21	12.18	0.17	4.16
0	15.95	9.29	2.02	6.30	4.99	11.83	0.19	4.45
-10	15.97	8.80	1.80	6.57	4.72	11.43	0.21	4.89
-20	16.16	8.63	1.59	7.00	4.46	11.05	0.24	5.43
-40	16.67	8.38	1.20	7.89	3.99	10.24	0.28	6.98
-60	17.47	8.10	0.92	9.06	3.60	9.54	0.32	8.80
-80	18.40	7.91	0.73	10.25	3.32	8.99	0.35	10.84
-100	19.25	7.69*	0.57*	11.37	3.06	8.42	0.38	13.45
-120	19.95	7.51*	0.45*	12.29	2.86	7.94	0.39	16.69
-160	21.10*	7.26*	0.29*	13.84	2.58	7.26	0.41	25.03

* extrapolation

Table 9. Elastic moduli as a function of temperature. $S=0.2$.

T ($^{\circ}$ C)	H= 0 (modulus in units of 10^{11} dyn/cm 2)							
	C_L	C	C'	B	G	E	ν	A
180	25.40	9.52	2.88	14.92	5.91	15.66	0.32	3.31
140	24.65	9.55	2.88	14.14	5.92	15.58	0.32	3.32
100	23.80	9.58	2.86	13.27	5.92	15.44	0.30	3.35
80	23.10	9.58	2.85	12.57	5.91	15.32	0.30	3.36
60	22.10	9.57	2.80	11.60	5.86	15.06	0.28	3.42
40	20.80	9.50	2.72	10.39	5.77	14.62	0.27	3.49
20	18.90	9.35	2.55	8.70	5.58	13.78	0.24	3.67
10	17.75	9.25	2.39	7.70	5.41	13.15	0.22	3.87
0	16.55	9.11	2.18	6.71	5.17	12.36	0.20	4.18
-20	18.00	8.78	1.70	8.65	4.62	11.77	0.27	5.16
-40	22.00*	8.43	1.26	13.15	4.07	11.06	0.36	6.69

* extrapolation

Table 10. Elastic moduli as a function of temperature. $S=0$.

$H=0$ (modulus in units of 10^{11} dyn/cm²)

T (°C)	C_L	C	C'	B	G	E	A
180	25.05	9.65	2.85	14.45	5.93	15.65	0.32 3.40
140	24.40	9.65	2.85	13.80	5.93	15.56	0.31 3.40
100	23.70	9.65	2.85	13.10	5.93	15.46	0.30 3.40
60	22.75	9.65	2.85	12.15	5.93	15.30	0.29 3.40
40	21.75	9.65	2.85	11.15	5.93	15.11	0.27 3.40
20	20.30	9.65	2.85	9.70	5.93	14.78	0.25 3.40
0	18.80*	9.65*	2.85*	8.20	5.93	14.33	0.21 3.40

* extrapolation

Table 11. Elastic properties of austenite and martensite at the M_s temperature
(modulus in units of 10^{11} dyn/cm²)

Austenite							
S	M_s	C_{11}	C_{12}	C_{44}	G	γ	A
0.6	<-196	15.60	15.14	7.38	2.50	0.43	32
0.4	-115	12.52	11.52	7.60	2.90	0.39	15
0.2	-45	14.84	12.50	8.33	3.90	0.36	7.3
0	0	11.99	6.31	9.65	5.93	0.21	3.4
Martensite							
0.6	<-196	20.13	13.05	8.31	5.77		2.35*
0.4	-115	20.13	13.05	8.31	5.77		2.35
0.2	-45	20.13	13.05	8.31	5.77		2.35
0	0	20.07	13.11	8.17	5.40		2.35

parallel. The spin moments remain parallel until at a certain distance, the force diminishes and then becomes zero. The original Bethe curve showed schematically this change in the energy J as a function of the distance between atoms. The Bethe-Slater curve (Figure 33) plotted the magnetic energy J associated with a series of elements in the iron-group versus the corresponding values of R/r , where R is the radius of the atom (half the internuclear distance in the crystal) and r , the radius of the 3d shell. Because r varies between elements, the slope of the continuous curve does not reflect the dependence of J on the interatomic distance. In reality, a different curve should be drawn for each element. One can construct a Bethe-Slater curve for alloys, as Hausch and Warlimont^[6] had done for the Fe-Ni Invar alloys. Since the width of the 3d band is likely to change when the composition is varied, the slope and the curvature of such a curve should not be interpreted to represent the first and second derivatives of the exchange interaction, as Hausch and Warlimont did in the case of Fe-Ni alloys. In an alloy that undergoes ordering, the composition is fixed. While ordering will probably introduce local exchange interactions^[58] and modify the fine structure of the 3d band, the width of the band is unlikely to change. Based on this assumption, the variation of the exchange interaction J and its derivative J' with ordering can be directly related to the variation of the lattice parameter with ordering.

According to the Weiss theory, the exchange integral J is directly proportional to the Curie temperature and J' can be determined from the magnetic contribution to the elastic constants. The results for Fe_3Pt are shown in Figure 34. Between $S = 0.4$ and 0.6 , there is only a

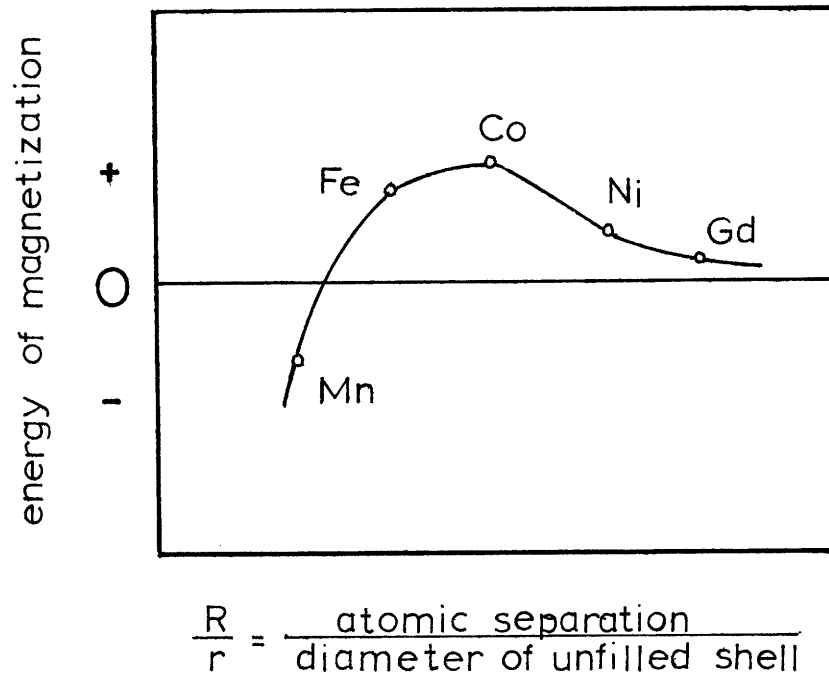


Figure 33. The Bethe-Slater curve.

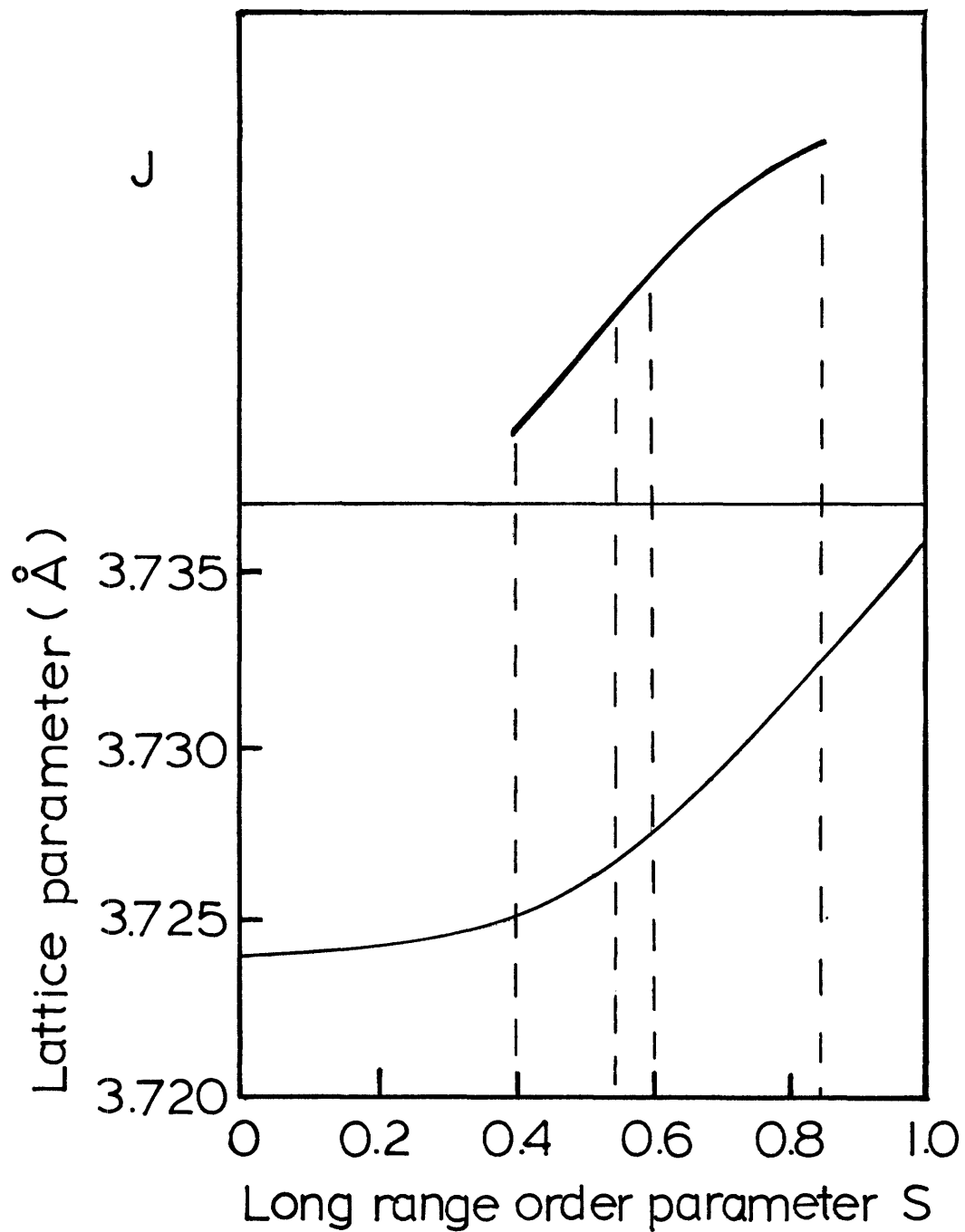


Figure 34. Spatial dependence of the nearest-neighbor exchange integral (schematic).

small change in the lattice parameter a_0 . The first derivative of J cannot vary significantly in this narrow range of interatomic distance. This was confirmed by the values of J' determined from the elastic constant measurement for $S = 0.4, 0.55$ and 0.6 . At larger interatomic distance, J' decreases and the curve becomes concave downward. This is understandable since for separations larger than those which occur in this alloy, J must vanish.

The isotropic exchange integral J is a function of $J_{\text{Fe-Fe}}$, $J_{\text{Fe-Pt}}$, $J_{\text{Pt-Pt}}$ and the degree of order S (Section 2.5.4). From the analysis of the magnetic properties of Pt, we can assume $J_{\text{Pt-Pt}} = 0$.^[89] However, a magnetic moment can be induced in a Pt atom in alloys. Therefore, $J_{\text{Fe-Pt}}$ has a finite value. We can calculate the values of $J_{\text{Fe-Fe}}$, $J_{\text{Fe-Pt}}$ and their first derivatives from Equation (22) and the values of J , J' for $S = 0.6$ and 0.55 , where the interatomic separations can be considered to be the same. At this separation,

$$J_{\text{Fe-Fe}} = -120.5 \text{ K}$$

$$J_{\text{Fe-Pt}} = 1074 \text{ K}$$

$$J'_{\text{Fe-Fe}} = 1.77 \times 10^{-4} \text{ dyne}$$

$$J'_{\text{Fe-Pt}} = -1.77 \times 10^{-4} \text{ dyne}$$

With an induced magnetic moment, neighboring Pt atoms might interact. Because the probability of Pt-Pt nearest-neighbor pair is small compared to Fe-Fe or Fe-Pt nearest-neighbor pair, the values of $J_{\text{Fe-Fe}}$ and

$J_{\text{Fe-Pt}}$ should not be too strongly dependent on the value of $J_{\text{Pt-Pt}}$ ¹²⁹. If $J_{\text{Pt-Pt}}$ is allowed to vary from 500 K to -500 K, $J_{\text{Fe-Fe}}$ varies by a factor of two while $J_{\text{Fe-Pt}}$ changes only by about 10%.

Based on a qualitative analysis of the magnetic properties of alloys of platinum with iron-group elements, Sato^[89] arrived at the result that near Fe_3Pt

$$J_{\text{Fe-Pt}} > J_{\text{Fe-Fe}}$$

$$J_{\text{Fe-Fe}} < 0$$

$$J_{\text{Fe-Pt}} > 0 \tag{38}$$

There is indirect evidence, a conclusion that has been reached from low-temperature studies of γ -phase iron alloys, that γ -Fe is antiferromagnetic with a Neel temperature of 80 K.^[31,139] This means $J_{\text{Fe-Fe}}$ is approximately -80 K. The numbers we calculated were in qualitative agreement with these results.

CHAPTER 5THERMOELASTIC MARTENSITE5.1 Introduction

The $\gamma \rightarrow \alpha$ transformation in Fe_3Pt proceeds martensitically.^[25] On ordering the austenite, the temperature at which the transformation starts on cooling, M_s , is decreased^[26] and the martensite formed becomes tetragonal. The kinetics of the forward, $\gamma \rightarrow \alpha$, and reverse, $\alpha \rightarrow \gamma$ transformation, as revealed by the change in electrical resistance with temperature, are reproducible on successful thermal cycles after the first cycle. The thermal hysteresis is decreased as the degree of long-range order of the γ -phase is increased.^[90-92] The crystallography of the martensitic transformation in disordered Fe-25 at. pct Pt has been investigated in detail^[93] and measurements of the shape strain and orientation relationship are in close agreement with the predictions of the phenomenological crystallographic theories. The transformation is of the $\{3, 15, 10\}_\gamma$ type observed in Fe-Ni^[94] and Fe-Ni-C^[95] alloys. Dunne and Wayman^[90] have shown that there is no significant change in the habit plane or the total shape strain of martensite formed in disordered and partially ordered (650°C for 0.5 hr) Fe-24.5 at.pct.Pt specimens. The lattice-invariant deformation is by twinning on $(112) [\bar{1}11]_\alpha$, in both ordered and disordered specimens.^[96,97] There are, however, differences in the width and the density of the twins. When the austenite is ordered, the twins in the martensite are thinner than in the disordered alloys. This difference may be closely related to the

accommodation of transformation strain at the interface and the ease with which the interface moves, as will be discussed in the next section.

On ordering the austenite, the difference between the M_s and A_s temperatures and the thermal hysteresis decrease markedly. Associated with a small hysteresis, as Dunne and Wayman showed in the most highly ordered specimens (500 hrs. at 550°C) of the 24 at.pct Pt alloy which they used in their experiments, is that the plates of martensite grow and shrink so slowly that the changes in size can be observed optically. The shape and volume changes involved in the growth of a plate in these specimens are accommodated by the austenite without deformation slip of a magnitude that can be detected on a prepolished surface of the specimen. From these observations, they concluded that the $\gamma \rightarrow \alpha$ and the $\alpha \rightarrow \gamma$ transformations in ordered alloys are thermoelastic. They also showed that, in the same specimens, the plates of martensite reappear in the same location after each thermal cycle, i.e. the microstructure of the martensite is reproducible each time a specimen is cooled through the $\gamma \rightarrow \alpha$ transition. Since they examined metallographically the growth and disappearance of plates of martensite only in the most highly ordered specimens, the extent to which microstructural memory and the thermoelastic effects are dependent upon the degree of order are not known from their work.

Kajiwara and Owen^[91] studied the effect of ordering on the microstructural memory in Fe-25 at.pct Pt and 27 at.pct Pt alloys and found somewhat different results. In the partially ordered Fe-25 at.pct Pt alloys (20 minutes at 650°C), the microstructural memory is perfect.

When the specimens were cooled a second time, new martensite plates appears in exactly the same locations as those occupied after the first cooling. The microstructure at -196°C was unchanged after thermal cycling between -196°C and 25°C . The most highly ordered specimen in this study (1 hr. at 650°C), however, exhibited only a partial microstructural memory. After the first cooling cycle, all the martensite plates appeared. The observation that partially ordered specimens have a perfect memory for the microstructure while highly ordered specimens have only an imperfect memory appears to be contradictory to the observation of Dunne and Wayman. Comparison between the two studies are difficult, however, because the relative degree of order are unknown, and the grain size, the composition and the cooling rate were all different.

In addition to microstructural reproducibility, it was found that when the austenite is disordered or partially ordered, a high density of dislocations, many in the form of elongated loops, are left behind in the austenite when the interface moves backward in the $\alpha \rightarrow \gamma$ transformation. The array of loops lie in the interfacial habit plane, which is approximately $\{3, 15, 10\}_{\gamma}$. The Burgers' vector of the dislocations is $\langle 110 \rangle_{\gamma}$ which is the principal slip direction in the austenite, but which does not lie in the habit plane. This direction is nearly parallel to the twinning shear direction of the transformation twins in the martensite. In the highly ordered specimen, very limited amounts of dislocation debris was detected. An important conclusion is that the formation, during the $\alpha \rightarrow \gamma$ transformation, of small volume of austenite with high dislocation density embedded in the untransformed austenite is essen-

tial if the specimen is to have a microstructural memory. This also implies that in the partially ordered specimens, the transformation strains at the interface are accommodated, in part, plastically in both the forward and reverse transformation. Only in the highly ordered specimens are the accommodation of this interfacial strain likely to be truly elastic. As will be discussed in the next section, a true thermoelastic growth should elastically accommodate the transformation strains at the interface on a microscopic scale and the shape change on a macroscopic scale. Hence thermoelastic growth and the reproducibility of the microstructure associated with the martensitic transformation in ordered alloys are phenomena related to each other indirectly through the ability of the austenite, dependent on the degree of order, to accommodate elastically the interfacial strain due to the lattice invariant deformation, twinning.

As the austenite becomes ordered, another crystallographic change occurs. The martensite becomes tetragonal, and the tetragonality increases with the degree of order of the γ -phase. Tadaki and Shimizu^[97,98] showed that in a Fe-24 at.pct Pt alloy, the thermoelastic martensite is body-centered tetragonal with an axial ratio $c/a = 1.1$ when the γ -phase has a degree of order $S = 0.8$. The volume of the tetragonal unit cell remains roughly constant independent of S . The lattice parameter of austenite with a degree of order S smaller than 0.5 remains almost constant between room temperature and M_s , whereas that of austenite with S larger than 0.6 increases appreciably with decreasing temperature. The result is that as S increases, the volume change during the transformation

decreases. The volume change is decreased from $\sim 1.4\%$ in the disordered alloy to $\sim 0\%$ in the highly ordered state, a change brought about the Invar Effect. Ordering raises the Curie temperature, T_C , above the M_S temperature and since the thermal expansion coefficient for Fe-25Pt is negative below T_C , the lattice parameter of the austenite increases with decreasing temperature between room temperature and M_S . As the volume of the BCT unit cell of the α phase remains constant with ordering, the larger depression of M_S below T_C in the highly ordered specimens results in a larger Invar effect, and hence a smaller volume change.

The thermoelastic growth of a plate of martensite in a matrix requires that all strains produced by the transformation be accommodated elastically. The extent to which elastic accommodation is achieved depends on the elastic properties, which determines the stress level in the austenite, and the plastic properties of the austenite, which determines the limit at which plastic flow occurs. Nilles^[85] observed that for Fe-25 at.pct Pt and 26 at.pct Pt alloys tested at 180°C, the rate of increase in the flow stress (0.2% yield stress) of the austenite is large in the early stages of ordering, but the rate of increase with ordering time diminishes as the highly ordered state is approached. The flow stress in the ordered state ($5.2 \times 10^8 \text{ N/m}^2$) is twice as large as that of the disordered state ($2.2 \times 10^8 \text{ N/m}^2$). The rate of decrease of the flow stress with increasing temperature is about 1 kg/mm^2 per 10 degree C, and insensitive to changes in the order. By taking into account the direct effect of ordering, which doubles the flow stress of austenite when fully ordered, and the lowering of the M_S temperature with ordering, the re-

sistance to plastic flow in the austenite at M_s is expected to increase significantly with ordering.

More drastic changes occur in the elastic properties of the Fe-Pt alloys in the Invar range. Just as the Invar effect introduces a magneto-volume contribution which produces the anomalous thermal expansion behavior, it also introduces a magnetic contribution to the elastic constants. This contribution is negative and, based on a localized interaction model, proportional to the square of the spontaneous magnetization. Cooling below the Curie temperature, T_c , the shear elastic constants C and C' are decreased, the magnitude of the decrease depending on the temperature interval below T_c . In a disordered Fe-28Pt single crystal, which does not transform martensitically, Hausch^[23] showed that the value of the C' elastic constant at -196°C is only one-fourth of that at room temperature. In a disordered polycrystalline Fe-25a/oPt specimen,^[20] the Young's modulus decreases by 20% between room temperature and the M_s temperature. In the ordered state (200 hr. at 600°C), the M_s temperature is below -196°C . Decrease by a factor of three in the Young's modulus is observed between room temperature and -196°C . Clearly, the elastic properties of the austenite at the start of the martensitic transformation are determined by the effects of ordering on M_s and the temperature interval between the M_s temperature and the Curie temperature. A systematic study of the dependence on ordering of the three independent single crystal elastic constants C , C' and C_L is presented in this thesis. The best estimates of the elastic properties of a polycrystalline specimen are those calculated from the single crystal

elastic constants using the Voigt-Reuss-Hill method. The shear modulus at M_s is 2.5×10^{11} dyn/cm² for $S = 0.6$ ($M_s < -196^\circ\text{C}$), 2.9×10^{11} dyn/cm² for $S = 0.4$ ($M_s = -110^\circ\text{C}$), 3.9×10^{11} dyn/cm² for $S = 0.2$ ($M_s = -45^\circ\text{C}$) and 5.9×10^{11} dyn/cm² for $S = 0$ ($M_s = 0^\circ\text{C}$), where the M_s temperatures for polycrystalline specimens are obtained from Kajiwara and Owen.^[91]

A change of a factor of two in the shear modulus is observed between the ordered state which exhibits the thermoelastic growth and the disordered state in which the transformation is burst-like and in which the transformation shape change is partially accommodated by plastic flow. Similar changes occur in the Young's modulus. The bulk modulus at M_s , however, increases with ordering (Table 11).

5.2 Theoretical Consideration

The thermoelastic growth of a plate of martensite in austenite requires that two kinds of transformation strain be accommodated elastically by the matrix: that associated with the total shape strain of the transformation as predicted by the phenomenological crystallographic theories^[99,100] and that associated with the interfacial strain in twinned martensite. The elastic accommodation of the shape strain in thermoelastic growth has been discussed extensively in a qualitative manner. A model of growth of martensite plates will be presented later to describe quantitatively the thermoelastic behavior of Fe_3Pt . The elastic accommodation of interfacial strain in twinned martensite has been discussed qualitatively by Kajiwara and Owen^[101] and will be briefly reviewed here.

The electron microscopy work by Kajiwara and Owen^[91] suggests why, in Fe_3Pt , the driving force needed to move the α/γ interface is

smaller in ordered than disordered specimens. In disordered or partially ordered alloys, the interface is a wall of sessile dislocation loops while in more ordered alloys the glide dislocations in the small amount of debris from the reverse transformation are paired superlattice dislocations. It is clearly more difficult to move an interface of sessile dislocation loops.

The lattice invariant deformation in Fe_3Pt is by twinning on $(112) [\bar{1}\bar{1}\bar{1}]_\alpha$ in both ordered and disordered specimens. [96,97] Using this shear, the formal crystallographic theories predict very well the observed habit plane, orientation relation and shape deformation for disordered alloys. In twin-related martensite plates, if the ratio of thickness of neighboring twins is that demanded by the crystallographic theories, the strains at the interface are zero when averaged over distances which are large compared with the twin thickness. On a smaller scale, however, significant strains are developed because within each twin, there is no lattice invariant strain. The strains at the γ - α interface of the two twin-related plates partly cancel each other, and the strain energy per unit area of the γ - α interface is reduced if the thickness of the twin-pair is decreased. There is a minimum thickness at which the decrease in the interfacial energy is balanced by the increase in the energy per unit volume of the internal twin interface. Hence a reduction in the twin boundary energy will produce finer twins, rendering more favorable the elastic accommodation of interfacial strains. Kajiwara and Owen suggested that ordering results in a substantial reduction of the twin boundary energy due to the ordered arrangement across the twin interface and the relaxation of the nearest interatomic

distance across the $(112)_{bct}$ twin boundary when the martensite tetragonality increases with ordering. The result is that in ordered alloys, the twins are sufficiently thin to accommodate the strains at the habit plane elastically. In this way they accounted for the observation that when the austenite is substantially disordered, high density of dislocations are left behind in the austenite when the interface moves backward in the $\alpha \rightarrow \gamma$ transformation whereas in a well-ordered specimen, very few such dislocations are found. Recently, Tadaki et al.^[97] showed experimentally that the twin widths in martensite in Fe-24 at%Pt are indeed decreased with increasing degree of order, lending support to the qualitative explanation advanced above.

Turning to the growth of a macroscopic plate of martensite, thermoelastic behavior requires that the chemical driving force be balanced by the elastic strain energy generated by the transformation. Elastic strain is reversible while plastic strain produced by slip is not. During truly thermoelastic growth, all the shape strain is accommodated elastically. A decrease in temperature permits the transformation to proceed at a small net driving force, while on raising the temperature, the chemical driving force is reduced as the stored elastic energy is released. Above T_0 , both the chemical driving force and the elastic strain energy drive the transformation in the reverse direction. At a fixed temperature, the martensite plates grow or shrink until they reach a thermoelastic equilibrium. Then small changes in temperature cause the plates to thicken or to shrink.

Christian^[102] summarized the four conditions which promote thermoelastic growth:

- 1) A small driving force
- 2) a small volume change
- 3) a small shear component of the shape strain
- 4) a matrix with a high elastic limit.

In both disordered and ordered Fe_3Pt , the lattice invariant deformation is by twinning on $(112)[111]_{\alpha}$. This is close to $\{110\}\langle 110\rangle$ in the austenite. In this orientation, the resistance to shear deformation is measured by the C' elastic constant. It has been shown that there is a large decrease in the C' elastic constant of the austenite at M_s when ordering increases. A small value of this elastic constant means that the twinning shear can proceed more readily. This is similar to the Zener softening^[103] which interprets a bcc \rightarrow fcc transition, like that in Fe at 910°C , in terms of the small value of the $(C_{11}-C_{12})/2$ coefficient likely to be associated with a bcc structure. Hence it can be reasoned that at the nucleation stage, the driving force will be much smaller for ordered specimens.

Experimentally it has been shown that the volume change during the transformation decreases until as S approaches unity, the volume change goes to zero. It should be noted that the bulk modulus at M_s increases with ordering. However, the decreasing volume change with ordering eliminates the effect of this unfavorable change in the bulk modulus on elastic accommodation. Finally, considering the magnitude of the volume change during the transformation (1.4% in disordered, 0% in ordered specimen) relative to the shear component of the shape

change ($m \approx 0.2$), it can be reasonably assumed that the decreasing volume change is not a significant factor in the change of growth behavior with ordering.

There is no measurable change in the habit plane or the magnitude of the shape strain between disordered or partially ordered (0.5 hr. at 650°C) Fe-24.5 Pt specimen.^[90] The situation in a highly ordered specimen has not been investigated. Theoretically, tetragonality should also affect the magnitude of the shape strain. When the lattice invariant shear involves only $\{112\}_\alpha$ type twins, the magnitude of the shape strain m can be expressed as^[92]

$$m = \eta - \frac{1}{\eta}$$

where $\eta = \sqrt{2} / \sqrt[3]{2q}$ and q is the axial ratio c/r . When $q = 1.0$ the value of m is 0.23, and when $q = 1.1$, m decreases to 0.17. If this decrease in the shape strain does occur in Fe₃Pt on ordering, we have another factor favoring thermoelastic growth in the ordered specimen.

The strains involved in the martensitic transformation are larger than the strain of 10^{-6} usually associated experimentally with the elastic limit. In discussing the initiation of plastic flow, the magnitude of the flow stress at a small macroscopic strain is a more appropriate criterion to consider. Nilles' results,^[85] discussed earlier, indicate that at M_s , the ordered austenite is much more resistant to plastic flow. It has also been shown that the average

shear modulus in the highly ordered state is a factor of two smaller than that of the disordered state. In an isotropic medium the stress concentration in the matrix due to an arbitrary-shape inclusion undergoing a shear transformation scales with the shear modulus. A small modulus and a high flow stress imply that it is more unlikely that plastic flow will occur in the ordered alloys.

In summary, all the factors that favor thermoelastic growth are accentuated by ordering in Fe_3Pt .

5.3 A Model of Growth

In this section, we consider the elastic accommodation of the total shape change associated with the martensitic transformation. This is favored by a high yield stress and low elastic shear modulus of the matrix, a small chemical free energy change per unit volume, Δg_c , and a small lattice shape change as a result of transformation. [102]

Δg_c is balanced by the elastic strain energy which is linearly proportional to the average elastic shear modulus and, consequently, the value of the modulus is a major factor determining whether or not growth is thermoelastic. The calculation of the stress field and the determination of the extent of the plastic zone associated with the growing plate of martensite serves to illustrate the combined effects of the elastic modulus and the flow stress.

A plate of martensite is assumed to be a thin, ellipsoidal coherent particle, of radius r and semithickness c , formed at the M_s temperature. The shape change of the particle is assumed to be

elastically accommodated in an infinite matrix of the parent austenite; the strain energy being stored in both particle and matrix. The macroscopic shape change can be resolved into a simple shear component parallel to the habit plane and a dilatation normal to it. As discussed earlier, the dilatation component is usually small compared to the transformation shear. Eshelby^[105-107] has shown that, if the transformation strain is a simple shear e_{13}^T in the plane of the particle the elastic strain energy stored per unit volume of particle is A_c/r , where

$$A = \frac{\pi(2-\nu)G}{8(1-\nu)} e_{13}^T{}^2 \quad (40)$$

G and ν being the shear modulus and Poisson's ratio, respectively. After radial growth is stopped by a barrier, such as a grain boundary, the shape of the particle is determined by a thermoelastic balance,^[108] assuming that the friction stress is zero,

$$\Delta g_c + 2A \frac{c}{r} = 0 \quad (41)$$

Accordingly, the equilibrium plate aspect ratio c/r , is determined by the magnitude of Δg_c . Alternatively, by calculating the aspect ratio at which the plastic zone becomes negligible, an upper limit to the value of Δg_c for thermoelastic growth can be deduced.

It is assumed that plastic flow will occur in a volume enclosed by a surface at which the von Mises criterion^[109] for yielding is satisfied, namely,

$$\sigma_{\text{eff}}^c \geq \sigma_y \quad (42)$$

where σ_y is the yield stress of the matrix and

$$\sigma_{\text{eff}}^{\text{C}} = \sqrt{\frac{1}{2}[(\sigma_{11}-\sigma_{22})^2 + (\sigma_{22}-\sigma_{33})^2 + (\sigma_{33}-\sigma_{11})^2] + 3(\sigma_{12}^2 + \sigma_{23}^2 + \sigma_{31}^2)} \quad (43)$$

$\sigma_{\text{eff}}^{\text{C}}$ is the maximum stress at each location (x,y,z) in the matrix without reference to available slip systems. When the matrix yields, some plastic relaxation will occur and consequently, the volume of the plastic zone will be different from that computed here. However since to understand thermoelastic behavior it is important to know only whether or not plastic flow occurs within a significant volume, it is not necessary to determine the profile of the relaxed zones.

After rapid radial growth is stopped by a barrier, a plate of martensite thickens. The balance between the chemical driving force and the elastic strain energy is maintained if the thickening is a thermoelastic process. It is the plastic zone in the broad interface separating martensite from austenite which determines whether or not thickening is accompanied by plastic deformation. This in turn determines an upper limit to the chemical driving force which permits thermoelastic growth. At the tapered ends of an ellipsoidal plate of martensite, the plastic zone extends into the barrier. This zone probably presents a restraining force in the final stage of the reverse transformation, for reasons discussed later, but it is not an essential factor in determining whether or not the growth is thermoelastic.

So far, we have considered the concept of thermoelastic equilibrium in the ideal case. If a finite stress is required to move an interface, then interfacial motion will deviate from true thermoelastic equilibrium. Taking into account that a shear stress τ_0 is required to move an inter-

face which accomplishes a transformation strain γ_T , equation (41) ¹⁴⁴
becomes [108]:

$$\Delta g_c + 2A\left(\frac{c}{r}\right) = \begin{array}{c} \text{heating} \\ + \\ \text{cooling} \end{array} \tau_o \gamma_T \quad (41a)$$

Then the criterion of no plastic zone associated with the broad interface determines an upper limit to the quantity $(\Delta g_c + \tau_o \gamma_T)$. In a well annealed crystal, $\tau_o \gamma_T$ amounts to a few cal/mole for interfacial dislocations moving against the Peierls stress. A high dislocation density in the matrix, as a result of plastic accommodation by slip, will increase the friction stress and hence the magnitude of the transformation hysteresis. It is found that in Fe_3Pt [91], increasing thermoelastic behavior on ordering is associated with a diminished density of dislocation debris after reversion. Hence in the ordered Fe_3Pt where the thermal hysteresis is smallest, it is reasonable to assume that the friction stress is nearly the same as the Peierls stress and $\tau_o \gamma_T$ is only a few cal/mole.

In an earlier investigation of the problem of elastic accommodation, [110] the austenitic matrix and the plate of martensite were assumed to have the same average elastic moduli. The strain field was simulated by a continuous distribution of dislocation loops lying in the interface of the ellipsoidal plate and the shape change was assumed to be a simple shear. That is, the dilatation normal to the habit plane was neglected. In the next section, we shall extend Eshelby's model of the strain field surrounding an inclusion to calculate the stress fields inside and outside an ellipsoidal plate of martensite in an infinite matrix of austenite. This model is three dimensional, takes into account

the dilatational strains and is capable of treating the situation in which the average elastic moduli of the inclusion and the matrix are different. It is useful to point out that 'average' elastic moduli are calculated by averaging the single crystal elastic constants over all crystal orientations. The anisotropy ratio of the single crystal A , which is the ratio of the C and C' elastic constants, is greater than 1. Hence "average" elastic moduli are applicable to polycrystalline specimens, which are considered to be elastically isotropic. This is to be distinguished from an isotropic elastic modulus of a single crystal which implies that the C and C' elastic constants are equal in magnitude and the anisotropy ratio A is 1.

For the present calculation of an inclusion in an isotropic matrix, the elastic moduli of the austenite and the martensite at the M_s temperature are required. Without available data on the elastic moduli of Fe-25 Pt martensite, we adopted the values measured for a Fe-22Pt specimen (section 4.3.3). For the austenite, the average elastic moduli calculated from the single crystal elastic constants were used. The values are listed in Table 11. Flow stress measurements by Schmutz^[112] indicated that a specimen with a degree of order $S = 0.5$ has a 0.2% flow stress of $5 \times 10^8 \text{ N/m}^2$ at room temperature. The flow stress increases with decreasing temperature $0.5 \times 10^8 \text{ N/m}^2 / 10 \text{ degree C}$. The yield stress used in the Von Mises criterion for the three ordered states $S = 0.6, 0.4$ and 0.2 was chosen to be the value on this curve (0.2% flow stress) at the respective M_s temperatures (Fig. 35). This probably results in an over-estimation of the yield stress for $S = 0.2$.

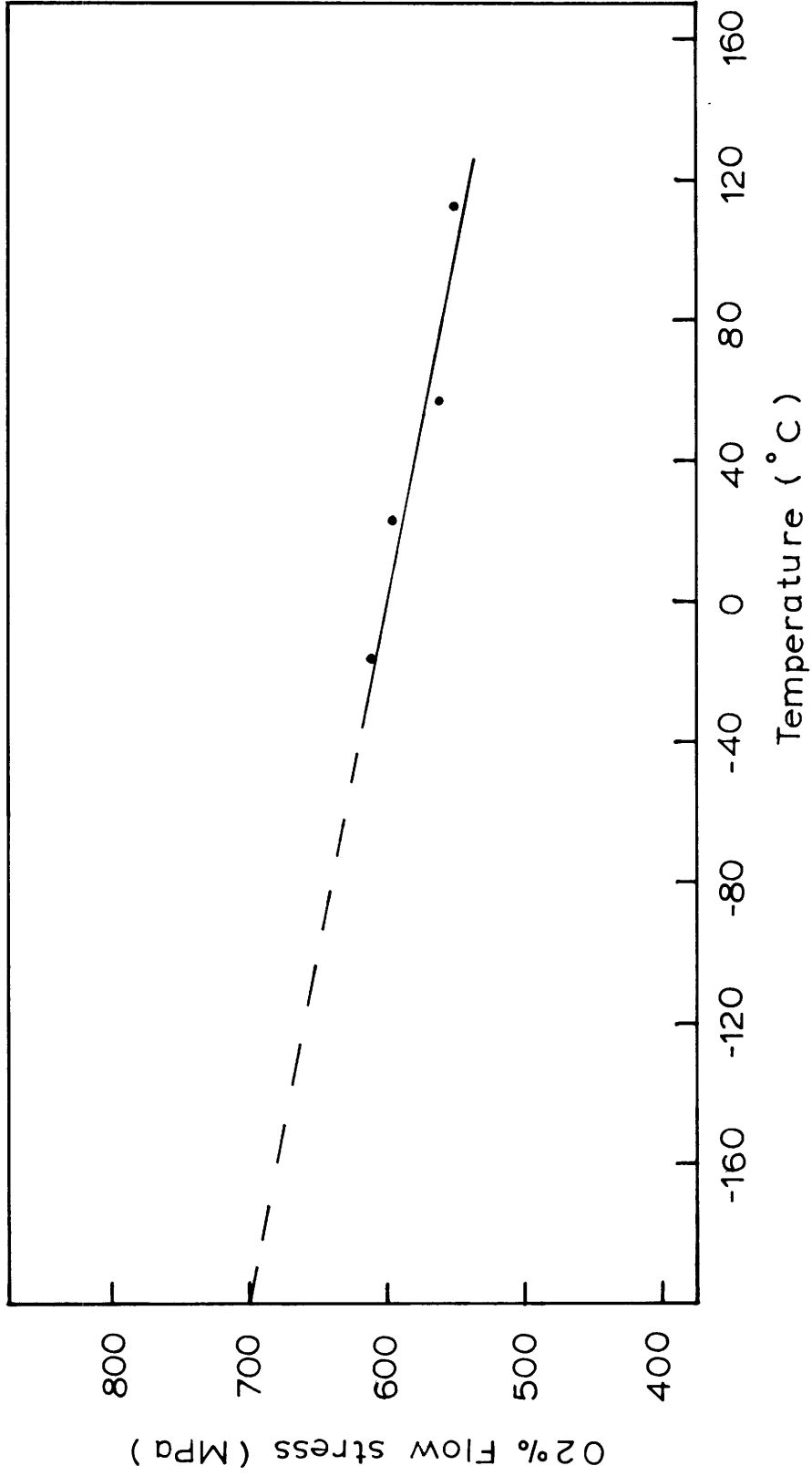


Figure 35. Flow stress versus temperature. Fe₃Pt ordered. S=0.5 . 146
(reference 112)

For the disordered state, a value of $2.2 \times 10^8 \text{ N/M}^2$ was used^[88]. 147

It was further assumed that the transformation volume change in the three ordered cases is zero. In the disordered case, a dilatation of 1.4% normal to the habit plane was included in addition to the shear component of the shape strain. The shear component was assumed to be 0.2 in all cases.

5.4 The Model

Formally, for an inclusion undergoing a "stress-free" transformation e_{ij}^T in an infinite matrix, the displacement is^[105-107]

$$u_i^C(\vec{r}) = \int_S dS'_k \sigma_{jk}^T G_{ij}(\vec{r}-\vec{r}') \quad (44)$$

where S is the boundary between the inclusion and the matrix, and $G_{ij}(\vec{r}-\vec{r}')$ is the displacement at a point \vec{r} due to a unit force at \vec{r}' .

σ_{jk}^T are related to e_{jk}^T by Hooke's law. If the matrix and the inclusion are elastically isotropic and have the same moduli,

$$G_{ij}(\vec{r}-\vec{r}') = \frac{1}{4\pi G} \frac{\delta_{ij}}{|\vec{r}-\vec{r}'|} - \frac{1}{16\pi G(1-\nu)} \frac{\partial^2}{\partial x_i \partial x_j} |\vec{r}-\vec{r}'| \quad (45)$$

where G and ν are the average shear modulus and the Poisson's ratio.

By Gauss' theorem,

$$\int_S |\vec{r}-\vec{r}'| dS'_k = - \frac{\partial}{\partial x_R} \int_V |\vec{r}-\vec{r}'| dv'$$

where v is the volume of the inclusion. Hence

$$u_i^c(r) = \frac{1}{16\pi G(1-\nu)} \sigma_{jk}^T \psi_{,ijk} - \frac{1}{4\pi G} \sigma_{jk}^T \phi_{,k} \quad (46)$$

$$\text{where} \quad \phi(r) = \int \frac{dv'}{|\vec{r}-\vec{r}'|}, \quad \psi(r) = \int |\vec{r}-\vec{r}'|^2 dv' \quad (47)$$

and the notation $_{,i}$ means differentiation with respect to x_i . $\phi(r)$ is the Newtonian (harmonic) potential similar to that due to an attractive matter of unit density filling the volume V and bounded by a surface S . ψ is the corresponding biharmonic potential. The strain field is defined in the usual way,

$$e_{ij}^c = \frac{1}{2} (u_{i,j}^c + u_{j,i}^c) \quad (48)$$

and the stresses are related to the strains by Hooke's law. In the matrix,

$$\sigma_{ij}^c = \lambda e^c \delta_{ij} + 2\mu e_{ij}^c \quad (49a)$$

and in the inclusion,

$$\sigma_{ij}^I = \sigma_{ij}^c - \sigma_{ij}^T \quad (49b)$$

λ and μ are the Lamé constants. The total elastic energy is

$$E = -\frac{1}{2} \int_V \sigma_{ij}^I e_{ij}^T dv \quad (50)$$

If the inclusion undergoes a transformation strain $e_{ij}^T^*$ and has different elastic moduli, λ^* and μ^* , from the matrix, it can produce the same strain field in the matrix as an equivalent inclusion, which has the same modulus as the matrix and undergoes a transformation strain e_{ij}^T , provided that the stresses inside the inclusion are the same in both cases, i.e.

$$\begin{aligned}\sigma_{ij}^I &= \sigma_{ij}^C - \sigma_{ij}^T && \text{in the equivalent inclusion} \\ &= \sigma_{ij}^C - \sigma_{ij}^{T^*} && \text{in the actual inclusion} \quad (51)\end{aligned}$$

Expressing σ_{ij}^C in terms of e_{ij}^T using Eq'ns (46)-(49) and knowing $\lambda, \mu, \lambda^*, \mu^*$ and $e_{ij}^T^*$, one can solve for e_{ij}^T and, consequently, for σ_{ij}^C .

For an ellipsoidal inclusion, a closed-form solution exists for the harmonic potential ϕ .^[111] As shown by Eshelby, derivatives of the biharmonic potential ψ can be expressed in terms of those of ϕ . The stresses can readily be calculated from Eqn's (46)-(49). The resulting formulae are listed in Appendix A.

5.5 Results and Discussion

5.5.1 A Single Plate

A single ellipsoidal plate of martensite is assumed to lie in the xy plane with the transformation shear in the x direction ($e_{13}^T \neq 0$). The plate thickens in the z direction. For each state of atomic

order, the stress fields were calculated as a function of the aspect ratio c/r . Figure 36(a) and (b) shows the shear stress σ_{13}^C in the plane of the plate (along the x axis) and normal to the plane (along the z axis) for $S = 0.6$. Along these two axes, σ_{13}^C is the only non-zero stress component. In the plane of the plate, curves of σ_{13}^C for various aspect ratios always exceed the critical shear stress, σ_{CRSS} , at some distance from the tip of the plate, where $\sigma_{CRSS} = \frac{\sigma_y}{\sqrt{3}}$. Along the z direction, σ_{13}^C favors the formation of a neighboring plate with an opposite shape strain. The critical shear stress is exceeded only for plates with an aspect ratio larger than 0.035.

The extent of the plastic zone, determined by the von Mises criterion, in ordered and disordered Fe_3Pt are shown in Fig. 37. The shear modulus of the martensite phase remains nearly constant in the four cases considered: $S = 0.6, 0.4, 0.2$ and 0 . Hence changes in the size of the plastic zone with the degree of order of the austenite reflects the combined effect of changes in the elastic moduli and the flow stress of the austenite. In the disordered case, the plastic zone encloses a volume several times larger than that of the plate itself, indicating that elastic accommodation is impossible. On ordering, the plastic zone disappears entirely from the broad interface for plates with small aspect ratio. This is a dramatic demonstration of the influence of ordering; an influence produced by an increase in the flow stress and a decrease in the shear modulus. By calculating the aspect ratio at which the plastic zone vanishes, an upper limit to the chemical driving force, Δg_c , for thermoelastic growth can be

deduced. A quantitative measure of the size of the plastic zone is the distance along the z axis at which the yield stress is exceeded. This parameter, r_p , as a function of aspect ratio is shown in Fig. 38 for $S = 0.6, 0.4$ and 0.2 . The aspect ratio at which r_p is zero decreases with decreasing degree of order. For $S = 0.6$, this critical aspect ratio is 0.04 . A plate of this size has an elastic strain energy of 77 cal/mole. According to Eq'n (41), the upper limit to Δg_c is 154 cal/mole. If we consider the plastic zone associated with the broad interface a more stringent upper limit is obtained. Figure 39 shows the parameter r_p , as a function of aspect ratio, at different points along the $[100]$ direction for $S = 0.6$. At $x = 0.75r$, plastic deformation disappears at an aspect ratio of 0.03 . The elastic strain energy of such a plate is 59 cal/mole. Thus the upper limit of Δg_c is lowered to 118 cal/mole. For $S = 0.4$ and 0.2 , the critical aspect ratios are 0.025 and 0.02 respectively. The upper limit of Δg_c is 108 cal/mole in both cases. Since the chemical driving force decreases with ordering, it can be concluded that Δg_c cannot exceed 108 cal/mole in the three ordered states under consideration. A chemical driving force between 0 and 108 cal/mole will allow thermoelastic equilibrium to be maintained at the M_s temperature with the equilibrium plate size determined by the magnitude of Δg_c . Cooling below M_s further decreases the elastic moduli of the austenite, thus permitting thicker plates to exist without plastic deformation. At the same time Δg_c increases, causing the plate to thicken. In this way thermoelastic equilibrium is maintained in the thickening process.

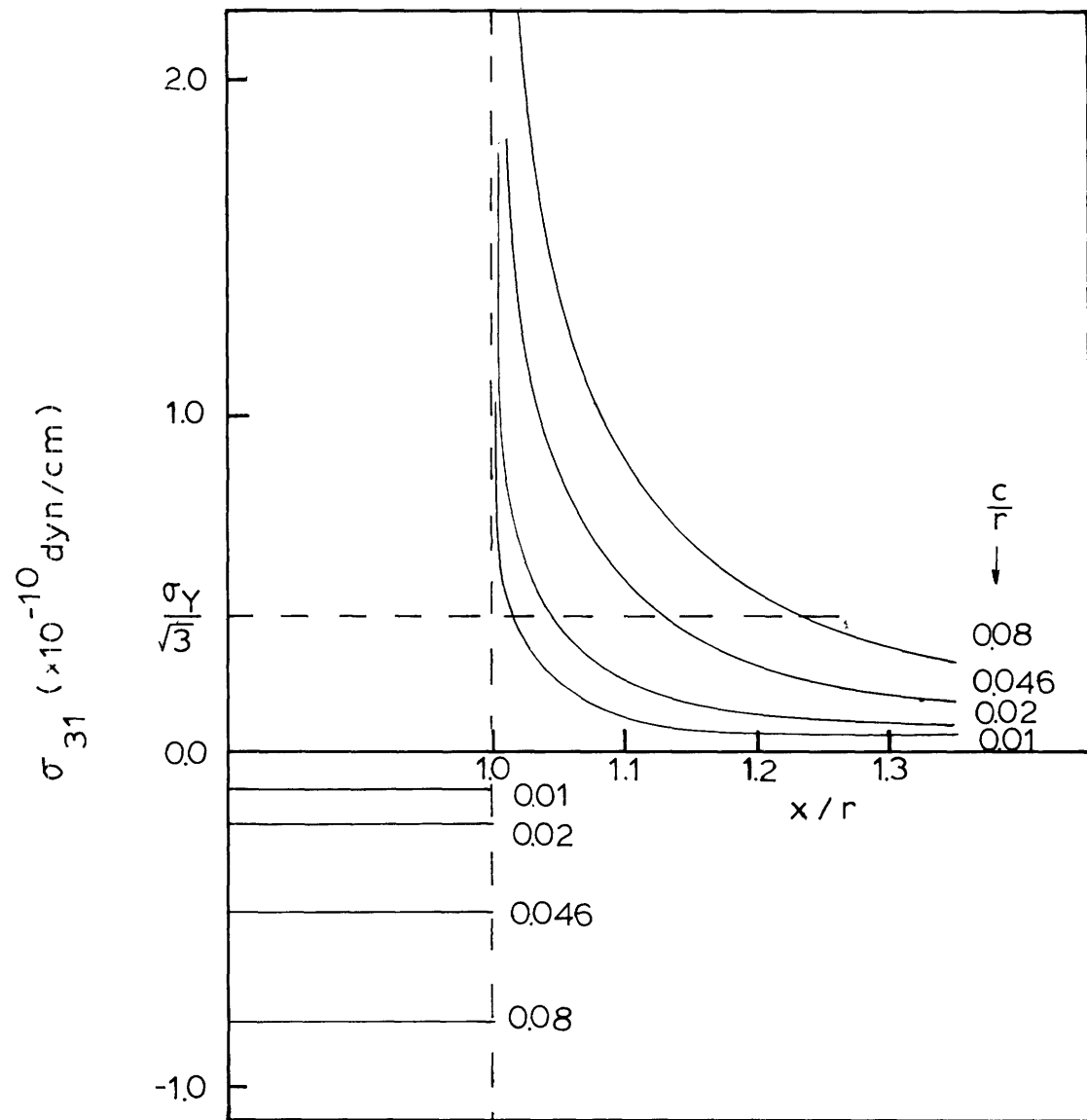


Figure 36a. The shear stress σ_{31} along x axis due to an ellipsoidal plate lying in $x y$ plane with shear in x direction. $S=0.6$.

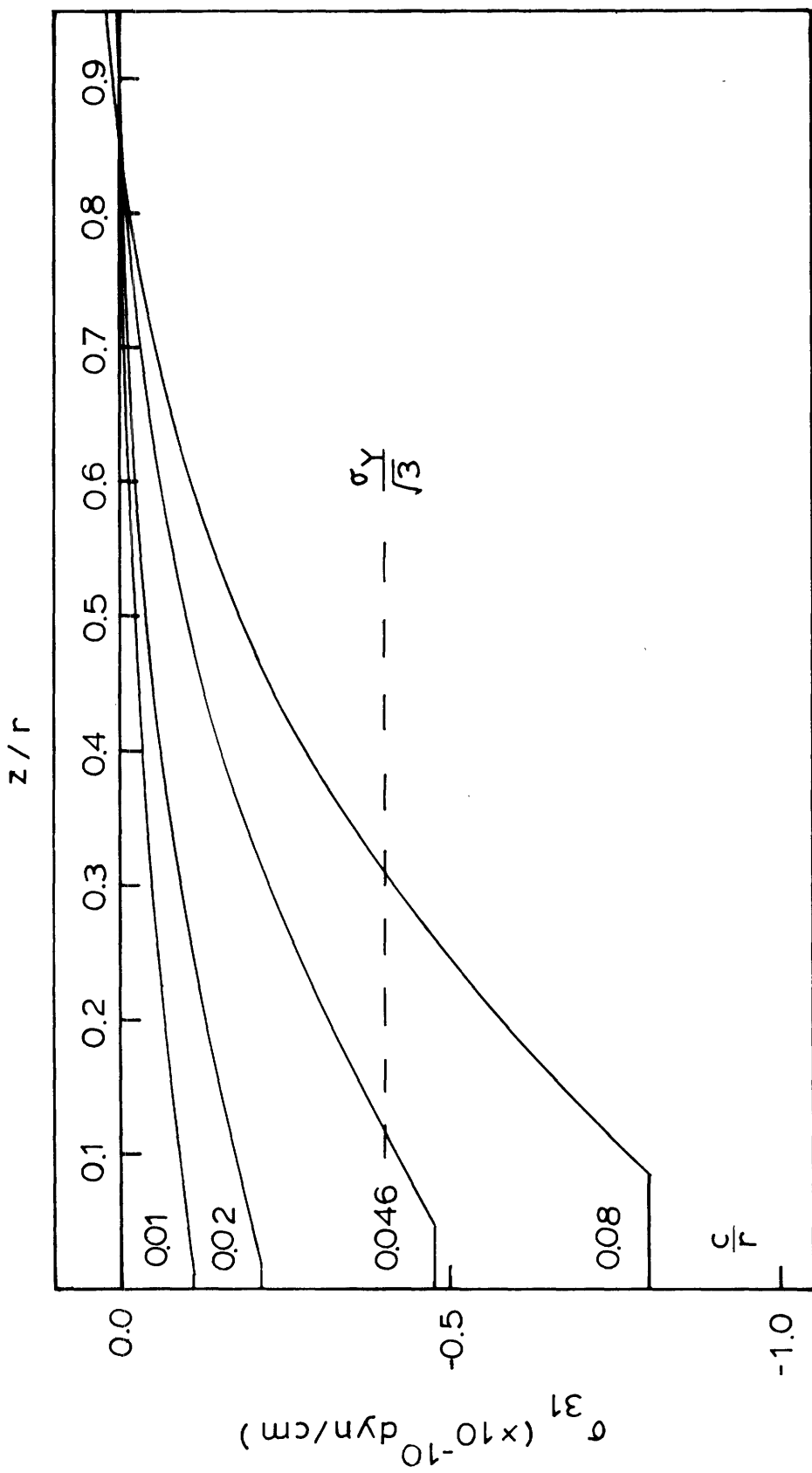


Figure 36b. The shear stress σ_{31} along z axis due to an ellipsoidal plate lying in x y plane with shear in x direction. $S = 0.6$.

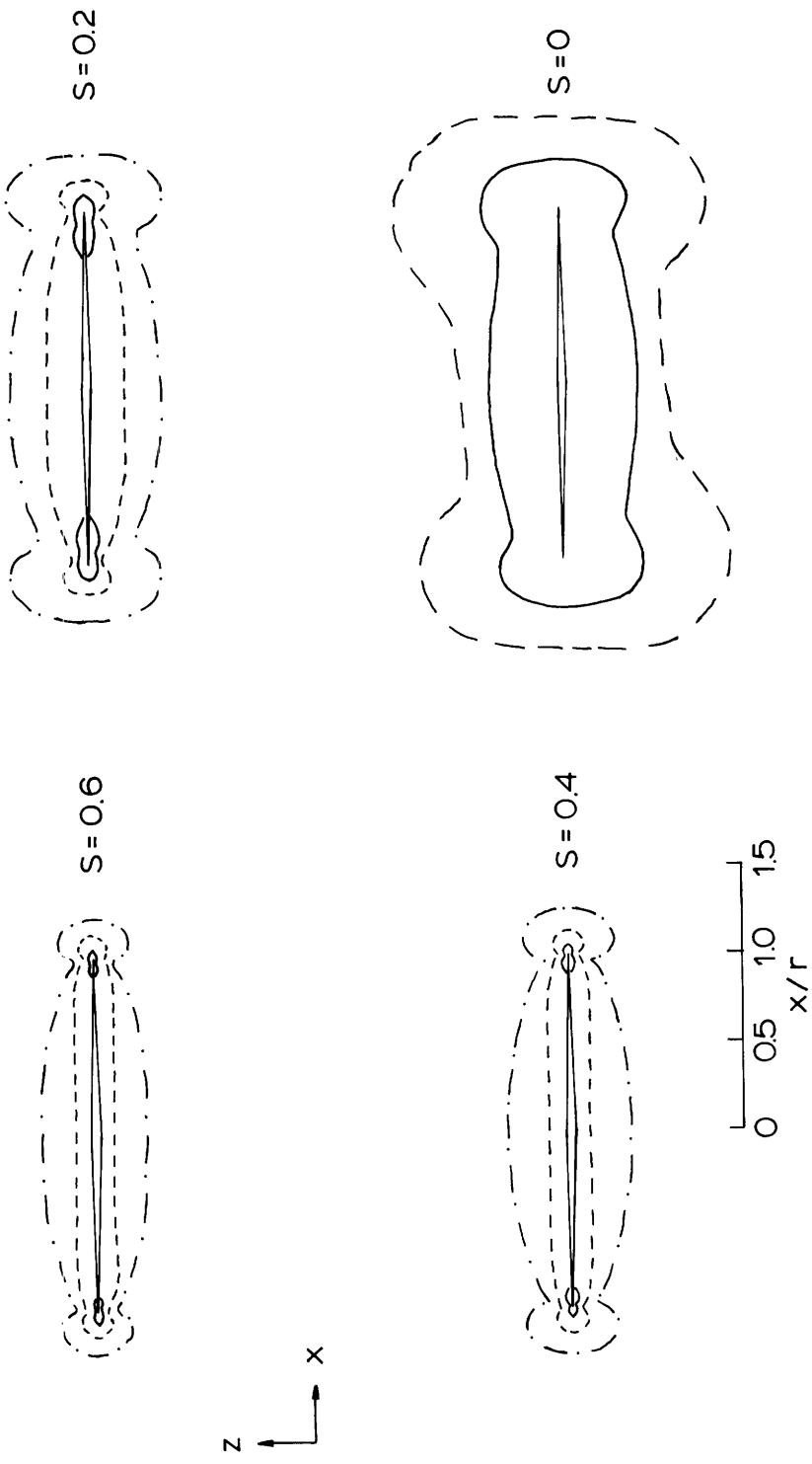


Figure 37a. Matrix yield stress contours of an ellipsoidal plate lying in $x-y$ plane with shear in x direction. Aspect ratios 0.02 (—), 0.04 (---) and 0.08 (-·-·-).

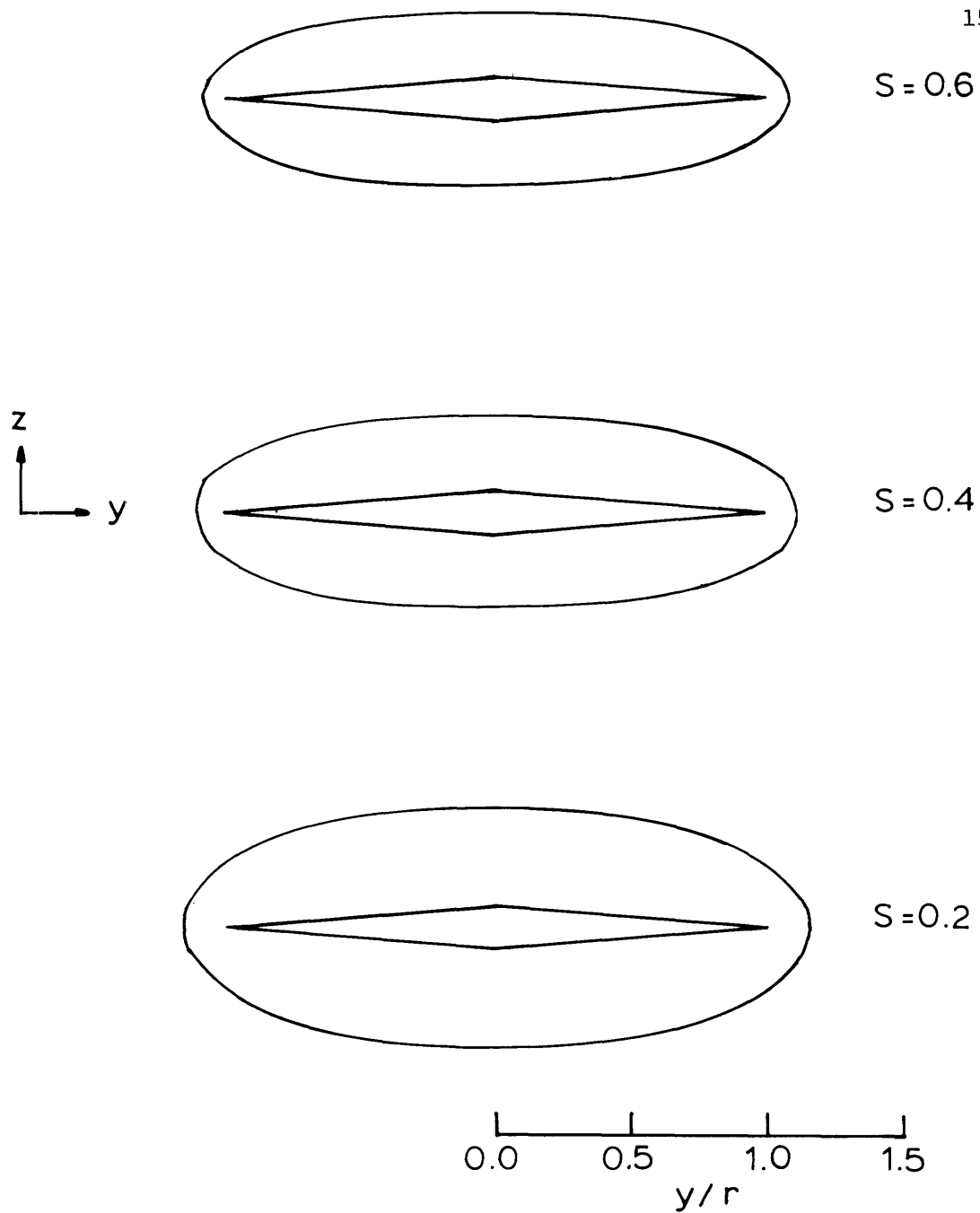


Figure 37b. Matrix yield stress contours of ellipsoidal plate lying in $x y$ plane with shear in x direction. Aspect ratio 0.08.

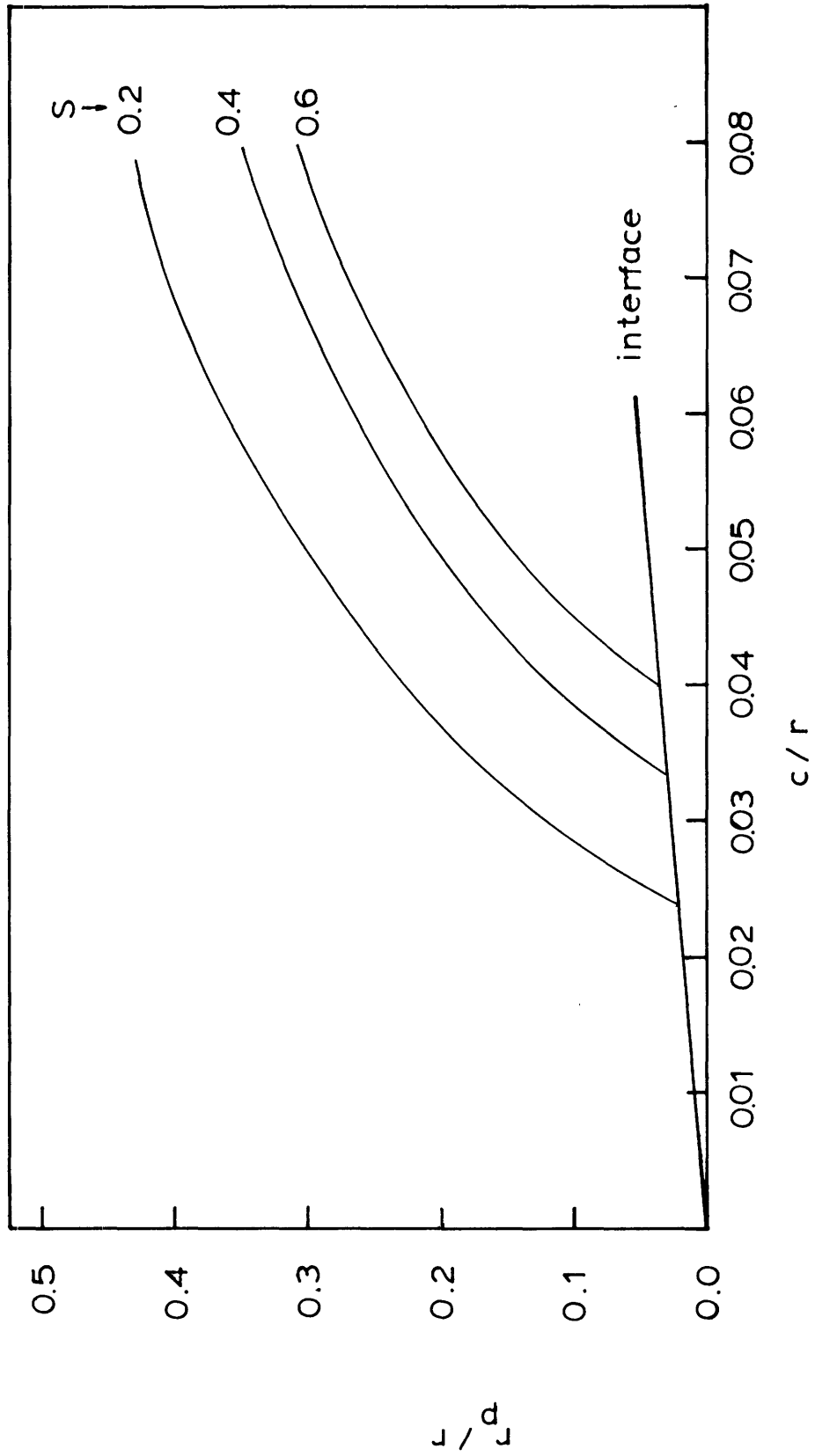


Figure 38. The yield stress envelope, r_p , along z axis as a function of aspect ratio.

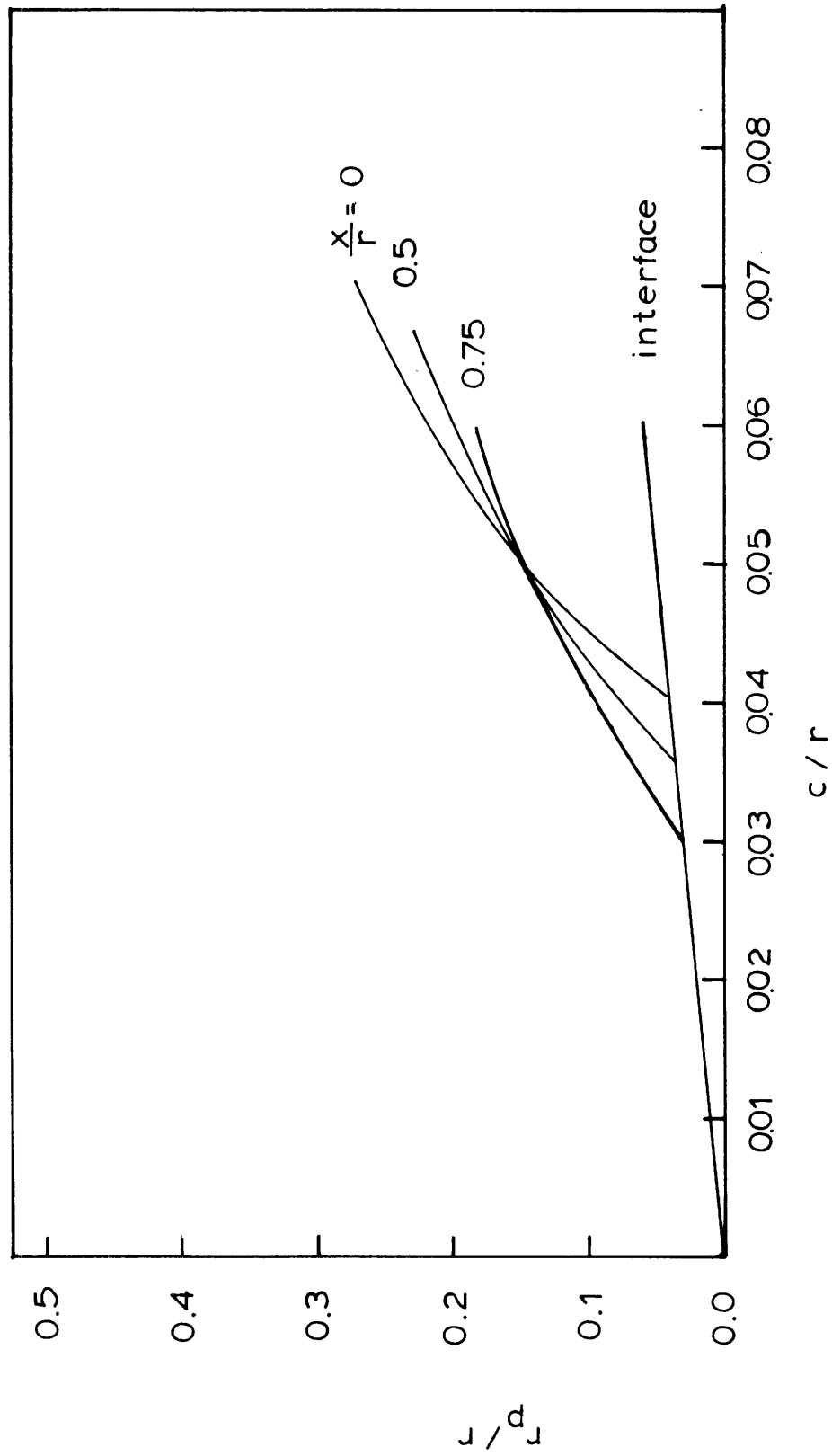


Figure 39. The radius of yield stress envelope, r_p , along [001] measured at various points x in [100] direction. $S = 0.6$.

Experimentally, Tong and Wayman [134] reported that the total energy change during the martensitic transformation in Fe_3Pt is 80 cal/mole. Djuric [135] arrived at a similar value (50-80 cal/mole) for Fe-27Pt. An estimate of Δg_c , however, requires an experimental method of measuring separately the contribution of the chemical and the stored elastic energy to the total transformation energy. An upper limit of 80 cal/mole determined experimentally is compatible with the upper limit established in the growth model.

5.5.2 An Assembly of Plates

In most, but not all thermoelastic martensites, plates of martensite grow in stacks of nearly parallel plates alternating in shear direction so that the total assembly of plates is self-accommodating. [133] As shown in Section 5.5.1, the development of σ_{13} stress in the [001] direction in the matrix due to a martensite plate lying in the xy plane with transformation strain in the x direction favors the formation of a second plate of opposite shape strain. If we allow ellipsoidal plates of opposite shear to touch along the z-axis, the total strain energy of the system is reduced. Thus, for the same chemical driving force, Δg_c , self-accommodation allows thicker plates to exist at thermoelastic equilibrium. The effect on the plastic zones of putting together two plates is illustrated by the Von Mises yield contours plotted in Fig. 40 for plates with an aspect ratio of 0.08. An isolated plate has a plastic zone extending 30 percent of the plate radius in the [001] direction (Fig. 37). Two parallel, touching plates of opposite shear produce only a small plastic zone confined to the edges of the plates.

Ellipsoidal plates in contact at a point is unlikely to be the most effective geometry to minimize the strains accommodating the transformation shape change. It is expected that the most effective accommodation is achieved when parallel plates of opposite shear are in mutual contact over a large area. Thus, we have examined the plastic zone contours associated with flat plates. The harmonic and biharmonic potential functions have been calculated for a square plate $[111], [113]$, thus enabling us to calculate the stress field and the plastic zone surrounding a square plate with a e_{13}^T transformation strain (Appendix B). For small values of c/r , the elastic strain energy of such a plate is linearly proportional to c/r with the proportionality constant, A , about twice as large as for an ellipsoidal plate. Thus, for the same chemical driving force, Δg_c , we have to compare a square plate with $c/r = 0.042$ with an ellipsoidal plate with $c/r = 0.08$. The results are presented in Fig. 41. The plastic zone is confined to the vicinity of the edge of the square, flat plate and is slightly more extensive along the $[100]$ direction than the zone surrounding a plate which tapers to the edge (Fig. 37).

We were not able to determine the exact shape of an isolated plate which minimize the plastic zone because the potential functions ϕ and ψ cannot be obtained in closed form for plates of arbitrary shape. It is probable that a flat disc would be a better representation than a flat, square plate, but this shape could not be analyzed because in this case also closed forms of ϕ and ψ are not known. Based upon the analyses of the plastic zones around square, flat plates and tapered (ellipsoidal)

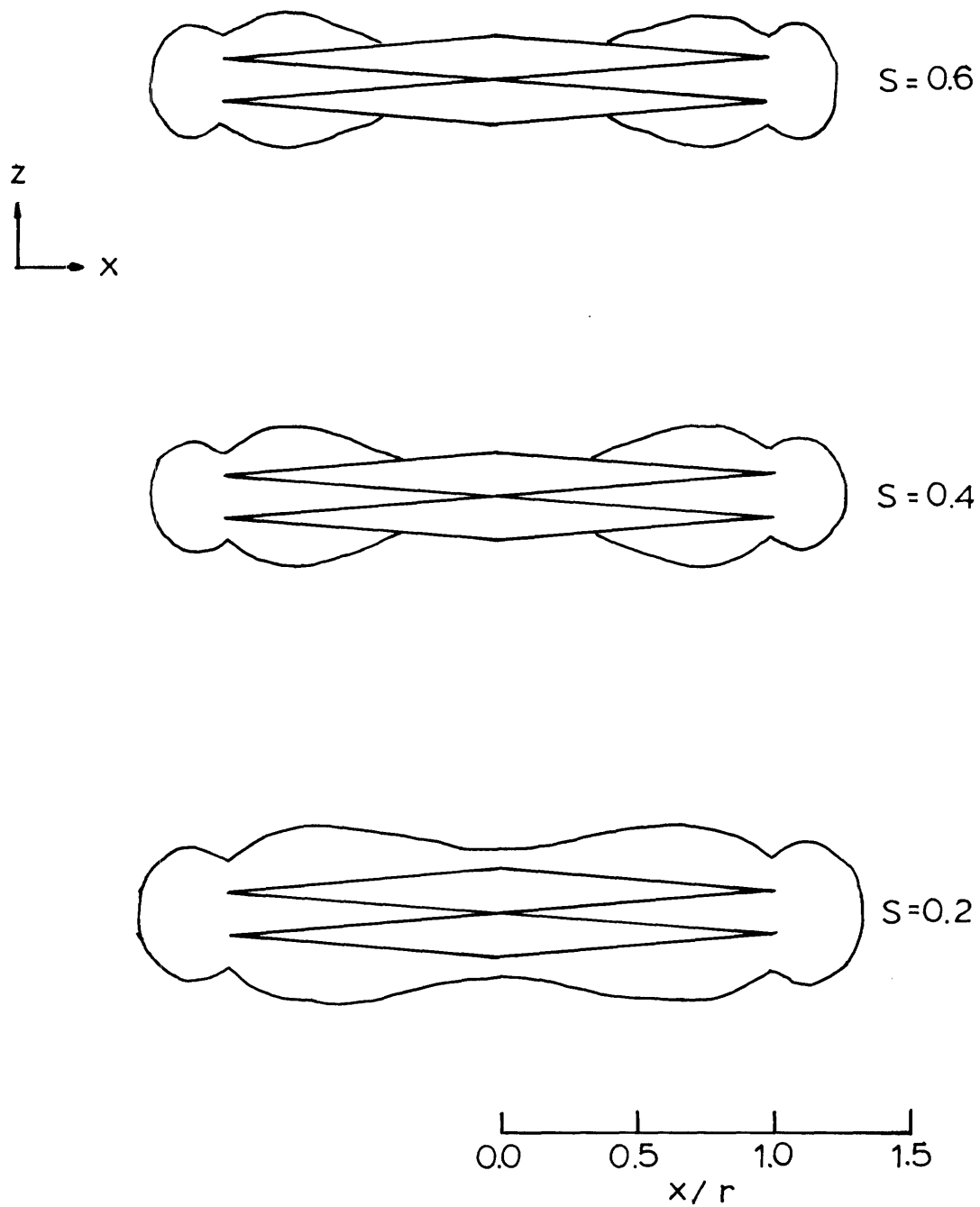


Figure 40. Matrix yield stress contours of an assembly of two ellipsoidal plates with opposite shear strain. Aspect ratio 0.08.

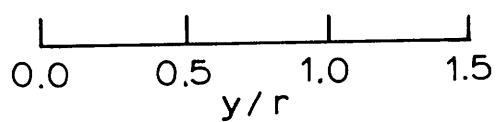
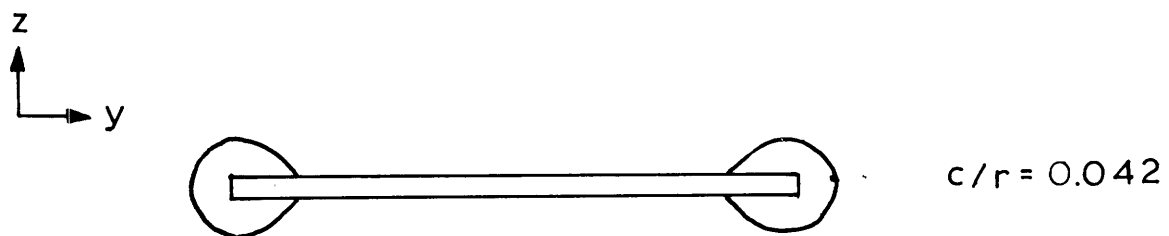
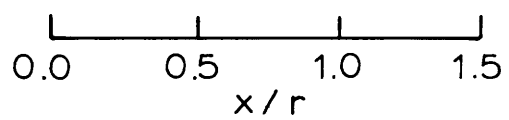
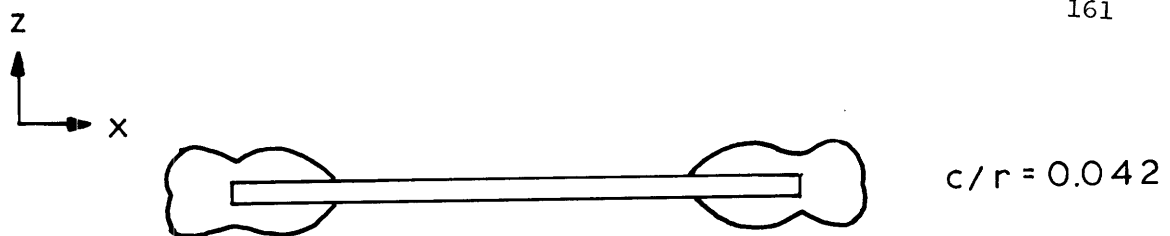


Figure 41. Matrix yield stress contours for square plate lying in xy plane with shear in x direction. $S=0.6$.



0.1 mm

Figure 42. An assembly of two plates with flat interface and tapered edge. $S = 0$.

plates, we conclude that the configuration most likely to minimize the volume of plastic deformation is parallel flat plates of opposite shear in contact over a large area, but with the plates, or pairs of plates, tapering to a point at the edges. Umemoto^[92] has found martensite plates in Fe₃Pt associated with other plates with nearly opposite shear directions and with habit planes that are nearly parallel ($P_1^A \cdot P_1^C \approx 23^\circ$) (Figure 42); a good example of the accommodation proposed here.

5.5.3 Anisotropic Calculation of the Elastic Strain Energy and The Stress Field

In the previous two sections, the elastic accommodation of martensite plates in austenite was discussed assuming that the plate is embedded in an isotropic elastic medium. The elastic moduli used in the computation are averages of the anisotropic elastic constants and the fact that a martensite plate has definite crystallographic orientations is ignored. It is known that ordered Fe₃Pt alloys are highly anisotropic at the M_s temperature. Since both the habit plane and the shape strain direction have irrational indices, it cannot be determined qualitatively what effect the increasing anisotropy of the austenite has on the elastic accommodation of the transformation strain. Hence an anisotropic calculation was undertaken to determine the elastic strain energy and the stress field in the matrix. As in the earlier calculations, a plate of martensite is assumed to be ellipsoidal. As in the isotropic case, this shape of the inclusion simplifies the mathematical formulation. In this section, we shall first discuss the elastic strain energy of an ellipsoidal inclusion in an infinite matrix, both

phases being anisotropic. The stress field calculation will be described later.

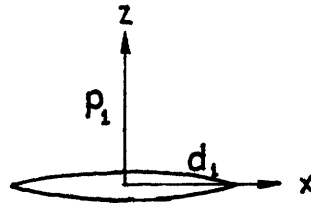
Eshelby first showed that^[105-107] when an ellipsoidal inclusion, which is embedded in an isotropic matrix, undergoes a uniform stress-free transformation strain e_{ij}^T , the constrained strain, e_{ij}^C , is also constant within the inclusion. He suggested that this result is also applicable in the anisotropic case. Subsequently, this suggestion was proved to be true.^[114-117] However, numerical values of the strain energy have only been obtained for the isotropic case^[118-120] despite the need for calculations based on anisotropic elasticity in many alloy systems.

Recently, Wert^[121] has calculated anisotropic strain energies associated with GP zones in the form of disc-shape precipitate using the approach of Kachaturyan^[122], with the assumption that the precipitate and the matrix have the same elastic constants. Eshelby's method does not require this restrictive assumption. Using this method Lee, et al.^[123] have calculated the anisotropic elastic strain energy of ellipsoidal precipitate as a function of aspect ratio and the orientation relationship between the precipitate and the matrix. They considered only the case of a pure dilatational stress-free transformation strain e_{ij}^{δ} . We shall present results pertinent to the martensitic transformation where the shape strain has a large shear component. The theory and the computation procedure are discussed in Appendix C, where a comparison with the exact isotropic calculation is also presented.

For ordered Fe_3Pt , the parameters which enter into the anisotropic calculation are listed in Table 12. Single-crystal elastic constants for the austenite are those given previously in Table 11. The martensite phase was assumed to have the same anisotropy ratio (2.35) as iron. The single-crystal elastic constants were then calculated from the polycrystalline elastic moduli. Results of the strain energy calculation are shown in Figures 43 and 44.

Figure 43 compares the elastic strain energy per unit volume, E_V , from three different models. The energy deduced from the model which assumes an anisotropic medium shows a large reduction from that given by the isotropic model in which the isotropic shear modulus is used ($G = C_{44}$, $A = 1$). However, it does not deviate significantly from the isotropic model in which the average shear modulus is used. The distinction between an isotropic modulus and an average modulus was discussed in Section 4.3. For small aspect ratios, the anisotropic elastic energy varies linearly with c/r . It is larger than the isotropic approximation by about 10%. Thus, as far as thermoelastic equilibrium is concerned, an anisotropic calculation does not alter to a significant extent the constant factor A in the elastic strain energy term in Eq'n (41) for the particular orientation of the martensite plate under consideration. Figure 44 shows the effect of the changing elastic properties of the austenite at M_s on ordering. For small c/r , the elastic energy in the ordered state $S = 0.6$ is reduced by a factor of two from the disordered state. This is approximately the same result one obtains from an isotropic calculation where the average shear modulus

Table 12. Input parameters for the anisotropic calculation of elastic strain energy and stress fields in ordered Fe₃Pt



habit plane $p_1 = (0.1641527 \quad 0.8207635 \quad 0.547175)$

shape strain $d_1 = -0.2218758 \quad 0.5712076 \quad -0.7902487$

$m_1 = 0.20$

Input into computer program:

stress-free transformation strain

$$e_{ij}^T * = \begin{bmatrix} 0 & 0 & 0.1 \\ 0 & 0 & 0 \\ 0.1 & 0 & 0 \end{bmatrix}$$

orientation of ellipsoid

$$\begin{bmatrix} x \\ y \\ z \end{bmatrix}_\gamma = \begin{bmatrix} -0.222 & 0.571 & -0.790 \\ -0.961 & 0.009 & 0.276 \\ 0.164 & 0.821 & 0.547 \end{bmatrix}$$

$$\begin{bmatrix} x \\ y \\ z \end{bmatrix}_\alpha = \begin{bmatrix} -0.550 & -0.379 & 0.745 \\ -0.700 & 0.696 & -0.163 \\ -0.459 & -0.611 & -0.646 \end{bmatrix}$$

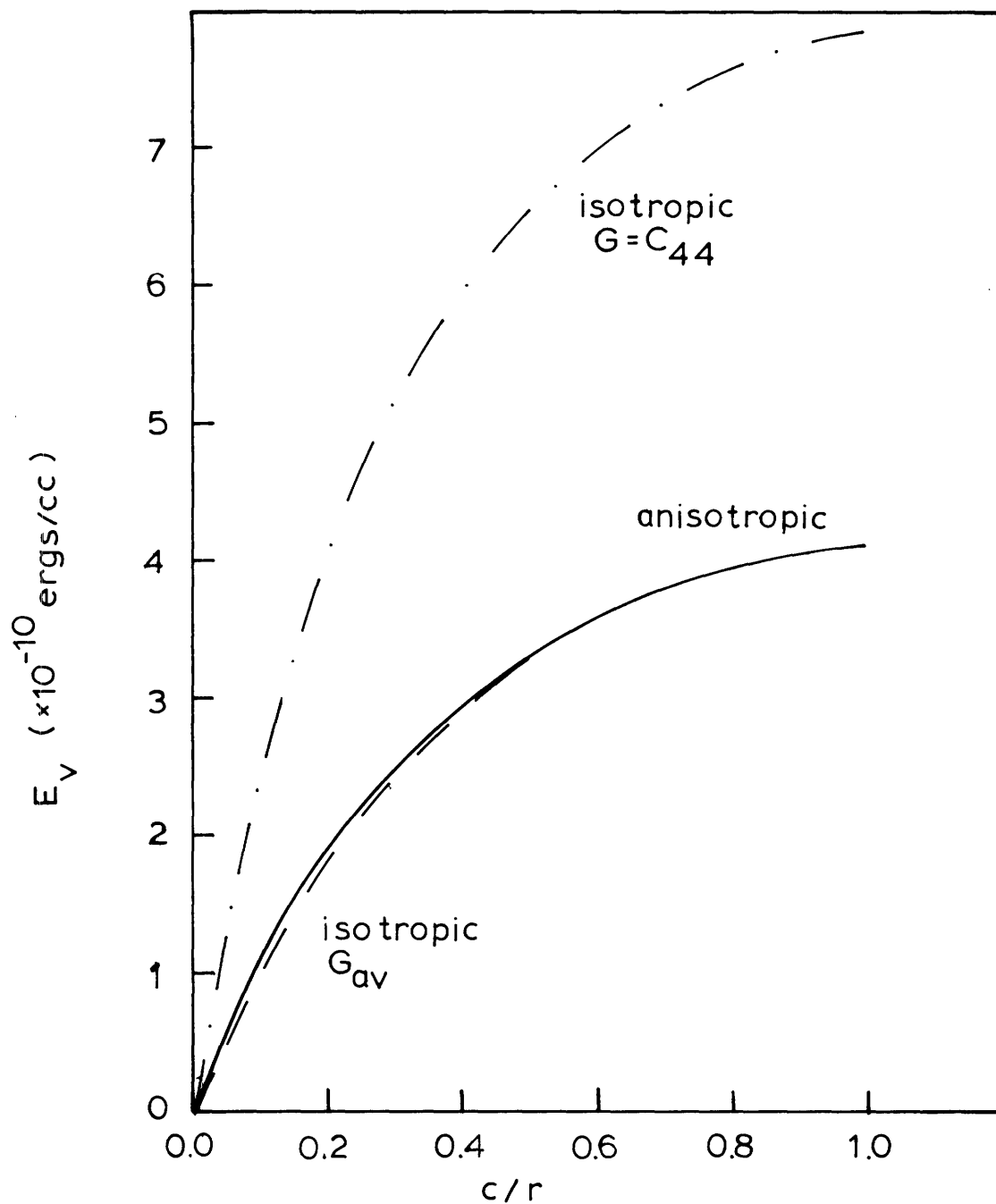


Figure 43. Elastic strain energy of an ellipsoidal plate of martensite in austenite at M_s as a function of aspect ratio, $S = 0.6$.

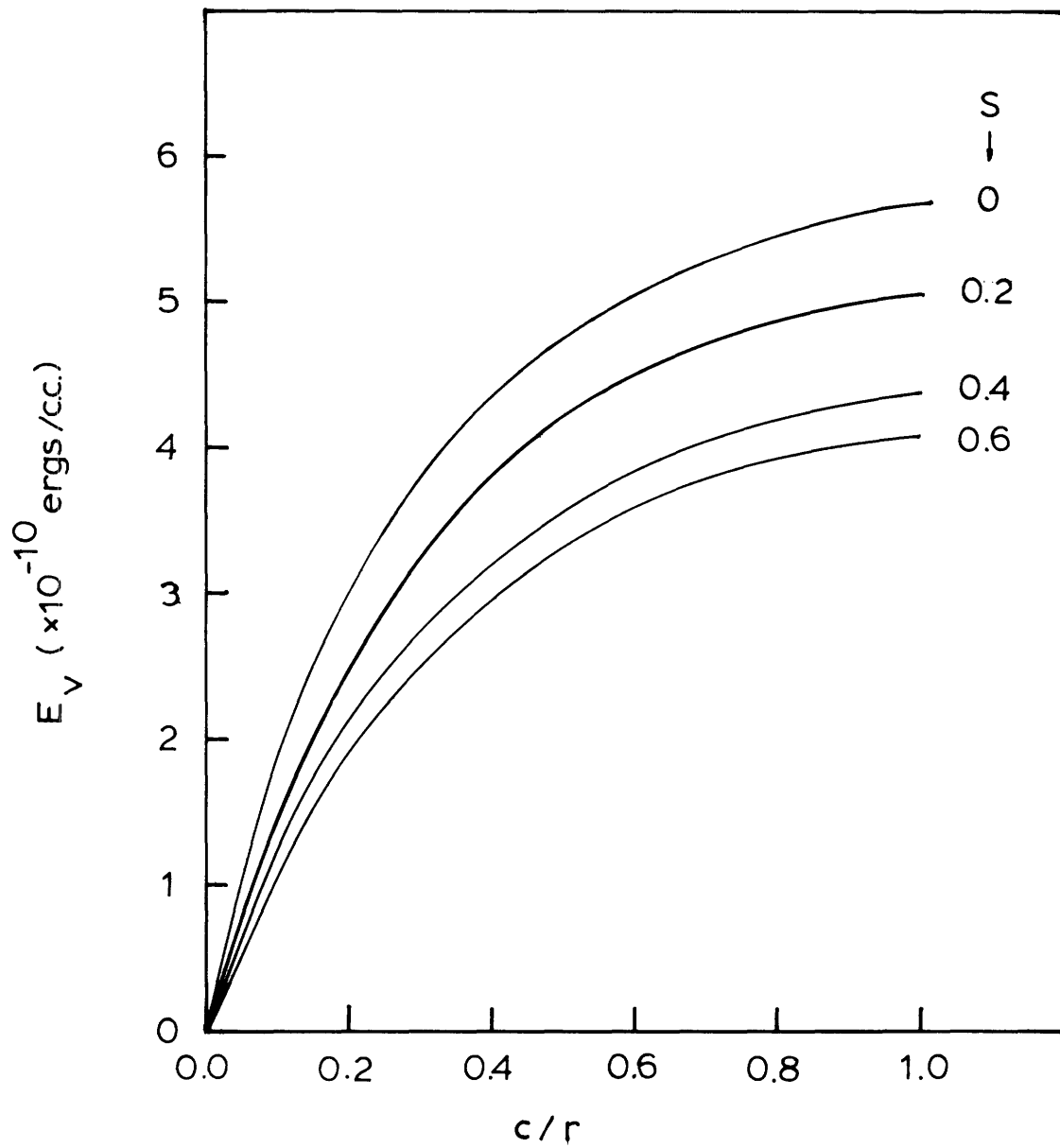


Figure 44. Anisotropic strain energy of an ellipsoidal plate of martensite in austenite at M_S as a function of aspect ratio.

for $S = 0.6$ is one-half of the value for the disordered alloy.

The calculation of the stress fields in an anisotropic matrix surrounding an ellipsoidal inclusion is similar to the evaluation of the elastic strain energy. The theory and the computation procedure are discussed in Appendix D. To obtain the stresses at each point in the matrix, an integration over the ellipsoid has to be carried out. It was not possible to do extensive calculation because of the amount of computing time involved. The calculation presented here utilized 1024 units of integration. Figure D1 shows that in the isotropic limit, the result from this computer program agrees with the exact isotropic calculation to within 10% for distances greater than $0.25r$ along the z axis. Results for the ordered state $S = 0.4$ are shown in Table 13. In the isotropic case, all stresses other than σ_{13} are zero along the principal axes of the ellipsoidal plate. In the coordinate system under consideration ($\hat{x} \parallel [0.\bar{2}2 \ 0.57 \ 0.\bar{7}9]$, $\hat{z} \parallel [3 \ 15 \ 10]$), all stresses are non-zero along the \hat{z} axis. For a $(3 \ 15 \ 10)$ habit plane and $[0.\bar{2}2 \ 0.57 \ 0.\bar{7}9]$ shear direction, the nearest slip system in the austenite is $(1\bar{1}1)[011]$. The resolved shear stress on this slip system is determined from

$$\sigma_{ns}^{\text{resolved}} = a_{ni} a_{sj} \sigma_{ij}' \quad (52)$$

where $\hat{n} = \frac{1}{\sqrt{3}} [1\bar{1}1]$, $\hat{s} = \frac{1}{\sqrt{2}} [011]$, σ_{ij}' are the stresses in the coordinate system of the ellipsoid and a_{ij} are components of the coordinate trans-

formation matrix. Values of $\sigma_{ns}^{\text{resolved}}$ are listed in the last column of Table 13. The critical shear stress for slip, σ_{crss} , is assumed to be $\sigma_Y/\sqrt{3}$ where σ_Y is the uniaxial flow stress. For an aspect ratio of 0.04, σ_{crss} is exceeded between 0.3r and 0.4r. It occurs at a larger distance from the interface than indicated by the isotropic calculation (Figure 38). This implies that the critical aspect ratio at which r_p vanishes will be smaller. The result for $c/r = 0.02$ indicates that σ_{crss} is not exceeded along the z axis in a plate of this size. If this aspect ratio is taken to be the lower limit to the critical aspect ratio, the corresponding chemical driving force is 100 cal/mole. Hence an anisotropic calculation has not changed significantly the estimate of the upper limit of Δg_c for the thermoelastic growth of a single martensite plate.

Table 13. The stresses along the z axis due to an ellipsoidal plate of martensite in an anisotropic matrix of austenite. S=0.4. ($\hat{z} \parallel [3 \ 15 \ 10]$)

(stress in units of 10^9 dyn/cm)

z/r	σ_{11}	σ_{22}	σ_{33}	σ_{23}	σ_{31}	σ_{12}	σ_{resolved}
$\frac{c}{r}=0.04$							
0	0.55	3.10	0.32	0.13	-5.20	0.05	4.30
0.3	-3.30	0.77	1.60	0.42	-6.80	-2.40	5.45
0.4	-3.20	0.39	1.30	-0.32	-4.10	-0.55	3.20
0.5	-1.80	0.59	-1.20	-0.52	-1.90	-0.01	1.62
0.6	-0.70	0.57	-0.75	-0.27	-1.20	0.12	1.05
$\frac{c}{r}=0.02$							
0	0.37	1.85	0.17	0.07	-2.80	0.07	2.30
0.25	-2.30	1.10	-4.10	-0.86	-3.30	-1.20	3.20
0.3	-1.50	0.37	1.25	0.32	-3.50	-1.20	2.70
0.4	-1.60	0.20	0.64	-0.18	-2.00	-0.25	1.60

THEORETICAL CALCULATION OF ΔG^{chem} AT M_s

6.1 A Nucleation Model

In a previous chapter, we have derived an upper limit to the chemical driving force at M_s that would permit thermoelastic growth of a plate of martensite in Fe_3Pt . This upper limit to ΔG^{chem} is one-third of the value that has been assumed by previous investigators for a typical burst type martensitic transformation. In Fe-30Ni, the magnitude of $\Delta G^{\text{fcc} \rightarrow \text{bcc}}$ at the observed M_s temperature is estimated to be about 300 cal/mole (1260 J/mole).^[136] Parallel estimates of ΔG^{chem} in disordered Fe_3Pt generally assume the same value as Fe-30Ni^[110,125] and it remains to be determined whether a direct theoretical calculation of ΔG^{chem} will show a decrease in its magnitude on ordering Fe_3Pt . We here use a nucleation model proposed by Olson and Cohen^[125] as the basis for such a calculation.

Olson and Cohen proposed that the general mechanism of martensitic nucleation is by faulting from groups of existing dislocations. The free energy of such faults relative to the perfect lattice may be expressed in terms of the chemical free energy difference between parent and product phases (ΔG^{chem}), a strain energy (E^{str}), and a surface energy (σ). The fault energy per unit area, γ , for a fault n planes in thickness can be written as:

$$\gamma(n) = n\rho_A (\Delta G^{\text{chem}} + E^{\text{str}}) + 2\sigma \quad (53)$$

where ρ_A is the density of atoms in a close-packed plane in moles per

unit area, ΔG^{chem} and E^{str} are defined as molar quantities. Under conditions where the volume energy change ($\Delta G^{\text{chem}} + E^{\text{str}}$) is negative, the fault energy decreases with increasing fault thickness n . The volume energy change is negative when the chemical driving force ($-\Delta G^{\text{chem}}$) is greater than the strain energy (E^{str}). This occurs below T_0^{coherent} , the temperature at which the parent and coherent product structures have equal volume free energies. The condition $\gamma(n) \leq 0$ defines the temperature at which nucleation of martensite can proceed spontaneously from existing defects of size n . The chemical free energy difference at the observed M_s temperature can now be calculated. By setting $\gamma = 0$ in Eq'n (53) and rearranging:

$$\Delta G^{\text{chem}} = - \left(\frac{2\sigma}{np_A} + E^{\text{str}} \right) \quad (54)$$

The fcc \rightarrow bcc transformation can be described in terms of a modified Bogers-Burgers two-shear mechanism. [137] The resulting martensite embryo is semicoherent and has an interfacial structure illustrated in Figure 45a. There are two sets of dislocations in the interface. The first set consists of seven $\frac{a_{\text{bcc}}}{8} \langle 01\bar{1} \rangle$ partial dislocations followed every eighth plane by an $\frac{a_{\text{bcc}}}{8} \langle 0\bar{1}1 \rangle$ partial dislocation and an $\frac{a_{\text{fcc}}}{6} \langle 112 \rangle$ Shockley partial dislocation.

The latter pair of dislocations maintain an unrotated fault plane by cancelling the edge components of the $\frac{a_{\text{bcc}}}{8} \langle 01\bar{1} \rangle$ dislocation displacements. The remaining portion of the screw component has a long range strain field which is cancelled by a second set of lattice screw

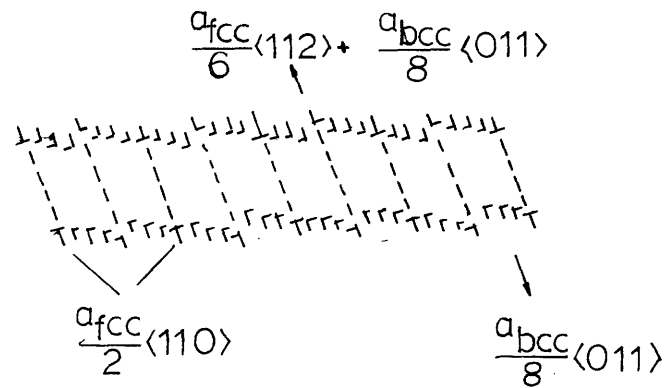


Figure 45a. Interfacial structure of nucleus in fcc \rightarrow bcc transformation.

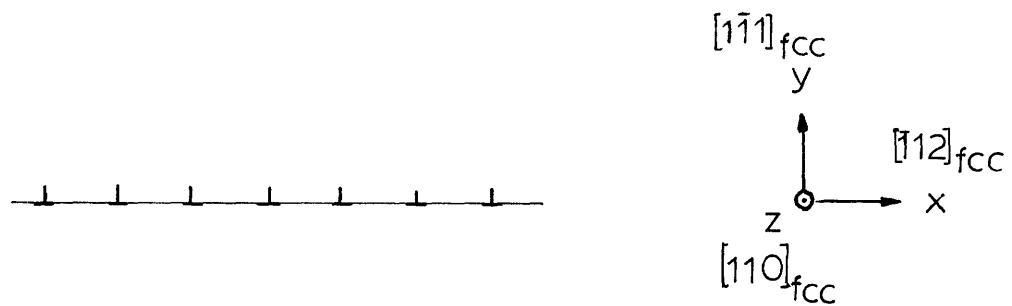


Figure 45b. An infinite $[110](1\bar{1}1)$ screw dislocation wall.

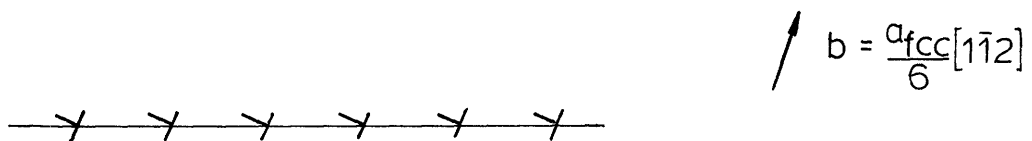


Figure 45c. An infinite $[110](1\bar{1}1)$ edge dislocation wall.

dislocations oppositely directed to the screw component of the $\frac{a_{bcc}}{8} \langle 01\bar{1} \rangle$ displacements. These dislocations will have a Burgers vector of $\frac{a_{fcc}}{2} \langle \bar{1}10 \rangle$ and are spaced every eighth $\{011\}_{bcc}$ plane. Both sets of dislocations contribute to the surface energy of the fault.

We shall calculate the energy associated with a simplified interface consisting of $\frac{a_{fcc}}{6} \langle 112 \rangle$ partial dislocations spaced every eighth $\{011\}_{bcc}$ plane and $\frac{a_{fcc}}{2} \langle \bar{1}10 \rangle$ screw dislocations spaced the same distance apart. The long-range strain field generated by these two sets of dislocations is assumed to be cancelled by the $\frac{a_{bcc}}{8} \langle 011 \rangle$ dislocations which are represented as a continuous distribution in this simplified calculation. In the coordinate system we are considering, there is no interaction between a screw dislocation and an edge dislocation. [126] Hence, the interface can be further decomposed into one consisting of an array of $\frac{a_{fcc}}{2} \langle \bar{1}10 \rangle$ screw dislocations and one made up of $\frac{a_{fcc}}{6} \langle 112 \rangle$ edge dislocations.

Transformation strains which contribute to E^{str} in Eq'n (53) arise from the 5.4% expansion normal to $(111)_{fcc}$ and the 3.6% expansion normal to $(011)_{bcc}$ which accompany the "hard-sphere" shears of the Bogers-Burgers mechanism. In addition, a uniform contraction of 2.9% must be superimposed to account for the zero volume change during transformation in ordered Fe_3Pt . In the coordinate system $\hat{x}_2 || \langle 111 \rangle_{fcc}$, $\hat{x}_3 || \langle 110 \rangle_{fcc}$, we can sum these contributions to obtain the stress-free transformation strain ϵ_{ij}^T :

$$\epsilon_{ij}^T = \begin{bmatrix} 0 & 0 & 0 \\ 0 & .054 & 0 \\ 0 & 0 & 0 \end{bmatrix} + \begin{bmatrix} .031 & .011 & 0 \\ .011 & .004 & 0 \\ 0 & 0 & 0 \end{bmatrix} + \begin{bmatrix} -.029 & 0 & 0 \\ 0 & -.029 & 0 \\ 0 & 0 & -.029 \end{bmatrix} = \begin{bmatrix} 0.002 & 0.011 & 0 \\ 0.011 & 0.028 & 0 \\ 0 & 0 & -0.03 \end{bmatrix}$$

Contributions of the surface energy σ and the strain energy E^{str} to the chemical free energy difference at M_s , ΔG^{chem} will be discussed in the following sections. The values of elastic constants and lattice parameter used in the calculations were those listed in Table 11.

6.2 An Infinite Screw Dislocation Wall

We assume an infinite array of screw dislocations with Burgers' vector $\frac{a_{\text{fcc}}}{2} [110]$ lying in the $(1\bar{1}1)$ plane and separated by a distance equal to 19.39\AA (Figure 45b). The problem of elastic stresses associated with interfacial screw dislocations in an anisotropic medium has been solved by Chou, et al. [127]. The formulae appropriate to the coordinate system under consideration here are listed in Appendix E. It is easily seen that the σ_{xz} stress, given by

$$\sigma_{xz}(x,y) = \frac{Lb_s}{2D} \left[\frac{L \sinh 2p - C_{45} \sin 2q}{C_{44} (\cosh 2p - \cos 2q)} \right] \quad (56)$$

where $p = -\frac{L}{C_{44}} \frac{\pi y}{D}$ and $q = \frac{\pi x}{D} + \frac{C_{45}}{C_{44}} \frac{\pi y}{D}$, has a finite value at large y .

This long-range strain field cancels the screw component of the $\frac{a_{\text{bcc}}}{8} \langle 110 \rangle$ dislocations discussed previously in Section 6.1. In calculating the energy of the dislocation wall, this constant strain must be subtracted from the dislocation stress field σ_{xz} . The energy per unit area of the dislocation wall is then given by

$$\begin{aligned}
E &= \frac{b_s}{2D} \int_{r_0}^R [\sigma_{xz}(x=0) - \sigma_{xz}(x=0, y=R)] dy \\
&= \frac{Lb_s^2}{4\pi D} \left\{ \frac{\pi\alpha r_0}{D} - \frac{1}{2} \ln 2 - \frac{1}{2} \ln \left[\cosh \frac{2\pi\alpha r_0}{D} - \cos \frac{2\pi\beta r_0}{D} \right] \right\} \quad (57)
\end{aligned}$$

where r_0 and R are the inner and outer cutoff radii,

$$\alpha = L/C_{44}, \quad \beta = -C_{45}/C_{44}$$

For the elastic constant matrix in Appendix E, the parameters reduce to

$$L = C_{44}^0/\sqrt{A}, \quad \alpha = 3\sqrt{A}/(2+A), \quad \beta = \sqrt{2}(A-1)/(2+A)$$

where A is the anisotropy ratio. A plot of the σ_{xz} stress as a function of distance from the dislocation wall is shown in Figure 46. A minimum exists at a distance of four Burger's vector from the interface. This minimum is more pronounced as the medium becomes more anisotropic. After subtracting the constant long-range stress from σ_{xz} , most of the contribution to the energy comes from the region near the core of the dislocations. Hence the energy of the screw dislocation wall is very sensitive to the choice of the core cutoff radius r_0 . If the value r_0/b_s is varied between 0.5 and 1, the energy changes by a factor of two in the disordered state, and by as much as a factor of four in the highly anisotropic ordered case. Comparing the disordered

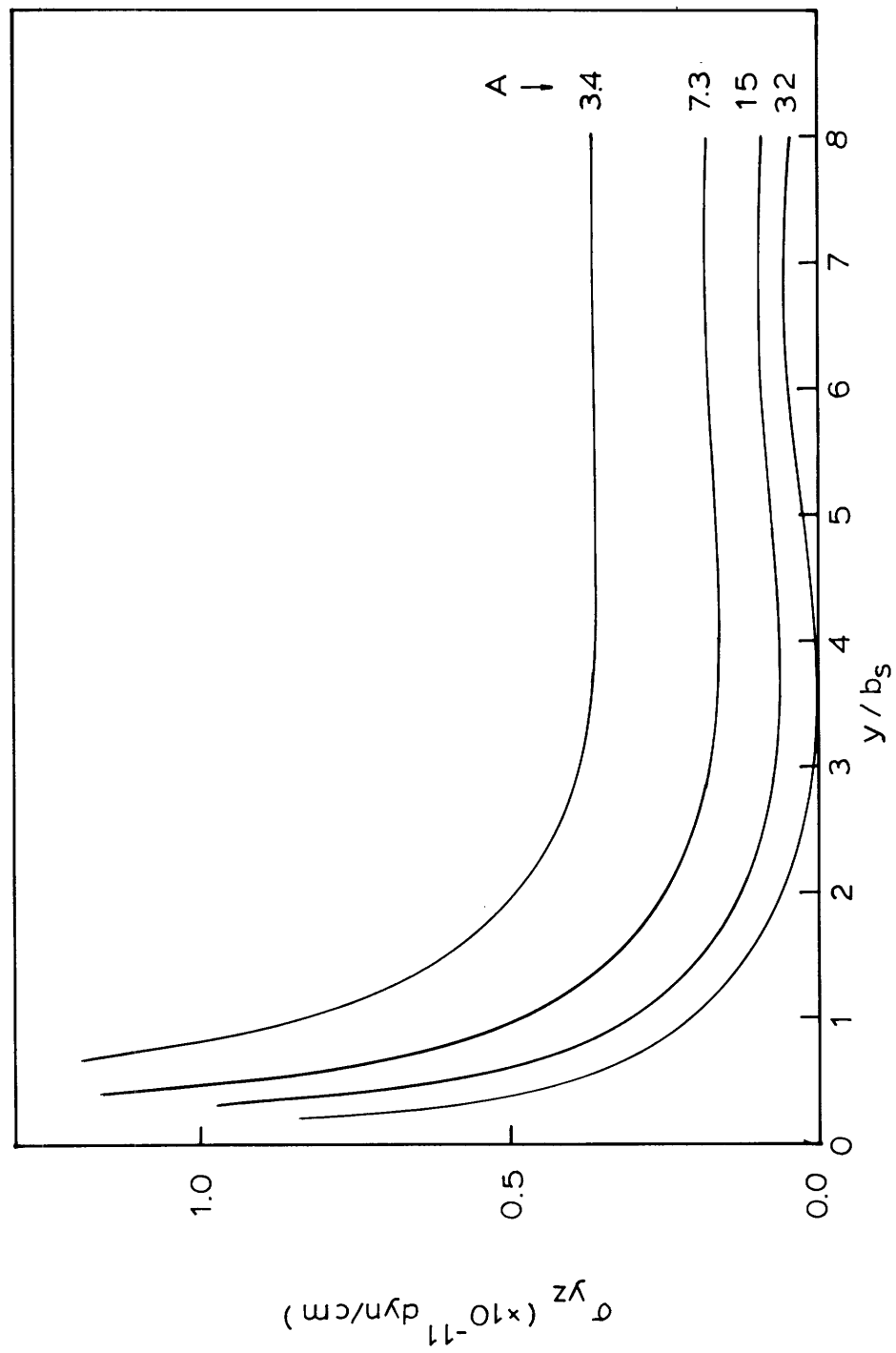


Figure 46. The σ_{yz} stress of an infinite $[110](\bar{1}\bar{1}1)$ screw dislocation wall.

$$b_s = \frac{a}{2} [110].$$

($A = 3.4$) and the ordered states, a reduction of an order of magnitude in the energy is seen. This is much larger than is predicted by an isotropic approximation, which assumes that the reduction in energy is proportional to the decrease in the average shear modulus. The calculated energies associated with an infinite screw dislocation wall are given in Table 14 for $r_o/b_s = 1$.

6.3 An Infinite Edge Dislocation Wall

We consider an infinite array of $\frac{a_{\text{fcc}}}{6} \langle 1\bar{1}\bar{2} \rangle$ edge dislocations lying in the $(1\bar{1}\bar{1})$ plane separated by the same distance as the screw dislocations considered in Section 6.2. These edge dislocations run along the $[110]$ direction (Figure 45c). The $\frac{a_{\text{fcc}}}{6} [1\bar{1}\bar{2}]$ edge dislocation is a partial dislocation in the fcc lattice. It has both glide and climb components. The general method of calculating stress fields of edge dislocations in an anisotropic media has been discussed in detail. [126-130] We obtained the stress fields for a $[110](1\bar{1}\bar{1})$ edge dislocation with Burgers' vector $b = (b_e, b_n, 0)$ from the expressions given by Chou, et al. [130] for a $[110](001)$ edge dislocation through a tensor transformation. The formulae are listed in Appendix F. Relevant stresses for the calculation of energy associated with the edge dislocation wall are σ_{xx} and σ_{xy} . These stress fields of a single edge dislocation were calculated on a computer and a summation over 2000 dislocations was made to approximate the infinite edge dislocation wall. Contributions from the far-away dislocations amount to less than 1% in the long-range stress fields.

σ_{xx} and σ_{xy} are shown in Fig. 47. There is a long-range stress field in σ_{xx} which cancels the edge component of the $\frac{a_{\text{bcc}}}{8} [110]$ dis-

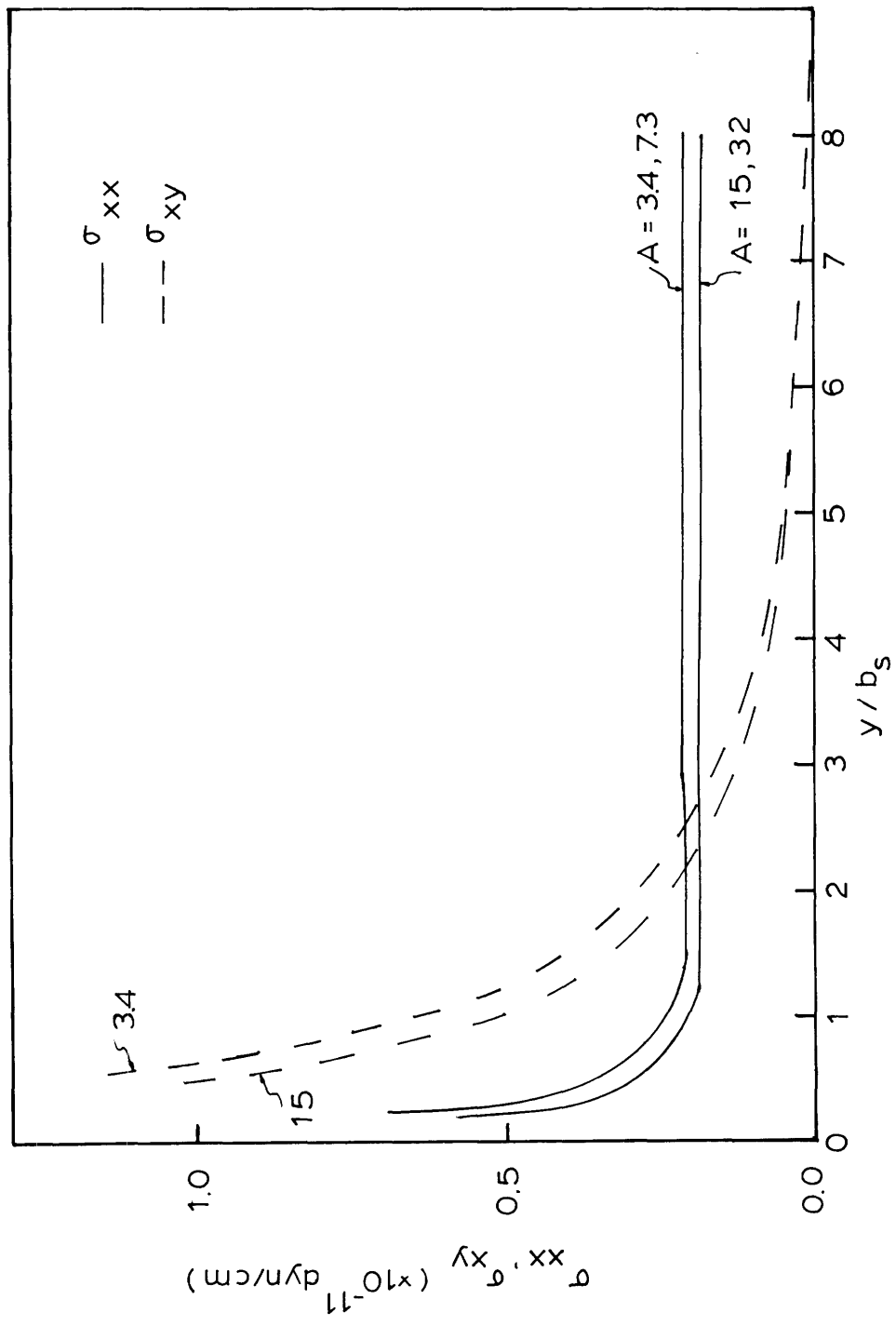


Figure 47. The σ_{xx} and σ_{xy} stresses of an infinite $[110](\bar{1}\bar{1})$ edge dislocation wall. $b = \frac{a}{6}[\bar{1}\bar{1}2]$.

locations as previously discussed. Again we subtracted this constant stress from σ_{xx} in performing the energy calculation. The remaining portion of σ_{xx} is localized near the core of the dislocations. Hence the energy due to the σ_{xx} stress is sensitive to the choice of the inner cut off radius, as in the case of the screw dislocations. σ_{xy} decreases monotonically with the distance from the dislocation wall. There is no long range component. The effect of increasing anisotropy and the changing values of elastic constants, as the austenite is ordered in Fe_3Pt , is a small decrease in the magnitude and the localization of the σ_{xx} and σ_{xy} stresses near the dislocation interface.

After subtracting the long-range component from σ_{xx} , the energy per unit area of the edge dislocation wall is:

$$E = \frac{1}{2D} \left\{ b_e \int_{r_0}^R [\sigma_{xx}^{e+n}(x=0) - \sigma_{xx}^{e+n}(x=0, y=R)] dy \right. \\ \left. + b_n \int_{r_0}^R [\sigma_{xy}^{e+n}(x=0)] dy \right\} \quad (58)$$

where b_e and b_n are the glide and climb components of the Burgers' vector and D the spacing between dislocations. The integration was performed numerically and the results are listed in Table 14.

The major contribution to the energy of the edge dislocation wall comes from the σ_{xy} stress because of its larger magnitude and the larger climb component of the Burgers' vector which interacts with this stress. The results indicate that σ_{xy} does not have a strong dependence on the

anisotropy of the lattice. Consequently, the energy showed a decrease of only about 20% in the ordered state. This decrease is small compared to an order of magnitude decrease calculated for the screw dislocation wall. The energy per unit area of the interface, which is the sum of the screw and the edge dislocation walls, changes from 190 erg/cm^2 in the disordered state to 112 erg/cm^2 in the state with degree of order $S = 0.6$.

6.4 Coherent Strain Energy

As discussed in Section 6.1, the coherent strain energy, E^{str} , in the Olson-Cohen model arises from the hard sphere nature of the Bogers-Burgers shear mechanism with an addition uniform contraction to arrive at the correct lattice parameter. The computer program described in Section 5.5.3 was used to calculate this energy. For the BCC lattice, we used the values of C_{11} , C_{12} and C_{44} determined from the polycrystalline elastic moduli of Fe-22a/oPt martensite (Section 4.3.3) and assuming that the martensite has the same anisotropy ratio of iron ($A = 2.35$). Two shapes of the martensite nucleus were assumed: a sphere and a rod with the axis along the $[110]$ direction. It was found that the energy per unit volume in the rod-shape nucleus is three times larger than a spherical nucleus. Evidently, $[110]$ is not the direction that minimizes E^{str} for a rod-shape inclusion. The stress-free transformation strain e_{ij}^T giving rise to the coherent strain energy is, in the ordered states (coordinate system $\hat{x}_2 || [\bar{1}\bar{1}1]$ and $\hat{x}_3 [110]$),

$$e_{ij}^T = \begin{bmatrix} .002 & .011 & 0 \\ .011 & .028 & 0 \\ 0 & 0 & -.03 \end{bmatrix} \quad (59a)$$

and in the disordered state,

$$e_{ij}^T = \begin{bmatrix} .006 & .011 & 0 \\ .011 & .032 & 0 \\ 0 & 0 & -.025 \end{bmatrix} \quad (59b)$$

The results for a spherical nucleus are listed in Table 14. The coherent strain energy decreases from 128 cal/mole in the disordered state to 88.5 cal/mole for $s = 0.6$.

6.5 ΔG^{chem} at M_s and the Effect of Tetragonality

The total energy of a fault, γ , described in the Olson-Cohen model depends on the chemical free energy difference ΔG^{chem} , coherent strain energy E^{str} , surface energy σ and the thickness of the fault n . The condition $\gamma < 0$ defines a critical fault thickness n^* for the spontaneous formation of a martensite nucleus. Assuming that in the disordered state, $\Delta G^{\text{chem}}(M_s)$ is 300 cal/mole as in the case of Fe-30Ni and with the values of σ and E^{str} determined in the previous sections, $n^* = 19$. This is equivalent to a group of 6 dislocations in the Olson-Cohen model. If we assume that the same number of dislocations are required at the nucleation stage in both the disordered and ordered states ΔG^{chem} for the ordered states can be calculated using Eq'n 54. The results are given in the last column of Table 14. $\Delta G^{\text{chem}}(M_s)$ decreases from 300 cal/mole in the disordered

Table 14. Theoretical calculation of ΔG^{chem} at M_s based on the Olson-Cohen nucleation model (fcc \rightarrow bcc transformation)

$$n^* = 19 \quad \rho_A = 2.76 \times 10^{-9} \text{ mole/cm}^2$$

S	A	screw wall ($r_o/b_s=1$)	edge wall ($r_o/b=1$)	σ (ergs/cm ²)	$\frac{2\sigma}{n^*\rho_A}$	E^{str} (cal/mole)	ΔG^{chem} (cal/mole)
0	3.4	58.4	131.8	190.2	165.5	128.2	-293.7
0.2	7.3	24.2	125.5	149.7	130.3	110.6	-230.7
0.4	15	9.9	107.8	117.7	102.4	94.7	-197.1
0.6	32	3.4	108.4	111.8	97.3	88.5	-185.8

state to 186 cal/mole in the state with $S = 0.6$. A chemical driving force of this magnitude is larger than the upper limit of 108 cal/mole that we have established in Chapter 5. It is unlikely that thermo-elastic growth can be achieved under this condition.

In the above discussion we have neglected friction stress. If a friction stress τ_0 is associated with dislocation motion, the force opposing the dissociation of a fault of size n is $n\tau_0 b$ where b is the Burgers' vector. The condition for spontaneous formation of a martensite nucleus is no longer $\gamma \leq 0$ but

$$\gamma \leq -n\tau_0 b$$

Combining with Eq'n 54, the chemical free-energy difference at M_s

$$\Delta G^{\text{chem}} = - \left(\frac{2\sigma}{n\rho_A} + E^{\text{str}} \right) - \frac{\tau_0 b}{\rho_A} \quad (60)$$

With the assumed value of ΔG^{chem} (-300 cal/mole) and the previous calculated σ and E^{str} for disordered Fe_3Pt , a finite value of τ_0 implies a larger n . The critical fault is thicker and involves more dislocations. It is not clear how changes in anisotropy and elastic properties of the austenite on ordering affect the friction stress. In an ideal lattice, the friction stress originates from the Peierls' stress of a periodic lattice. Nabarro^[131] showed that the critical shear stress to move a dislocation against a periodic lattice is

$$\tau_0 = \frac{2G}{1-\nu} e^{-\xi/(1-\nu)} \quad (61)$$

where G and ν are the shear modulus and the Poisson's ratio of the lattice and ξ is a measure of the width of a dislocation. If the appropriate values are used, τ_0 in ordered Fe_3Pt is 2 to 5% of that in disordered Fe_3Pt . The stress necessary to move a dislocation in a real crystal is higher because of additional resistance of impurities or vacant lattice sites. Not knowing the magnitude of the friction stress in Fe_3Pt , it is not possible to estimate the effect of τ_0 on the critical size of the fault.

So far we have based our calculation on the assumption of a fcc to bcc transformation in the ordered Fe_3Pt alloy. It is known, however, that the martensite becomes tetragonal as the austenite is ordered. The tetragonality reduces the Bain deformation by about 30% (Appendix G). It is expected, then, that both the coherent transformation strain and the number of interfacial dislocations are decreased. If the same number of $\frac{a_{\text{fcc}}}{2}\langle 110 \rangle$ screw dislocations are present to accomplish the first Bogers-Burgers shear as in the disordered case, each of these dislocations will spread over a larger number of $\{111\}$ planes because of the smaller shear in the Bain deformation. As a result, the thickness of the fault will increase. Taking into account of tetragonality, a calculation was made based on the following assumptions: the coherent transformation strain e_{ij}^T is decreased by 0.7; the spacing, D , of the interfacial dislocations discussed in Sections 6.2 and 6.3 is increased by a factor of $(1/0.7)$; the critical thickness of the fault, n^* , is increased by $(1/0.7)$. The results are listed in Table 15. A further reduction in ΔG^{chem} to 106 cal/mole is achieved in this rough calculation.

Although this value is within the upper limit of ΔG^{chem} established in Chapter 5, it is larger than the chemical driving force associated with thermoelastic martensites in copper- and gold-based alloys. In these systems, the parent phase has a bcc crystal structure. The chemical free energy difference at M_s is generally of the order of 10 cal/mole. [138]

Thus the martensitic transformation in noble-metal-base alloys requires considerably less nucleation free energy (by a factor of 30) than that in disordered ferrous alloys (300 cal/mole). It is not clear whether or not ordered Fe_3Pt , the parent phase of which has fcc crystal structure, has a similar value of ΔG^{chem} as the β type alloys. In ordered Fe_3Pt , tetragonality of the martensite phase reduces the Bain deformation in the fcc \rightarrow bct transformation, (Appendix G). In our estimate of ΔG^{chem} at M_s for the fcc - bct transformation, the role of tetragonality is accounted for by introducing a fudge factor to the parameters associated with the nucleus in the fcc - bcc transformation described by the Olson-Cohen model. However, because the Bain deformation is quite different in the two cases, different dislocation movement might be required to accomplish the fcc - bct transformation, resulting in a different interfacial structure of the nucleus. It is possible that a lower estimate of ΔG^{chem} at M_s can be achieved if the calculation is based on a correct description of the dislocation motion.

Table 15. Theoretical calculation of ΔG^{chem} at M_s (fcc \rightarrow bcc transformation)

$n^* = 27$ for $S = 0.2, 0.4$ and 0.6

$n^* = 19$ for $S = 0$ $\rho_A = 2.76 \times 10^{-9}$ mole/cm²

S	A	screw wall ($r_o/b_s=1$)	edge wall ($r_o/b=1$)	σ (ergs/cm ²)	$\frac{2\sigma}{n^* \rho_A}$	E^{str} (cal/mole)	ΔG^{chem} (cal/mole)
0	3.4	58.4	131.8	190.2	165.5	128.2	-293.7
0.2	7.3	31.4	125.5	156.9	99.6	54.2	-153.8
0.4	15	16.4	90.2	106.6	67.7	46.4	-114.4
0.6	32	8.9	90.5	99.4	63.1	43.4	-106.5

CHAPTER 7CONCLUSIONS

1. The ordering kinetics of Fe_3Pt was studied by "short-time" annealing at 650°C and by equilibrium annealing at various temperatures below the critical ordering temperature. From X-ray diffraction and elastic constant measurements, it is concluded that ordering in Fe_3Pt is by a nucleation and growth mechanism. The growth of the ordered domains is slow.
2. The C_L elastic constant softens above the Curie temperature, passes through a minimum and increases again at lower temperatures. The minimum becomes broader and shallower with increasing degree of order. For the two shear constants C and C' , the magnetic contribution is negative and begins near the Curie temperature. They decrease monotonically as the temperature decreases.
3. Softening of the C and C' elastic constants decreases as the austenite is highly ordered. This means that the Invar effect decreases in magnitude with increasing degree of order in Fe_3Pt . This behavior is explained qualitatively by the spatial dependence of a localized exchange integral. On the Bethe curve Fe_3Pt , in its various ordered states, lies in the range where the first derivative of the exchange integral is positive. In this range of interatomic separation, the exchange interaction between γ -Fe atoms is antiferromagnetic and that between Fe and Pt atoms, ferromagnetic.
4. Increasing softening of the elastic moduli of the austenite at the M_s temperature as it is ordered reduces drastically the plastic zone

associated with a plate of martensite. In an isotropic calculation, the criterion of no plastic deformation along the broad γ/α interface indicates an upper limit of 108 cal/mole for the chemical driving force for thermoelastic growth. An anisotropic calculation does not alter this estimate significantly.

5. Theoretical calculation of the chemical free energy difference, ΔG^{chem} , at M_s based on the Olson-Cohen nucleation model results in a lowest estimate of -106 cal/mole. Although this value is compatible with the upper limit one obtains by considering the disappearance of the plastic zone surrounding a martensite plate, it is larger than the value usually associated with thermoelastic martensites.

6. Self-accommodation between plates with parallel habit plane and opposite shape strain limits the plastic zones to the edges of the plates. An optimum configuration which minimize plastic deformation is for such two plates, each with tapered edges, to be in contact over a large area.

CHAPTER 8SUGGESTIONS FOR FUTURE WORK

1. Measure the short-range order in addition to the long-range order to properly characterize the nearest-neighbor correlation of atom pairs, especially in specimens with small degree of long-range order.

2. Study the nucleation and growth of ordered domains using transmission electron microscopy.

3. There are currently two views regarding the nucleation of martensite. The soft-mode theory considers the nucleation of martensite as a cooperative displacive motion of atoms from the lattice sites in the parent phase to the lattice positions in the martensite phase. The other view is that nucleation is by dislocation propagation from existing defects. The alloy Fe_3Pt presents a good system for studying this problem because of the simple crystal structures of the austenite and the martensite. Electron microscopy and X-ray diffraction can be carried out as a function of temperature to observe the crystallographic changes near the M_s temperature. Neutron scattering experiments can be utilized to investigate the existence of soft-modes.

4. Based on a nucleation by faulting mechanism, the correct dislocation motions for the fcc \rightarrow bct transformation can be worked out. A recalculation of the chemical free energy difference between the austenite and martensite phases at M_s will decide whether or not ΔG^{chem} is of the magnitude usually associated with thermoelastic martensite.

5. The interaction between external applied stresses and the martensite phase is essential to explain various effects such as pseudo-elastic, ferroelastic, shape memory and two-way shape memory. Ideal behavior

always requires that no plastic deformation accompanies the interaction so that reversibility can be achieved by either releasing the external stress or by heating. Methods used in this thesis can be adapted to study the interaction of external stresses with martensite plates.

APPENDIX A: THE STRAIN FIELDS OF AN ELLIPSOIDAL INCLUSION IN AN ISOTROPIC MATRIX

For an ellipsoidal inclusion undergoing a stress-free transformation strain e_{ij}^T in an infinite isotropic matrix, the displacement u_i can be expressed in terms of a single harmonic potential ϕ . Outside the inclusion, the harmonic potential

$$\phi = \frac{2\pi abc}{\ell^3} \left\{ \left(\ell^2 - \frac{x^2}{k^2} + \frac{y^2}{k'^2} \right) F(\theta, k) + \left(\frac{x^2}{k^2} - \frac{y^2}{k'^2} + \frac{z^2}{k'^2} \right) E(\theta, k) \right. \\ \left. + \frac{\ell}{k'^2} \left(\frac{C}{AB} y^2 - \frac{B}{AC} z^2 \right) \right\}$$

$$\text{where } A = (a^2 + \lambda)^{1/2} \quad B = (b^2 + \lambda)^{1/2} \quad C = (c^2 + \lambda)^{1/2}$$

$$\ell = (a^2 - c^2)^{1/2} \quad k^2 = 1 - k'^2 = \frac{a^2 - b^2}{a^2 - c^2}$$

$$\theta = \sin^{-1} (\ell/A)$$

$$F(\theta, k) = \int_0^\theta \frac{d\alpha}{\sqrt{1 - k^2 \sin^2 \alpha}} \quad E(\theta, k) = \int_0^\theta \sqrt{1 - k^2 \sin^2 \alpha} d\alpha$$

and λ is the largest positive root of

$$\frac{x^2}{a^2 + \lambda} + \frac{y^2}{b^2 + \lambda} + \frac{z^2}{c^2 + \lambda} = 1.$$

The potential inside inclusion can be obtained by letting $\lambda = 0$. For a oblate spheroid ($a = b > c$), the harmonic potential reduces to

$$\phi = \frac{2\pi a^2 c}{\ell} \left(1 - \frac{x^2 + y^2 - 2z^2}{2\ell^2}\right) \sin^{-1}(\ell/A) + \frac{\pi a^2 c}{\ell^2} \frac{C}{A} (x^2 + y^2) - \frac{\pi a^2 c}{\ell^2} \frac{2z^2}{C}$$

The strains are listed below for $e_{13}^T = e_{31}^T \neq 0$, $e_{33}^T \neq 0$

A.1 Inside Inclusion

$$e_{11}^C = \frac{a^2 c e_{33}^T}{2(1-\nu)\ell^3} \left\{ -\frac{\nu}{2} (\sin 2\theta - 2\theta) + \frac{1}{\ell^2} \left[\frac{a^2}{4} (\sin 2\theta - 2\theta) - c^2 \left(\theta - \frac{\ell}{c} \right) \right] \right\}$$

$$e_{22}^C = e_{11}^C$$

$$e_{31}^C = \frac{a^2 c e_{33}^T}{2(1-\nu)\ell^3} \left\{ -2(1-\nu) \left[\theta - \frac{\ell}{c} \right] + \frac{a^2 + 2c^2}{\ell^2} \theta - \frac{3c}{\ell} \right\}$$

$$e_{31}^C = \frac{a^2 c e_{31}^T}{(1-\nu)\ell^3} \left\{ -(1-\nu) \left[\frac{\theta}{2} - \frac{\ell}{c} + \frac{\sin 2\theta}{4} \right] + \frac{1}{\ell^2} \left[\frac{a^2}{4} (\sin 2\theta - 2\theta) - c^2 \left(\theta - \frac{\ell}{c} \right) \right] \right\}$$

$$e_{12}^C = 0.$$

$$e_{23}^C = 0.$$

$$e^C = \frac{a^2 c e_{33}^T}{2(1-\nu)\ell^3} \left\{ -\nu (\sin 2\theta - 2\theta) - 2(1-\nu) \left(\theta - \frac{\ell}{c} \right) \right\}$$

A.2 Outside Inclusion

A.2.1 Shear Contribution ($e_{13}^T = e_{31}^T \neq 0$; all terms multiplied by

$$\frac{ce_{13}^T}{4(1-\nu)l^3}).$$

$$e_{11}^C = \frac{4l^3 xz}{h^2 A^4 C^3} \left[\frac{3\lambda}{A^2} - 2(1-\nu) \right] + \frac{8l^3 xz^3}{h^4 A^8 C^3} \left[1 - \frac{4\lambda}{A^2} - \frac{3\lambda}{2C^2} + \frac{2\lambda}{h^2} \left(\frac{x^2+y^2}{A^6} + \frac{z^2}{C^6} \right) \right]$$

$$e_{22}^C = \frac{4l^3 xz}{h^2 A^4 C^3} \frac{\lambda}{A^2} + \frac{8l^3 xy^2 z}{h^4 A^8 C^3} \left[1 - \frac{4\lambda}{A^2} - \frac{3\lambda}{2C^2} + \frac{2\lambda}{h^2} \left(\frac{x^2+y^2}{A^6} + \frac{z^2}{C^6} \right) \right]$$

$$e_{33}^C = \frac{4l^3 xz}{h^2 A^4 C^3} \left[\frac{3\lambda}{C^2} - 2(1-\nu) \right] + \frac{8l^3 xz^3}{h^4 A^4 C^7} \left[1 - \frac{2\lambda}{A^2} - \frac{7\lambda}{2C^2} + \frac{2\lambda}{h^2} \left(\frac{x^2+y^2}{A^6} + \frac{z^2}{C^6} \right) \right]$$

$$e_{23}^C = \frac{4l^3 xy}{h^2 A^6 C} \left[\frac{\lambda}{C^2} - (1-\nu) \right] + \frac{8l^3 xyz^2}{h^4 A^6 C^5} \left[1 - \frac{3\lambda}{A^2} - \frac{5\lambda}{2C^2} + \frac{2\lambda}{h^2} \left(\frac{x^2+y^2}{A^6} + \frac{z^2}{C^6} \right) \right]$$

$$\begin{aligned} e_{31}^C &= 4 \left(\frac{l}{C} - \theta \right) (1-\nu + \frac{C^2}{2l}) + (\sin 2\theta - 2\theta) \left[\frac{1}{2} - (1-\nu) \right] \\ &+ \frac{4l^3 z^2}{h^2 A^2 C^5} \left[\frac{\lambda}{A^2} - (1-\nu) \right] + \frac{4l^3 x^2}{h^2 A^6 C} \left[\frac{\lambda}{C^2} - (1-\nu) \right] \\ &+ \frac{8l^3 xz^2}{h^4 A^6 C^5} \left[1 - \frac{3\lambda}{A^2} - \frac{5\lambda}{2C^2} + \frac{2\lambda}{h^2} \left(\frac{x^2+y^2}{A^6} + \frac{z^2}{C^6} \right) \right] \end{aligned}$$

$$e_{12}^C = \frac{4\ell^3 yz}{h^2 A^4 C^3} \left[\frac{\lambda}{A^2} - (1-\nu) \right] + \frac{8\ell^3 x^2 yz}{h^4 A^8 C^3} \left[1 - \frac{4\lambda}{A^2} - \frac{3\lambda}{2C^2} + \frac{2\lambda}{h^2} \left(\frac{x^2+y^2}{A^6} + \frac{z^2}{C^6} \right) \right]$$

A.22 Dilatational Contribution ($e_{33}^T \neq 0$; all terms multiplied by $\frac{ce_{33}^T}{4(1-\nu)\ell^3}$)

$$e_{11}^C = \frac{2\ell^3 \lambda}{h^2 A^4 C^3} \left(\frac{x^2}{A^2} + \frac{z^2}{C^2} \right) + \frac{2}{\ell^2} \left[\left(\frac{\sin 2\theta}{4} - \frac{\theta}{2} \right) - c^2 \left(\theta - \frac{\ell}{C} \right) \right]$$

$$+ \frac{4\ell^3 x^2 z^2}{h^4 A^6 C^5} \left[1 - \frac{3\lambda}{A^2} - \frac{5\lambda}{2C^2} + \frac{2\lambda}{h^2} \left(\frac{x^2+y^2}{A^6} + \frac{z^2}{C^6} \right) \right] - 4\nu \left[\frac{\sin 2\theta}{4} - \frac{\theta}{2} + \frac{x^2 \ell^3}{h^2 A^6 C} \right]$$

$$e_{22}^C = \frac{2\ell^3 \lambda}{h^2 A^6 C^3} \left(\frac{y^2}{A^2} + \frac{z^2}{C^2} \right) + \frac{2}{\ell^2} \left[\left(\frac{\sin 2\theta}{4} - \frac{\theta}{2} \right) - c^2 \left(\theta - \frac{\ell}{C} \right) \right]$$

$$+ \frac{4\ell^3 y^2 z^2}{h^4 A^6 C^5} \left[1 - \frac{3\lambda}{A^2} - \frac{5\lambda}{2C^2} + \frac{2\lambda}{h^2} \left(\frac{x^2+y^2}{A^6} + \frac{z^2}{C^6} \right) \right] - 4\nu \left[\frac{\sin 2\theta}{4} - \frac{\theta}{2} + \frac{y^2 \ell^3}{h^2 A^6 C} \right]$$

$$e_{33}^C = -\frac{2\ell^3 \lambda}{h^2 A^4 C^3} \left(\frac{2z^2}{C^2} + \frac{x^2+y^2}{A^2} \right) - \frac{4}{\ell^2} \left[\left(\frac{\sin 2\theta}{4} - \frac{\theta}{2} \right) - c^2 \left(\theta - \frac{\ell}{C} \right) \right]$$

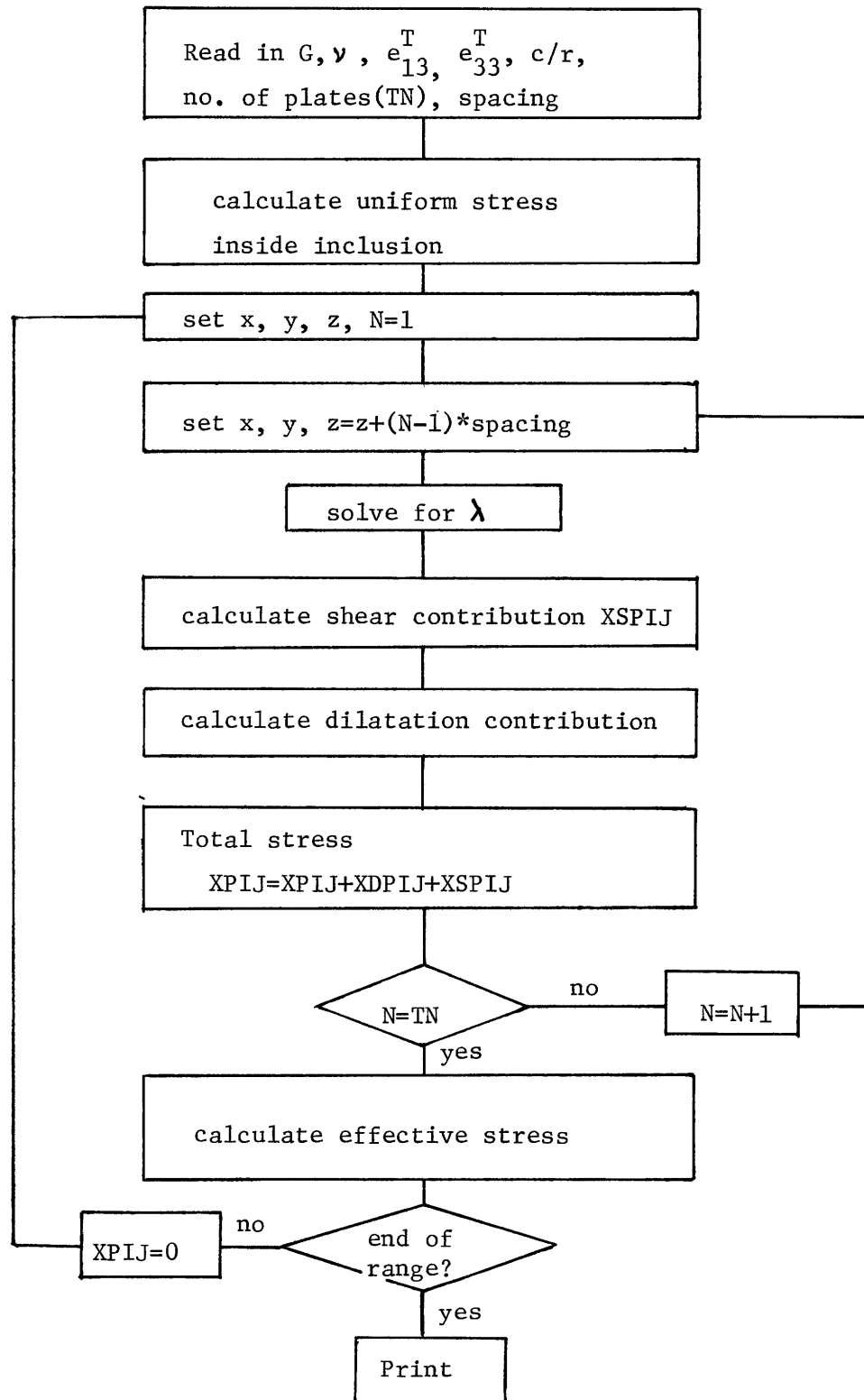
$$- \frac{4\ell^3 z^2}{h^4 A^6 C^5} (x^2+y^2) \left[1 - \frac{3\lambda}{A^2} - \frac{5\lambda}{2C^2} + \frac{2\lambda}{h^2} \left(\frac{x^2+y^2}{A^6} + \frac{z^2}{C^6} \right) \right]$$

$$- 4(1-\nu) \left[\theta - \frac{\ell}{C} + \frac{\ell^3 z^2}{h^2 A^2 C^5} \right]$$

$$\begin{aligned}
e_{23}^C &= -\frac{2\ell^3 yz}{h^2 A^4 C^3} + \frac{y\ell^3 z\lambda}{h^2 A^6 C^3} \left[\frac{3\ell^2}{C^2} - 1 \right] \\
&\quad - \frac{2\ell^3 yz}{h^4 A^8 C^3} (x^2 + y^2) \left[1 - \frac{4\lambda}{A^2} - \frac{3\lambda}{2C^2} + \frac{2\lambda}{h^2} \left(\frac{x^2 + y^2}{A^6} + \frac{z^2}{C^6} \right) \right] \\
&\quad + \frac{2\ell^3 yz^3}{h^4 A^4 C^7} \left[1 - \frac{2\lambda}{A^2} - \frac{7\lambda}{2C^2} + \frac{2\lambda}{h^2} \left(\frac{x^2 + y^2}{A^6} + \frac{z^2}{C^6} \right) \right] \\
e_{31}^C &= -\frac{2\ell^3 xz}{h^2 A^4 C^3} + \frac{xz\ell^3 \lambda}{h^2 A^6 C^3} \left[\frac{3\ell^2}{C^2} - 1 \right] \\
&\quad - \frac{2\ell^3 xz}{h^4 A^8 C^3} (x^2 + y^2) \left[1 - \frac{4\lambda}{A^2} - \frac{3\lambda}{2C^2} + \frac{2\lambda}{h^2} \left(\frac{x^2 + y^2}{A^6} + \frac{z^2}{C^6} \right) \right] \\
&\quad + \frac{2\ell^3 xz^3}{h^4 A^4 C^7} \left[1 - \frac{2\lambda}{A^2} - \frac{7\lambda}{2C^2} + \frac{2\lambda}{h^2} \left(\frac{x^2 + y^2}{A^6} + \frac{z^2}{C^6} \right) \right] \\
e_{12}^C &= -\nu \frac{4\ell^3 xy}{h^2 A^6 C} + \frac{2xy\ell^3 \lambda}{h^2 A^6 C^3} + \frac{4xyz^2 \ell^3}{h^4 A^6 C^5} \left[1 - \frac{3\lambda}{A^2} - \frac{5\lambda}{2C^2} + \frac{2\lambda}{h^2} \left(\frac{x^2 + y^2}{A^6} + \frac{z^2}{C^6} \right) \right]
\end{aligned}$$

where

$$h^2 = \frac{x^2 + y^2}{A^2} + \frac{z^2}{C^4}$$



```

C THIS PROGRAM CALCULATES THE SHEARS DUE TO AN ELLIPSOIDAL INCLUSION
C UNDER UNIFORM TRANSFORMATION SHEAR IN AN ISOTROPIC MEDIUM
C E31 NOT EQUAL 0
C
C
C TITLE: ALLOY, STATE: ORDERED OR DISORDERED
C XMODUL: SHEAR MODULUS, POISSO: POISSON'S RATIO
C XMOD1: SHEAR MODULUS OF INCLUSION
C E31 IS TRANSFORMATION STRAIN IN INCLUSION
C C: C/A RATIO OF ELLIPSOID
C ITRIAL IS INTEGER ASSIGNED TO INPUT DATA SET; MUST BE 0 FOR LAST SET
C NPLATE IS NUMBER OF PLATFS IN PARALLEL
C SPACE IS SPACING
C
C IMPLICIT INTEGER (I-N), REAL (A-H, O-Z)
C REAL*8 TITLE, STATE, XCOF(4)
C COMPLEX*16 ROOTS(3)
C DIMENSION XP31(30,1,30), XP12(30,1,30), XP23(30,1,30), XP11(30,1,3
10), XP22(30,1,30), XP33(30,1,30), YIELD(30,1,30)
1 FORMAT (E10.3,3F10.5,I1)
2 FORMAT (3X,'X',5X,'Y',5X,'Z',11X,'P11',8X,'P22',10X,'P33',10X,'P23
1',10X,'P31',10X,'P12',8X,'QUADRATIC YIELD')
3 FORMAT (1X,3F6.3,5X,7E12.3)
4 FORMAT (2A8)
5 FORMAT ('1',2A8,'0')
6 FORMAT (15H SHEAR MODULUS:, E12.3, 13H DYNES/CM**2)
7 FORMAT (17H POISSON'S RATIO:, F10.5)
8 FORMAT (33H EQUIVALENT TRANSFORMATION SHEAR:, F10.5)
9 FORMAT (5H C/A:, F10.5,'C')
10 FORMAT (4F10.5, 2I2)
11 FORMAT (18H VOLUME EXPANSION:, F10.5)
12 FORMAT (2F10.5)
13 FORMAT (I2,F10.5)
14 FORMAT (31H INSIDE SINGLE INCLUSION: P11=,E12.3,5H P22=,E12.3,5H
1P33=,E12.3,5H P31=,F12.3)

```



```

E31=RMODU*E31/(1.-S1313*RRMODU)
CONST=C*E31/(4.*XPOISS)
XIP31=2.*XMODUL*(CONST*4./XL3)*((ALP1-C2*ALP2)/XL2-XPOISS*(ALP1+AL
*P2))-2.*XMODUL*E31
XIP12=0.
XIP23=0.
XIP11=0.
XIP22=0.
XIP33=0.
C FROM NOW ON, E31 IS CALCULATED EQUIVALENT TRANSFORMATION STRAIN
C
C SOLVING THE THIRD ORDER POLYNOMIAL FOR THE LARGEST POSITIVE ROOT
C
DO 101 IX=1,NSTEPX
X=XINCRR*(IX-1)+XSTART
DO 101 IZ=1,NSTEFZ
ZZ=ZINCRR*(IZ-1)+ZSTART
DO 200 N=1,NPLATE
Z=ZZ+SPACE*(N-1)
R=X**2+Y**2+7**2/C**2
IF (R.LE.1.) GO TO 110
CONST=C*E31*((-1)**(N-1))/(4*XPOISS)
112 X2=X**2
Y2=Y**2
ZZ=Z**2
Y3=Y**3
Z3=Z**3
X3=X**3
XCOP(4)=(1-X2-Y2)*C2-Z2
XCOP(3)=2*C2+1.-(1+C2)*X2-(1+C2)*Y2-2*Z2
XCOP(2)=2.+C2-X2-Y2-Z2
XCOP(1)=1.
M=3
CALL ZPOLR(XCOP,M,ROOTS,IER)
IF (IER) 110,100,110
110 XSP11=XIP11

```

```

XSP22=XIP22
XSP33=XIP33
XSP31=XIP31*((-1)**(N-1))
XSP12=XIP12*((-1)**(N-1))
XSP23=XIP23*((-1)**(N-1))
GO TO 303
100 ROOT=0
DO 102 J=1, 3
IF (DIMAG(ROOTS(J))) 102,104,102
104 IF (DREAL(ROOTS(J))=ROOT) 102,102,105
105 ROOT=DREAL(ROOTS(J))
102 CONTINUE
C
C CALCULATE THE SHEAR STRESSES
C
XA=SQRT(1.+ROOT)
XA2=XA**2
XA4=XA2**2
XA6=XA2**3
XA8=XA4**2
XC=SQRT(C2+ROOT)
XC3=XC**3
XC4=XC**4
XC5=XC**5
XC6=XC**6
XC7=XC**7
XFI=AR SIN(XL/XA)
XH2=X2/XA4+Y2/XA4+Z2/XC4
XH4=XH2**2
XHH=(X2/XA6+Y2/XA6+Z2/XC6)**2*ROOT/XH2
ROOTA=ROOT/XA2
ROOTC=ROOT/XC**2
XHH1=(1-4*ROOTA-1.5*ROOTC+XHH)/(XH4*XA8*XC3)
XHH2=(1-3*ROOTA-2.5*ROOTC+XHH)/(XH4*XA6*XC5)
XHH3=(1-2*ROOTA-3.5*ROOTC+XHH)/(XH4*XA4*XC7)
XSP31
=2*XMODUL*(4*(XL/XC-XFI)*(XPOISS+(C/XL)**2)/XL3+(S

```

```

1 IN(2*YFI)-2*YFL)*(XL**(-2)-XPOISS)/XL3+4*Z2*(ROOTA-XPOISS)/(XH2*XA
22*XC5)+4*X2*(ROOTC-XPOISS)/(XH2*XA6*XC)+8*X2*Z2*XHH2)*CONST
XSP12
=2*XMODUL*(4*Y*Z*(ROOTA-XPOISS)/(XH2*XA4*XC3)+8*Y*Z*
1 X2*XHH1)*CONST
XSP23
=2*XMODUL*(4*X*Y*(ROOTC-XPOISS)/(XH2*XA6*XC)+8*X*Y*Z
12*XHH2)*CONST
XSP11
=2*XMODUL*(4*X*Z*(3*ROOTA-2*XPOISS)/(XH2*XA4*XC3)+8*
17*Y3*XHH1)*CONST
XSP22
=2*XMODUL*(4*X*Z*ROOTA/(XH2*XA4*XC3)+8*X*Z*Y2*XHH1)*
1 CONST
XSP33
=2*XMODUL*(4*X*Z*(3*ROOTC-2*XPOISS)/(XH2*XA4*XC3)+8*
1 X*Z3*XHH3)*CONST
XSP=POISSO*(XSP11+XSP22+XSP33)/(1-2*POISSO)
XSP11=XSP11+XSP
XSP22=XSP22+XSP
XSP33=XSP33+XSP
303 XP31(IX,IY,IZ)=XP31(IX,IY,IZ)+XSP31
XP12(IX,IY,IZ)=XP12(IX,IY,IZ)+XSP12
XP23(IX,IY,IZ)=XP23(IX,IY,IZ)+XSP23
XP11(IX,IY,IZ)=XP11(IX,IY,IZ)+XSP11
XP22(IX,IY,IZ)=XP22(IX,IY,IZ)+XSP22
XP33(IX,IY,IZ)=XP33(IX,IY,IZ)+XSP33
200 CONTINUE
FIELD(IX,IY,IZ)=SQRT(((XP11(IX,IY,IZ)-XP22(IX,IY,IZ))**2+(XP22(IX,
1 IY,IZ)-XP33(IX,IY,IZ))**2+(XP33(IX,IY,IZ)-XP11(IX,IY,IZ))**2)/2+3*
2(XP31(IX,IY,IZ)**2+XP12(IX,IY,IZ)**2+XP23(IX,IY,IZ)**2))
101 CONTINUE
C
WRITE(6,5) TITLE, STATE
WRITE(6,6) XMODUL
WRITE(6,7) POISSO
WRITE(6,22) XMOD1
WRITE(6,9) C
WRITE(6,8) E31
WRITE(6,14) XIP11, XIP22, XIP33, XIP31

```

```
WRITE (6,2)
DO 106 IX=1, NSTEPX
X=XINCRP*(IX-1)+XSTART
DO 106 I7=1, NSTEPZ
Z=ZINCRE*(I7-1)+ZSTART
WRITE (6,3) X,Y,Z,XP11 (IX,IY,IZ), XP22 (IX,IY,IZ), XP33 (IX,IY,IZ),
1XP23 (IX,IY,IZ), XP31 (IX,IY,IZ), XP12 (IX,IY,IZ), YIELD (IX,IY,IZ)
106 CONTINUE
124 IF (ITRIAL) 108,107,108
107 CONTINUE
STOP
END
```


APPENDIX B: THE STRAIN FIELDS OF A SQUARE PLATE IN AN ISOTROPIC MATRIX

The harmonic potential:

$$\phi(r) = [xy \ln(r+z) + yz \ln(r+x) + zx \ln(r+y) -$$

$$\frac{1}{2} \{ x^2 \tan^{-1} \left(\frac{yz}{xr} \right) + y^2 \tan^{-1} \left(\frac{zx}{yr} \right) + z^2 \tan^{-1} \left(\frac{xy}{zr} \right) \}]_{x-a, y-b, z-c}^{x+a, y+b, z+c}$$

The biharmonic potential:

$$\psi(r) = \left[\frac{1}{4} xyzr + \frac{1}{6} \{ (r^2 - x^2) yz \ln(r+x) + (r^2 - y^2) zx \ln(r+y) + (r^2 - z^2) xy \ln(r+z) \} \right.$$

$$\left. - \frac{1}{12} \{ x^4 \tan^{-1} \left(\frac{yz}{xr} \right) + y^4 \tan^{-1} \left(\frac{zx}{yr} \right) + z^4 \tan^{-1} \left(\frac{xy}{zr} \right) \} \right]_{x-a, y-b, z-c}^{x+a, y+b, z+c}$$

$$\text{where } [f(x, y, z)]_{x_1, y_1, z_1}^{x_2, y_2, z_2} = \sum_{i, j, k=1}^2 (-1)^{i+j+k} f(x_i, y_j, z_k)$$

The stresses for $e_{13}^T = e_{31}^T \neq 0$ are: (all subjected to the summation $\sum_{i=1}^2$ and multiply by $\frac{e_{13}^T}{4\pi(1-\nu)}$)

$$e_{11}^C = \ln(y+r) - \frac{x^2 y}{r(r^2 - y^2)} - 2(1-\nu) \ln(y+r)$$

$$e_{22}^C = \frac{y}{r}$$

$$e_{33}^C = \ln(y+r) - \frac{z^2 y}{r(r^2 - y^2)} - 2(1-\nu) \ln(y+r)$$

$$e_{23}^C = \frac{z}{r} - (1-\nu)\ln(z+r)$$

$$e_{31}^C = \frac{xyz}{r(y^2-r^2)} + (1-\nu) \left\{ \tan^{-1}\left(\frac{xy}{zr}\right) + \tan^{-1}\left(\frac{zy}{xr}\right) \right\}$$

$$e_{12}^C = \frac{x}{r} - (1-\nu)\ln(r+x)$$

$$e^C = 2(2\nu-1)\ln(y+r)$$

APPENDIX C: ANISOTROPIC CALCULATION OF THE ELASTIC STRAIN ENERGY OF AN ELLIPSOIDAL INCLUSION IN AN INFINITE MATRIX

C.1 Theory

As presented in Section 5.4, the treatment by Eshelby of an ellipsoidal inclusion which undergoes a uniform stress-free transformation strain e_{ij}^T showed that the constrained displacement U_i^C is given by

$$U_i^C(\bar{r}) = \iint \sigma_{kj}^T G_{ik}(\vec{r}, \vec{r}') ds' \quad (C1)$$

$$= - \iiint \sigma_{kj}^T G_{ik,j}(\vec{r}, \vec{r}') dv' \quad (C2)$$

where

$$\sigma_{kj}^T = C_{kjlm} e_{lm}^T$$

G_{ik} are the elastic Green's functions, C the elastic constant tensor, and Eq'n (C1) is transformed into Eq'n (C2) by means of Gauss' divergence theorem.

In the general anisotropic case, the constrained strains e_{ij}^C are constant when e_{ij}^T are constant. [114-117] Then

$$e_{ij}^C = S_{ijkl} C_{klmn} e_{mn}^T \quad (C3)$$

where

$$S_{ijkl} = \frac{1}{8\pi} \int_0^{2\pi} d\theta \int_0^{\pi} \beta \sin\phi d\phi \frac{z_i z_l M_{jk}^{-1} + z_j z_l M_{ik}^{-1}}{(\sin^2\phi + \beta^2 \cos^2\phi)^{3/2}} \quad (C4)$$

$$M_{ik} = C_{ijkl} z_j z_l \quad (C5)$$

$$\vec{z} = (\sin\phi\cos\theta, \sin\phi\sin\theta, \cos\phi) \quad (C6)$$

β is the aspect ratio, c/r , of an ellipsoid, r and c are the semi-major and semi-minor axes, respectively. The elastic constant tensor C_{ijkl} must be referred to a Cartesian coordinate system whose \hat{X}_3 axis is the axis of revolution of the ellipsoid and ϕ is the angle between \vec{z} and \hat{X}_3 . The elastic strain energy per unit volume of inclusion is given by

$$\begin{aligned} W &= -\frac{1}{2V} \iiint (\sigma_{ij}^C - \sigma_{ij}^T) e_{ij}^T dv' \\ &= \frac{1}{2} (e_{kl}^T - e_{kl}^C) C_{ijkl} e_{ij}^T \end{aligned} \quad (C7)$$

In the case of an inhomogeneous system, in which the elastic constants of the inclusion and the matrix are not the same, an "equivalent" stress-free transformation strain is first obtained by solving

$$C_{ijkl}^* (e_{kl}^C - e_{kl}^{T*}) = C_{ijkl} (e_{kl}^C - e_{kl}^T) \quad (C8)$$

where C_{ijkl}^* are the elastic constants and e_{ij}^{T*} are the actual stress-free transformation strain of the inclusion. The strain energy per unit volume is then given by

$$W = \frac{1}{2} (e_{kl}^{T*} - e_{kl}^C) C_{ijkl}^* e_{ij}^{T*} \quad (C9)$$

C.2 Computational Procedure

The maximum possible number of independent components of S_{ijkl} is 54 because $S_{ijkl} = S_{jikl}$. Since $\sigma_{kl}^T = \sigma_{lk}^T$, a matrix Q_{ijkl} can be defined such that

$$\begin{aligned} e_{ij}^C &= Q_{ijkl} \sigma_{kl}^T \\ &= Q_{ijkl} C_{klmn} e_{mn}^T \end{aligned} \quad (C10)$$

where

$$Q_{ijkl} = \frac{1}{2} (S_{ijkl} + S_{ijlk}) \quad (C11)$$

It is easily seen that

$$Q_{ijkl} = Q_{jikl} = Q_{ijlk}$$

$$Q_{ijkl} = Q_{klij}$$

The maximum number of independent components of Q_{ijkl} is 21. The actual number, however, can be less depending on both the symmetry of the matrix and the orientation of the matrix relative to the inclusion.

Whenever the principal axes of the ellipsoid are not parallel to the cartesian crystal axes of the matrix and/or the inclusion on

which the standard elastic constant tensor C_{ijkl} are based, the values of C_{ijkl} are transformed to the coordinate system of the ellipsoid through the tensor transformation law:

$$C'_{ijkl} = a_{im} a_{jn} a_{ko} a_{lp} C_{mnop} \quad (C12)$$

where a_{im} are components of the coordinate transformation matrix.

Numerical calculation of Q was undertaken with the Gaussian quadrature integration scheme. [124] Compared with the exact solutions for the isotropic case, the accuracies using the Gaussian Legendre formula of 16, 20 and 48 points are shown in Table C.1. The flow chart and the computer program are listed in Section C.4.

C.3 The Isotropic Limit

For the case in which both the matrix and the inclusion are elastically isotropic, the elastic strain energy as a function of the aspect ratio are shown in Fig. C.1 and C.2. The elastic moduli of copper were used ($\nu = 0.308$, $G = 0.754 \times 10^{12}$ dyn/cm²) in the computation. In Fig. C.1, where the stress free transformation strain is an uniform dilatation, the case $G = G^*$ (i.e. the matrix and the inclusion have the same shear modulus) has a shape-independent energy per unit volume.

$$W_0 = 2G \frac{1+\nu}{1-\nu} e_{11}^T{}^2 \quad (C13)$$

The minimum energy configuration of a soft inclusion ($G^* < G$) is a disc while that of a hard inclusion ($G^* > G$), a sphere. This result is in

211

agreement with the isotropic calculation by Barnett, et al. [119] When the stress-free transformation strain is a simple shear ($e_{13}^T \neq 0$), the elastic strain energy is shape-dependent in the case $G = G^*$. For small aspect ratio,

$$W_o = \frac{\pi(2-\nu)}{8(1-\nu)} G e_{13}^T{}^2 \left(\frac{c}{r}\right) \quad (C14)$$

While a hard inclusion increases and a soft inclusion decreases the elastic strain energy relative to case when the matrix and the inclusion have the same shear modulus, a disc-shape inclusion always has the lowest energy which vanishes as the aspect ratio approaches zero.

TABLE C1

ACCURACY OF NUMERICAL CALCULATION OF ANISOTROPIC ELASTIC STRAIN ENERGY USING GAUSS LEGENDRE FORMULA AS COMPARED WITH THE ISOTROPIC CALCULATION
 $\beta = c/r$

	16 points	20 points	48 points
	$\beta \geq 0.1$	$0.1 \geq \beta \geq 0.06$	$\beta \geq 0.01$
$e_{ij}^T = e_{ij}^T$	$\epsilon \leq 0.01\%$	$\epsilon < 0.2\%$	$\epsilon \leq 0.5\%$
$e_{ij}^T = e_{13}^T$	$\epsilon < 0.5\%$	$\epsilon \leq 1.0\%$	$\epsilon \leq 0.6\%$

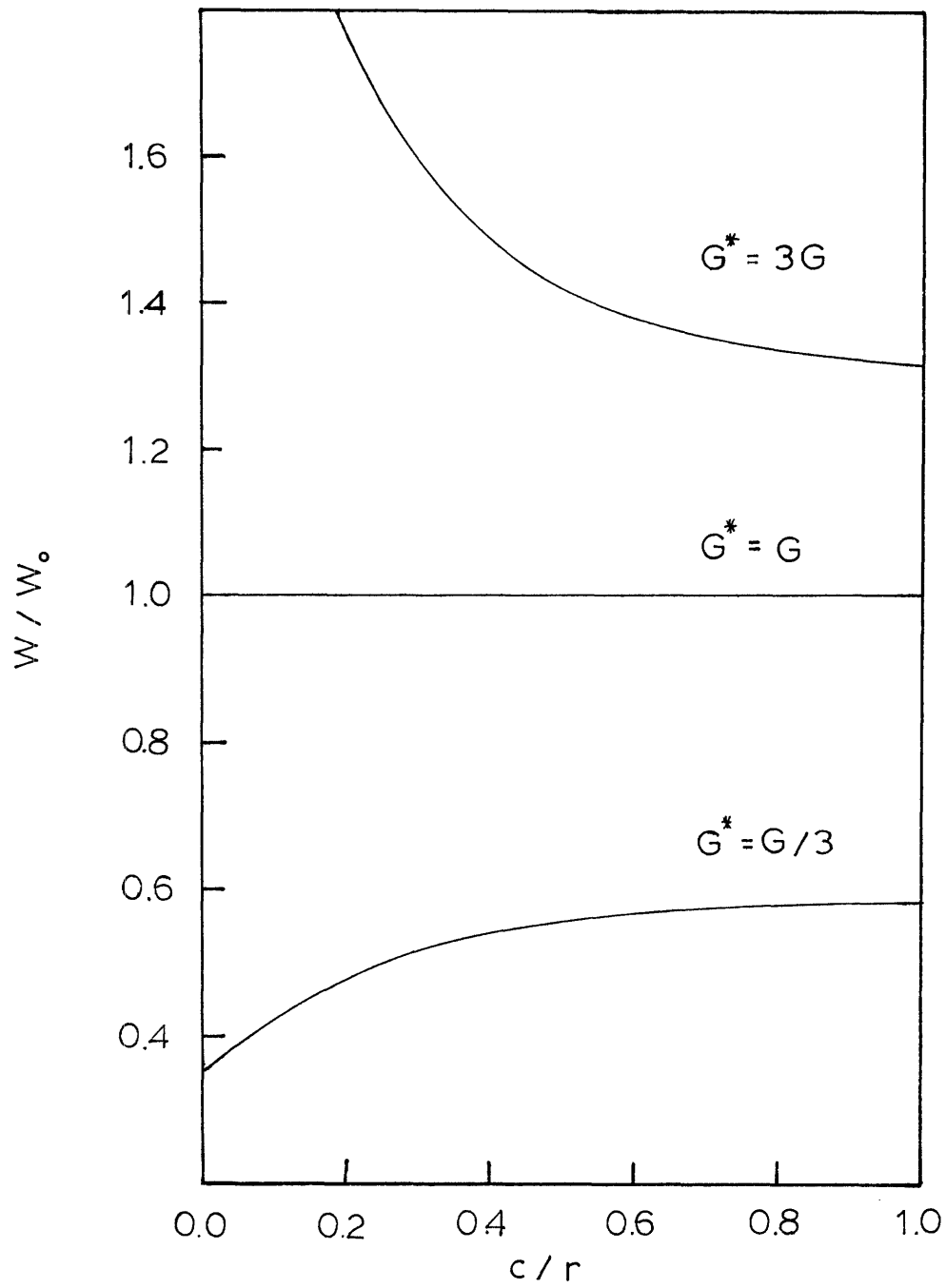


Figure C1. Elastic strain energy, W , of an ellipsoidal inclusion with uniform dilatation in an isotropic matrix vs. aspect ratio.

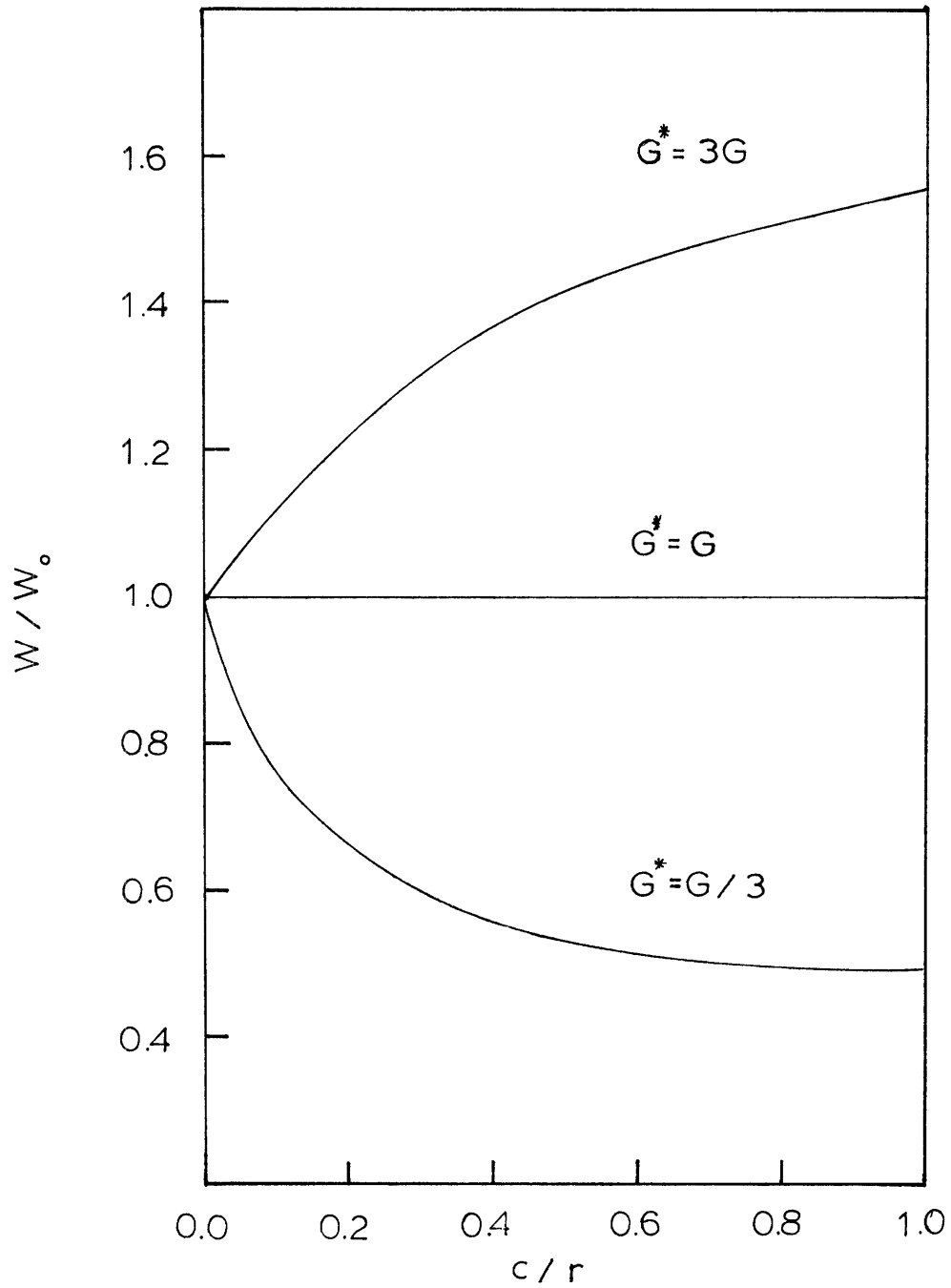
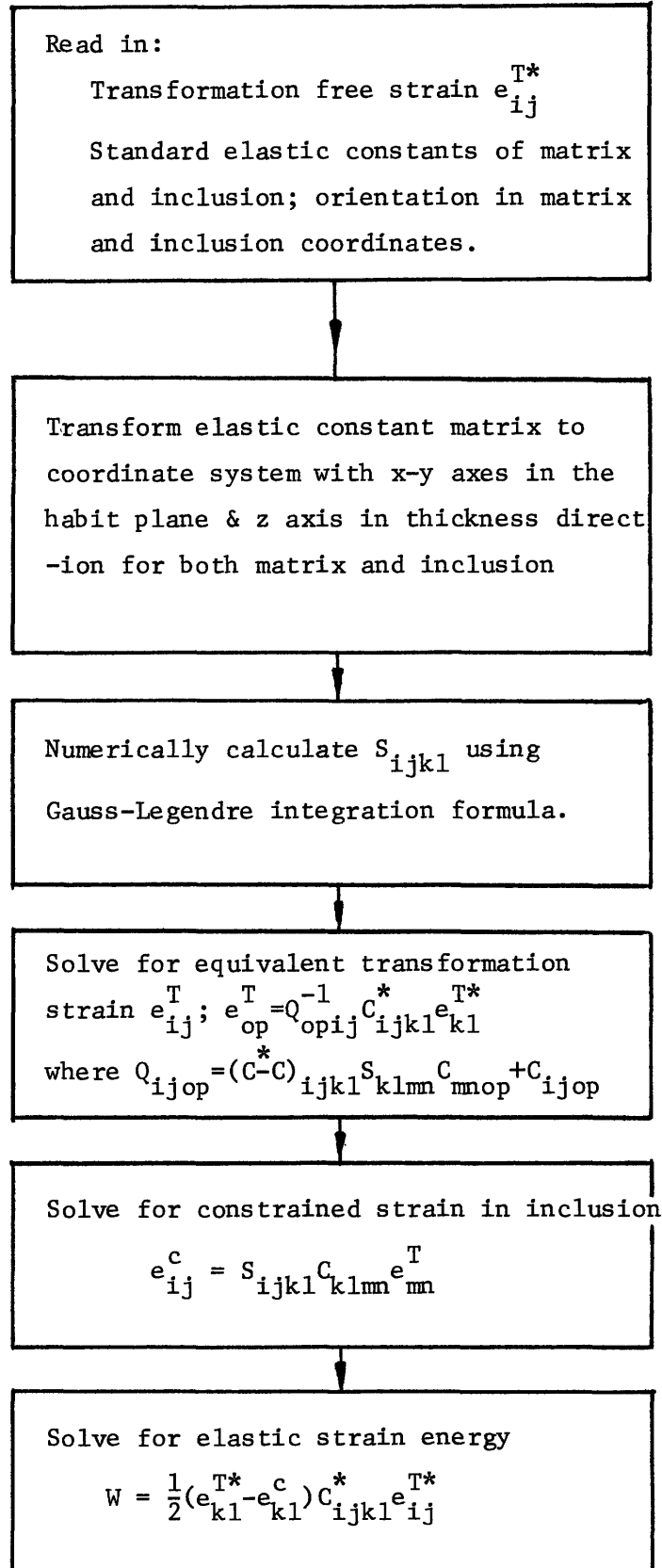


Figure C2. Elastic strain energy, W , of an ellipsoidal inclusion with uniform shear in an isotropic matrix vs aspect ratio,



```

C C THIS PROGRAM CALCULATES THE ELASTIC ENERGY OF AN ELLIPSOID IN AN
C C ANISOTROPIC MEDIA
C C
C C THIS PROGRAM USES THE 16 POINT GAUSS-LEGENDRE FORMULA FOR DOUBLE
C C INTERGRATION
C C
C C C, C1, C2, C3, AA, BB, WKAREA ARE WORKING AREA
C C BETA IS ASPECT RATIO
C C LCCNSM AND KCONSI ARE INPUT STANDARD PLASTIC CONSTANTS OF MATRIX
C C AND INCLUSION IN SYMPLECTIC STORAGE MODE
C C CONSM AND CONSI ARE TRANSFORMED ELASTIC CONSTANT MATRIX
C C STRAII: INPUT TRANSFORMATION STRAIN
C C SIPALE: EQUIVALENT TRANSFORMATION STRAIN
C C STRAIC: CALCULATED STRAIN
C C W: ELASTIC STRAIN ENERGY
C C
C C IMPLICIT INTEGER (I-N), REAL (A-H,O-Z)
C C DOUBLE PRECISION DX(48),DA(48),ECONSM(45),ECONSI(45),CCNSM(9,9),CO
1 NSI(9,9),ORIENTE(9,9),ORIENT(9,9),STRAIM(9,1),STRAIC(9,1),STRAII(9,
2 1),W(1,1),S1(9,9),C(9,9),C1(9,9),C2(9,9),C3(9,9),XM(3,3),XMINV(3,3
3 ),AA(45),BB(45),S(45),WKAREA(50),TITLE,Z(3),PI,THA,W1
C C DIMENSION AOPR(3,3),AOPR1(3,3),X(48,2),A(48,2),O1(6,6),SS(6,6)
C
101 FORMAT (1X,A8)
102 FORMAT (7E10.3)
103 FORMAT (9F5.2)
104 FORMAT (9F8.5)
105 FORMAT (1X,'STANDARD ELASTIC CONSTANT OF MATRIX:',/,5X,'C11=',E10.
14,5X,'C12=',E10.4,5X,'C44=',E10.4,/)
106 FORMAT (1X,'STANDARD ELASTIC CONSTANT OF INCLUSION:',/,5X,'C11=',E
110.4,5X,'C12=',E10.4,5X,'C44=',E10.4,/)
107 FORMAT (1X,'ORIENTATION OF INCLUSION:',3F10.5,/,26X,3F10.5,/,26X,3
1F10.5,/)
108 FORMAT (1X,'CO-ORDINATE OF INCLUSION:',3F10.5,/,26X,3F10.5,/,26X,3
1F10.5,/)

```

```

109 FORMAT (1X, 'TRANSFORMED ELASTIC CONSTANT OF MATRIX:')
110 FORMAT (1X, 'TRANSFORMED ELASTIC CONSTANT OF INCLUSION:')
111 FORMAT (1X, 'TRANSFORMATION STRAIN:',/,1X,9E12.3,/)
112 FORMAT (1X, 'EQUIVALENT TRANSFORMATION STRAIN:',/,1X,9E12.3,/)
113 FORMAT (1X, 'CALCULATED STRAIN INSIDE INCLUSION:',/,1X,9E12.3,/)
114 FORMAT (1X, 'TOTAL ELASTIC ENERGY:',E12.4)
115 FORMAT (I1)
116 FORMAT (1X, 'ELASTIC ENERGY IN ISOTROPIC MATRIX:',E12.4)
117 FORMAT (1X, 'SHEAR MODULUS:',E12.4)
118 FORMAT (1X, 'POISSON RATIO:',F10.4)
119 FORMAT (1X, 'ANISOTROPY:',F10.3/)
120 FORMAT (10X,9E12.4)
121 FORMAT (/,1X, 'ASPECT RATIO:',F10.4)
122 FORMAT (/,1X, 'W/WO:',F10.4///)
123 FORMAT (1X, 'S MATRIX:')
124 FORMAT (1H1,1X,A8)
130 FORMAT (I2,F10.3)

C 500 READ (5,101) TITLE
      READ (5,102) ECONSM
      READ (5,102) ECONSI
      READ (5,103) STRAII
      READ (5,104) AOPIM
      READ (5,104) ACRIL
      READ (5,130) LOVE1, XINCRC
      READ (5,115) ISIGN

C TRANSFORMATION OF ELASTIC CONSTANT MATRIX
C
C
      DO 1 I=1,3
      DO 1 J=1,3
      DO 1 K=1,3
      DO 1 L=1,3
      CALL DIGIT(1,J,K,L,N1,N2)
      IF (N1.LT.4) GO TO 150
      GO TO (151,152,153), I

```

```
151 IF (J.EQ.2) GO TO 154
    N1=8
    GO TO 150
154 N1=6
    GO TO 150
152 IF (J.EQ.1) GO TO 155
    N1=4
    GO TO 150
155 N1=9
    GO TO 150
153 IF (J.EQ.1) GO TO 156
    N1=7
    GO TO 150
156 N1=5
150 IF (N2.LT.4) GO TO 160
    GO TO (161,162,163), K
161 IF (L.EQ.2) GO TO 164
    N2=8
    GO TO 160
164 N2=6
    GO TO 160
162 IF (L.EQ.1) GO TO 165
    N2=4
    GO TO 160
165 N2=9
    GO TO 160
163 IF (L.EQ.1) GO TO 166
    N2=7
    GO TO 160
166 N2=5
160 CONTINUE
    CRITRM(N1,N2)=ACRIM(I,K)*ACRIM(J,L)
    ORIENI(N1,N2)=ACRII(I,K)*ACRII(J,L)
    1 CONTINUE
    N=9
    IA=9
```

```

IC=9
IDGT=3
CALL VMULFS(ORIENM, ECONS, N, N, IA, C1, IC)
CALL VMULFS(ORIENI, ECONS, N, N, IA, C2, IC)
DO 100 I=1,9
DO 100 J=1,9
C(I,J)=ORIENM(J,I)
C3(I,J)=ORIENI(J,I)
100 CONTINUE
CALL VMULFF(C1, C, N, N, IA, IA, CONSM, IC, IER)
CALL VMULFF(C2, C3, N, N, IA, IA, CONSI, IC, IER)

C
SHEAR=ECONS(10)
SIGMA=ECONSM(2)/(2*(ECONS(2)+SHEAR))
ANISO=2*SHEAR/(ECONSM(1)-ECONSM(2))
SIGMAI=ECONSI(2)/(2*(ECONSI(2)+ECONSI(1)))
ANISOI=2*ECONSI(10)/(ECONSI(1)-ECONSI(2))

C
WRITE(6,124) TITLE
WRITE(6,105) ECONSM(1),ECONSM(2),ECONSM(10)
WRITE(6,117) ECONSM(10)
WRITE(6,118) SIGMA
WRITE(6,119) ANISO
WRITE(6,106) ECONSI(1),ECONSI(2),ECONSI(10)
WRITE(6,117) ECONSI(10)
WRITE(6,118) SIGMAI
WRITE(6,119) ANISOI
WRITE(6,107) AORPLM
WRITE(6,108) AORRI
WRITE(6,109)
WRITE(6,120) ((CONSM(I,J),J=1,9),I=1,9)
WRITE(6,115)
WRITE(6,120) ((CONSI(I,J),J=1,9),I=1,9)
WRITE(6,111) STRALI
PY=3.1+15927
DC 700 LCVE=1,LOVE1

```

```

BETA=XINC*RE*I.COV5
CONST=BETA*PY/B.
BETA2=BETA**2

C C C
CALCULATE W0 IN ISOTROPIC MATRIX
C C C
W0=2*SHEAR*(1.+SIGEA)*(STRAII(1,1)**2)/(1.-SIGMA)
PA=(ACOS(BETA)-SQRT(1.-BETA2)*BETA)*2*PY*BETA/((1.-BETA2)**1.5)
GAMMA=(PA*(2.-SIGEA)-3ETA2*(4.*PY-3.*PA)/(1.-BETA2))/(4.*PY*(1.-SI
1GMA))
W0=W0+2.*GAMMA*SHEAR*(STRAII(5,1)**2)

C C C
CALCULATE S DEFINED TO BE SYMMETRIC
C C C
CALL GL016(DX,DA,-1.D0,1.D0)
DC 201 I=1,16
XX=DX(I)
AB=DA(I)
X(I,1)=XX
Y(I,2)=XX
A(I,1)=AB
A(I,2)=AB
201 H1=(1.-0.)/2.
G1=(1.+0.)/2.
DO 3 I=1,3
DO 3 J=1,9
3 S1(I,J)=0.
DO 4 II=1,16
UI=H1*X(II,1)+G1
AI=H1*A(II,1)
THA=UI*2*PY
H=(1.-0.)/2.
G=(1.+0.)/2.
DC 5 I=1,6
DC 5 J=1,6

```



```

C SOLVE QD=C*E*
C USE REDUCED 6 BY 6 MATRIX; MULTIPLY BY APPROPRIATE CONSTANT
C
C CALL VVULFF(CONSI,STRAI,N,N,1,IA,IA,STRAI,IC,IER)
DO 300 I=1,9
300 C(I,1)=STRAI(I,1)
DO 301 I=1,6
DO 301 J=4,6
301 C3(I,J)=C3(I,J)*2
CALL LEQTF(C3,1,6,IA,STRAI,IDGT,WKAREA,IER)
DO 302 I=4,6
J=I+3
302 STRAI(J,1)=STRAI(I,1)
C
C CALCULATE E(C)=SCE(T)
C
C CALL VVULFF(C2,STRAI,N,N,1,IA,IA,STRAI,IC,IEP)
C
C CALCULATE W=(E*(T)-E(C))C*E*(T)/2
C
DO 400 I=1,9
400 C1(1,I)=STRAI(I,1)-STRAIC(I,1)
CALL VVULFF(C1,C,1,N,1,IA,IA,W1,1,IER)
W(1,1)=W1/2.
W2=W(1,1)/WO
C
WRITE (6,121) BETA
WRITE (6,116) WO
WRITE (6,123)
WRITE (6,120) ((S1(I,J),J=1,9),I=1,9)
WRITE (6,112) STRAI
WRITE (6,113) STRAIC
WRITE (6,114) W
WRITE (6,122) W2
C
700 CONTINUE
C

```

```

IF (ISIGN) 500,600,500
600 CONTINUE
STOP
END
C
C
SUBROUTINE GLC16 (X,A,C,D)
DOUBLE PRECISION C,D,X(48),A(48),XX(24),AA(24)
DATA XX(1),AA(1),XX(2),AA(2),XX(3),AA(3),XX(4),AA(4),XX(5),AA(5),X
*X(6),AA(6),XX(7),AA(7),XX(8),AA(8)/
*.9894029349916499325961541734DC ,.2715245941175409485178057245D-1,
*.9445750230732325760779884155D0 ,.6225352393864789286284383699D-1,
*.8656312023878317438804678977DC ,.9515851168249278480992510760D-1,
*.75540440833550030338951011948D0 ,.1246289712555338720524762821D0 ,
*.6178762444026437484466717640DC ,.1495959888165767320815017305D0 ,
*.4580167776572273863424194429D0 ,.1691565193950025381893120790D0 ,
*.2816035507792589132304605014D0 ,.1826034150449235888667636679D0 ,
*.950125093763744013531953542D-1,.1894506104550684962853967232D0 /
DPC = .5D0*(D-C)
DPC = .5D0*(D+C)
DO 2000 I=1,8
NI=17-I
X(I)=-DMC*XX(I)+DPC
X(NI)= DMC*XX(I)+DPC
A(I)=DMC*AA(I)
2000 A(NI)=DMC*AA(I)
RETURN
END
C
C
SUBROUTINE DIGT(NI,NJ,NK,NL,N1,N2)
TRANSFORMATION FROM TENSOR TO MATRIX NOTATION: 11-1, 22-2, 33-3,
23-4, 31-5, 12-6
NUMBER1=NI+NJ

```

```
NUMBER2=NK+NL
IF (NI-NJ) 11, 12, 11
12 N1=NI
GO TO 16
11 GO TO (12, 12, 13, 14, 15), NUMBER 1
13 N1=6
GO TO 16
14 N1=5
GO TO 16
15 N1=4
16 IF (NK-NL) 21, 22, 21
22 N2=NK
GO TO 26
21 GO TO (22, 22, 23, 24, 25), NUMBER 2
23 N2=6
GO TO 26
24 N2=5
GO TO 26
25 N2=4
26 CONTINUE
RETURN
END
```

APPENDIX D: ANISOTROPIC CALCULATION OF THE STRESS FIELD IN AN INFINITE MATRIX DUE TO AN ELLIPSOIDAL INCLUSION UNDERGOING UNIFORM TRANSFORMATION STRAIN

D.1 Theory

The calculation of the stress field in an anisotropic medium due to an ellipsoidal inclusion undergoing uniform transformation strain follows the formulation developed in Appendix C. In terms of the elastic Green's function $G_{ik}(\vec{r}-\vec{r}')$ for the infinite anisotropic medium, the constrained displacement is given by

$$U_i^C(\vec{r}) = \sigma_{jk}^T \iint G_{ik}(\vec{r}-\vec{r}') n_j(\vec{r}') dS' \quad (D1)$$

or

$$U_i^C(\vec{r}) = -\sigma_{jk}^T \iiint \frac{\partial G_{ik}(\vec{r}-\vec{r}')}{\partial x_j} dv' \quad (D2)$$

The constrained strains are equal to the first derivatives of displacement and hence involve the first derivative of G_{ik} in the surface integration or the second derivative of G_{ik} in the volume integration. These quantities have been reduced by Barnett^[132] to a single integration in the $\vec{z} \cdot \vec{T} = 0$ plane where

$$\vec{T} = \frac{\vec{r}-\vec{r}'}{|\vec{r}-\vec{r}'|} \quad (D3)$$

$$\vec{z} = \frac{\vec{K}}{|\vec{K}|} \quad (D4)$$

and \vec{K} is the wavevector in the Fourier transform of G_{ik} . Computation indicated that for the same accuracy, surface integration requires much less computer time. The following development is relevant to the use of surface integration. The constrained strains are^[132]

$$e_{ip}^C = \sigma_{ik}^T \iint dS' n_j(\vec{r}') \frac{1}{8\pi^2 |\vec{r}-\vec{r}'|} \int_0^\pi d\psi \{ -T_p M_{ik}^{-1} + z_p F_{ik} - T_i M_{pk}^{-1} + z_i F_{pk} \} \quad (D5)$$

where

$$M_{ik} = C_{ijkl} z_j z_l = M_{ki} \quad (D6)$$

$$F_{ik} = C_{jmnq} M_{ij}^{-1} M_{nk}^{-1} (z_m^T z_q^T + z_q^T z_m^T) = F_{ki} \quad (D7)$$

and ψ is an integration variable in the plane $\vec{z} \cdot \vec{T} = 0$. The stresses σ_{jk}^T are related, by Hooke's law, to the stress-free transformation strains of a homogeneous inclusion (same elastic constants as matrix) or to the equivalent transformation strains of an inhomogeneous inclusion (different elastic constants from matrix).

If θ and ϕ are the angular spherical polar coordinates of \vec{T} in the coordinate system that the elastic constant tensor C_{ijkl} is based, the vector components T_j are given by

$$T_1 = \sin\phi \cos\theta \quad T_2 = \sin\phi \sin\theta \quad T_3 = \cos\theta \quad (D8)$$

Choose two fixed orthogonal unit vectors, \vec{a} and \vec{b} , in the plane $\vec{z} \cdot \vec{T} = 0$

as follows:

$$\begin{aligned} a_1 &= \sin\theta & a_2 &= -\cos\theta & a_3 &= 0 \\ b_1 &= \cos\phi\cos\theta & b_2 &= \cos\phi\sin\theta & b_3 &= -\sin\phi \end{aligned} \quad (D9)$$

Then in the plane $\vec{z} \cdot \vec{T} = 0$, the vector \vec{z} is given by

$$z_s = a_s \cos\psi + b_s \sin\psi \quad (D10)$$

In Eq'n (D5), all quantities are expressed in terms of \vec{z} given by Eq'n (D10). The constrained stress in the matrix is

$$\sigma_{lm}^C = C_{lmip} e_{ip}^C \quad (D11)$$

D.2 Computational Procedure

From Eq'n (D5), a matrix Q' can be defined such that

$$e_{ip}^C = \sigma_{jk}^T \iint ds' Q'_{ipkj}$$

and

$$\begin{aligned} Q'_{ipkj} = \frac{1}{2} \int_0^\pi d\psi \{ & n_j(\bar{r}') [-T_{pM_{ik}}^{-1} - T_{iM_{pk}}^{-1} + z_p^F{}_{ik} + z_i^F{}_{pk}] \\ & + n_k(\bar{r}') [-T_{pM_{ij}}^{-1} - T_{iM_{pj}}^{-1} + z_p^F{}_{ij} + z_i^F{}_{pj}] \} \end{aligned} \quad (D12)$$

$$Q'_{ipkj} = Q'_{pikj} = Q'_{ipjk}$$

$$Q'_{ipkj} \neq Q'_{kjip}$$

There are 36 independent quantities in Q' . Numerical calculation of Q' was undertaken with the Gaussian quadrature integration scheme. Integration over the surface of the ellipsoid was first transformed into integrating over the projection of such a surface on the plane perpendicular to the c axis before numerical integration was carried out. To obtain the stresses at a point in the matrix, the computing time is 1.2 minutes on an IBM 370-168. The computer program is listed in D.3. The result in the isotropic limit is compared with an exact isotropic calculation in Figure D.1.

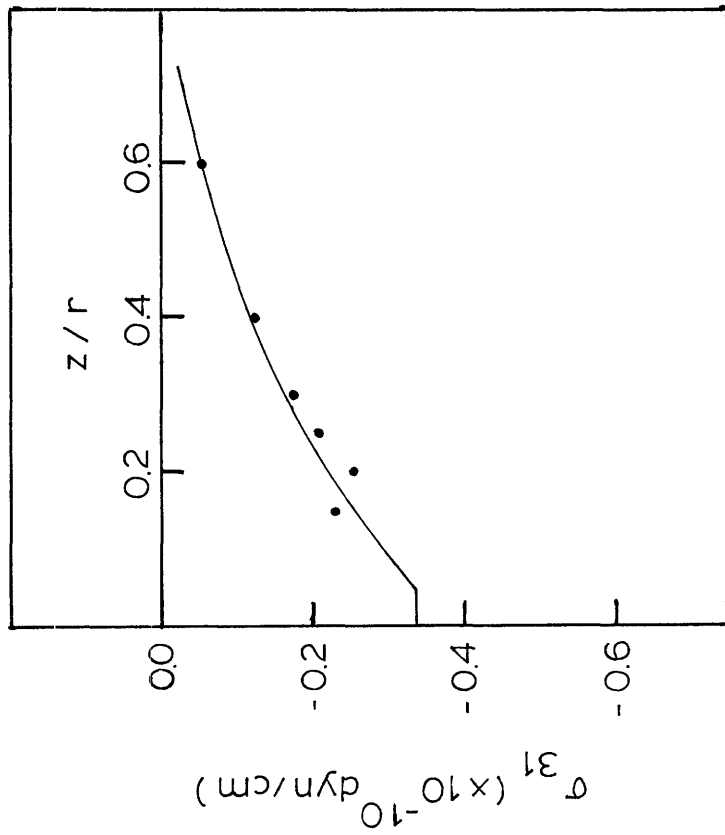
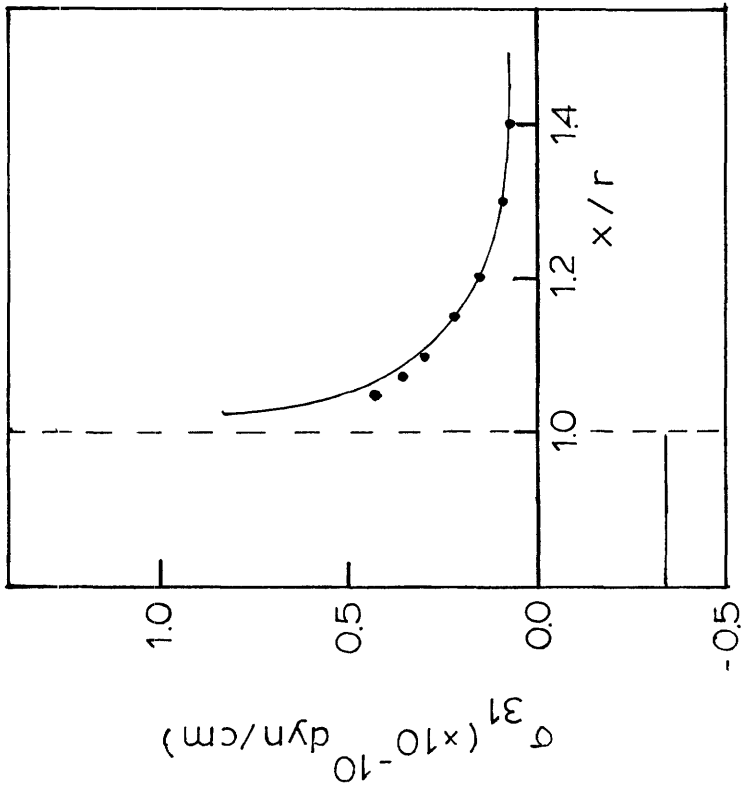


Figure D1. Isotropic limit of anisotropic stress field calculation (\bullet) compared with exact isotropic calculation (—). Fe_3Pt ordered. Aspect ratio 0.046.

```

C
C THIS PROGRAM CALCULATES THE STRESS FIELD OUTSIDE AN ELLIPSOID
C UNDERGOING UNIFORM TRANSFORMATION IN ANISOTROPIC MEDIUM
C
C ECONSM IS ELASTIC CONSTANTS (SYMMETRIC MODE) OF MATRIX BASED ON
C COORDINATION SYSTEM OF ELLIPSOID
C STRAIN IS THE EQUIVALENT TRANSFORMATION STRAIN TENSOR
C BOTH ECONSM AND STRAIN ARE COMPUTED IN THE ELASTIC STRAIN ENERGY
C PROGRAM
C
C IMPLICIT INTEGER (I-N), REAL (A-H,O-Z)
C DOUBLE PRECISION TITLE,DX(48),DA(48),ECONSM(45),CONSM(9,9),STRAIN(
*9,1),STRAIC(9,1),STRESC(9,1),C(9,1),XM(3,3),XMINV(3,3),WKAREA(50)
*,S1(9,9)
C DOUBLE PRECISION Q1(6,6),T(3),Z(3),XF(3,3),XA(3,3),SSS(6,6),Q11(6,
*6),SINTH,COSPH,COSEFL,SINFI,XMU,XMU1,SS1,SS2,SS3
C DIMENSION X(20),A(20),K(20),B(20),XX(20),XN(3)
C DATA P/ .146908258, .3188522562, .487665201, .6389700139,
* .7692316434, .8733648750, .9478044306, .9990226907,
* -.1409082258, -.3188522562, -.487665201, -.6389700139,
* -.7692316434, -.8733648750, -.9478044306, -.9990226907/,
* B/ .0253071341, .0555952586, .0784266615, .0926709458,
* .0906709458, .0784266615, .0555952586, .0253071341,
* .0253071341, .0555952586, .0784266615, .0906709458,
* .0906709458, .0784266615, .0555952586, .0253071341/
C DATA XX/ .9951847266, .9569403357, .8819212643, .7730104533,
* .6343932841, .4713967368, .2902846772, .0980171403,
* -.9951847266, -.9569403357, -.8819212643, -.7730104533,
* -.6343932841, -.4713967368, -.2902846772, -.0980171403/,
* P18/ .196349548/
C
101 FORMAT (1H1,A8)
102 FORMAT (7F10.3)
103 FORMAT (9F8.5)
104 FORMAT (I1)
105 FORMAT (3F10.3)

```

```

110 FORMAT (1H1, A8/)
111 FORMAT (1X, 'TRANSFORMED ELASTIC CONSTANT OF MATRIX:')
112 FORMAT (10X, 9E12.4)
113 FORMAT (/1X, 'ASPECT RATIO C/A:', F10.5)
114 FORMAT (/1X, 'EQUIVALENT TRANSFORMATION STRAIN:', /1X, 9E12.3)
115 FORMAT (/1X, 'Q MATRIX:')
116 FORMAT (/1X, 'CALCULATED STRAIN AT X,Y,Z :', /1X, 9E12.3/)
117 FORMAT (/1X, 'AT X=', F10.3, 5X, 'Y=', F10.3, 5X, 'Z=', F10.3/)
118 FORMAT (/1X, 'EFFECTIVE STRESS=', E12.5)
119 FORMAT (1X, 'CALCULATED STRESS AT X,Y,Z:', /1X, 9E12.5)

C
      READ (5,101) TITLE
      READ (5,102) ECONSM
      CALL VCVTSP (LCONSM,9, CONSM,9)
      ID=16
      PY=3.1415927
      IDGT=3
      WRITE (6,110) TITLE
      WRITE (6,111)
      WRITE (6,112) ((CONSM(I,J), J=1,9), I=1,9)
      DO 3000 IIG=1,2
      BETA=0.04+0.04*(IIG-1)
      READ (5,103) STRAIN
      CONST=BETA/(8.*(PY**2))
      BETA2=BETA**2

C
      WRITE (6,113) BETA
      WRITE (6,114) STRAIN

C
201 READ (5,105) U, V, ZZ
      READ (5,104) ISIGN
      W=ZZ/BETA
      H=PY/2.
      G=PY/2.
      DO 3 I=1,9
      DC 3 J=1,9

```

```

3 S1(I,J)=0.
DC 5 I=1,6
DO 5 J=1,6
5 Q1(I,J)=0.
CALL GLC16(DX,DA,-1.D0, 1.D0)
DC 4 II=1,2
IS=(-1)**II
DO 6 JJ=1,ID
RJ=P(JJ)
BJ=B(JJ)
DO 9 KK=1,ID
SK=XX(KK)
CK=SQR1(1.-SK*SK)
UI=RJ*CK
VI=RJ*SK
WI=IS*SQR1(1.-UI**2-VI**2)
XN(1)=JI
XN(2)=VI
XN(3)=WI/BETA
XMU=SQRT((U-UI)**2+(V-VI)**2+BETA2*(W-WI)**2)
XEU1=SQRT((U-UI)**2+(V-VI)**2)
COSFI=(W-WI)*BETA/XMU
SINFI=XEU1/XMU
COSTH=(U-UI)/XEU1
SINTH=(V-VI)/XEU1
T(1)=SINFI*COSTH
T(2)=SINFI*SINTH
T(3)=COSFI
C
C INTEGRATE IN Z.T=0 PLANE
C
DC 61 I=1,6
DC 61 J=1,6
61 Q11(I,J)=0.
DC 61 IJ=1,4
SI=H*DX(IJ)+G

```

```

C
C
C
      ALL=H*DA(I,J)
      Z(1)=SINTH*COS(SI)+COSFI*COSTH*SIN(SI)
      Z(2)=-COSTH*COS(SI)+COSFI*SINTH*SIN(SI)
      Z(3)=-SINFI*SIN(SI)
C
C
C
      CALCULATE M SYMMETRIC MATRIX AND ITS INVERSE
      DO 32 I=1,3
      DO 32 K=1,I
      XM(I,K)=0.
      DO 33 J=1,3
      DO 33 L=1,3
      CALL DIGIT (I,J,K,L,N1,N2)
      XM(I,K)=XM(I,K)+CONSM(N1,N2)*Z(J)*Z(L)
      33 CONTINUE
      XM(K,I)=XM(I,K)
      32 CONTINUE
      CALL LINV2F (XM,3,3,XMINV,LDGT,WKAREA,IER)
C
C
C
      CALCULATE F SYMMETRIC MATRIX
      DO 42 I=1,6
      DO 42 K=1,I
      XF(I,K)=0.
      DO 43 J=1,3
      DO 43 L=1,3
      DO 43 N=1,3
      DO 43 JQ=1,3
      CALL DIGIT (J,L,N,JQ,N1,N2)
      XF(I,K)=CONSM(N1,N2)*XMINV(I,J)*XMINV(N,K)*(Z(M)*I(JQ)+Z(JQ)*I(M))
      **XF(I,K)
      43 CONTINUE
      XF(K,I)=XF(I,K)
      42 CONTINUE
C
C

```

```

C      CALCULATE THE INTEGRAL IN Z.T=0 PLANT Q11 SYMMETRIC MATRIX
C
DO 60 I=1,3
DO 60 IP=1,3
DO 60 K=1,3
DO 60 J=1,3
CALL DIGIT (I,IP,K,J,N1,N2)
SS1=(-T(LP)*XMINV(I,K)-T(I)*XMINV(IP,K)+Z(IP)*XF(I,K)+Z(I)*XF(IP,K
*)) *XN(J)
SS2=(-T(LP)*XMINV(I,J)-T(I)*XMINV(IP,J)+Z(IP)*XF(I,J)+Z(I)*XF(IP,J
*)) *XN(K)
SSS(N1,N2)=(SS1+SS2)*0.5
Q11(N1,N2)=Q11(N1,N2)+ALL*SSS(N1,N2)
60 CONTINUE
DC 9 N1=1,6
DO 9 N2=1,6
Q1(N1,N2)=Q1(N1,N2)+BJ*Q11(N1,N2)/((XMU**2)*ABS(WI))
9 CONTINUE
6 CONTINUE
4 CONTINUE

C      FORM THE WHOLE S MATRIX
C
DC 8 I=1,6
DO 8 J=1,6
IF (I.LE.3.AND.J.LE.3) IU=1
IF (I.GT.3.AND.J.GT.3) IU=4
IF (I.GT.3.AND.J.LE.3.OR.I.LE.3.AND.J.GT.3) IU=2
S1(I,J)=Q1(I,J)*PI8*CONST/IU
8 CONTINUE
DC 7) I=4,6
DO 7) J=1,3
S1(I+3,J)=S1(I,J)
7) S1(J,I+3)=S1(J,I)
DC 8) I=4,6
DO 8) J=4,6

```



```

X(L)=-DMC*XX(I)+DEC
X(NL)=DMC*XX(L)+DPC
A(L)=DAC*AA(L)
2000 A(NL)=DMC*AA(L)
      RETURN
      END
      SUBROUTINE DIGIT(NI,NJ,NK,NL,N1,N2)
C
C TRANSFORMATION FROM TENSOR TO MATRIX NOTATION: 11-1, 22-2, 33-3,
C 23-4, 31-5, 12-6
C
      NUMB1=NI+NJ
      NUMB2=NK+NL
      IF (NI-NJ) 11,12,11
12 N1=NI
      GO TO 16
11 GO TO (12,12,13,14,15),NUMB1
13 N1=6
      GO TO 16
14 N1=5
      GO TO 16
15 N1=4
16 IF (NK-NL) 21,22,21
22 N2=NK
      GO TO 26
21 GO TO (22,22,23,24,25),NUMB2
23 N2=6
      GO TO 26
24 N2=5
      GO TO 26
25 N2=4
26 CONTINUE
      RETURN
      END

```


APPENDIX E: THE STRESS FIELDS OF A $(\bar{1}\bar{1}\bar{1})$ $[110]$ SCREW DISLOCATION WALL

For the coordinate system shown in Figure 45b, the elastic constant matrix is

$$C = \begin{bmatrix} C_{11} & C_{12} & C_{13} & 0 & 0 & 0 \\ 0 & C_{22} & C_{23} & 0 & 0 & C_{26} \\ 0 & 0 & C_{33} & 0 & 0 & C_{36} \\ 0 & 0 & 0 & C_{44} & C_{45} & 0 \\ 0 & 0 & 0 & 0 & C_{55} & 0 \\ 0 & 0 & 0 & 0 & 0 & C_{66} \end{bmatrix}$$

where

$$C_{11} = C_{11}^{\circ} + \frac{2}{3}H^{\circ}$$

$$C_{12} = C_{13} = C_{12}^{\circ} - H^{\circ}/3$$

$$C_{22} = C_{33} = C_{11}^{\circ} + H^{\circ}/2$$

$$C_{23} = C_{12}^{\circ} - H^{\circ}/6$$

$$C_{44} = \frac{2}{3}C_{44}^{\circ} - (C_{12}^{\circ} - C_{11}^{\circ})/6$$

$$C_{55} = C_{66} = C_{44}^{\circ} - H^{\circ}/3$$

$$C_{45} = C_{36} = -C_{26} = \frac{\sqrt{2}}{6}H^{\circ}$$

$$H^{\circ} = 2C_{44}^{\circ} + C_{12}^{\circ} - C_{11}^{\circ}$$

C_{11}° , C_{12}° and C_{44}° are the standard elastic

constants.

For a single dislocation ($b_s = \frac{a}{2} \langle 110 \rangle$) in a one-phase medium, the stresses are

$$\sigma_{yz}^{(1)} = \frac{b_s L}{2\pi} \left(\frac{C_{44} x - C_{45} y}{C_{55} y^2 - 2C_{45} xy + C_{44} x^2} \right) \quad (E1)$$

$$\sigma_{xz}^{(1)} = \frac{b_s L}{2\pi} \left(\frac{C_{45} x - C_{55} y}{C_{55} y^2 - 2C_{45} xy + C_{44} x^2} \right) \quad (E2)$$

The stress fields of an equally spaced (spacing = D), infinite wall of screw dislocations are obtained from Equations (E1) (E2) by summation.

They are

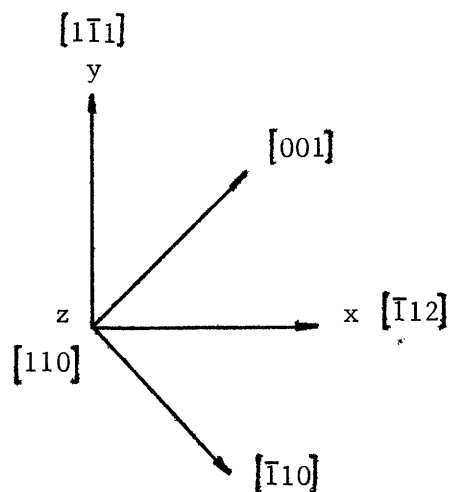
$$\sigma_{yz} = - \frac{b_s L}{2D} \frac{\sin 2q}{\cosh 2p - \cos 2q} \quad (E3)$$

$$\sigma_{xz} = \frac{b_s L}{2D} \left(\frac{L \sinh 2p - C_{45} \sin 2q}{C_{44} (\cosh 2p - \cos 2q)} \right) \quad (E4)$$

where $L = (C_{44} C_{55} - C_{45}^2)^{1/2}$

$$p = - \frac{L}{C_{44}} \frac{\pi y}{D} \quad q = \frac{\pi x}{D} + \frac{C_{45}}{C_{44}} \frac{\pi y}{D}$$

APPENDIX F: THE STRESS FIELDS OF A $(\bar{1}\bar{1}1)$ $[110]$ EDGE DISLOCATION WITH
BURGERS' VECTOR $\frac{a_{fcc}}{6} [\bar{1}\bar{1}2]$.



F.1 Based on the $[\bar{1}\bar{1}0]$ $[001]$ $[110]$ System with $b = (b_e, b_n, 0)$:

$$\sigma_{xx}^e = -(K_e b_e \lambda^2 / 2\pi Q) y [(C+3)x^2 + \lambda^2 y^2]$$

$$\sigma_{yy}^e = (K_e b_e / 2\pi Q) y (x^2 - \lambda^2 y^2)$$

$$\sigma_{zz}^e = \{1 - [2c_{11}^{\circ} c_{44}^{\circ} / ((\bar{c}_{12}^{\circ})^2 - (c_{12}^{\circ})^2)]\} \sigma_{xx}^e + [2c_{12}^{\circ} c_{44}^{\circ} / ((\bar{c}_{12}^{\circ})^2 - (c_{12}^{\circ})^2)] \sigma_{yy}^e$$

$$\sigma_{xy}^e = (K_e b_e / 2\pi Q) x (x^2 - \lambda^2 y^2)$$

$$\sigma_{xx}^n = (K_n b_n \lambda^2 / 2\pi Q) x (x^2 - \lambda^2 y^2)$$

$$\sigma_{yy}^n = (K_n b_n / 2\pi Q) x [x^2 + (C+3)\lambda^2 y^2]$$

$$\sigma_{zz}^n = \{1 - [2c_{11}^{\circ}c_{44}^{\circ}/((\bar{c}_{12}^{\circ})^2 - (c_{12}^{\circ})^2)]\}\sigma_{xx}^n + [2c_{12}^{\circ}c_{44}^{\circ}/((\bar{c}_{12}^{\circ})^2 - (c_{12}^{\circ})^2)]\sigma_{yy}^n$$

$$\sigma_{xy}^n = (K_n b_n \lambda^2 / 2\pi Q) y (x^2 - \lambda^2 y^2)$$

where $\bar{c}_{12}^{\circ} = [\frac{1}{2} c_{11}^{\circ} (c_{11}^{\circ} + c_{12}^{\circ} + 2c_{44}^{\circ})]^{1/2}$

$$c = [(\bar{c}_{12}^{\circ} + c_{12}^{\circ})(\bar{c}_{12}^{\circ} - c_{12}^{\circ} - 2c_{44}^{\circ})] / \bar{c}_{12}^{\circ} c_{44}^{\circ}$$

$$\lambda = (\bar{c}_{12}^{\circ} / c_{11}^{\circ})^{1/2}$$

$$K_e = (\bar{c}_{12}^{\circ} + c_{12}^{\circ}) [c_{44}^{\circ} (\bar{c}_{12}^{\circ} - c_{12}^{\circ}) / c_{11}^{\circ} (\bar{c}_{12}^{\circ} + c_{12}^{\circ} + 2c_{44}^{\circ})]^{1/2}$$

$$Q = Q_{\{100\}} = (x^2 + \lambda^2 y^2)^2 + c \lambda^2 x^2 y^2$$

c_{11}° , c_{12}° and c_{44}° are the standard elastic constants.

F.2 To Transform to the New System $[\bar{1}\bar{1}2]$ $[\bar{1}\bar{1}\bar{1}]$ $[\bar{1}10]$, let the Primed Quantities be in the Old System $[\bar{1}10]$ $[001]$ $[\bar{1}10]$,

$$x = Rx'$$

$$\sigma_{ij} = R_{ik} R_{jl} \sigma'_{kl}$$

or $\sigma = R\sigma'R$

where the coordinate transformation matrix

$$R = \begin{bmatrix} \cos\theta & \sin\theta & 0 \\ -\sin\theta & \cos\theta & 0 \\ 0 & 0 & 1 \end{bmatrix} = \begin{bmatrix} \frac{\sqrt{1}}{\sqrt{3}} & \frac{\sqrt{2}}{\sqrt{3}} & 0 \\ -\frac{\sqrt{2}}{\sqrt{3}} & \frac{\sqrt{1}}{\sqrt{3}} & 0 \\ 0 & 0 & 1 \end{bmatrix}$$

$$\sigma_{xx} = \frac{1}{3} (\sigma_{xx}' + 2\sqrt{2} \sigma_{xy}' + 2\sigma_{yy}')$$

$$\sigma_{yy} = \frac{1}{3} (\sigma_{xx}' - 2\sqrt{2}\sigma_{xy}' + \sigma_{yy}')$$

$$\sigma_{xy} = \frac{1}{3} (-\sqrt{2} \sigma_{xx}' - \sigma_{xy}' + \sqrt{2} \sigma_{yy}')$$

$$x' = \frac{\sqrt{1}}{\sqrt{3}} x - \frac{\sqrt{2}}{\sqrt{3}} y$$

$$y' = \frac{\sqrt{2}}{\sqrt{3}} x + \frac{\sqrt{1}}{\sqrt{3}} y$$

$$z' = z$$

$$b_e' = \frac{\sqrt{1}}{\sqrt{3}} b_e - \frac{\sqrt{2}}{\sqrt{3}} b_n$$

$$b_n' = \frac{\sqrt{2}}{\sqrt{3}} b_e + \frac{\sqrt{1}}{\sqrt{3}} b_n$$

F.3 Based on the $[\bar{1}12]$ $[1\bar{1}\bar{1}]$ $[110]$ system,

$$\sigma_{xx}^e = - \frac{K_e b_e}{2\pi Q_{[111]} \lambda^2} \left\{ \frac{\sqrt{2}}{3} [2\lambda^6 + (C+21)\lambda^4 - (4C+21)\lambda^2 - 2] x^3 \right.$$

$$+ [2\lambda^6 - (C-9)\lambda^4 + 12\lambda^2 + 4]x^2y + \sqrt{2}[\lambda^6 + 3\lambda^4 + 2C\lambda^2 - 4]xy^2$$

$$+ \frac{1}{3} [\lambda^6 + 2(C+3)\lambda^4 + 4(C+3)\lambda^2 + 8]y^3\}$$

$$\sigma_{xy}^e = \frac{K_e b_e}{2\pi Q_{\{111\}}} \frac{1}{\sqrt{3}} \left\{ \begin{array}{l} [4\lambda^4 + 2(C+2)\lambda^2 + 1]x^3 + 3\sqrt{2}[2\lambda^4 - (C+5)\lambda^2]x^2y \\ + 3[2\lambda^4 - 3\lambda^2 - 2]xy^2 + \sqrt{2}[\lambda^4 + 2(C+2)\lambda^2 + 4]y^3 \end{array} \right\}$$

$$\sigma_{xx}^n = \frac{K_e b_n}{2\pi Q_{\{111\}}\lambda^2} \left\{ \frac{1}{3} [4\lambda^6 + 2\lambda^4(C+6) + (4C+9)\lambda^2 + 2]x^3 \right.$$

$$+ \sqrt{2}[2\lambda^6 - \lambda^4(C+3) + 3\lambda^2 - 2]x^2y + [2\lambda^6 - 3\lambda^4 - 2\lambda^2(C+6) + 4]xy^2$$

$$\left. + \frac{\sqrt{2}}{3} [\lambda^6 + \lambda^4(2C+3) - 2C\lambda^2 - 4]y^3 \right\}$$

$$\sigma_{xy}^n = \frac{K_e b_n}{2\pi Q_{\{111\}}\lambda^2} \frac{1}{\sqrt{3}} \left\{ \begin{array}{l} \sqrt{2}[4\lambda^4 + 2\lambda^2(C+2) + 1]x^3 + 3[2\lambda^4 + 3\lambda^2 - 2]x^2y \\ + \sqrt{2}[-3(C+5)\lambda^2 + 6]xy^2 - [\lambda^4 + 2(C+2)\lambda^2 + 4]y^3 \end{array} \right\}$$

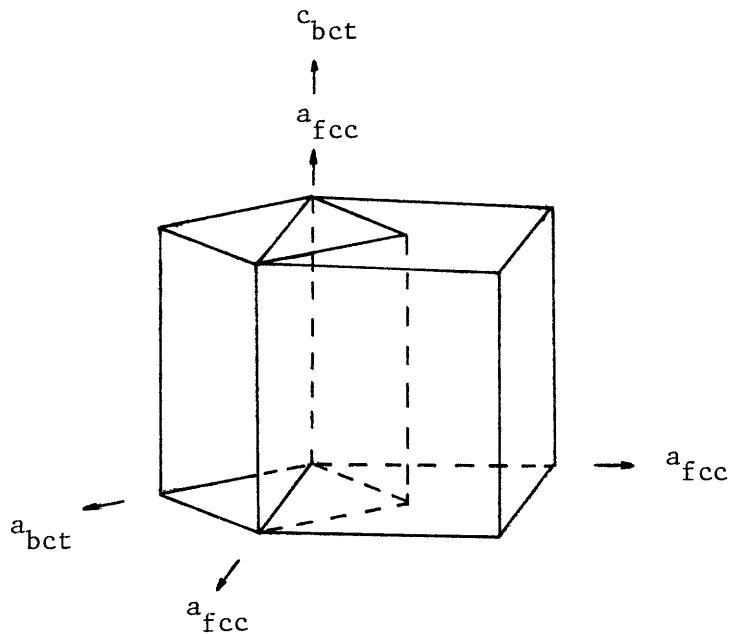
where

$$Q_{\{111\}} = [4\lambda^4 + \lambda^2(2C+4) + 1]x^4 + 2\sqrt{2}[4\lambda^4 - \lambda^2(C+2) - 2]x^3y$$

$$+ 3[4\lambda^4 - \lambda^2(C+2) + 4]x^2y^2 + 2\sqrt{2}[2\lambda^4 + (C+2)\lambda^2 - 4]xy^3$$

$$+ [\lambda^4 + 2\lambda^2(C+2) + 4]y^4$$

APPENDIX G: BAIN DEFORMATION IN THE fcc→bct TRANSFORMATION OF ORDERED Fe₃Pt



transformation: $\frac{a_{fcc}}{\sqrt{2}} \rightarrow a_{bct}, a_{fcc} \rightarrow c_{bct}$

Bain deformation: $\frac{a_{bct} - a_{fcc}/\sqrt{2}}{a_{fcc}/\sqrt{2}} = 0.082$

$$\frac{c_{bct} - a_{fcc}}{a_{fcc}} = -0.148$$

where { $a_{fcc} = 3.729\text{\AA}$
 $a_{bct} = 2.857\text{\AA}$
 $c_{bct} = 3.176\text{\AA}$

Comparison: along a axis:

$$\frac{\text{ordered Fe}_3\text{Pt}}{\text{disordered Fe}_3\text{Pt}} = \frac{0.082}{0.128} = 0.66$$

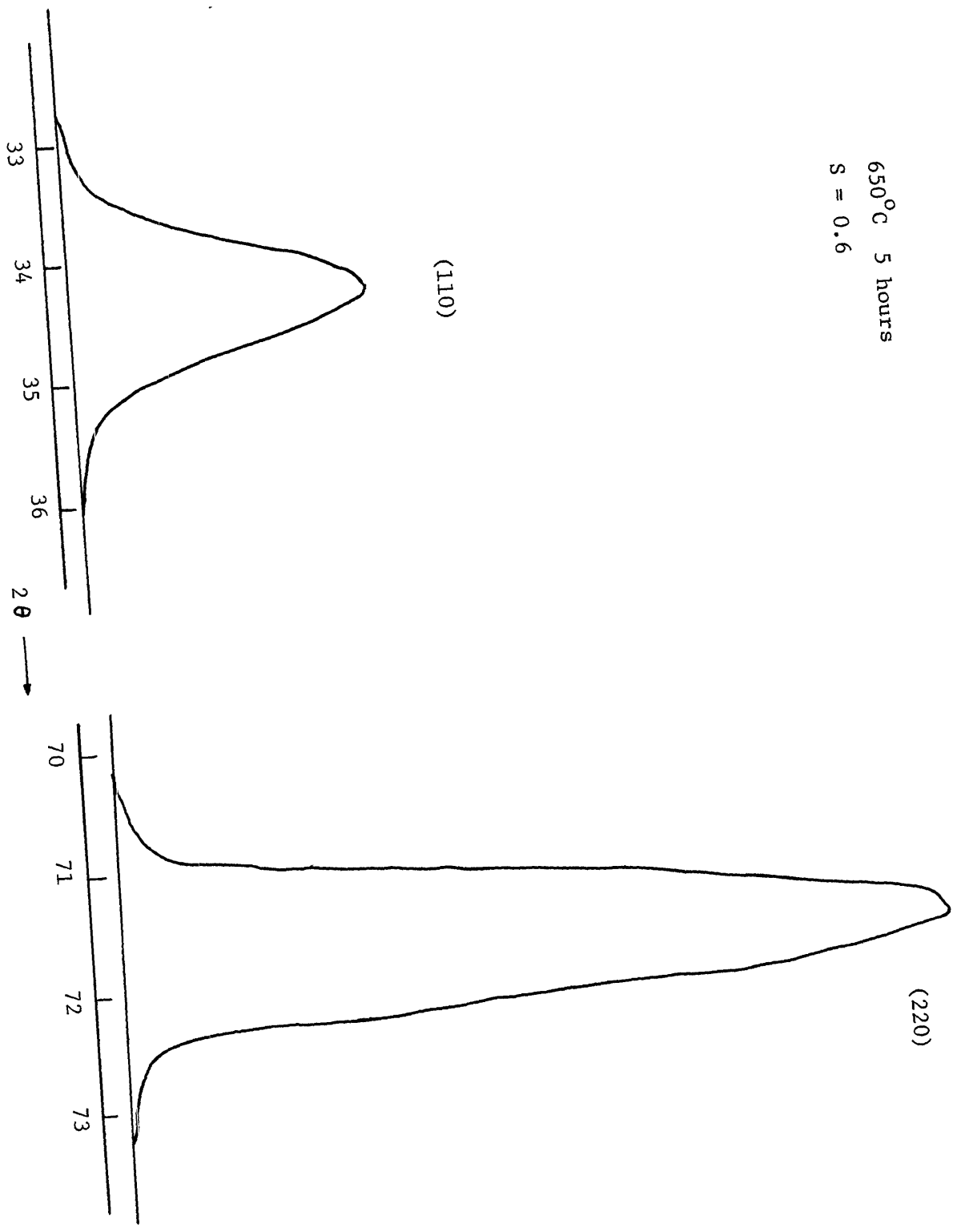
along c axis:

$$\frac{\text{ordered Fe}_3\text{Pt}}{\text{disordered Fe}_3\text{Pt}} = \frac{0.148}{0.203} = 0.73$$

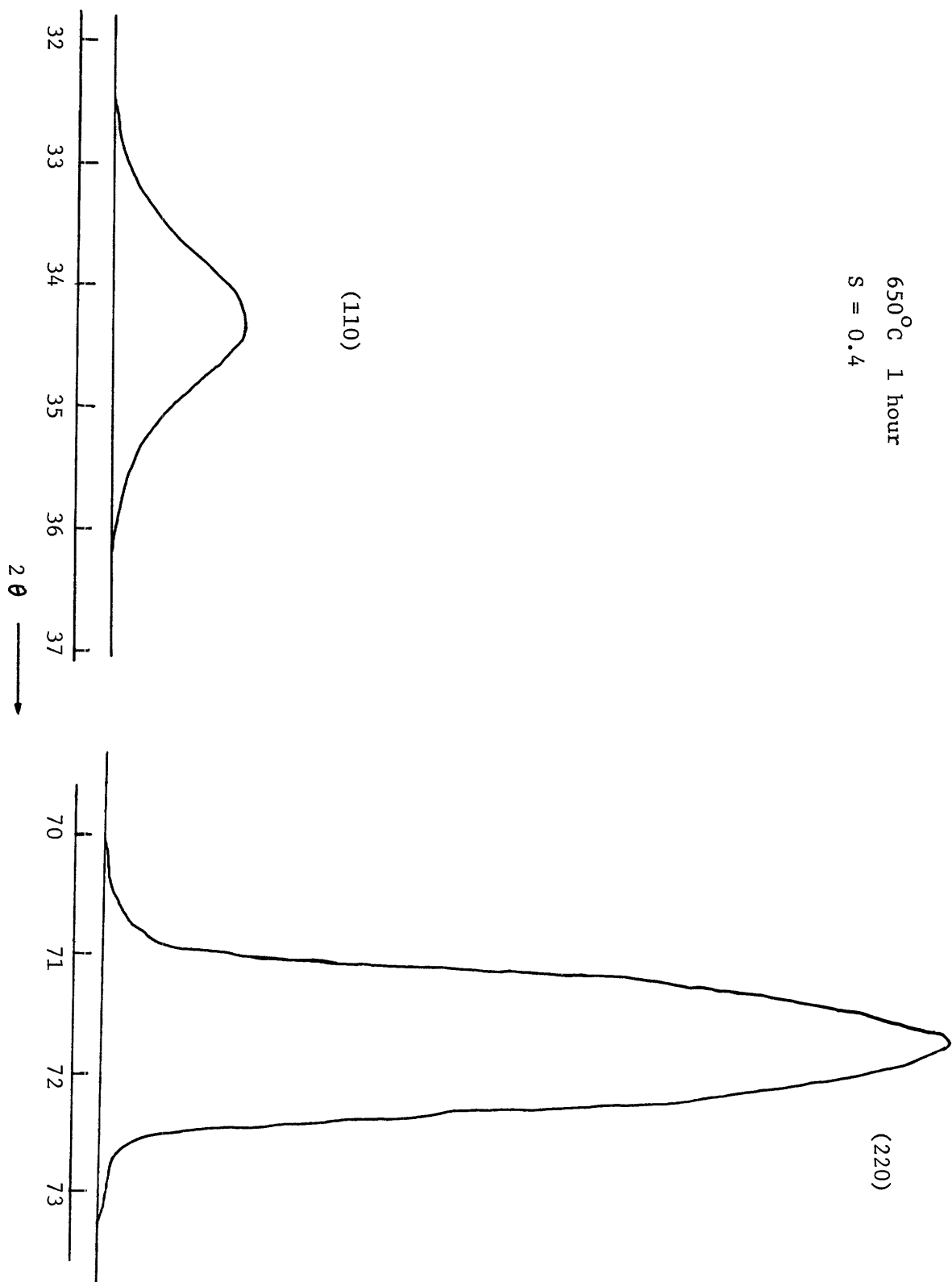
An average change of 0.7 is seen.

APPENDIX H: INTENSITY TRACES OF SINGLE CRYSTAL (110) AND (220)
DIFFRACTION PEAKS IN Fe₃Pt

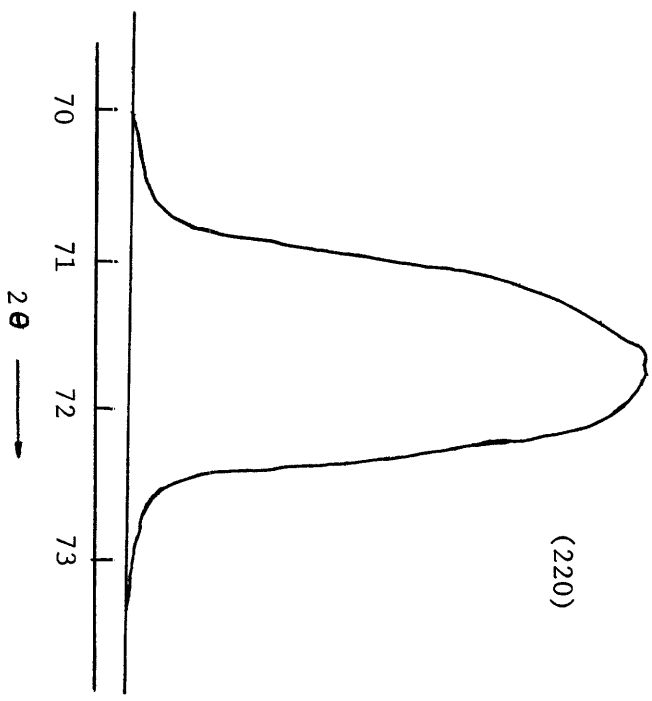
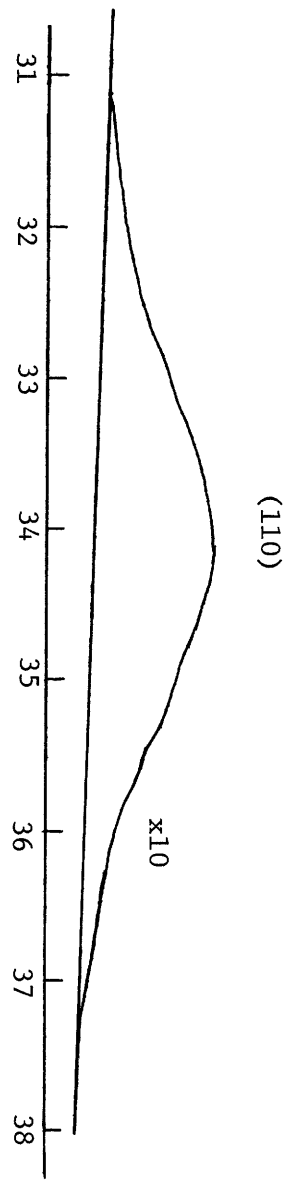
650°C 5 hours
S = 0.6



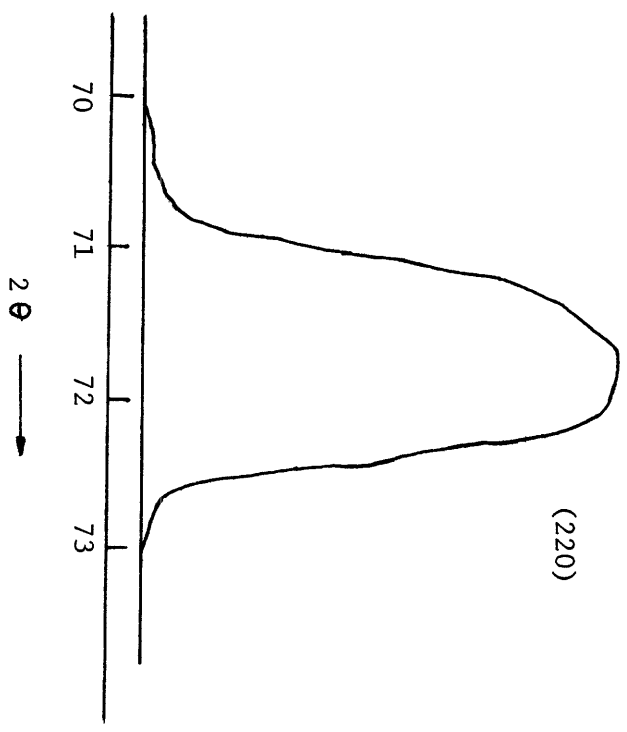
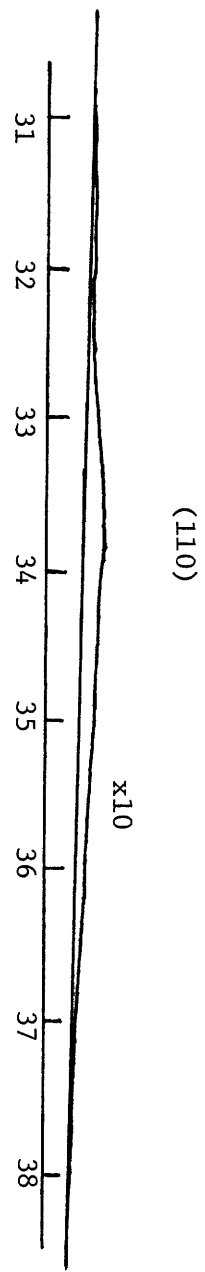
650°C 1 hour
S = 0.4



650°C 10 minutes
S = 0.2



900°C 1 hour
S = 0



REFERENCES

1. F.C. Nix and D. MacNair, *Phys. Rev.*, 60, (1941) 597.
2. Y. Tanji and Y. Shirakawa, *Sci. Rep. RITU*, A22, (1971) 135.
3. H. Masumato and T. Kobayashi, *Trans. Jap. Inst. Metals*, 6 (1965) 113.
4. M. Chevenard, *Compt. Rend*, 172 (1921) 594.
5. M. Chevenard, *Compt. Rend*, 172 (1921) 1655.
6. G. Hausch and H. Warlimont, *Acta Met.*, 21, (1973) 401.
7. K. Sumiyama, M. Shiga and Y. Nakamura, *J. Phys. Soc. Japan*, 40, (1976) 996.
8. J.M. Leger, C. Susse and B. Vodar, *Solid State Commun*, 5, (1967) 755.
9. J.M. Leger and C. Susse-Loriers, *Phys. Letters (Netherlands)* 37A, (1971) 145.
10. J.J. Leger, C. Susse-Loriers and B. Vodar, *Phys. Rev.*, B6, (1972) 4250.
11. R.C. Wayne and L.C. Bartel, *Phys. Letters (Netherlands)*, 38A, (1968) 196.
12. T. Nakajima, *J. Phys. Soc. Japan*, 19, (1964) 520.
13. K.P. Belov and Z.D. Sirota, *Soviet Phys. JETP*, 36, (1959) 752.
14. Y. Nakamura, M. Hayase, Y. Miyamoso and N. Kawai, *J. Phys. Soc. Japan*, 30, (1971) 720.
15. M. Matsumoto, T. Kaneko and K. Kamigaki, *J. Phys. Soc. Japan*, 24, (1968) 953.
16. R.M. Bozorth, Ferromagnetism, Van Nostrand, New York, 1961.
17. A.J. Goldman and W.D. Robertson, *Acta Met.*, 12, (1964) 1265.
18. This Thesis.
19. G.I. Kataev and Z.D. Sirota, *Soviet Phys. JETP*, 11, (1960) 747.

20. G. Hausch, *J. Phys. Soc. Japan*, 37, (1974) 824.
21. G.A. Alers, J.R. Neighbors and H. Sato, *J. Appl. Phys.*, 30, (1959) 231S.
22. K. Salama and G.A. Alers, *J. Appl. Phys.*, 39, (1968) 4857.
23. G. Hausch, *J. Phys. Soc. Japan*, 37, (1974) 819.
24. M. Hayase, M. Shiga and Y. Nakamura, *J. Phys. Soc. Japan*, 34, (1973) 925.
25. A. Kussmann and G. Countess of Rittberg, *Metallkunde*, 41, (1950) 470.
26. A.E. Berkowitz, F.J. Donahoe, A.D. Franklin and R.D. Steijn, *Acta Met.*, 5 (1957) 1.
27. O. Herbeuval, Ph.D. Thesis, L'Universite de Nancy, 1973.
28. T. Mizguchi, M. Akimitsu and S. Chikazumi, *J. Phys. Soc. Japan*, 34, (1973) 932.
29. E.I. Kondorsky and V.L. Sedov, *J. Appl. Phys.*, 31, (1960) 331S.
30. M. Shiga and V. Nakamura, *J. Phys. Soc. Japan*, 26, (1969) 24.
31. R.J. Weiss, *Proc. Phys. Soc. (London)*, 82, 281 (1963); *Phil. Mag.*, 26, (1972) 261.
32. D.A. Colling and W.J. Carr, Jr., *J. Appl. Phys.*, 41, (1970) 5125.
33. H. Asano, *J. Phys. Soc. Japan*, 27, (1969) 542.
34. S. Kachi, H. Asano and N. Nakanishi, *J. Phys. Soc. Japan*, 25, (1968) 285; 25, (1968) 909.
35. Y. Tanji, *J. Japan Inst. Metals*, 35, (1971) 1.
36. W.J. Carr, Jr., and D.A. Colling, *J. Appl. Phys.*, 44, (1973) 875.
37. A. Katsuki and K. Terao, *J. Phys. Soc. Japan*, 26, (1969) 1109.
38. K. Terao and A. Katsuki, *J. Phys. Soc. Japan*, 27, (1969) 321.
39. N.D. Lang and H. Ehrenreich, *Phys. Rev.*, 168, (1968) 605.

40. J. Hubbard, Proc. Roy. Soc. (London), A276, (1963) 238; A277, (1964) 237; A281, (1964) 401.
41. J. Kanamori, Progr. Theoret. Phys. (Kyoto), 30, (1963) 275.
42. M.C. Gutzwiller, Phys. Rev. Letters, 10, (1963) 159; Phys. Rev., 134, (1964) A923.
43. E.P. Wohlfarth, J. Phys. C, 2, (1969) 68.
44. J. Mathon and E.P. Wohlfarth, Phys. Stat. Sol., 30, (1968) K131.
45. E.P. Wohlfarth, Phys. Letters, 28A, (1969) 569; 31A (1970) 525.
46. E.C. Stoner, Rept. Progr. Phys., 11, (1948) 43 and references therein.
47. E.C. Stoner, J. Phys. Radium, 12 (1951) 372; and references therein.
48. D.M. Edwards and E.P. Wohlfarth, Proc. Roy. Soc. (London) 303, (1968) 127.
49. E.P. Wohlfarth, J. Appl. Phys., 39, (1968) 1061.
50. H. Sato, J. Appl. Phys., 29 (1958) 456.
51. G.A. Alers, J.R. Neighbours and H. Sato, J. Phys. Chem. Solid, 13, (1960) 401.
52. G. Hausch, Phys. Stat. Sol.(a), 15 (1973) 501.
53. G. Hausch, Phys. Stat. Sol.(a), 16 (1973) 371.
54. G. Hausch, Phys. Stat. Sol.(a), 18 (1973) 735.
55. W. Heisenberg, Z. Physik, 49, (1928) 619.
56. F. Bloch, Z. Physik, 57 (1929) 545.
57. C. Herring, Magnetism, vol. IV, Academic Press, 1966.
58. J.S. Kouvel, in Magnetism and Metallurgy, Vol. 2, edited by A.E. Berkowitz and E. Kneller, Academic Press, 1969.
59. C. Zener, Trans. AIME, 203, (1955) 619.

60. C. Zener, *Phys. Rev.*, 81 (1951) 440.
61. C.G. Shull and M.K. Wilkinson, *Phys. Rev.*, 97 (1955) 304.
62. G.G. Low and M.F. Collins, *J. Appl. Phys.*, 34, (1963) 1195.
63. M.F. Collins and G.G. Low, *Proc. Phys. Soc.*, (London) 86 (1965) 535.
64. M.F. Collins and G.G. Low, *J. Phys.*, (Paris) 25, (1964) 596.
65. R.P. Messmer, S.K. Knudson, K.H. Johnson, J.B. Diamond and C.Y. Yang, *Phys. Rev. B*, 13 (1976) 1396.
66. J.C. Slater, The Self-Consistent Field for Molecules and Solids Vol. 4, McGraw Hill, 1974.
67. H.B. Huntington, Solid State Phys. Vol. 7, Academic Press, 1958.
68. Ferromagnetism, by Bozorth.
69. W. Döring, *Ann Phys. (Germany)*, 32 (1938) 465.
70. F. Reif, Statistical and Thermal Physics, McGraw Hill, 1965.
71. A.P. Levanyuk, *Soviet Phys JETP*, 22 (1966) 901.
72. P.L. Young and A. Bienenstock, *J. Phys. Chem. Solids*, 33, (1972) 1.
73. K. Fuchs, *Proc. Roy. Soc.*, A153 (1935) 622.
74. B.D. Cullity, Elements of X-ray Diffraction, Addison-Wesley, 1956.
75. S.B. Palmer and G.A. Forster, *Am. J. Phys.*, 38 (1970) 814.
76. H.J. McSkimin, *J. Acoust. Soc. Am.*, 33, (1961) 12.
77. H.J. McSkimin, *J. Acoust. Soc. Am.*, 32, (1960) 1401.
78. J. Krautkrämer, Ultrasonic Testing of Materials, Springer-Verlag, 1969.
79. O.L. Anderson, Physical Acoustics IIIB, Academic Press, New York (1965).
80. W. Voigt, Lehrbuch der Kristallphysik, Teubner Verlag, Leipzig (1928).

81. A. Reuss, *Z. angew. Math. Mech.*, 9 (1929) 49.
82. R. Hill, *Proc. Roy. Soc.*, A65 (1952) 349.
83. B. Djuric, Unpublished.
84. R.G. Davies and N.S. Stoloff, *Trans. Amer. Inst. Met. Engrs.*, 230, (1964) 390.
85. Y. Tanji, H. Asano and H. Moriya, *J. Japan Inst. Metals*, 36, (1972) 1100.
86. M. Umemoto and C.M. Wayman, *Proc. Intern. Symp. on New Aspects of Martensitic Transformation*, Kobe (1976).
87. R.P. Reed and R.E. Schramm, *J. Appl. Phys.*, 40, (1969) 3453.
88. J.L. Nilles, Ph.D. Thesis, Cornell University, 1970.
89. H. Sato, *J. Appl. Phys.*, 31, (1960) 327S.
90. D.P. Dunne and C.M. Wayman, *Met. Trans.*, 4, (1973) 137.
91. S. Kajiwara and W.S. Owen, *Met. Trans.*, 5, (1974) 2047.
92. M. Umemoto, Ph.D. Thesis, University of Illinois, 1977.
93. E.J. Efsic and C.M. Wayman, *Trans. TMS-AIME*, 239 (1967) 873.
94. E.S. Machlin and M. Cohen, *J. Metals*, 3, (1951) 1019.
95. A.B. Greninger and A.R. Troiano, *AIME Trans.*, 185 (1949) 590.
96. T. Tadaki and K. Shimizu, *Trans. Japan Inst. Met.*, 11, (1970) 44.
97. T. Tadaki, K. Katsuki and K. Shimizu, *Proc. Intern. Symp. (JIMIS-I) on New Aspects of Martensitic Transformation*, Kobe (1976).
98. T. Tadaki and K. Shimizu, *Scripta Met.*, 9, (1975) 771.
99. M.S. Wechsler, D.S. Lieberman and T.A. Read, *Trans. AIME*, 197, (1953) 1503.
100. J.S. Bowles and J.K. Mackenzie, *Acta Met.*, 2, (1954), 129, 138, 224.
101. S. Kajiwara and W.S. Owen, *Scripta Met.*, 11, (1977) 137.

102. J.W. Christian, The Theory of Transformation in Metals and Alloys, Pergamon Press, Oxford, 1965.
103. C. Zener, Elasticity and Anelasticity of Metals, University of Chicago Press, 1948.
104. G.V. Kudjurov and L.C. Khandros, Dokl. Akad. Nauk SSSR, 66, (1949) 211.
105. J.D. Eshelby, Proc. Roy. Soc. A, 241, (1957) 376.
106. J.D. Eshelby, Proc. Roy. Soc. A, 252, (1959) 561.
107. J.D. Eshelby, Prog. in Solid Mechanics, Vol. 7 (1961).
108. G.B. Olson and M. Cohen, Scripta Met., 9, (1975) 1247.
109. W.A. Backofen, Deformation Processing, Addison-Wesley, 1972.
110. G.B. Olson and W.S. Owen, Proc. Intern. Symp. on New Aspects of Martensitic Transformation, Kobe (1976).
111. W.D. McMillan, The Theory of the Potential, Dover 1958.
112. M.J. Schmutz, Ph.D. Thesis, M.I.T., 1978.
113. J.K. Lee and W.C. Johnson, Paper presented at AIME, Atlanta, March 1977.
114. L.J. Walpole, Proc. Roy. Soc., A300, (1967) 270.
115. J.R. Willis, Asymmetric Problems of Elasticity, University of Cambridge (1970).
116. N. Kinoshita and T. Mura, Phys. Stat. Sol., 25, (1971) 759.
117. R.J. Asaro and D.M. Barnett, J. Mech. Phys. Solids, 23, (1975) 77.
118. K. Robinson, J. Appl. Phys., 22, (1951) 1945.
119. D.M. Barnett, J.K. Lee, H.I. Aaronson and K.C. Russell, Scripta Met., 8, (1974) 1447.
120. M. Shibata and K. Ono, Acta Met., 23 (1975) 587.
121. J.A. Wert, Acta Met., 24, (1976) 65.
122. A.G. Khachaturyan, Sov. Phys. Solid State, 8, (1967) 2163.

123. J.K. Lee, D.M. Barnett and H.I. Aaronson, *Met. Trans.*, 8A, (1977) 963.
124. A.H. Stroud, Approximate Calculation of Multiple Integrals, Prentice-Hall, 1971.
125. G.B. Olson and M. Cohen, *Met. Trans.*, 7A, (1976) 1897.
126. Hirth and Lothe, Theory of Dislocations, McGraw-Hill, 1968.
127. Y.T. Chou and C.S. Pande, *J. Appl. Phys.*, 44, (1973) 3355.
128. C.S. Pande and Y.T. Chou, *J. Appl. Phys.*, 43 (1972) 840.
129. Y.T. Chou, C.S. Pande and H.C. Yang, *J. Appl. Phys.*, 46, (1975) 5.
130. Y.T. Chou and G.T. Sha, *J. Appl. Phys.*, 42, (1971) 2625.
131. A.H. Cottrell, Dislocations and Plastic Flow in Crystals, Oxford University, 1953.
132. D.M. Barnett, *Phys. Stat. Sol.(b)*, 49, (1972) 741.
133. J.W. Christian, Physical Properties of Martensite and Bainite, Iron and Steel Inst. Spec. Report 93, (1965) 4.
134. H.C. Tong and C.M. Wayman, *Acta Met.*, 22, (1974) 887.
135. B. Djuric, M.I.T., unpublished.
136. L. Kaufman and M. Cohen, *Progr. Metal Phys.*, vol. 7, (1958) 165.
137. A.J. Bogers and W.G. Burgers, *Acta Met.*, 12, (1964) 255.
138. H. Warlimont and L. Delaey, *Prog. in Mat. Sci.*, vol. 18, Pergamon Press, 1974.
139. L. Kaufman, E. Clougherty and R.J. Weiss, *Acta Met.*, 11, (1963) 323.

BIOGRAPHICAL NOTE

Hung C. Ling was born on April 22, 1950 in Wenchow, China. Raised and educated in Hong Kong, he entered M.I.T. in September, 1969. He received the S.B. degree in Physics in 1972, with a Thesis titled "Alkali Dimer Formation in a Supersonic Nozzle Beam". In 1974, he received the M.A. degree in Physics from the State University of New York at Stony Brook. Then he returned to M.I.T. and entered a doctoral program in Materials Science with a minor in management. His interest includes sports and photography.